Strategies for Design and Fabrication of Nanoplasmonic Metasurfaces with Extreme Geometric Features

by

Mitchell James Tanner Semple

A thesis submitted in partial fulfillment of the requirements for the degree of

Doctor of Philosophy

in

Electromagnetics and Microwaves

Department of Electrical and Computer Engineering

University of Alberta

Abstract

The ever-increasing integration density of optical components has pushed engineers and physicists to rethink the fundamentals of bulky dielectric lensing systems. Metasurfaces, which are two-dimensional, periodic arrays of metallic (plasmonic) or dielectric scatterers that exhibit exotic interactions with light, have been suggested as a robust and easily-integrated alternative to perform a variety of optical functions. In particular, plasmonic metasurfaces have a number of advantages when applied to imaging systems and sensors due to their small size and their ability to strongly enhance electric fields. Unfortunately, intuitive design methods have failed to meet physical performance requirements. Computational inverse design methods are now being explored to approach these limits, but are hindered by practical nanofabrication considerations. One of the main enabling technologies for nanofabrication of plasmonic metasurfaces has been the Ga^+ focused ion beam, which uses a stream of heavy ions to knock away sample material. The recently commercialized He^+ focused ion beam is able to pattern metals more accurately, but thus far, has suffered from low reproducibility, which has made fabricating large devices such as metasurfaces nearly impossible.

This thesis pushes the boundaries of top-down plasmonic gold metasurface nanofabrication to a feature size of 10 nm using helium ion beam milling. Metasurfaces demand stringent fabrication performance, often requiring hundreds of identical elements with fine, complex features and large aspect ratios (depth:feature size). As examples, three metasurfaces were designed using

conventional design methods, two to make full use of the potential of 10-nm features – a mere 60 atoms across – with the helium ion microscope, and one contrasting design making use of 100-nm features patterned by electron beam lithography.

The first design acts as a bandpass filter for near-infrared wavelengths, making use of fine plasmonic kinetic inductive nanowires lining an aperture. An equivalent circuit model is developed using generalizable techniques that can predict the performance of the metasurface near resonance. The designed metasurface uses 10-nm wide and 50-nm thick nanowires that meet at the centre, separated by 10-nm wide nanogaps. The structure is used to study the ion beam control parameters in detail, and the most impactful parameters to increase reliability are found to be the ion dosage and ion beam current. A prototype is fabricated over a large 225 μm^2 ($> 90\lambda_0^2$) area, and fabrication defects are analyzed in detail using representative simulations to show that even with tuned beam parameters, grain defects from the gold crystal structure, redeposition of the milled material, and poor substrate contrast of the nanogaps suppress the metasurface performance. A subwavelength imaging metasurface making use of this design is proposed, which can achieve a subdiffraction resolution of at least $\lambda_0/3.6$ in simulation.

The second design acts as a polarization filter for visible wavelengths and is accurately modelled using the same equivalent-circuit approach developed for the previous design. It is shown that the aforementioned fabrication challenges can be overcome by patterning single-crystal gold films specially grown on lattice-matched LiF crystals and by removing the LiF substrate through dissolution in HF. The fabricated prototypes show reliable 10-nm features with a variation on the order of 1 nm, fabricated over an area of > 12 μm^2 ($> 16\lambda_0^2$). The metasurface is experimentally characterized and shows a clear separation between orthogonal polarizations. This design is then used to simulate a meta-

surface that refracts a normal-incidence plane wave to 48.5° with an efficiency above 2%.

Finally, the third design acts as a CO_2 sensor in the mid-infrared. Plasmonic nanowires are combined with meandered capacitors with a 100-nm feature size to strongly enhance the local electric field around the metasurface, showing a nearly 5× enhancement over the conventional approach. A simple electron-beam lithography lift-off process is developed and validated. The fabricated metasurfaces are integrated into a custom gas cell and experimentally show a strong enhancement of the bending resonance of CO_2 at a wavelength of 15 µm. The addition of a thin functionalization layer is studied numerically, showing a significant increase in the absorption enhancement.

Preface

This thesis is an original work by Mitchell Semple. Parts of this thesis have been submitted for publication, published, and co-authored as described below.

1. **M. Semple**, E. Baladi, and A. K. Iyer, "Optical Metasurface Based on Subwavelength Nanoplasmonic Metamaterial-Lined Apertures". *IEEE Journal of Selected Topics in Quantum Electronics Special Issue on Metamaterial Photonics and Integration*, vol. 25, no. 3, pp. 1–8, Jan 2019. doi: 10.1109/JSTQE.2019.2896277

I performed all the simulations, analysis, and fabrication, and wrote the manuscript. E.B. assisted with the early design, and A.K.I. conceived of and supervised the project. All authors contributed to editing the manuscript.

The design and parametric simulations in Sec. 3.1 were taken from this paper, along with some of the background in Ch. 2.

2. A. Bhardwaj, Dheeraj Pratap, **Mitchell Semple**, Ashwin K. Iyer, Arun M. Jayannavar, S. Anantha Ramakrishna, "Properties of waveguides filled with anisotropic metamaterials". *Comptes Rendus. Physique*, vol. 21, no. 7-8, pp. 677-711, Jan 2021. ***Invited***

I contributed the review of metamaterial (MTM)-lined waveguides and apertures, Secs. 4.5–7 of the paper, under the supervision of A.K.I. I also contributed new results for MTM-lined apertures with thick liners, translated the abstract and edited the full manuscript.

The results at the end of Sec. 3.1.5 were taken from this paper.

3. **M. Semple**, A. C. Hryciw, P. Li, E. Flaim, and A. K. Iyer, "Patterning of Complex, Nanometer-Scale Features in Wide-Area Gold Nanoplasmonic Structures Using Helium Focused Ion Beam Milling". *ACS Applied Materials and Interfaces*, vol. 13, no. 36, pp.43209-43220, Sep 2021.

I designed and performed all the experiments and analysis in this paper, and wrote the manuscript under the supervision of A.K.I. Training and general fabrication process development recommendations were provided by A.C.H. and P.L. under the supervision of E.F. All authors contributed to editing the manuscript.

Some of the background in Ch. 2 was adapted from this paper, along with the background in Sec. 4.1. Additionally, the experimental results in Sec. 4.3 and the analysis in Sec. 4.5 were taken from this paper.

4. **M. Semple** and A. K. Iyer, "Surface-Enhanced Mid-Infrared Absorption Spectroscopy Using Miniaturized-Disc Metasurface". *Sci Rep*, vol. 11, 23557, Dec 2021.

For this paper, I performed all the design, simulations, and experiments under the supervision of A.K.I. I conceived of the application, and A.K.I. and I conceived of the design. The fabrication was performed in part by the nanoFAB staff, the Quantum Nanofab staff, and myself. I designed the gas cell, had it fabricated by Jason Dibbs at the Chemistry Faculty Glass Shop, and had assistance from the nanoFAB centre's Glenn Elaschuk in mounting it to the fourier-transform infrared (FTIR) microscope. I wrote the manuscript and all authors contributed to editing.

Once again, some of the background was adapted from this paper. The parametric sweeps in Sec. 3.3, the fabrication, characterization, and analysis

in Sec. 4.8, and the experiment in Sec. 5.3 were published in this paper. Appendix F was included as supplementary material in the original publication.

5. **M. Semple**, K. G. Scheuer, R. G. DeCorby, and A. K. Iyer, "Complex 10-nm Resolution Nanogap and Nanowire Geometries for Plasmonic Metasurface Miniaturization". ***(Under Review, Jul 2022).***

I performed all the design, simulations, fabrication, and analysis for this paper under the supervision of A.K.I. A.K.I. and I conceived of the design. The characterization setup was built by K.G.S., and K.G.S. and I performed the characterization experiments under the supervision of R.G.D. I wrote the manuscript and all authors contributed to editing.

This paper includes some of the background presented in this thesis, the analysis of Sec. 3.2.3, and parts of the fabrication, characterization, and analysis in Sec. 4.6 and Sec. 4.7.

For the following conference papers, I performed all the design and simulations, and wrote the manuscript under the supervision of A.K.I. All authors contributed to editing the manuscript.

1. **M. Semple** and A. K. Iyer, "Asymmetric Metamaterial-Lined Apertures for Plasmonic Phase-Gradient Optical Metasurfaces". *2022 USNC-URSI National Radio Science Meeting*, Boulder, CO. Jan 2021. (Online) ***Invited***

Fig. 5.4a was taken from this paper.

2. **M. Semple** and A. K. Iyer, "Mu-Negative and Near-Zero Lined Disks for Surface-Enhanced Mid-Infrared Spectroscopy". *2020 IEEE AP-S Symposium on Antennas and Propagation and USNC-URSI Radio Science Meeting*, Montreal, QC. Jul 2020. (Online)

The nominal design of the mid-infrared (MIR) MTM-lined disc in Sec. 3.3 was adapted from this paper.

3. **M. Semple** and A. K. Iyer, "Design and Simulation of Polarization-Sensitive ENNZ-Lined Apertures for Visible-Light Metasurfaces". *14^{th} European Conference on Antennas and Propagation, EuCAP 2020*, Copenhagen, Denmark. Mar 2020.

The nominal design of the two-wire MTM-lined aperture in Sec. 3.2 was taken from this paper.

Finally, the following conference paper was coauthored between myself, E.B., and A.K.I. I contributed all results and analysis on near-infrared (NIR)-based imaging and wrote the relevant sections. E.B. contributed the results on microwave-based imaging and wrote the remaining portions of the paper. All authors contributed to editing the manuscript.

1. E. Baladi, **M. Semple**, and A. K. Iyer, "Imaging of Subwavelength Features in the Far-Field Using Resonant Metasurfaces: Design from Microwave to Infrared Frequencies". *URSI EM Theory Symposium 2019*, San Diego, CA, May 2019. ***Invited***

The figures in Sec. 5.1 were adapted from this paper.

Acknowledgements

First of all, I would like to extend my sincere thanks to my supervisor, Prof. Ashwin K. Iyer, for his guidance, support, and encouragement throughout my doctoral program. His insight was invaluable and his feedback constantly pushed me to learn something new and expand my breadth of knowledge.

The support of the nanoFAB and their staff was absolutely critical to the success of this project. I would like to thank Peng Li and Dr. Shihong Xu for their training, assistance, and insights, particularly on the helium ion microscope. I would also like to thank Dr. Aaron Hryciw for his contributions to the development of the fabrication processes, including the helium ion microscope patterning, the epitaxial growth of gold, and the electron-beam lithography. Finally, I deeply appreciate Dr. Eric Flaim for supporting the project for so long, despite the numerous setbacks.

I would like to thank all my lab colleagues for their assistance and for providing a supportive social network throughout my program. In particular, I extend my thanks to Stuart for the numerous discussions over breakfast and always being available to provide feedback and the numerous breakfast discussions; Justin for getting me started with simulation software; and Elham for our fruitful collaborations.

I would like to thank Prof. Behrad Gholipour and Prof. Ray DeCorby for opening their labs to me, and their students Avik Mandal, Kyle Scheuer, and Graham Hornig for their assistance in characterizing my devices.

I would like to thank Dr. Richard McCreery and Dr. Adam Bergren for

giving me an early introduction to research.

I would like to thank the campus communities I was a part of, such as the University Symphony Orchestra, for providing an artistic outlet.

I would like to thank my family for their endless encouragement and advice.

I would like to thank my wonderful partner Ashly. Thank you for cooking for me, for tolerating my long hours, and for making my studies easier every step of the way.

Finally, I would like to acknowledge the agencies that helped to fund this work: the Natural Sciences and Engineering Research Council of Canada, Alberta Innovates, CMC microsystems, the Association of Professional Engineers and Geoscientists of Alberta, the University of Alberta, and the Government of Alberta.

Contents

1 Introduction **1**
- 1.1 Motivation . . . 4
- 1.2 Objectives . . . 5
- 1.3 Thesis Outline . . . 6

2 Background **9**
- 2.1 Plasmonics . . . 9
- 2.2 Aperture Arrays . . . 10
- 2.3 Metasurfaces . . . 12
- 2.4 MTM-Lined Aperture MTSs . . . 14
  - 2.4.1 Analytical Modeling of MTM-lined Apertures . . . 15
  - 2.4.2 Microwave Implementation . . . 16
- 2.5 Surface-enhanced Spectroscopy . . . 18
- 2.6 Metasurface Nanofabrication . . . 21
- 2.7 Helium Ion Microscope . . . 22
  - 2.7.1 Gallium vs Helium . . . 23
  - 2.7.2 Sputtering . . . 25

3 Design and Modelling **28**
- 3.1 Scaling MTM-Lined Apertures to the NIR . . . 29
  - 3.1.1 Thin Liner Aperture . . . 31
  - 3.1.2 Wagon-Wheel Aperture/Thick Liner . . . 33
  - 3.1.3 Asterisk-Shaped Aperture . . . 34
  - 3.1.4 NIR Parametric Studies . . . 35
  - 3.1.5 Analytical Modelling of a Thick and Anisotropic MTM Liner . . . 40
  - 3.1.6 Wagon-wheel Liner Equivalent Circuit . . . 47
- 3.2 Scaling MTM-lined Apertures to Visible Wavelengths . . . 59
  - 3.2.1 Two-wire Liner Equivalent Circuit Model . . . 62
  - 3.2.2 Two-wire Parametric Studies . . . 68
  - 3.2.3 Comparison to Bowtie Nanoantennas . . . 69
  - 3.2.4 Comparison to V-shaped Nanoantennas . . . 72
- 3.3 Scaling MTM-Lined Discs to the MIR . . . 79
  - 3.3.1 MIR Parametric Studies . . . 84
- 3.4 Summary . . . 86

4 Experimental Realization **89**
- 4.1 HIM Milling – Sample-Ion Interactions . . . 90
  - 4.1.1 Secondary Electron Generation . . . 91
  - 4.1.2 Sputtering . . . 92
  - 4.1.3 Ion-Activated Reactions . . . 93
  - 4.1.4 Implantation . . . 93
- 4.2 Sample Pre-Processing . . . 93

4.2.1 Sample Preparation . . . 93
4.2.2 Pattern Development . . . 94
4.2.3 Contamination Investigations . . . 98
4.3 HIM Milling – Processing Parameters . . . 102
4.3.1 Target Dosage . . . 103
4.3.2 Beam Current and Spot Size . . . 104
4.3.3 Dwell Time . . . 106
4.3.4 Array Patterning . . . 108
4.4 Wagon-Wheel MTS . . . 108
4.4.1 Wagon-Wheel MTS Fabrication . . . 108
4.4.2 Wagon-Wheel MTS Characterization . . . 110
4.5 HIM Milling – Parameter Analysis . . . 112
4.5.1 Target Dosage & Overmilling . . . 112
4.5.2 Grain Defects . . . 114
4.5.3 Current & Spot Size . . . 115
4.5.4 Dwell Time & Redeposition . . . 116
4.5.5 Pattern Drift . . . 118
4.5.6 Focus & Stigmation . . . 120
4.5.7 Array Drift . . . 121
4.6 Additional Process Development . . . 123
4.6.1 Single-Crystal Gold Films . . . 124
4.6.2 Substrate Removal . . . 128
4.7 Two-Wire MTS . . . 132
4.7.1 Two-Wire MTS Fabrication . . . 132
4.7.2 Two-Wire MTS Characterization . . . 134
4.8 MIR MTS . . . 142
4.8.1 EBL Process . . . 142
4.8.2 MIR Fabrication Analysis . . . 145
4.8.3 MIR MTS Characterization . . . 148
4.9 Summary . . . 150

5 Applications **153**
5.1 NIR Imaging of Subwavelength Features . . . 153
5.2 Phase-Gradient Visible MTS . . . 158
5.2.1 Unit Cell Library . . . 160
5.2.2 Nonuniform Array . . . 161
5.3 Long-Wavelength MIR SEIRA of CO2 . . . 164
5.3.1 Experimental Setup . . . 164
5.3.2 Modelling CO2 . . . 165
5.3.3 CO2 Sensing Experiment . . . 167
5.3.4 Functionalization Layer . . . 170
5.4 Summary . . . 172

6 Conclusion **174**
6.1 Summary . . . 174
6.2 Outlook . . . 176
6.2.1 Short-Term . . . 176
6.2.2 Long-Term . . . 178
6.3 Contributions . . . 180
6.3.1 Journal Publications . . . 180
6.3.2 Conference Proceedings . . . 181
6.3.3 Technical Reports . . . 183

References **184**

Appendix A Simulation Procedure **207**
A.1 COMSOL Multiphysics 207
A.2 Limitations of COMSOL 208
A.3 Ansys Lumerical FDTD 209
A.4 Limitations of Lumerical 210

Appendix B Wagon-Wheel MTS Equivalent Circuit **211**
B.1 Intuitive Equivalent Circuit Model Construction 211
B.2 Analytical Calculations for Initial Values 216
B.2.1 Zw 216
B.2.2 Zo 217
B.2.3 Za 218
B.2.4 M12 219
B.2.5 CN 220
B.2.6 ZB 221
B.2.7 CG, CGN, and M22 221
B.3 The Drude Model 222

Appendix C Isolated NIR Plasmonic Nanowire **225**

Appendix D Comparable MIR Dipole Array **228**
D.1 Field Intensity Enhancement Metric 228
D.2 MIR Coupled-Dipole Array 229

Appendix E Detailed Experimental Parameters **232**
E.1 Wagon-Wheel Fabrication 232
E.2 Two-Wire Fabrication 233
E.2.1 Epitaxial Growth of Gold on LiF 233
E.2.2 Removal of LiF Substrate 233
E.3 Two-wire Characterization 233
E.4 MIR Fabrication 235
E.5 MIR Characterization 235
E.5.1 Helium Ion Microscopy 235
E.5.2 FTIR Spectroscopy 235
E.5.3 Gas Cell 236

Appendix F MIR experiment noise analysis **238**

List of Tables

3.1 Parameter multipliers used to match the circuit model to the simulation. The parameters are nominally unity. 54

4.1 Geometric parameters used in the nonuniform simulation model. 140

List of Figures

2.1 Aperture array classification based on electrical size p/λ_0 and resonant or nonresonant constitutive elements. Reproduced with permission from [92], ©2019 IEEE. 11

2.2 A selection of plasmonic metasurfaces (MTSs): (a) nanodisks fabricated by template stripping (polyurethane), (b) rod antennas fabricated by nanoimprint lithography, (c) an MTS composed of different V-shaped nanoantennas fabricated by electron-beam lithography (EBL), (d) double-layer right-handed (top) and left-handed (bottom) gammadions forming a chiral MTM fabricated by EBL (scale bars are 500 nm), (e) split-ring resonators fabricated by EBL (scale bar is 500 nm), (f) split-ring resonator with inner and outer diameters of 108 nm and 188 nm, respectively, fabricated by nanosphere lithography, (g) inverse asymmetric split-ring resonator fabricated by ion-beam milling 25-nm-wide slits into a gold film resulting in a 495 nm × 495 nm meta-atom, and (h) double fishnet structure fabricated by nanoimprint lithography. Figures reproduced with permission from: (a) [104], ©2011 Nature, (b) [105], ©2009 APS, (c) [106], ©2011 AAAS, (d) [107], ©2007 OSA, (e) [108], ©2011 APS, (f) [109], ©2009 Wiley, (g) [110], ©2010 APS, (h) [111], ©2007 Springer. Composite and caption reproduced with permission from [9], ©2014 Nature. 13

2.3 (a) Planar view if an MTM-lined aperture. Region 1 ($\rho < a$) is filled with vacuum (but may generally take on any ϵ_{r1}, μ_{r1}), region 2 ($a < \rho < b$) is filled with an MTM that has arbitrary ϵ_{r2} and μ_{r2}, and the outer region ($b < \rho$) is a perfect electric conductor (PEC). From [62], Fig. 1 (a). (b) Practical implementation of the epsilon-negative and near-zero (ENNZ)-MTM lined aperture from [62], Fig. 1 (c). a,b, and p are borrowed from Fig. 2.3a, and L refers to discrete radial inductors, w is the azimuthal trace width, and g is the azimuthal capacitive gap width. (c) The scattering parameters for an infinite array of ENNZ MTM-lined and unlined apertures with the same outer radius b. Reproduced with permission from [62], ©2015 OSA. 17

2.4 A selection of plasmonic and dielectric surface-enhanced infrared absorption spectroscopy (SEIRA) substrates: (a) Colloidal silver nanorods grown by Au nanobipyramid-directed Ag overgrowth, (b) gold nanotubes grown by galvanic replacement reaction to synthesize hollow Au nanotubes from the sacrificial Ag nanorod templates, (c) gold nanocrosses on Si substrate, patterned by EBL (d), (e) gold pad-rod nanoantennas fabricated on Al_2O_3 with a gold backing and patterned by EBL, (f) coupled gold nanobars on Si, patterned by EBL, (g) hydrogenated amorphous Si elliptical resonators fabricated by EBL and reactive ion etching, and (h) 2D photonic crystal, silicon on insulator, patterned by EBL and reactive ion etching. Figure reproduced with permission from: (a), (b) [121], ©2018 Wiley, (c) [123], ©2019 Elsevier, (d), (e) [126], ©2019 IOP, (f) [120], ©2017 AIP, (g) [122], ©2018 AAAS, and (h) [125], ©2019 IEEE. 20
2.5 The Zeiss Orion NanoFab Helium Ion Microscope housed at the University of Alberta nanoFAB Centre. Image courtesy of Peng Li, reproduced with permission from [147]. 23
2.6 The probe size vs image-side half angle for a 30 keV landing energy helium beam. The two graphs are for optimal conditions (a) for a 0.5 pA helium ion beam, and (b) for a 20 pA beam. Figure and caption reproduced with permission from [149], ©2016 Springer. 25
2.7 Cascade simulations with Stopping Range of Ions in Matter (SRIM) of noble gas ions impinging on bulk silicon with 30 keV energy in comparison to Ga^+ ions. Sputter yields Y_SP are indicated. The simulated impinging beams had zero diameters. Trajectories of primary ions are black while the green dots are collisions between recoiling target atoms. The red dots signify target atoms knocked from their lattice by the incident primary ion. Figure and caption reproduced with permission from [150], ©2016 Springer. 26

3.1 Evolution of the NIR design: (a) the thin liner case, (b) the wagon-wheel case, and (c) the asterisk case. Reproduced with permission from: (a), (b) [92], ©2019 IEEE, and (c) [154], ©2018 IEEE. 30
3.2 Transmission and reflection responses for the thin-liner optical MTS depicted in Fig. 3.1a. 32
3.3 Log-scale electric-field profiles at resonance of: (a) the thin liner case (270 THz, maximum 80), (b) the wagon-wheel case (193 THz, maximum 140), and (c) the asterisk case (215 THz, maximum 45). Reproduced with permission from: (a), (b) [92], ©2019 IEEE, and (c) [154], ©2018 IEEE. 32
3.4 Transmission and reflection responses for the thick-liner optical MTS depicted in Fig. 3.1b. Reproduced with permission from [92], ©2019 IEEE. 34
3.5 Transmission frequency response for varying inner radius a (solid), showing the transmission peak corresponding to the HE_{11} mode for each value of a. The unlined case with outer radius $b = 120$ nm (dashed) is also plotted for comparison. Reproduced with permission from [92], ©2019 IEEE. 36

3.6 Transmission frequency response for varying array periodicity p, lined cases (solid) and unlined cases (dashed). Reproduced with permission from [92], ©2019 IEEE. 37
3.7 Transmission frequency response for varying gold film thickness t_f, lined case (solid) and unlined case (dashed). Reproduced with permission from [92], ©2019 IEEE. 38
3.8 Transmission frequency response of the lined aperture case (solid) and the unlined aperture case (dashed) for varying values of outer radius b. Reproduced with permission from [92], ©2019 IEEE. 39
3.9 Transmission frequency response for varying number of wires N inside the aperture (solid) and the unlined case (dashed). Reproduced with permission from [92], ©2019 IEEE. 40
3.10 Surface plot of HE_{11} cutoff frequency with respect to anisotropic liner permittivity parameters for (a) a thin liner ($b = 140$ nm, $a = 120$ nm), and (b) a thick liner ($b = 140$ nm, $a = 14$ nm). The magenta line denotes 193 THz, or 1.55 µm, the wavelength of optical telecommunications. Reproduced from [155], CC BY 4.0. 46
3.11 (a) Schematic showing the intuitive description of each part of the MTM-lined aperture as an equivalent lumped circuit element, and (b) the equivalent circuit model. 50
3.12 Comparison of the reflection and transmission spectra of the circuit model to COMSOL simulations for (a) the nominal predicted circuit model, and (b) the tuned circuit model. For the simulations, the substrate was removed, the MTS was excited with a vertically polarized plane wave, and the nominal parameters were $b = 120$ nm, $p = 300$ nm, $t = 50$ nm, $w = g = 10$ nm, and $N = 8$. 53
3.13 Comparison of the circuit model to COMSOL simulations for varied geometrical parameters. (a) $b = 100$–140 nm, (b) $p = 260$–340 nm, (c) $w = 5$–15 nm. The coloured curves represent the COMSOL simulation data, the grey mesh represents the circuit model data, and the black curves highlight the circuit model data where the circuit model can be compared directly to the COMSOL data. 57
3.14 (a) Optical two-wire MTM-lined aperture design for visible-frequency operation, and (b) the transmission, reflection and absorption spectra for a nominal design resonating at 425 THz/700 nm. Geometric parameters for this design are $w = g = 10$ nm, $b = 25$ nm, $p = 150$ nm, and the film thickness is $t = 50$ nm. Reproduced with permission from [169], ©2020 IEEE. 62
3.15 Circuit model describing the two-wire MTM-lined aperture. (a) Schematic overlay showing the physical source of each circuit element, and (b) the reduced circuit model derived to describe the MTS unit cell. 63

3.16 Comparison of reflection and transmission spectra from Lumerical FDTD simulations (dashed) and the MTM-lined aperture circuit model (solid), (a) for $b = 50$ nm, $p = 150$ nm, $t = 50$ nm, $w = g = 10$ nm and analytically derived circuit component values, (b) for $b = 25$ nm and analytically derived component values, (c) optimized circuit model for $b = 50$ nm and the circuit components scaled by $[1.22Z_c, 1.24Z_w, 1.25Z_a]$, and (d) optimized circuit model for $b = 25$ nm and the circuit components scaled by $[1.75Z_c, 1.90Z_w, 0.94Z_a]$. Simulation data taken from [169]. 65
3.17 Resonant (y-polarized incident wave) reflection spectra for two-wire MTM-lined aperture arrays with nominal feature sizes $b = 25$ nm, $p = 150$ nm, $w = g = 10$ nm, and $t = 50$ nm. (a) Parametric sweep of the periodicity p, and (b) parametric sweep of the aperture radius b. 68
3.18 (a) A schematic of the relation between a bowtie aperture ($\theta = 45°$) and a two-wire MTM-lined aperture ($\theta = 90°$). (b) Reflection spectra of the aperture shown in part (a), for various angles θ. The input is a y-polarized plane wave at normal incidence and $b = 40$ nm. 70
3.19 Electric-field profiles of the bowtie-shaped aperture arrays at resonance for a y-polarized, normally incident plane wave. The two-wire MTM-lined aperture is miniaturized by a factor of three quarters over the conventional bowtie antenna without a loss in field enhancement. 72
3.20 (a) V-shaped nanoaperture geometry, and (b) geometry of the asymmetric, two-wire MTM-lined nanoaperture. 74
3.21 Electric-field profiles of a representative $\theta = 90°$ V-shaped nanoantenna at (a) its asymmetric resonance frequency, and (b) its symmetric resonance frequency. Resonant electric-field profiles for an asymmetric $\theta = 90°$ MTM-lined aperture, (c) at its asymmetric resonance frequency, and (d) at its symmetric resonance frequency. The incident field is y-polarized. 75
3.22 Scattered transmission spectrum (a) magnitude, and (b) phase for the V-shaped nanoantenna and various angles θ, and scattered transmission spectrum (c) magnitude, and (d) phase for the asymmetric MTM-lined aperture and various angles θ. . . 77
3.23 (a) Microwave MTM-lined disc, where θ is the angular interdigitated capacitor span, a is the radius of the inner solid disc, b is the disc radius including the liner, w is the inductive connecting trace width, t is the capacitor trace width, and p is the array pitch. (b) NIR MTM-lined disc, where b is the disc radius, w is the capacitive gap width and minimum central nanowire width, and p is the array pitch. (c) MIR MTM-lined disc, where b is the total disc radius, w is the nanowire width throughout the unit cell, g is the nanogap width throughout the unit cell, and p is the array pitch [179]. Each panel includes an inset with the capacitive gaps highlighted in green. (a) licensed under CC BY 4.0, modified with axis and highlighted gap insets [63], (c) ©IEEE 2020, modified with permission [179]. 81

3.24 (a) Reflection, transmission, and absorption spectra for the nominal MTS-lined MTS structure (solid) and an equivalent unlined-disc array (dashed). (b) Electric-field enhancement ratio for the nominal MTM-lined MTS at the resonance wavelength of 15 µm. The nominal structure has $b = 1.2$ µm, $p = 3$ µm, and $g = w = 100$ nm. ©IEEE 2020, modified with permission to add scale bars to part (b) [179]. 83
3.25 (a) Simulated average field intensity enhancement factor, field intensity enhancement ratio (F_I), at 15 µm (20 THz) with respect to the wire width w and the gap width g, and (b) with respect to the sum of w and g. Reproduced from [180], CC BY 4.0. 85
3.26 (a) Simulated R/T/A spectra for varied MTS pitch p, and (b) simulated reflection spectra for varied MTS disc radius b, while keeping the fill factor constant. Reproduced from [180], CC BY 4.0. 86

4.1 Schematic representation of the ion beam, selected from a single atom of the three-atom trimer, patterning the gold film surface (not to scale). Reproduced with permission from [182], ©2021 ACS. 90
4.2 Sputtered gold sample mounted on an aluminum stub. The sample is affixed with double-sided, conductive carbon tape for mechanical security, and a second strip of carbon tape is affixed between the gold film surface and the stub to guarantee electrical conductivity. Reproduced with permission from [182], ©2021 ACS. 92
4.3 An helium ion microscope (HIM) micrograph showing evacuated 45-degree sectors in the 100-nm gold film on borofloat. Image courtesy of Dr. Aaron Hryciw. 95
4.4 HIM micrographs showing the defects encountered while patterning asterisks into polycrystalline films. (a) grain defects due to varied crystal face orientations, (b) deposition of contamination films and substrate swelling, and (c) overmilling at the pattern centre. 96
4.5 Grey-scale patterning bitmap generated in MATLAB. 98
4.6 HIM micrographs showing an aperture patterned in two steps: (a) an aperture with a continuous wire through the centre, and (b) after a vertical line was cut through the centre of the wire. 99
4.7 Scanning electron microscope (SEM) energy-dispersive x-ray (EDX) results, showing (a) the imaged area, where imaging/focusing with the HIM and the SEM has grown contamination on the surface, (b) the collected EDX spectrum, showing contributions from Au, Cu, Al, O, and C, and (c) a map of the carbon signal, showing a strong localization of the carbon to the patterned area. 100
4.8 Results of the transmission electron microscope (TEM) analysis of the gold films grown on NaCl. (a) TEM micrograph of an aperture patterned in two steps, (b) the EDX map of the patterned area, showing the C signature (red), the Na signature (green), and the Cl signature (blue). The signatures of gold and copper were also detected, but not plotted. 101

4.9 HIM micrograph of patterns with varying target dosage for (a) the 50-nm thick film, (b) the 70-nm thick film, and (c) the 90-nm thick film. From bottom-left to top-right, the dosage is increased from 1.5 nC/µm^2 to 12 nC/µm^2 in steps of 1.5 nC/µm^2. Reproduced with permission from [182], ©2021 ACS. 104
4.10 HIM micrograph showing patterning differences as the current is increased for (a) the 50-nm thick film, (b) the 70-nm thick film, and (c) the 90-nm thick film. From bottom-left to top-right, the current is increased from 1.5 pA to 15 pA in steps of 1.5 pA. Reproduced with permission from [182], ©2021 ACS. 106
4.11 HIM micrographs that capture the effect of varying dwell times on the milled pattern for (a) the 50-nm thick film, (b) the 70-nm thick film, and (c) the 90-nm thick film. From bottom-left to top-right, the dwell time is increased from 0.5 µs to 5 µs in steps of 0.5 µs. Reproduced with permission from [182], ©2021 ACS. 107
4.12 HIM micrographs depicting small-scale arrays for (a) the 50-nm film and (b) the 70-nm film. Problems associated with large-scale reproducibility become increasingly evident for thicker films. Beam drift between patterns, redeposition, and grain defects are all present. Reproduced with permission from [182], ©2021 ACS. 109
4.13 An HIM micrograph showing a section of the 15 µm×15 µm wagon-wheel MTS. 110
4.14 Photographs of (a) the measured wagon-wheel MTS die, mounted on a Si chip with clamps and carbon tape, and (b) visible image of the patterned wagon-wheel MTS under the FTIR microscope. 111
4.15 Simulation of the wagon-wheel aperture MTS transmission with reduced wire width w = 10–5 nm and correspondingly increased gap width g = 10–15 nm, representative of overmilling. From Reproduced with permission from [182], ©2021 ACS. 113
4.16 Simulation of the effect of a 20-nm radius grain defect placed in various locations on the wagon-wheel aperture MTS transmission performance. Insets show the defect location in the unit cell, with coloured borders to identify the associated curve. Reproduced with permission from [182], ©2021 ACS. 115
4.17 HIM micrographs of the 90-nm film showing the effects of redeposition on nearby unit cells. The top half shows 5 cells immediately after patterning, and the bottom half shows the same 5 cells after patterning nearby. Reproduced with permission from [182], ©2021 ACS. 117
4.18 Transmission simulation of the effect of redeposition by increasing the wire width w from 10 nm to 15 nm in 1-nm increments, and decreasing the gap width g from 10 nm to 5 nm in 1-nm increments. Reproduced with permission from [182], ©2021 ACS. 118
4.19 HIM micrograph showing (a) a cell patterned on the nominal 50-nm film, (b) a cell patterned on the 90-nm, and (c) the nominal 70-nm film small array, imaged at a 45° angle. Despite grain defects, the central area of each aperture is well-milled, and most wires are continuous. The wire thickness degrades towards the centre of the aperture, and approximate measurement of the depth shows each film lost 10 nm to the plasma cleaning process or deposition rate inaccuracy. Reproduced with permission from [182], ©2021 ACS. 119

4.20 Transmission simulation with a thickness gradient applied to the nanowires. The labelled thickness is the difference between the nanowire thickness at the edge of the aperture ($t = 50$ nm) and at the nanowire tips at the centre of the aperture. Reproduced with permission from [182], ©2021 ACS. 120
4.21 HIM micrograph depicting a large patterned array of $20 \times 14 = 280$ unit cells. Reproduced with permission from [182], ©2021 ACS. 123
4.22 Simulation of array drift on the wagon-wheel aperture MTS transmission performance. The array pitch, p, is varied from 260 nm–340 nm in steps of 20 nm. Reproduced with permission from [182], ©2021 ACS. 124
4.23 HIM micrographs of the films grown on a mica substrate, (a) at room temperature, and (b) at 400°C. 126
4.24 HIM micrograph showing a well-patterned asterisk aperture patterned into a gold film grown on mica at high temperatures. . 127
4.25 atomic force microscope (AFM) micrographs of the various films grown on LiF, (a) the 100-nm film, courtesy of Dr. Aaron Hryciw, (b) the 20-nm, discontinuous film, and (c) the nearly continuous 65-nm film. 127
4.26 x-ray diffraction (XRD) spectra for (a) the 100-nm film on LiF, courtesy of Dr. Aaron Hryciw, (b) the 20-nm film on LiF, and (c) the 65-nm film on LiF. 129
4.27 HIM micrographs of (a) the 20-nm film on LiF, and (b) the 65-nm film on LiF. 130
4.28 HIM micrographs of the films grown on LiF, showing (a) a bubble created by the overmilling of a single aperture taken normal incidence, and (b) a bubble created by patterning a small array of apertures taken at a 45° angle to accentuate the topography. 131
4.29 HIM micrographs showing (a) the 40×35-cell MTS array, and (b) the same array magnified to better resolve the features. . . 135
4.30 (a) Melted two-wire MTM-lined aperture MTS from Fig. 4.29a after illumination, and (b) second patterned array, fabricated under suboptimal current and stability conditions. 136
4.31 Experimental data normalized to the raw gold film background compared to nominal simulation data. The experimental data were smoothed using a 31-sample Savitzky-Golay filter, and the nominal geometric parameters were $b = 40$ nm, $g = w = 10$ nm, $p = 120$ nm, and $t = 65$ nm. 137
4.32 Profile view of the fabricated MTS array at 45° oblique incidence, (a) parallel to the patterned nanowires, and (b) rotated with respect to the nanowires. 140
4.33 (a) Simulation model layout incorporating fabrication variation. The array is divided into four 2×2 cells, and (b) shows a cutaway highlighting the reduced nanowire thickness. 141
4.34 Final simulation results, tuned to match the experimentally acquired spectra. $BG_{ratio} = 0.26$ and $P_{Exp} = 1.17$. 141
4.35 Pictographic representation of the EBL exposure process. . . . 143
4.36 HIM micrographs of the overexposed patterns on the first sample after development for (a) an electron beam dosage of 600 µC/cm^2, and (b) an electron beam dosage of 700 µC/cm^2. 144
4.37 Geometric parameters of second MTM-lined disc arrays fabricated by EBL for electron beam dosages of 400–800 µC/cm^2. . 145

4.38 HIM micrographs of patterned MTM-lined discs for dosages (a) 450 µC/cm^2, (b) 500 µC/cm^2, (c) 550 µC/cm^2, and (d) 600 µC/cm^2. Reproduced from [180], CC BY 4.0. 147
4.39 Geometric parameters of MTM-lined disc arrays fabricated by EBL for electron beam dosages of 450-600 µC/cm^2. Reproduced from [180], CC BY 4.0. 147
4.40 Relative reflection spectra of (a) the fabricated reference disc arrays (coloured) and the simulated reference disc array (black), and (b) the fabricated MTM-lined disc arrays (coloured) and the simulated MTM-lined disc array (black) normalized to the total reflectance of the bare ZnSe surface (eq. (4.4): $R = \sim 0.28$). The dashed curves correspond to the $(g, w) = 80/110$ nm case, while the solid curves correspond to the $(g, w) = 80/80$ nm case. The spectra have been normalized to remove source and environmental effects. Reproduced from [180], CC BY 4.0. . . 150

5.1 Subwavelength imaging mechanism example, where (a) a random distribution of reflecting subwavelength obstacles (shown in white) is imaged using an aperture array with a period of $\lambda_0/6$, and with a diffraction-limited microscope in reflection mode. (b) the diffraction-limited image. The subwavelength-resolution image is divided into three images, each excited at the resonance frequency of a particular set of apertures, denoted by (c) red, (d) green, and (e) blue. (f) the image with subwavelength resolution in the horizontal direction. 155
5.2 (a) Overall structure of the 3×1 imaging array, (b) the transmission of each of the three apertures individually, with -3 dB marked with a red dotted line, and (c) the overall transmission response of the structure depicted in (a). Adapted with permission from [217]. 157
5.3 (a) Geometry of the displaced gap simulation, where g now refers to the distance by which the gap is displaced, (b) the scattered transmission magnitude for various gap displacements g, and (c) the scattered transmission phase for various gap displacements g. 161
5.4 (a) Layout of the non-uniform phase-gradient MTS, with the scattered phase of each cell labeled above, (b) scattered transmission magnitude for each individual unit cell, where the curve colours correspond to the labels above, and (c) the scattered transmission phase for each individual unit cell, where the curve colours correspond to the labels above. (a) adapted with permission from [219]. 162
5.5 Real part of the right-hand circular polarization (RHCP) scattered electric field of the phase-gradient MTS for a normally-incident, left-hand circular polarization (LHCP) plane wave, showing the clear scattering to an angle of 48.5°, denoted by the dashed black lines. The inset shows the simulation setup, where the purple arrow is the propagation direction of the incident wave. 163

5.6 Schematic of the fabricated gas cell, with inset showing a cartoon of the excitation of CO_2 by the MTS (not to scale). The microscope illumination is shown in blue, the ZnSe substrate is shown in yellow with the MTS patterned on the inside surface, and the glass gas cell is clear with two gas inlets. Adapted from [180], CC BY 4.0. 165
5.7 High-resolution complex refractive index model for CO_2. Reproduced from [180], CC BY 4.0. 166
5.8 Resampled and apodized complex refractive index model for CO_2. Reproduced from [180], CC BY 4.0. 167
5.9 (a) Differential MTS reflection data when the gas cell is filled with different pressures of CO_2 (10 PSI solid, 26 PSI dotted), relative to the case with N_2 filling. Bare ZnSe is plotted in blue, the case of 600 $\mu C/cm^2$ in orange, and 500 $\mu C/cm^2$ in red. (b) Differential reflection data for the 26 PSI case (dotted) plotted against the differential reflection data for a representative simulation with a CO_2 model (solid). (c) Simulated differential reflectance for a 100-nm functionalization layer of CO_2 at 26 PSI, bare ZnSe vs. MTS vs. reference disc array. (d) Calculated field intensity enhancement factor, F_I, and absorption enhancement factor, F_A, for the two fabricated cases and various functionalization layer thicknesses. The green dots reproduce the data in Fig. 3.25, and *Inf.* represents a full half-space of CO_2, as in the experiment. Reproduced from [180], CC BY 4.0. 169

B.1 (a) Circuit model representing a resonant monopole and a resonant loop, and (b) the spectrum produced by the circuit model with circuit elements derived from rough approximations. Two reflective resonances are observed. 212
B.2 (a) Circuit model after adding a parallel nonresonant aperture impedance Z_a, and (b) the spectrum produced by the circuit model with circuit elements derived from rough approximations. Two asymmetric, Fano-shaped transmissive resonances are observed. 213
B.3 (a) Circuit model after adding capacitive and inductive coupling elements, and (b) the spectrum produced by the circuit model with circuit elements derived from rough approximations. The two resonances have been merged into one. 214
B.4 (a) Circuit model after rearranging the layout of the loop resonator, and (b) the spectrum produced by the circuit model with circuit elements derived from rough approximations. The two separated resonances have reappeared at approximately the correct frequencies. 215
B.5 (a) The final circuit model after adding the loop feeding element Z_B, and (b) the spectrum produced by the circuit model with circuit elements derived from rough approximations, compared to the spectrum computed in COMSOL. The circuit model is able to match all the features of the spectrum. 215
B.6 Layout of quasi-static problem used to derive the inductive coupling parameter M_{12}. 219

C.1 Simulation layout of the representative resonant nanowire simulation. For periodicity, horizontal boundaries are perfect magnetic conductor (PMC)s, while vertical boundaries are PECs. Ports that excite a normal incidence, y-polarized plane wave terminate the z-boundaries (port 1 is highlighted in blue), and the scattering parameters are measured to find the reflection peak of the resonating nanowire. 226
C.2 Scattering spectrum of the grounded nanowire near the predicted resonance frequency of 255 THz. The maximum reflection is observed at 260 THz, very close to our prediction. . . . 226
C.3 Electric-field profile of the grounded nanowire at 260 THz, which demonstrates a quarter-wave monopolar resonance. 227

D.1 (a) Layout of dipole array simulation, (b) electric-field profile at resonance, showing strong field enhancement at the coupled nanogaps, and (c) plane-wave scattering spectrum for an incident plane wave polarized parallel to the dipoles. 231

E.1 Reflection-mode supercontinuum microspectrophotometer component layout used to measure the reflectance of the polarization-sensitive MTM-lined aperture MTS. Image courtesy of Kyle Scheuer. 234

F.1 Experimental data with calculated standard error bars (dotted) and simulation data (solid) for comparison. Reproduced from [180], CC BY 4.0. 239

List of Symbols

λ_0	Free-space wavelength
Q	Quality factor, charge
ϵ_0	Free-space permittivity
μ_0	Free-space permeability
I	Identity tensor, current
E	Electric field
$\sigma_t, \sigma_x, \sigma_a, \sigma_b$	Standard deviation
F	Filling factor
ρ	Radial cylindrical coordinate
ϕ	Azimuthal cylindrical coordinate
γ_ρ^μ	EH radial propagation constant
γ_ρ^ϵ	HE radial propagation constant
γ	Complex propagation constant
β	Propagation constant
α	Attenuation constant
D	Electric displacement field
f	Frequency
ω	Angular frequency
Z	Impedance
Z_0	Free-space impedance
R	Reflectance, Resistance
T	Transmittance
L	Inductance
C	Capacitance
d_{50}	Probe size
F_{AF}	Long-range fine patterning figure of merit
Φ	Scattered phase
c	Speed of light in free space
σ	Conductivity
$\bar{J}$	Current density
V	Electric scalar potential
t	Time
e	Elementary charge
τ	Relaxation time

Glossary

atomic force microscope (AFM)

de-ionized (DI)

electron-beam lithography (EBL)

energy-dispersive x-ray (EDX)

epsilon-negative and near-zero (ENNZ)

extraordinary optical transmission (EOT)

face-centred cubic (FCC)

Fibics Nanopatterning and Visualization Engine (NPVE)

field intensity enhancement ratio (F_I)

focused ion beam (FIB)

fourier-transform infrared (FTIR)

frequency selective surface (FSS)

gas field ion source (GFIS)

helium ion microscope (HIM)

IBSS Chiaro Plasma Contamination Control System (IBSS)

isopropyl alcohol (IPA)

left-hand circular polarization (LHCP)

liquid metal ion source (LMIS)

localized surface plasmon (LSP)

metamaterial (MTM)

metasurface (MTS)

mid-infrared (MIR)

near-infrared (NIR)

non-dispersive infrared (NDIR)

perfect magnetic conductor (PMC)

perfect electric conductor (PEC)

physical vapour deposition (PVD)

polymethyl methacrylate (PMMA)

Quantum NanoFab Facility (QNF)

right-hand circular polarization (RHCP)

scanning near-field optical microscope (SNOM)

scanning electron microscope (SEM)

signal-to-noise ratio (SNR)

simplicial homology global optimisation (SHGO)

Stopping Range of Ions in Matter (SRIM)

surface-enhanced Raman spectroscopy (SERS)

surface-enhanced infrared absorption spectroscopy (SEIRA)

transmission-line metamaterial (TL-MTM)

transmission electron microscope (TEM)

x-ray diffraction (XRD)

Chapter 1

Introduction

The drive to integrate complicated photonic functionalities into handheld devices requires alternatives for bulky free-space optical components. If lenses could be replaced with electrically thin equivalents, microscopes and camera lens systems could be miniaturized and integrated seamlessly into mobile devices [1], [2]. Compact and reconfigurable phase plates could be used to generate holograms [3] and reduce the weight of lenses for augmented reality [4] and night vision goggles [5]. Moreover, on-chip spectrometers, hyperspectral, and polarization-resolved imaging systems have been proposed [6]–[8].

Two-dimensional arrays of subwavelength scatterers, called metasurfaces (MTSs), have been suggested as a miniaturization solution, and indeed, many designs have emerged to create comparable lenses, polarizers, and more [9]–[12]. Unfortunately, current design methods have been insufficient to entirely replace conventional optical components due to limitations on efficiency and bandwidth. Emerging design methods promise to improve MTS performance through numerical optimization, but they are limited by practical fabrication considerations [13]–[17]. Improving the limits on MTS nanofabrication methods may unlock the performance required to replace conventional optical components and miniaturize a number of optical functionalities.

MTSs are commonly designed to discretize a desired field transformation across the surface, then reconstruct it using individual unit cells, or to create hotspots of maximum electromagnetic field enhancement. Improved unit cell miniaturization increases the MTS efficiency as field discretization errors are

reduced, and elements can be placed closer together to increase the density of hotspots. Moreover, sufficiently small unit cells allow several MTS functionalities to be multiplexed into a single surface with tolerable losses in efficiency. Plasmonic MTSs consist of metallic nanoantennas and support extreme field confinement and can be miniaturized significantly at resonance. Plasmonic MTSs have been used to demonstrate a wide variety of exotic properties, such as thin perfect absorption [18], electromagnetic cloaking [19], polarizers [20], [21], holography [22], [23], and lensing [24], [25]. Moreover, with the strong near-field enhancement, plasmonic MTSs have been designed for surface-enhanced spectroscopy [26]–[28], enhancing nonlinear light-matter interactions [29], [30], and near-field super-resolution imaging [31]. There is a wide variety of MTS applications and this is by no means an exhaustive list.

Babinet's principle predicts complementary scattering performance between complementary metallic nanoantennas and nanoapertures in a metal film but does not address near-field enhancement or loss [32]. Complementary aperture-based plasmonic resonators can exhibit better performance than their nanoantenna-based counterparts, for example, the increased metallic area can improve heat dissipation, apertures have been shown to better localize fields leading to increased field enhancement [32], [33], and strong magnetic fields can be localized by the excitation of enhanced conduction currents [34].

For aperture-based MTSs, the metal film often must be thicker than for nanoantenna-based MTSs to render the film opaque away from resonance. This significantly increases the signal-to-noise ratio for transmissive MTSs [25], but implies that top-down approaches must be used to fabricate the structures. Few options exist for the creation of features as fine as those available for nanoantenna-based MTSs, which often rely on focused ion beams (FIBs).

Recently, He^+ gas field ion sources (GFISs) have emerged for FIB-based imaging applications to produce a sub-nm probe size. He^+ ions are lighter than Ga^+ ions and are hence less destructive when imaging and boast smaller surface interaction volumes, which leads to increased patterning resolution when applied to milling. Helium ion microscope (HIM) milling has proven to be the only fabrication technology that can achieve both high aspect ratios

(over 1:10) and extremely fine features in noble metals (as small as 3 nm), but has been hampered by relatively slow speed and reproducibility [35]–[40].

MTSs have typically relied on the maximum possible lumped element loading to miniaturize the unit cell and apply continuous effective surface parameter models. Enhancing control over plasmonic element width, length, and height at a nm-scale resolution will enable increased miniaturization, allowing MTSs based on scattered phase gradients to sample quickly varying phase profiles more accurately [41], and higher resolution for holograms with improved viewing angles [42]–[45], super-resolution imaging [31], [46]–[48], plasmonic lithography [49], and magnetic memory [50]. Moreover, thin nanogaps in plasmonic elements exhibit improved field confinement and enhancement as the gap size falls below 10 nm [51], which can be used to achieve exceptional surface-enhanced spectroscopy [52], [53], to demonstrate quantum plasmonic effects [54], and to excite nonlinearities for second- and third-harmonic generation [55]–[58] and stimulated emission [59].

As MTS technology is scaled to increasingly short wavelengths and applied to ultraviolet and x-ray nanophotonics, feature scales will necessarily need to be minimized to engineer the scattering spectra [60]. For example, a compact x-ray source using 10-nm silver features and high aspect ratios has been suggested, but has yet to be implemented experimentally [61].

First designed for operation in the microwave regime, metamaterial (MTM)-lined apertures and discs are single-layer MTS unit cells that make use of a thin transmission-line MTM liner with fine patterning of capacitive gaps and inductive wires for strong miniaturization [62]–[64]. Transmission line MTMs are transmission lines periodically loaded with circuit elements on a subwavelength scale to create exotic propagation characteristics along the line. The effective-medium model – a hallmark of MTMs – shows that the MTM liner region acts like an effective plasma, where strong field enhancement is observed at resonance. These properties have been used to create compact filtering and imaging devices [47], [64].

1.1 Motivation

The majority of advances in plasmonic MTSs have been limited to nanoantenna-based MTSs and simple aperture-based MTSs due to ease of fabrication. Given the observed benefits of nanoapertures over nanoantennas, nanometre-scale features on plasmonic aperture-based MTSs could impart many of the improvements seen in nanoantenna-based MTSs, such as increased field enhancement and miniaturization. Moreover, optimal inverse-designed MTSs have continually reached for finer and finer control over their geometry and exceptional patterning resolution will be required for future extensions of MTS technology to extreme wavelengths. Reliable, nanometre-scale features could significantly improve their efficiency, reducing operating power requirements and increasing bandwidths. The main challenges motivating this thesis can be summarized as follows:

1. Reproducibility is particularly important for MTSs since a practical MTS must encompass as full an extent of the illuminating field as possible, which is generally several wavelengths across. For a subwavelength unit cell, this implies the periodic or quasi-periodic arrangement of hundreds or more of such cells. Increasing the reliability of HIM nanofabrication is a compelling challenge to improve the potential patterning resolution for not only plasmonic MTSs, but any number of plasmonic applications that require repeatable fine features over a large area.

2. MTM-lined apertures and discs in the microwave domain show exceptional properties reminiscent of plasmonics. If scaled to the optical domain, the fine patterning of the metallic features poses an extreme fabrication challenge. However, MTM-lined apertures and discs could offer additional paths to miniaturization and field confinement in resonant plasmonic MTS unit cells.

3. Effective surface-enhanced infrared absorption spectroscopy (SEIRA) in the long-wavelength mid-infrared (MIR) regime requires frequency-scalable field enhancement techniques. The strong field enhancement of

MTM-lined resonators could be harnessed to improve the detection and characterization of materials with resonances within this band.

4. The MTM-lined aperture is well-described by a transmission-line metamaterial (TL-MTM) circuit and accompanying effective-medium model. Extending these models to the optical domain would simplify the description of optical MTM-lined apertures and other nanoplasmonic MTS designs, and offer important intuition for interpreting the effects of fabrication defects.

5. The resolution of near-field microscopy systems is set by aperture size or field hotspots (depending on the implementation) and the deflection angle of phase-gradient MTSs is limited by the miniaturization of the MTS's unit cells. Both could potentially be improved by implementations with finely featured MTS elements.

1.2 Objectives

In this thesis, we assess the practicality of using the HIM to pattern aperture-based plasmonic MTSs over wide areas with reliable features as small as 10 nm. As a prime example, we study MTM-lined aperture and disc MTSs. The main objectives addressing the above motivations are to:

1. Develop repeatable procedures to increase the reliability of the HIM patterning method.

2. Design MTM-lined aperture MTSs for operation in the optical domain, making use of dense, 10-nm features and demonstrate their fabrication with the HIM.

3. Design an MTM-lined disc MTS operating in the long-wavelength MIR and experimentally demonstrate surface-enhanced absorption.

4. Extend the MTM-lined aperture effective-medium model to apertures with thick and anisotropic liners and develop a general equivalent-circuit

model that can describe plasmonic MTSs and apply it to the MTM-lined aperture.

5. Suggest implementations of a subwavelength imaging MTS and a phase-gradient MTS using MTM-lined apertures.

1.3 Thesis Outline

The layout of this thesis is as follows. In Ch. 3, we discuss the design and numerical modeling of MTM-lined apertures and discs with fine features for operation in the near-infrared (NIR), visible, and MIR. The first design is a simple proof-of-principle MTM-lined aperture MTS, created to act as a resonant filter in the NIR optical telecommunications band at a wavelength of 1.55 µm. The structure is first modelled on the basis of an effective medium, then with an equivalent-circuit approach to fully characterize the resonant plasmonic features. The fabrication of this device requires four features typically unachievable in tandem: (1) extremely fine features (limited to 10 nm), (2) extreme aspect ratios (feature width:feature depth, limited to 1:5), (3) complex geometries (many closely spaced nanowires and nanogaps), and (4) long-range order to achieve the desired results. These features cannot be achieved with any fabrication method other than HIM.

Making use of the equivalent-circuit model derived above, the second design is a maximally miniaturized two-wire MTM-lined aperture MTS that nominally resonates in the visible spectrum. The MTS acts as a simple polarizer, but we show that this MTS is also able to mimic the behaviour of popular conventional nanoplasmonic MTS unit cells, with better miniaturization and/or field enhancement.

Finally, we propose a novel approach to long-wavelength MIR SEIRA making use of a combination of plasmonic and capacitive field confinement on MTM-lined discs. We create a circular MTM-lined disc unit cell, lined with long meandered capacitors to shift its resonance frequency into the long-wavelength MIR regime. The MTS is designed to be fabricated with electron-beam lithography (EBL) to compare the difficulties of HIM to a more estab-

lished fabrication method. We compare the MIR MTM-lined disc MTS to a conventional coupled-dipole array to demonstrate improved field enhancement at the 15-µm absorption band of CO_2.

In Ch. 4, the three MTSs designed in the previous chapter are fabricated and characterized. We begin with a detailed study of the HIM beam parameters, and identify the key parameters for reliable pattern fabrication. The NIR MTM-lined aperture MTS is fabricated, and a detailed numerical analysis is performed to identify process parameters outside the HIM that can increase patterning reliability.

Using these results, procedures are developed to create free-standing and epitaxial gold films that significantly improve the patterning fidelity. We use these films to fabricate the two-wire MTM-lined aperture MTS and optically characterize it, showing accurate comparisons to simulations.

We then describe the EBL lift-off process development for the MIR MTM-lined disc MTS. The MTM-lined disc MTS is fabricated and the results are inspected under HIM to determine the fabrication fidelity. We characterize the MTS by fourier-transform infrared (FTIR), showing excellent agreement with simulation.

The chapter concludes with a short comparison of the challenges encountered during HIM and EBL patterning.

In Ch. 5, we show how a number of applications may benefit from fine features, and implementations using MTM-lined apertures and discs. The strong miniaturization of the NIR MTM-lined apertures is harnessed to propose a subwavelength imaging array that multiplexes near-field information about the sample to the far-field spectrum at a resolution of at least $\lambda_0/3.6$.

We propose a beam-steering MTS implemented using two-wire MTM-lined apertures. Due to the improved miniaturization, the proposed MTS supports comparable scattering efficiency, but with a wider field of view than its conventional counterpart.

For the MIR MTM-lined disc MTS, we create a custom gas cell and experimentally demonstrate the enhancement of the 15-µm absorption band of CO_2. Further, we demonstrate a numerical model for CO_2 and use the model to val-

idate the experimental result. The study is extended numerically to suggest the potential improvements afforded by a functionalization layer.

Finally, in Ch. 6, we summarize the important results of this thesis and suggest directions for future research.

Chapter 2

Background

2.1 Plasmonics

Since the discovery of electromagnetic waves coupled to electron plasma oscillations at the surface of a metal by Ritchie in the 1950s [65], [66], research into the control of plasmonic waves has advanced at a furious pace. These waves, called surface plasmons, have two main properties that are otherwise not found in the optical domain. Propagating surface plasmon modes are tightly bound in one dimension to the metal-dielectric interface along which they propagate, and hence support (1) reduced wavelength and (2) large electric-field magnitudes, but cannot be excited directly from free space [67]. Nevertheless, there are a number of well-developed approaches for exciting a surface plasmon at a metal surface, such as frustrated evanescent coupling [68], [69], diffraction [70], [71], and electron beams [65]. The strong fields at the metal interface promote light-matter interactions that would otherwise be too weak to study, such as molecular vibrational absorption, inelastic Raman scattering, and other nonlinear processes.

The discovery that plasmonic metal nanoparticles can confine and control surface plasmon waves at their surface on a deeply subwavelength scale has created intense interest in the nanopatterning of metals. Surface plasmons confined to the surface of a nanoparticle are known as localized surface plasmons (LSPs) and are controlled by altering the size, shape, and arrangement of metal nanoparticles, nanoapertures, nanogaps, and nanowires. Ever-tighter tolerance requirements of these metal nanostructures have led to stringent de-

mands on nanopatterning methods, often over very wide areas. Several forefront plasmonic applications demand complicated arrangements of nanowires and nanogaps with features < 10 nm wide over ranges of several microns [72], [73]. Nanophotonic plasmonic circuit applications require fine geometric control for logic gates and resonators. Moreover, propagating surface plasmons must be guided over large distances, which requires precise control over the waveguide width, length, and film properties to reduce losses [74]–[76]. For nonlinear plasmonics, smaller features induce stronger field enhancement and hence amplify the effect of nonlinearities, particularly in large arrays [77], [78].

2.2 Aperture Arrays

An aperture array consists of a periodic or semiperiodic array of perforations in a metallic film. Aperture arrays have been suggested for countless applications over the entire electromagnetic spectrum due to the ease of controlling their transmission/reflection response and their ability to strongly confine and enhance fields on a subwavelength scale [79]. These applications include partially reflecting surfaces for antennas, beam splitting and steering, biological material sensing, surface-enhanced spectroscopy, and the demonstration of extraordinary optical transmission (EOT) [80]–[87].

Aperture arrays can be classified into four operating regimes based on two important parameters: the electrical size of the unit cell (array periodicity/wavelength in free space $= p/\lambda_0$) and whether the apertures are resonant or nonresonant, as shown by the four quadrants in Fig. 2.1. Arrays with $p \sim \lambda_0$ and resonant apertures (quadrant I) are the building blocks of frequency selective surfaces (FSSs). FSSs are widely used as superstrates/substrates for polarization control, transmission/reflection spectrum manipulation, and beam shaping [88], [89]. Arrays with $p \sim \lambda_0$ and small nonresonant apertures (quadrant II) exhibit diffraction-grating anomalies, also known as EOT (originally interpreted as the so-called 'spoof' surface plasmon resonance [90]). Such structures generally use the high sensitivity of the spoof surface plasmon resonance to the metal/dielectric interface to create high-quality sensors or make

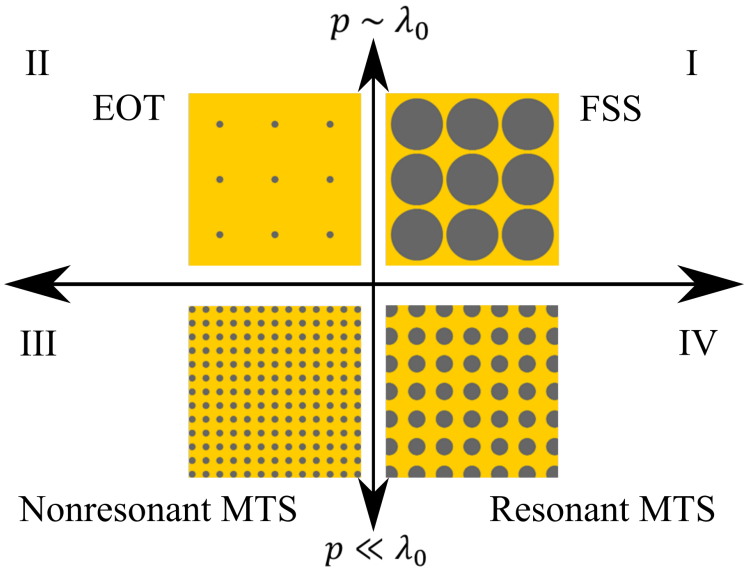

Figure 2.1: Aperture array classification based on electrical size p/λ_0 and resonant or nonresonant constitutive elements. Reproduced with permission from [92], ©2019 IEEE.

use of their strong field enhancement to increase the probability of nonlinear scattering events such as Raman scattering [85]. Unfortunately, due to their necessarily (electrically) large dimensions, both EOT devices and FSSs can become very large and bulky. Indeed, if both the aperture size and period could be decreased to subwavelength scales, such devices could be more easily integrated into electromagnetic systems and may be expected to demonstrate enhanced performance associated with higher packing densities/filling fractions. For example, manipulating the features of wavefronts with subwavelength spatial resolution can enable a wide range of phenomena, such as extremely directive beams and wide scan angles [91].

When $p \ll \lambda_0$, an aperture array can be described as a set of homogenized or 'effective' surface properties, and when these properties are engineered to demonstrate unusual or otherwise special phenomena, such arrays may be described as electromagnetic or optical MTSs. An MTS with $p \ll \lambda_0$ and nonresonant apertures (quadrant III) generally demonstrates qualities such as low dispersion and simple element shapes [93]. Finally, quadrant IV describes resonant MTSs, where $p \ll \lambda_0$, but the subwavelength apertures are made to

resonate by various means. Such MTSs are most valued for their high degree of miniaturization, their strong dispersion, and their resonance qualities when compared to dielectric and nonresonant MTSs [94].

2.3 Metasurfaces

MTSs have garnered significant interest due to their ability to manipulate electromagnetic waves on a subwavelength scale. MTSs are periodic or quasiperiodic two-dimensional arrays composed of subwavelength meta-atoms or unit cells, where each meta-atom is tailored to exhibit a specific electromagnetic scattering response, such as amplitude, phase, and polarization. With the proper implementation, MTSs have been designed for a variety of applications, including beam redirection at arbitrary angles, polarization conversion, perfect absorption, and other more complex wavefront transformations such as holograms and Bessel beams [94], [95]. Furthermore, when placed in the near-field of a sample under test, MTSs have been realized for subdiffraction imaging and magnification, material sensing, and surface-enhanced spectroscopy [47], [96]–[99].

Numerous MTS unit-cell structures based on Mie and plasmonic resonances have been explored in the optical domain; however, only plasmonic resonators can be made deeply subwavelength in size, which increases numerical aperture and wavefront conversion efficiency by avoiding diffraction grating effects [9], [100]. In the microwave domain, there exists a myriad of subwavelength resonant MTS unit cells based on finely patterned metal structures that expand the scope of achievable MTS properties [47], [101]–[103]. Applying these techniques in the optical domain has remained a challenge due to the difficulties of patterning intricate MTSs at a subwavelength scale and different material properties that make the simple scaling of lower-frequency designs impossible. A selection of optical plasmonic MTS unit-cells is shown in Fig. 2.2, where it is clear that the structures are limited in their patterning resolution and are generally quite simple in geometry.

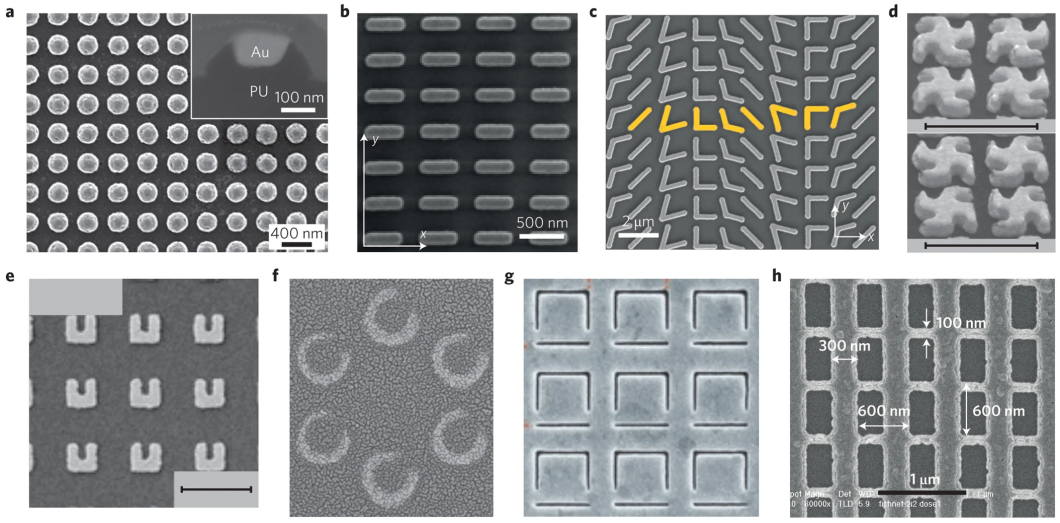

Figure 2.2: A selection of plasmonic MTSs: (a) nanodisks fabricated by template stripping (polyurethane), (b) rod antennas fabricated by nanoimprint lithography, (c) an MTS composed of different V-shaped nanoantennas fabricated by EBL, (d) double-layer right-handed (top) and left-handed (bottom) gammadions forming a chiral MTM fabricated by EBL (scale bars are 500 nm), (e) split-ring resonators fabricated by EBL (scale bar is 500 nm), (f) split-ring resonator with inner and outer diameters of 108 nm and 188 nm, respectively, fabricated by nanosphere lithography, (g) inverse asymmetric split-ring resonator fabricated by ion-beam milling 25-nm-wide slits into a gold film resulting in a 495 nm × 495 nm meta-atom, and (h) double fishnet structure fabricated by nanoimprint lithography. Figures reproduced with permission from: (a) [104], ©2011 Nature, (b) [105], ©2009 APS, (c) [106], ©2011 AAAS, (d) [107], ©2007 OSA, (e) [108], ©2011 APS, (f) [109], ©2009 Wiley, (g) [110], ©2010 APS, (h) [111], ©2007 Springer. Composite and caption reproduced with permission from [9], ©2014 Nature.

2.4 MTM-Lined Aperture MTSs

In the optical domain, devices are created on the nanoscale, and the overall size of EOT and FSS screens are thus less limiting; however, a reduction of size implies higher spatial resolution and stronger field enhancement, leading to a more sensitive response. Moreover, a higher filling fraction of the apertures (perforations) in a certain area will result in higher transmission levels and contrast [47], [112].

The simplest way to create resonant, subwavelength apertures may be to fill the apertures with a high-permittivity dielectric, but such an approach is counterproductive in certain applications. Applications that make use of the high sensing potential of the field confinement that can be produced by structuring the metallic features of the otherwise empty aperture region require a different approach. It was recently shown in the microwave regime that introducing a thin, epsilon-negative and near-zero (ENNZ) MTM liner inside a circular aperture can cause the aperture to resonate well below its natural fundamental resonance frequency [62] while leaving the interior open to visual inspection and sensing liquids or gases. This MTM-lined aperture was used to create a filtering MTS of subwavelength and densely packed apertures, and later to create a near-field subwavelength imaging array for conductive obstacles [47].

The MTM-lined aperture technology has plasmonic-like properties that create many applications not previously achievable with FSSs and that may be useful at optical frequencies, such as optical characterization of the dielectric properties of inhomogeneous materials with subwavelength spatial resolution. This is enabled by the fields in the apertures that are strongly confined to the liner region, much like in a conventional plasmonic nanoaperture, and it has been shown that the aperture resonance frequency is strongly dependent on the dielectric environment of the liner [113]. Therefore, a densely packed array of such apertures, each designed for slightly different resonance frequencies, could be used to detect spatial variations in properties of a dielectric material under test. A uniform MTM-lined aperture MTS might be used to detect

minute changes in concentrations by surface-enhanced Raman spectroscopy (SERS) when submerged in a liquid analyte, and could be used to measure microfluidic diffusion in real-time [85]. Combined with a nonlinear material, an optical MTM-lined aperture MTS may demonstrate high-quality switching phenomena [114]. The subwavelength period of this MTM-lined aperture MTS allows higher-density beam splitting/steering and general wavefront manipulation, and the addition of spatial information to surface-plasmon sensors [112].

2.4.1 Analytical Modeling of MTM-lined Apertures

An aperture in a metal screen may be viewed as the limiting case of a very short metallic waveguide with the same cross-section as the aperture. While the waveguide supports propagating modes with cutoff frequencies that may often be solved analytically, an aperture has no propagation length and instead supports only resonances at the cutoff frequencies of the equivalent waveguide's modes. Although Bethe's well-known aperture theory [115] predicts that an empty aperture will transmit poorly when it is electrically small (below what would be the cutoff frequency of the equivalent fundamental waveguide mode), the below-cutoff modes introduced by the MTM lining create strong, resonant transmission for subwavelength apertures [62]. This resonance is unlike those most commonly produced by larger apertures as it exhibits a characteristic asymmetric Fano lineshape, which is a strong enhancement followed by strong extinction of the transmission (or vice-versa), as seen in Fig. 2.3c. We borrow the HE_{xx} (hybrid electric) and EH_{xx} (hybrid magnetic) mode notation, which are equivalent to the TE_{xx} and TM_{xx} modes of a conventional aperture [116].

The Fano response is well-described by a dual resonator model, under the conditions where a high-Q resonator (*i.e.*, sharp or discrete resonance) interacts with a low-Q resonator spectrum (*i.e.*, wide or continuous spectral response) in the weak-coupling regime [117]. The high-Q resonator has a 180-degree phase shift at resonance, and the wide spectrum follows a continuous phase response. The two constructively then destructively interfere near the discrete resonance frequency to produce the characteristic asymmetric Fano

lineshape. In the case of the apertures described here, the sharp, frequency-reduced HE_{11} resonance interacts with the low, wide-band background transmission of an unlined aperture predicted by Bethe's theory to produce a Fano lineshape.

To find the resonance frequencies, the Helmholtz equation is solved in cylindrical coordinates, subject to appropriate boundary conditions. The problem layout is shown in Fig. 2.3a, where there is a central region of radius a filled with air ϵ_0, μ_0, a thin MTM liner region of thickness $t = b - a$ with permittivity and permeability ($\epsilon_2 = I(\epsilon_{\rho 2}, \epsilon_{\phi 2}, \epsilon_{z2}), \mu_2 = I(\mu_{\rho 2}, \mu_{\phi 2}, \mu_{z2})$), and finally an outer perfect electric conductor (PEC). This is similar to finding the dispersion relation of the equivalent waveguide system, as was done by Pollock *et al.*, but enforcing the propagation constant to be 0 [116]. Plotting the resonance frequency with respect to liner permittivity for each mode leads to an interesting result for the HE_{11} resonance: the resonance frequency is strongly reduced for negative and near-zero values of permittivity. This resonance shows weak, collimated fields in the centre and strong fields in the liner. Since PECs are not available at optical frequencies, extending this model requires considering the finite field penetration depth into the outer metallic region, which will act as a plasma described by the Drude model (see Appendix B).

2.4.2 Microwave Implementation

A suitable TL-MTM to realize the above ENNZ property employs an azimuthally directed coplanar-strip transmission line loaded using discrete inductors to create an ENNZ response, as shown in Fig. 2.3b [62]. According to TL-MTM theory, the shunt inductors compete with the intrinsic capacitance of the transmission line to create an effective negative permittivity when describing the propagation constant along the line [118]. Moreover, the effective permittivity follows a Drude-like dispersion model, with an equivalent plasma frequency at the branch resonance condition.

Series capacitors are included in this implementation that could lead to a negative effective permeability, and as a result, a negative index on the line. However, the capacitor values are kept small such that they only sup-

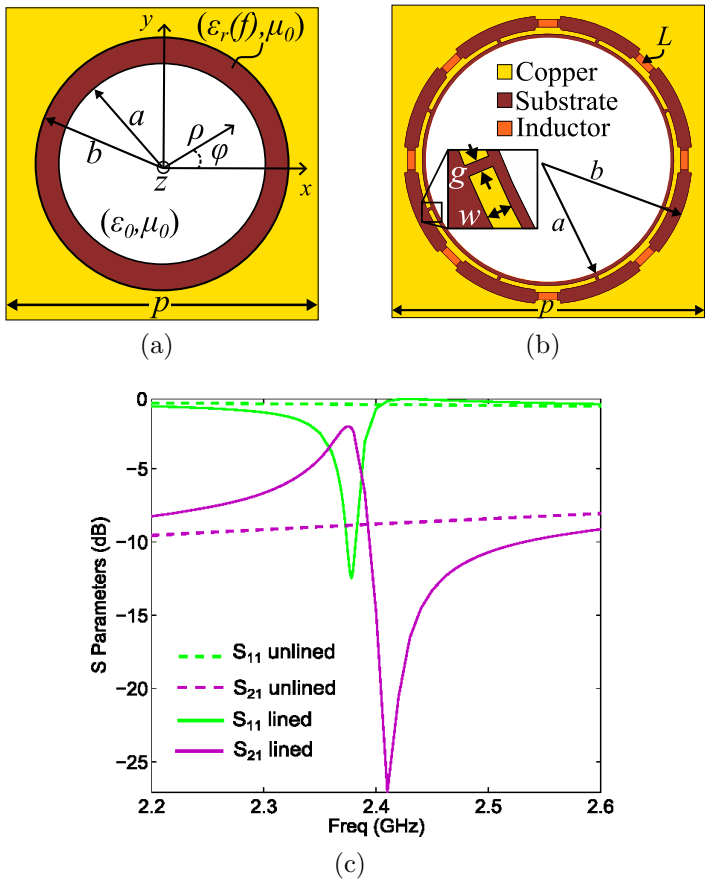

Figure 2.3: (a) Planar view if an MTM-lined aperture. Region 1 ($\rho < a$) is filled with vacuum (but may generally take on any ϵ_{r1}, μ_{r1}), region 2 ($a < \rho < b$) is filled with an MTM that has arbitrary ϵ_{r2} and μ_{r2}, and the outer region ($b < \rho$) is a PEC. From [62], Fig. 1 (a). (b) Practical implementation of the ENNZ-MTM lined aperture from [62], Fig. 1 (c). a,b, and p are borrowed from Fig. 2.3a, and L refers to discrete radial inductors, w is the azimuthal trace width, and g is the azimuthal capacitive gap width. (c) The scattering parameters for an infinite array of ENNZ MTM-lined and unlined apertures with the same outer radius b. Reproduced with permission from [62], ©2015 OSA.

press azimuthal modes and marginally change the effective permeability of the line at the operating frequency. The EH_{01} mode also necessarily exists in the frequency-reduced regime below the liner's plasma frequency, but is orthogonal to the HE_{11} mode and may therefore be suppressed through proper excitation. Extending this implementation to optical frequencies will require finding optical alternatives to the lumped inductors, potentially requiring very fine features for practical realization.

2.5 Surface-enhanced Spectroscopy

Surface-enhanced spectroscopy is a well-known and widely used technique for nondestructive chemical analysis and imaging. Typically, the material under test is loaded onto a metallic (plasmonic) surface and the metal is excited at its surface plasmon resonance frequency. This induces a strong local electric field (E), which enhances a particular Raman scattering or absorption line. Depending on sample preparation, Raman scattering efficiency can be improved by a factor of $> |E|^4$, whereas absorption can be improved by a factor of $\sim |E|^2$ [28], [119]. In fact, in the case of Raman scattering, even single molecules have been detected using arrays of resonant plasmonic metal nanoparticles with small inter-particle gaps to excite strong electric-field "hotspots". Although a number of fundamental molecular vibrational modes are exclusively Raman-active, *i.e.*, requiring a shift in the polarizability of the molecule, other molecular vibrations are exclusively infrared-active, *i.e.*, requiring a shift in the dipole moment of the molecule (in symmetric molecules, these categories are mutually exclusive). SEIRA spectroscopy is hence required for complementary characterization of a sample's vibrational spectrum. In particular, gases are difficult to characterize using SEIRA spectroscopy due to their low density and variable adsorption rates. Instead, bulky and expensive non-dispersive infrared (NDIR) absorption methods that rely on transmission through a gas sample are generally used. Despite the reliability of NDIR, increasing the sensitivity SEIRA spectroscopy to gases by optimizing the hotspots or adding functionalization layers would decrease the cost and required size, increase

the selectivity, and create miniaturized on-chip real-time gas sensors. SEIRA spectroscopy generally targets the chemical fingerprinting region of the MIR spectrum. The chemical fingerprinting region lies between 1500 cm^{-1} and 500 cm^{-1} (6.67 µm–20 µm wavelength), where every material has a unique set of absorption bands, *i.e.*, a unique spectral "fingerprint", controlled by photons exciting higher-order vibrational states in the molecular structure.

A wide variety of materials, fabrication methods, and nanoparticle shapes have been developed within the last few years to improve the signal enhancement in SEIRA, a collection of which are shown in Fig. 2.4 [120]–[130]. Unfortunately, long-wavelength SEIRA (beyond $\sim$700 cm^{-1}) has developed more slowly due to the scarcity of transparent substrate materials, lower signal levels, more costly sources/detectors, and difficulties making use of plasmonic resonant nanoparticle field enhancement at these wavelengths. The natural plasmonic effect is unable to miniaturize resonators at these wavelengths, which leads to large inter-particle distances and a low density of electric-field hotspots. An ideal SEIRA surface would be made of miniaturized, subwavelength elements that are closely spaced, which allows them to exhibit a high density of hotspots across the sample surface for maximum efficiency in a similar manner to colloidal metal surfaces [26]. Nevertheless, the capacitive and plasmonic field enhancement between resonant nanoantenna tips has been successfully used to significantly enhance SEIRA signals at these hotspots [131]–[133]. Commonly used dipole-nanoantenna arrays require creating large, resonant elements (on the order of $\lambda_0/4$ or larger) that exhibit a mere two hotspots per period, making inefficient use of the illuminated sample area. Dipole-nanoantenna arrays also respond only to electric fields polarized along their axis, requiring the addition of polarizing elements to the measurement setup and only enhancing the absorption of aligned molecules. One approach to address this challenge has been to use cross-shaped dipoles instead, which allows any randomly oriented molecule to be excited, but the elements still exhibit only a maximum of four hotspots per period [123].

CO_2 detection is a critical step in carbon capture systems for reducing air pollution and is important in measuring air quality, testing lung function,

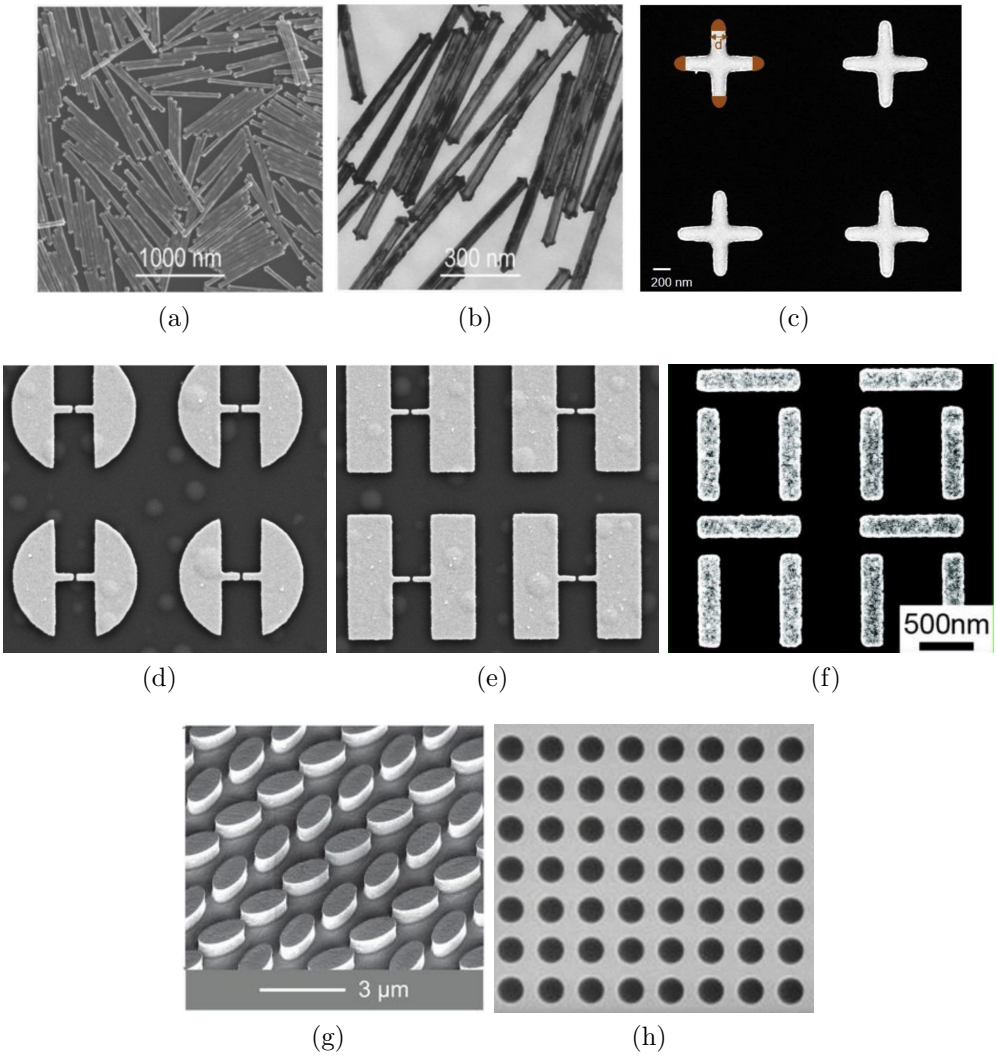

(a) (b) (c)

(d) (e) (f)

(g) (h)

Figure 2.4: A selection of plasmonic and dielectric SEIRA substrates: (a) Colloidal silver nanorods grown by Au nanobipyramid-directed Ag overgrowth, (b) gold nanotubes grown by galvanic replacement reaction to synthesize hollow Au nanotubes from the sacrificial Ag nanorod templates, (c) gold nanocrosses on Si substrate, patterned by EBL (d), (e) gold pad-rod nanoantennas fabricated on Al_2O_3 with a gold backing and patterned by EBL, (f) coupled gold nanobars on Si, patterned by EBL, (g) hydrogenated amorphous Si elliptical resonators fabricated by EBL and reactive ion etching, and (h) 2D photonic crystal, silicon on insulator, patterned by EBL and reactive ion etching. Figure reproduced with permission from: (a), (b) [121], ©2018 Wiley, (c) [123], ©2019 Elsevier, (d), (e) [126], ©2019 IOP, (f) [120], ©2017 AIP, (g) [122], ©2018 AAAS, and (h) [125], ©2019 IEEE.

and quantifying industrial and automotive emissions. CO_2 is usually sensed near 4.2 µm, however, this wavelength range has many other confounding species often found in exhaust plumes, such as H_2O, O_3, and CO, that may diminish sensitivity when wavelength resolution or the concentration is low [134]–[136]. Targeting the strong 15-µm bending-vibration absorption band responsible for the majority of atmospheric heating by CO_2 may be useful in multispectral sensing to better discriminate between CO_2, and other materials. This wavelength range can also be used individually to distinguish aromatic isomers, such as xylenes [137].

Meta-atoms based on metallic discs lined with MTMs have been developed for filtering applications in the microwave regime [63], [64]. The discs are the Babinet complement of the ENNZ-lined apertures described above, where metal was replaced by air/dielectric, air/dielectric was replaced with metal, and capacitors and inductors are swapped. The plasmon-like resonances of the MTM-lined disc are ideal for SEIRA applications as they have been developed using single-layer fabrication technologies, are highly miniaturized at resonance, can be densely packed, and exhibit strong resonant field enhancement in the liner region throughout the electromagnetic spectrum. Scaling the MTM-lined meta-atoms to operate in the fingerprinting region while preserving their strong field enhancement and miniaturization may significantly improve the sensitivity of SEIRA measurements with a marginal increase in complexity, particularly in the long-wavelength MIR. This could allow miniaturization of SEIRA spectroscopic devices and require less sample material for accurate analysis.

2.6 Metasurface Nanofabrication

More recently, He^+ GFIS have emerged for FIB-based imaging applications to produce a sub-nm probe size. He^+ ions are lighter than Ga^+ ions and are hence less destructive when imaging and boast smaller surface interaction volumes, which, when applied to milling, leads to increased patterning resolution. HIM has proven to be the only fabrication technology that can achieve both high

aspect ratios (over 1:10) and extremely fine features in noble metals (as small as 3 nm), but has been hampered by relatively slow speed and reproducibility [35]–[40], [138]. Reproducibility is important for MTSs in particular since a practical MTS must encompass as full an extent of the illuminating field as possible, which is generally several wavelengths across. For a subwavelength unit cell, this implies on the order of hundreds of such cells arranged periodically or quasi-periodically. Hahn *et al.* have recently shown that HIM can achieve 15 nm features with a 1:4 aspect ratio reliably over a 10 µm×10 µm area [38].

Other emerging nanofabrication methods for MTS development include nanoimprint lithography and atomic layer lithography [139], [140]. Unfortunately, although nanoimprint lithography is able to reproduce EBL features on a wafer scale, it also requires a masking layer and some form of etchant, which cannot transfer sufficiently fine, high-aspect-ratio features to a gold surface. Atomic layer lithography can achieve high-aspect-ratio features and very fine nanogaps in gold, however, this process requires several steps and the features must still be templated (*e.g.*, by EBL or FIB). Moreover, arbitrary gap shapes with variable widths cannot be made due to the uniform deposition rate of the atomic layer deposition process. A modified EBL process has also been suggested for achieving 10-nm nanogaps with high aspect ratios, but this process also limits the size and shape of conducting features [141]. Therefore, the HIM is invaluable for prototyping complex plasmonic structures due to its ability to pattern sub-10-nm features in conductive films. These high-resolution features could allow unprecedented control over polarization and incidence-angle response, as has been developed for larger-scale microwave-regime MTSs [39], [91], [142]–[145].

2.7 Helium Ion Microscope

The HIM used throughout this thesis was the Zeiss Orion NanoFab Helium Ion Microscope shown in Fig. 2.5, housed at the University of Alberta nanoFAB Centre [146]. Our HIM is equipped with two sources: a He^+ GFIS, which

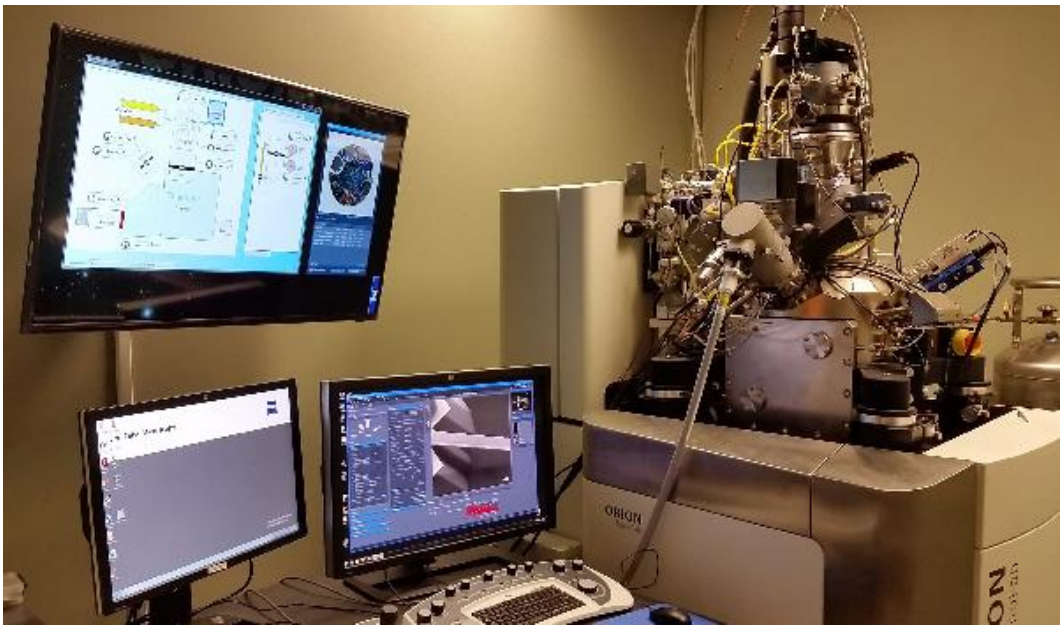

Figure 2.5: The Zeiss Orion NanoFab Helium Ion Microscope housed at the University of Alberta nanoFAB Centre. Image courtesy of Peng Li, reproduced with permission from [147].

is the standard source for imaging and high-fidelity patterning, and a Ga^+ liquid metal ion source (LMIS), which is historically the standard source and is used for larger-scale nanofabrication and sectioning samples for transmission electron microscope (TEM) analysis. Since we are creating dense arrangements of fine features, only the He^+ source can be used. In this section, we detail the key differences that enable reliable nanometre-scale resolution with the HIM.

2.7.1 Gallium vs Helium

The maximum theoretical resolution of a FIB instrument is limited by the source size, chromatic aberrations, spherical aberrations, and diffraction in the optics. The source size is the size of the emission area at the source, chromatic aberrations are a function of the energy spread of extracted ions, spherical aberrations are a function of the angular spread of the source, and diffraction is a function of the particle wavelength [148]. Each aberration is characterized by a probabilistic spreading of the source image, known as the "circle of confusion". The size of the circle of confusion is generally taken as the standard radial deviation of the aberration, modeled as a Gaussian

distribution. The limiting aberration changes depending on the source used. Generally, chromatic aberrations are the limiting factor (assuming diffraction contributions are sufficiently small to be ignored). In reality, the ultimate resolution is limited by the sputtering of the sample.

The Ga^+ LMIS consists of a source of Ga and a heated filament (usually made of W) above an extractor electrode. To extract an ion beam, the Ga is melted and a potential is applied between the filament and the extractor. Electrostatic forces and surface tension draw the liquid metal into a "Taylor cone", and past the extraction voltage V_s, the strong field at the tip of the Taylor cone causes spontaneous ionization of the Ga. For an optimized source operating at 30 keV, the virtual source size is 3.8 nm (real source size 30 nm multiplied by lens magnification), the chromatic aberration circle of confusion has a diameter of 2.93 nm, and the spherical aberration circle of confusion has a diameter of 0.03 nm [148]. Treating each circle of confusion as a standard radial deviation σ_x, the total probe size is found from the total variance:

$$\sigma_t = \sqrt{\sum_x \sigma_x^2}, \tag{2.1}$$

and the total probe size evaluates to ∼5 nm.

The He^+ GFIS operates on similar principles, but the filament is instead cooled and the He source is a carefully purified stream of gas. The tip of the filament is electrically machined into a triangular pyramidal shape, topped by a three-atom "trimer" [149]. The filament is cooled to ∼80 K using solidified nitrogen and a conductive heat path to minimize vibrations. It has been suggested that this temperature is ideal since it promotes the adsorption of He to the filament, but does not critically reduce the surface diffusion and a constant source of atoms is available in the ionization region. Cryogenic cooling also reduces the energy spread of the source, minimizing chromatic aberrations. The trimer is used as the ionization region, and the extraction optics select the emission from a single atom to minimize the source size. The typical virtual source size for the HIM GFIS is < 0.25 nm, and the optimal probe size is 0.35 nm. Plots of the different contributing factors are shown in

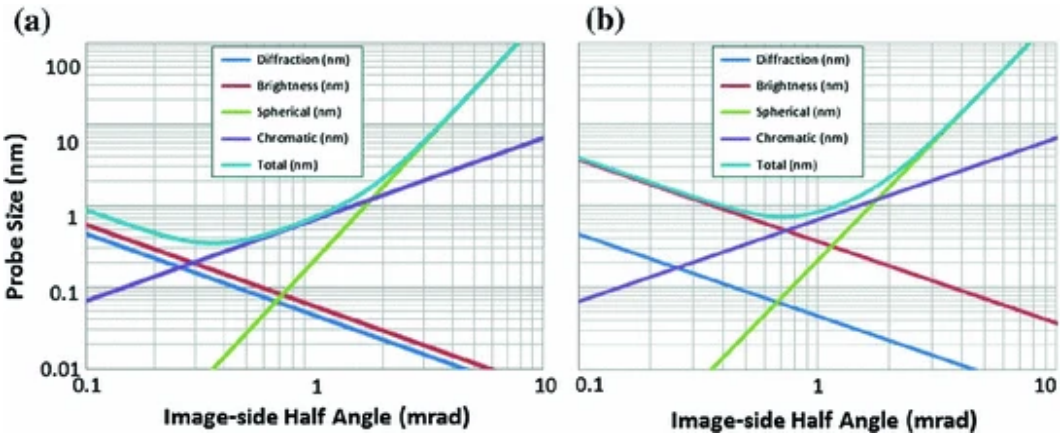

Figure 2.6: The probe size vs image-side half angle for a 30 keV landing energy helium beam. The two graphs are for optimal conditions (a) for a 0.5 pA helium ion beam, and (b) for a 20 pA beam. Figure and caption reproduced with permission from [149], ©2016 Springer.

Fig. 2.6, where the brightness is related to the real emission source size [149].

2.7.2 Sputtering

Although the HIM probe size can be made much smaller than the Ga^+ LMIS, we are more interested in which source supports the best patterning resolution. When an ion impinges on the surface of a sample, it loses kinetic energy through a number of interactions with the sample atoms. Of most importance to us is sputtering, which is the transfer of energy and momentum to sample atoms that causes a collision cascade that can eventually eject atoms from the sample surface. Fig. 2.7 shows the results of Monte Carlo simulations using the standard Stopping Range of Ions in Matter (SRIM) software [150] for several ions including Ga^+ and He^+. For heavier ions, the collisions occur closer to the surface and the ions scatter more laterally at the surface, increasing sputter yields but also increasing the width of patterned features. He^+ ions scatter weakly at the surface of the sample and penetrate deep into the surface, creating low sputtering yields but confined to a very small region around the impact area.

When simulated on gold with a landing energy of 30 keV, SRIM predicts a primary sputtering radius for He^+ to be $\sim$5 nm, but the deeply penetrating

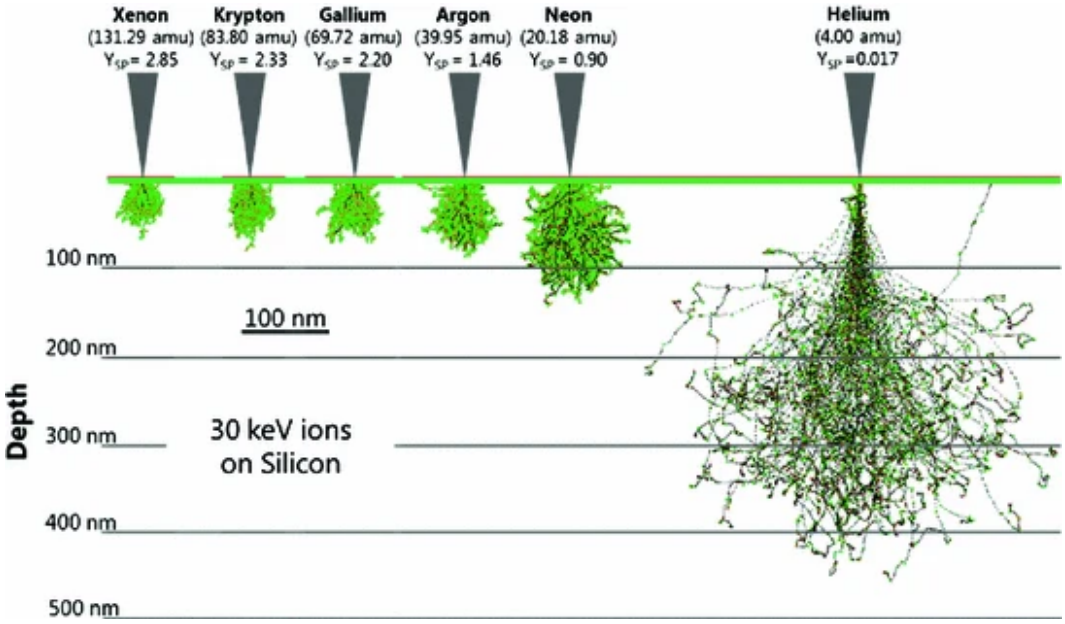

Figure 2.7: Cascade simulations with SRIM of noble gas ions impinging on bulk silicon with 30 keV energy in comparison to Ga^+ ions. Sputter yields Y_SP are indicated. The simulated impinging beams had zero diameters. Trajectories of primary ions are black while the green dots are collisions between recoiling target atoms. The red dots signify target atoms knocked from their lattice by the incident primary ion. Figure and caption reproduced with permission from [150], ©2016 Springer.

ions lead to secondary long-range sputtering over an area of nearly 100 nm, though at a much lower rate. When the ion dosage is particularly high, this can be observed in experiment. The total sputtering area is the sum of the spot size and the cascade area, and hence the He^+ GFIS can achieve significantly better patterning resolution than the Ga^+ LMIS and any other gas used in the GFIS source. Under ideal conditions, a theoretical maximum resolution of < 5 nm may be possible.

Chapter 3

Design and Modelling

Although the HIM has been shown to pattern individual features as small as 5 nm and features on the order of 15 nm over wide areas [38], [39], [151], to date, no structures with dense arrangements of fine features, *i.e.*, both fine nanowires and nanogaps, have been studied experimentally. Increasingly fine features offer additional control over the field distribution inside a plasmonic resonator, increasing field enhancement, mitigating losses, and increasing the achievable miniaturization for subwavelength sensing and imaging. Studies in the microwave domain have shown that MTSs based on apertures and discs loaded with MTM liners make excellent use of fine, deeply subwavelength features to achieve strong miniaturization and field confinement. Such features may be enhanced by the plasmonic properties of metals at optical frequencies; however, a scaling of deeply subwavelength features from the microwave domain to the optical domain requires extremely fine features. Moreover, an MTS array must be large enough to encompass the majority of its illumination, which may require hundreds of identical unit cells when the unit cell is strongly miniaturized. This makes an optical implementation of MTM-lined apertures an ideal study for assessing the feasibility of HIM patterning for large, complex, and finely featured plasmonic devices. In this chapter, we show the design and modelling of three MTM-lined resonator MTS unit cells (apertures and discs) making use of extremely fine nanometre-scale features for operation in the NIR, the visible wavelengths, and the MIR.

3.1 Scaling MTM-Lined Apertures to the NIR

First, we must scale the MTM-lined aperture to have a transmission resonance in the optical domain. As an initial design, we chose a target wavelength of 1550 nm (193 THz) for applications in optical telecommunications, and because sources and detectors are readily available for this wavelength range. A maximum unit cell size of $\lambda_0/5$ (*i.e.*, 310 nm) was targeted such that the unit cell can be considered subwavelength. Miniaturization by a factor of 5 is the minimum goal, and we will extend this goal to higher degrees of miniaturization in Sec. 3.2. From a design perspective, simply scaling the microwave design has two main problems. First, recall that the ENNZ-MTM-lined apertures realized in the microwave domain used a PEC film, where transverse electric fields are entirely cancelled at the surface. At optical frequencies, metals act as charged plasmas, where the finite drift velocity of electrons in a metal limits their ability to screen electric fields, and hence fields may penetrate inside the metal an appreciable distance. Second, recall that the ENNZ liner was loaded with discrete inductors. Volumetric coils are extremely challenging to fabricate, especially if they must be < 50 nm in size since the majority of nanofabrication methods are planar. The gap capacitors may still be employed.

With these challenges in mind, the first step was to choose the materials and fabrication method, as these define the minimum possible feature size. The HIM can mill metals extremely precisely, with reproducible feature sizes below 10 nm. Many metals act as good conductors in the NIR, even though PECs do not exist. Gold and silver both have comparable losses due to absorption; however, gold is chosen as silver oxidizes in air, which would quickly damage the integrity of the proposed 10 nm features. The 10-nm features should be exposed as they exhibit the strongest enhanced fields and are ideal locations for loading analytes to be characterized. For the substrate, both the transmissivity and cost were considered, and Borofloat glass was chosen as a suitable substrate.

The following designs were simulated in COMSOL, a full-wave, finite element, frequency-domain solver, or Lumerical, a full-wave finite-difference,

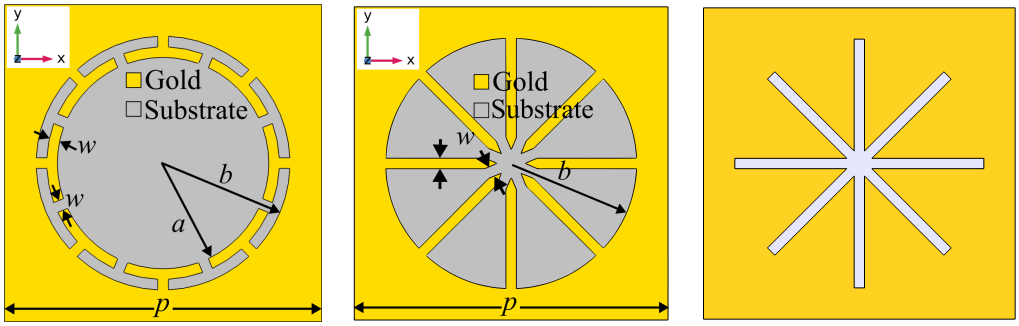

Figure 3.1: Evolution of the NIR design: (a) the thin liner case, (b) the wagon-wheel case, and (c) the asterisk case. Reproduced with permission from: (a), (b) [92], ©2019 IEEE, and (c) [154], ©2018 IEEE.

time-domain solver. A detailed tutorial on setting up MTS simulations in each software and considerations for the software choice are available in Appendix A. The simulation domain consists of three layers, stacked in the z-direction: i) the glass substrate (semi-infinite for the present purpose), ii) a patterned Au film of thickness t_f, and iii) air. The structure is excited by a linearly polarized plane wave at normal incidence ($-z$-direction) from the air region and the transmission is measured at the end of the substrate layer. Periodic boundaries separated by a periodicity p are used in the x and y (*i.e.*, transverse) directions to simulate conditions for an infinite array. In COMSOL, we used the Drude permittivity dispersion model of gold, with a plasma frequency of $\omega_p = 2\pi \times 2184$ THz, a damping frequency of $\Gamma_d = 2\pi \times 17$ THz, and $\epsilon(\infty) = 9.6$ F/m [152]. A detailed derivation of the Drude model is available in Appendix B. The glass was modelled with a lossless, nondispersive index of 1.47 [153]. The apertures are patterned into the metallic layer and possess a radius of b. Additionally, an example of the lined unit cells is shown in Fig. 3.1a, which possesses an MTM liner of thickness $t = b - a$, where a is the radius of the inner aperture air region. The gap and wire widths are w, and the number of wires is N, which defines the number of identical loading inclusions arranged about the azimuth in the liner region.

3.1.1 Thin Liner Aperture

As a first design, we will attempt to reduce the fundamental resonance frequency of a plasmonic nanoaperture using a MTM liner directly inspired by the microwave design. This will allow us to understand the role of replacing all PEC conductors with gold. The first design, called the "thin liner" design, is a faithful reconstruction of the microwave unit cell with the minimum feature size set to $w = 10$ nm, the minimum feature size reliably achievable by the HIM, and the inductors replaced with straight wires, as shown in Fig. 3.1a. The period is set to $p = 300$ nm (approximately $\lambda_0/5$, as identified previously), the aperture radius is set to $b = 120$ nm (ensures weak coupling between apertures across the symmetry boundaries), and $N = 8$ azimuthal wires are included for polarization isotropy and to meet the conditions required for an effective-medium model. With the liner as thin as possible, the liner thickness is $t = 20$ nm, and the inner radius is $a = 100$ nm. The film is set to a thickness of $t_f = 50$ nm in the z-direction for optical opacity, which enforces a 1:5 aspect ratio on the inductors. Such aspect ratios are only achievable by HIM, and the small 10-nm features around the full aperture edge are particularly challenging to accurately fabricate.

The described lined aperture's transmission and reflection spectra are shown in Fig. 3.2, where a clear transmission resonance is seen at 270 THz. For comparison, an aperture array with the same outer radius $b = 120$ nm but no liner resonates at 521 THz (or 732 THz for an aperture in a PEC screen), for an electrical size reduction by a factor of $\sim$2 ($\sim$3). This is a reasonable reduction, and an inspection of the electric field profile at resonance in Fig. 3.3a reveals features expected of an HE_{11} mode: collimated central fields, an electric-field direction reversal in the liner region, and much stronger fields in the liner region than in the centre. This validates that the MTM liner miniaturization method may be practical at optical frequencies, but does not reach the target of 193 THz (1550 nm) alone.

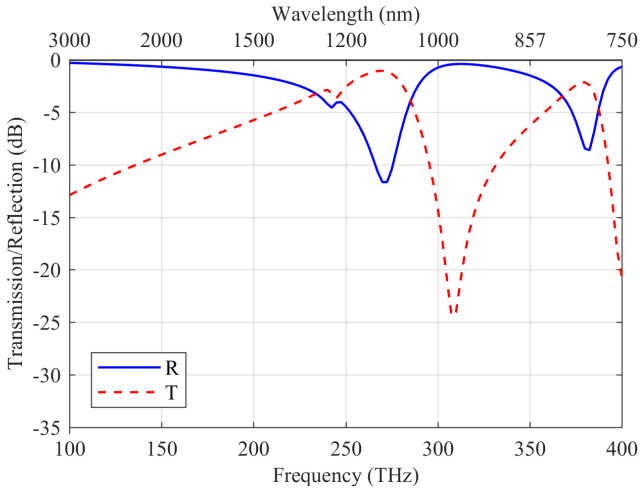

Figure 3.2: Transmission and reflection responses for the thin-liner optical MTS depicted in Fig. 3.1a.

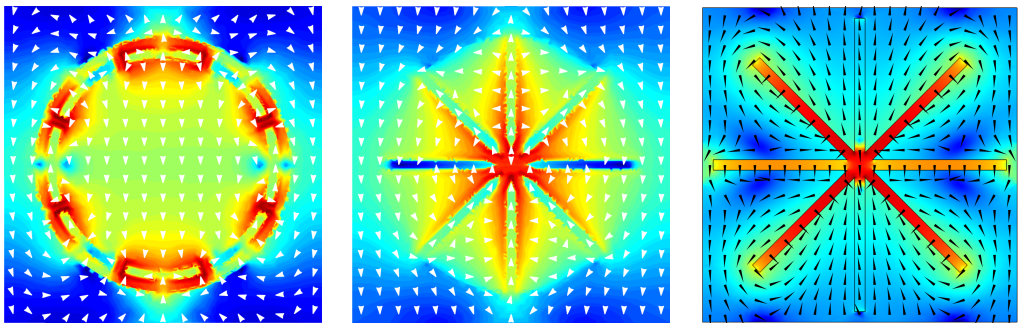

(a) (b) (c)

Figure 3.3: Log-scale electric-field profiles at resonance of: (a) the thin liner case (270 THz, maximum 80), (b) the wagon-wheel case (193 THz, maximum 140), and (c) the asterisk case (215 THz, maximum 45). Reproduced with permission from: (a), (b) [92], ©2019 IEEE, and (c) [154], ©2018 IEEE.

3.1.2 Wagon-Wheel Aperture/Thick Liner

To reach our goal of $\lambda_0/5$, we must further reduce the resonance frequency of the aperture. This is done by extending the liner to fill the entire aperture, and the aperture looks like a "wagon wheel," as shown in Fig. 3.1b. Keeping a 10-nm minimum feature size, the fabrication complexity of this design is similar to that of the thin liner, with the most challenging area being the dense 10-nm features at the aperture centre.

The transmission response of the wagon-wheel aperture is plotted in Fig. 3.4, which shows a resonance at the desired frequency of 193 THz with a characteristic asymmetric Fano lineshape. Inspection of the electric field profile at resonance (shown in Fig. 3.3b) reveals one similarity to the thin liner case. The strongest fields are inside the capacitive gap regions, which have been pushed to the centre of the aperture. Mutual coupling between adjacent cells has been reduced as the strongest field components are farther from the boundaries. This is ideal for applications such as SERS, where strong local field intensity enhancement is desired. Note that the electric fields inside the liner have become largely azimuthally directed, hence the isotropic permittivity model used by Pollock *et al*. to describe MTM-lined waveguides no longer applies [116].

There are many ways to explain the resonance frequency shift observed between the wagon-wheel and thin liner structures. From a circuit theory perspective, increasing the aspect ratio of a straight wire increases its inductance. This reduces the plasma frequency of the TL-MTM, and hence reduces the resonance frequency of the aperture. From an effective-medium perspective, extending the liner region increases the anisotropy of the liner and may also reduce the resonance frequency of the aperture, as we will show in Sec. 3.1.5. From a plasmonics perspective, increasing the aspect ratio of the plasmonic nanowires that load the aperture reduces their LSP resonance frequency to 260 THz, and the capacitive coupling between many wires reduces their resonance frequency further (see Appendix C). We use this interpretation to develop an equivalent-circuit model in Sec. 3.1.6 that models the majority of the aperture's behaviour near resonance accurately and predicts the spectral

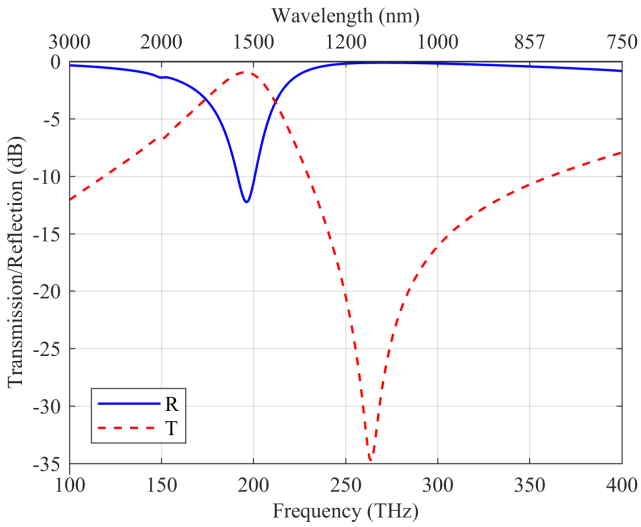

Figure 3.4: Transmission and reflection responses for the thick-liner optical MTS depicted in Fig. 3.1b. Reproduced with permission from [92], ©2019 IEEE.

variations due to changes in the size of the aperture, the array period, and the nanowire width.

3.1.3 Asterisk-Shaped Aperture

Although the performance of the wagon-wheel design meets the desired specifications, early fabrication attempts were less than successful. To increase the chances of successful fabrication, we created another design that maintains the dense, 10-nm features at the centre of the aperture but simplifies the remaining patterning. If the majority of the fields are focused towards the centre of the wagon-wheel aperture, what is lost by expanding the spokes (*i.e.*, the nanowires) and shrinking all removed material to 10 nm gaps? This choice (reflected in Fig. 3.1c) significantly decreases the required milling time for each aperture, which reduces the effect of instabilities in the HIM system on the milling of each aperture. The result is an "asterisk"-shaped aperture, with a resonance frequency of 215 THz for $b = 140$ nm. The electric fields at resonance are plotted in Fig. 3.3c, showing that the fields are less well-confined to the centre of the aperture, which leads to increased mutual coupling between apertures and increased resonance bandwidth. Despite the shape of the

metallic features ending in a sharp tip, the uniform gaps reduce the preference of the fields to focus to the centre of the aperture the way they are focused in the wagon-wheel case. Additionally, some higher-order resonances are pushed lower in frequency, decreasing the free spectral range of the resonances.

3.1.4 NIR Parametric Studies

The parametric studies below provide insight into the tunable geometrical parameters of the nanoplasmonic aperture arrays as well as the underlying mechanism of the observed resonant transmission. With the broad application space of MTSs, flexibility in the design of the unit cell is crucial. For subwavelength imaging, miniaturization is important to increase resolution. For spectroscopy and sensing applications, high sensitivity, strong field enhancement, and high contrast are required. For each of the studies below, we compare the MTM-lined apertures against their corresponding unlined apertures of the same outer radius b.

Inner Radius (a)

From the design of the aperture geometry, we expect a decrease in the inner radius a to lower the resonance frequency of the aperture since it is akin to increasing L, as was shown by Baladi *et al.* [62]. Additionally, the overall transmission magnitude should be constant due to a constant unit cell filling factor F (aperture area over unit cell area, $F = \pi b^2/p^2$).

The transmission results for this study are plotted in Fig. 3.5. To achieve a resonance frequency of 193 THz, an inner radius $a = 10$ nm is required, as we saw previously. The bandwidth of the resonance is also reduced for smaller a as the strong fields located in the capacitor regions are forced towards the center of the unit cell where they are much further from the unit cell boundary, and hence, cannot interact as strongly with neighbouring apertures. Since the resonance frequency can be tuned without changing the aperture size, a can be used to tune the unit cell miniaturization, though differences in field localization, free spectral range, and contrast must be considered.

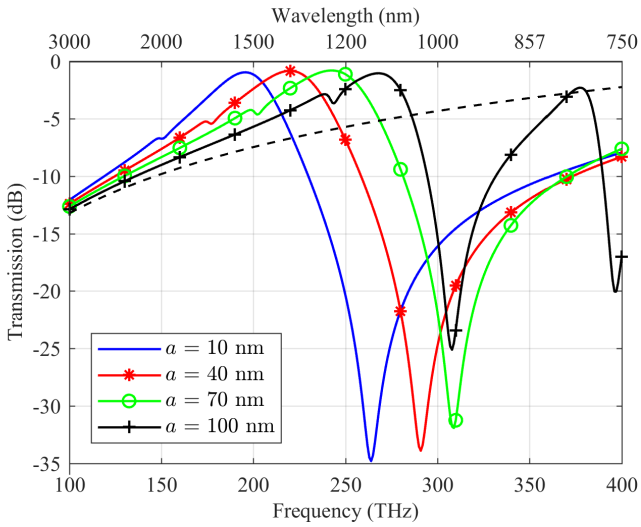

Figure 3.5: Transmission frequency response for varying inner radius a (solid), showing the transmission peak corresponding to the HE_{11} mode for each value of a. The unlined case with outer radius $b = 120$ nm (dashed) is also plotted for comparison. Reproduced with permission from [92], ©2019 IEEE.

Array Periodicity (p)

As shown in Fig. 3.6, the transmission of both the MTM-lined and unlined apertures decreases with decreasing filling factor F. The resonance frequency of the MTM-lined apertures remains largely constant due to weak coupling with neighbouring unit cells, though the small dip in transmission at 150 THz deepens significantly as the apertures come closer together. Additionally, increased fill factor F increases the bandwidth of the resonance. These data are consistent with those shown by Baladi *et al.* [62]. This verifies that this resonant transmission enhancement is dominated by the localized resonance of individual apertures and not diffraction anomalies, which would be highly dependent on the periodicity. This result also shows that closely spaced resonators may be practical for multiplexing numerous functionalities into a single surface since mutual interactions do not play a significant role in the overall response of the MTS. We will use this property to create a frequency-multiplexed imaging MTS in Ch. 5.

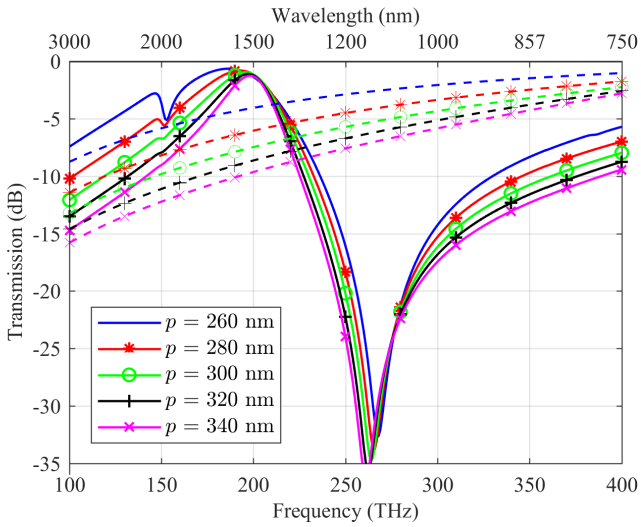

Figure 3.6: Transmission frequency response for varying array periodicity p, lined cases (solid) and unlined cases (dashed). Reproduced with permission from [92], ©2019 IEEE.

Film Thickness (t_f)

For a thin film, the finite penetration depth of the gold layer allows power to be transmitted through the surface, but the properties of a thicker film will approach bulk values. Fig. 3.7 shows the transmission response of the MTM-lined and unlined aperture arrays for varying thickness t_f. While the unit cells for thinner film thicknesses are well-described as apertures in a thin sheet, the propagation distance through the aperture becomes non-trivial for thicker films, and the unit cells may be better described as short waveguides with a complex propagation constant. The resonance is blue-shifted as the bulk properties of the gold become dominant and the plasmonic nanowire resonance is pushed to higher frequencies. Although thicker t_f implies better transmission and reflection enhancement over the unlined-aperture case, fabricating higher aspect ratios is a significant challenge in practice. For most applications, a thicker film is desired to reduce losses and increase opacity, or to induce resonances in the longitudinal dimension.

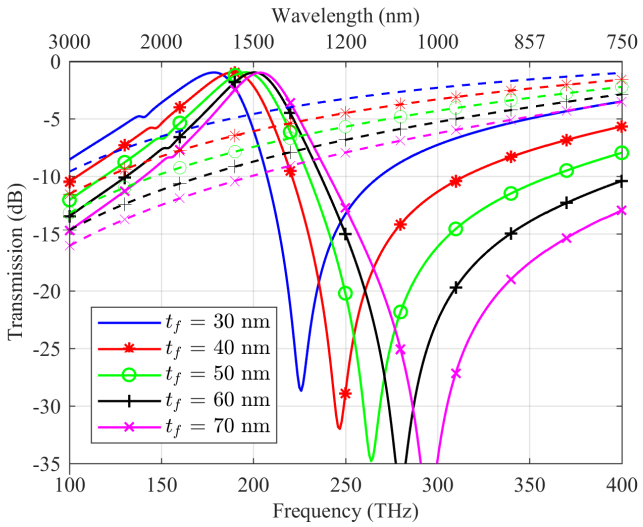

Figure 3.7: Transmission frequency response for varying gold film thickness t_f, lined case (solid) and unlined case (dashed). Reproduced with permission from [92], ©2019 IEEE.

Aperture Outer Radius (b)

Fig. 3.8 shows the transmission frequency response for varying aperture radius b. It should be noted that a change in outer radius also implies a change to the liner, as the radially directed wires must be lengthened for a constant. Varying b causes a resonance frequency red-shift for larger apertures due to the scaling property. Both b and a can therefore be used to tune the MTS resonance frequency to meet application design requirements. Although MTM-lined versus unlined aperture array transmission contrast is reduced as b grows due to the increase in fill factor F, $b = 140$ nm shows the best unit cell miniaturization.

Wire Density (N)

For a thick liner, a is not exactly 10 nm. The 10-nm capacitive gaps between the nanowires require that an N-sided polygon fit between the tips of the nanowires, thus $a = 5 \times \sec(\pi/N)$ nm. The transmission spectra for a varying number N of loading nanowires are plotted in Fig. 3.9. From the effective-medium perspective, the nanowires inside the aperture act as parallel inductors; therefore, combined with decreasing the wire length, an increasing

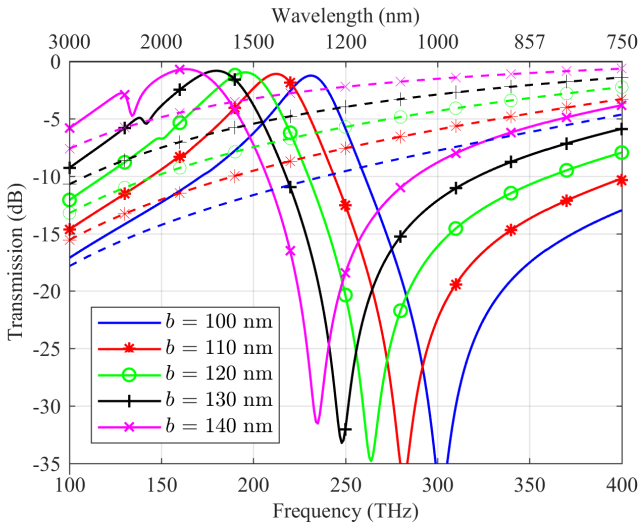

Figure 3.8: Transmission frequency response of the lined aperture case (solid) and the unlined aperture case (dashed) for varying values of outer radius b. Reproduced with permission from [92], ©2019 IEEE.

number of wires decreases the overall inductance as well as the capacitive coupling of the liner, which causes a blue-shift of the resonance frequency. Of the cases studied, maximum inductance is achieved for four wires and hence the lowest frequency resonance is observed. If we reduce N further, the liner exhibits a slow periodic variation in the azimuthal direction, which leads to different responses for different polarization angles. This could be harnessed in beam splitters to polarize each outgoing beam. Although polarization sensitivity and loss decrease for increasing N, the miniaturization also decreases and fabrication becomes more difficult. $N = 8$ gives a good balance of fabrication complexity, polarization sensitivity, and loss.

Extracting optimal performance from the MTM-lined aperture requires balancing the unit cell electrical size, the contrast compared to the reference array, and fabrication complexity. An optimal design therefore minimizes a, balances p and b between contrast and electrical size, and uses as thick of a film t as is practical in fabrication. These trade-offs lead to choosing the wagon-wheel structure as the optimal design.

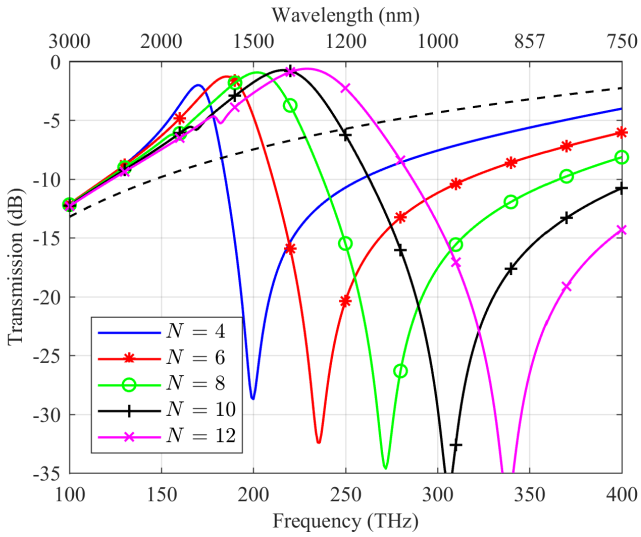

Figure 3.9: Transmission frequency response for varying number of wires N inside the aperture (solid) and the unlined case (dashed). Reproduced with permission from [92], ©2019 IEEE.

3.1.5 Analytical Modelling of a Thick and Anisotropic MTM Liner

We now look to model the behaviour of the wagon-wheel MTS analytically in order to extract additional intuition as to its operation, streamline the design process, and model the effects of fabrication inconsistencies.

We begin by extending the work of Pollock *et al.* [116] by solving the modes of an inhomogeneously filled circular waveguide with a *thick* liner exhibiting an ENNZ permittivity response. The cutoff frequencies of the waveguide modes correspond to the resonance frequencies of apertures with identical cross-sections. The modes of the ENNZ-lined waveguide are solved as follows, keeping the analysis as general as possible, but with some choice assumptions. The problem consists of three regions, described in cylindrical coordinates: 1) a central region with diagonal permittivity $\bar{\bar{\epsilon}}_1$ and permeability $\bar{\bar{\mu}}_1$ tensors (*i.e.*, anisotropic, but not bianisotropic), and radius a; 2) a liner region with diagonal permittivity $\bar{\bar{\epsilon}}_2$ and permeability $\bar{\bar{\mu}}_2$ tensors, and radius b; and 3) an outer metal region with isotropic permittivity $\bar{\bar{\epsilon}}_3$ and permeability $\bar{\bar{\mu}}_3$, that extends to $\rho = \infty$. Borrowing notation from Pollock *et al.* [116], the Helmholtz equation is to be solved in all 3 regions. Once separated into ρ,ϕ and z components,

it reads:

H_z:

$$\rho^2\frac{d^2R}{d\rho^2}+\rho\frac{dR}{d\rho}+(\gamma_\rho^{\mu 2}\rho^2-\tau^2)R=0 \tag{3.1}$$

E_z:

$$\rho^2\frac{d^2R}{d\rho^2}+\rho\frac{dR}{d\rho}+(\gamma_\rho^{\epsilon 2}\rho^2-\nu^2)R=0, \tag{3.2}$$

where the ϕ and z components are easily solved:

$$\sin(n\phi),\cos(n\phi),e^{-\gamma z}, \tag{3.3}$$

τ,ν, and the propagation constants γ are:

$$\tau^2=\frac{\mu_\phi}{\mu_\rho}\frac{\gamma_{c,\phi,\rho}^2}{\gamma_{c,\rho,\phi}^2}n^2 \qquad \nu^2=\frac{\epsilon_\phi}{\epsilon_\rho}\frac{\gamma_{c,\rho,\phi}^2}{\gamma_{c,\phi,\rho}^2}n^2 \tag{3.4}$$

$$\gamma_\rho^{\mu 2}=\gamma_{c,\phi,\rho}^2\frac{\mu_z}{\mu_\rho} \qquad \gamma_\rho^{\epsilon 2}=\gamma_{c,\rho,\phi}^2\frac{\epsilon_z}{\epsilon_\rho} \tag{3.5}$$

$$\gamma_{c,\rho,\phi}^2=\gamma^2+k_0^2\epsilon_\rho\mu_\phi \qquad \gamma_{c,\phi,\rho}^2=\gamma^2+k_0^2\epsilon_\phi\mu_\rho, \tag{3.6}$$

and the ϕ and ρ components of the fields can be found from the z components by:

$$E_\phi=\frac{-\gamma}{\gamma_{c,\phi,\rho}^2}\left[\frac{1}{\rho}\frac{\partial E_z}{\partial\phi}-\frac{j\omega\mu_\rho}{\gamma}\frac{\partial H_z}{\partial\rho}\right] \qquad H_\phi=\frac{-\gamma}{\gamma_{c,\rho,\phi}^2}\left[\frac{1}{\rho}\frac{\partial H_z}{\partial\phi}+\frac{j\omega\epsilon_\rho}{\gamma}\frac{\partial E_z}{\partial\rho}\right] \tag{3.7}$$

$$E_\rho=\frac{-\gamma}{\gamma_{c,\rho,\phi}^2}\left[\frac{\partial E_z}{\partial\rho}+\frac{j\omega\mu_\phi}{\gamma\rho}\frac{\partial H_z}{\partial\phi}\right] \qquad H_\rho=\frac{-\gamma}{\gamma_{c,\phi,\rho}^2}\left[\frac{\partial H_z}{\partial\rho}-\frac{j\omega\epsilon_\phi}{\gamma\rho}\frac{\partial E_z}{\partial\phi}\right]. \tag{3.8}$$

Due to the requirement that E and H be bounded as ρ approaches 0, E_{z1} and H_{z1} must be written using Bessel functions of the form:

$$E_{z1}(\rho,\phi,z)=C_1J_{\nu 1}(\gamma_{\rho 1}^{\epsilon}\rho)\cos(n\phi)e^{-\gamma z} \tag{3.9}$$

$$H_{z1}(\rho,\phi,z)=C_3J_{\tau 1}(\gamma_{\rho 1}^{\mu}\rho)\sin(n\phi)e^{-\gamma z}. \tag{3.10}$$

It follows from eq. (3.7) and eq. (3.8) that:

$$E_{\phi 1}(\rho,\phi,z)=\left[\frac{\gamma n\mu_{z1}}{\mu_{\rho 1}\gamma_{\rho 1}^{\mu\,2}\rho}C_1J_{\nu 1}(\gamma_{\rho 1}^{\epsilon}\rho)+\frac{j\omega\mu_{z1}}{\gamma_{\rho 1}^{\mu}}C_3J'_{\tau 1}(\gamma_{\rho 1}^{\mu}\rho)\right]\sin(n\phi)e^{-\gamma z} \tag{3.11}$$

$$E_{\rho 1}(\rho,\phi,z) = \left[\frac{-\gamma\epsilon_{z1}}{\epsilon_{\rho 1}\gamma^{\epsilon}_{\rho 1}} C_1 J'_{\nu 1}(\gamma^{\epsilon}_{\rho 1}\rho) - \frac{j\omega n\mu_{\phi 1}\epsilon_{z1}}{\epsilon_{\rho 1}{\gamma^{\epsilon}_{\rho 1}}^2\rho} C_3 J_{\tau 1}(\gamma^{\mu}_{\rho 1}\rho)\right]\cos(n\phi)e^{-\gamma z}, \tag{3.12}$$

and

$$H_{\phi 1}(\rho,\phi,z) = \left[\frac{-\gamma n\epsilon_{z1}}{\epsilon_{\rho 1}{\gamma^{\epsilon}_{\rho 1}}^2\rho} C_3 J_{\tau 1}(\gamma^{\mu}_{\rho 1}\rho) - \frac{j\omega\epsilon_{z1}}{\gamma^{\epsilon}_{\rho 1}} C_1 J'_{\nu 1}(\gamma^{\epsilon}_{\rho 1}\rho)\right]\cos(n\phi)e^{-\gamma z} \tag{3.13}$$

$$H_{\rho 1}(\rho,\phi,z) = \left[\frac{-\gamma\mu_{z1}}{\mu_{\rho 1}\gamma^{\mu}_{\rho 1}} C_3 J'_{\tau 1}(\gamma^{\mu}_{\rho 1}\rho) - \frac{j\omega n\epsilon_{\phi 1}\mu_{z1}}{\mu_{\rho 1}{\gamma^{\mu}_{\rho 1}}^2\rho} C_1 J_{\nu 1}(\gamma^{\epsilon}_{\rho 1}\rho)\right]\sin(n\phi)e^{-\gamma z}. \tag{3.14}$$

The open boundary on region 3 requires only outgoing waves, which can be represented as Hankel functions of the second kind:

$$E_{z3}(\rho,\phi,z) = C''_1 H^{(2)}_{\nu 3}(\gamma^{\epsilon}_{\rho 3}\rho)\cos(n\phi)e^{-\gamma z} \tag{3.15}$$

$$H_{z3}(\rho,\phi,z) = C''_3 H^{(2)}_{\tau 3}(\gamma^{\mu}_{\rho 3}\rho)\sin(n\phi)e^{-\gamma z}. \tag{3.16}$$

Applying eqs. (3.7) and (3.8) again to eq. (3.15) and eq. (3.16) results in:

$$E_{\phi 3}(\rho,\phi,z) = \left[\frac{\gamma n\mu_{z3}}{\mu_{\rho 3}{\gamma^{\mu}_{\rho 3}}^2\rho} C''_1 H^{(2)}_{\nu 3}(\gamma^{\epsilon}_{\rho 3}\rho) + \frac{j\omega\mu_{z3}}{\gamma^{\mu}_{\rho 3}} C''_3 H^{(2)\prime}_{\tau 3}(\gamma^{\mu}_{\rho 3}\rho)\right]\sin(n\phi)e^{-\gamma z} \tag{3.17}$$

$$E_{\rho 3}(\rho,\phi,z) = \left[\frac{-\gamma\epsilon_{z3}}{\epsilon_{\rho 3}\gamma^{\epsilon}_{\rho 3}} C''_1 H^{(2)\prime}_{\nu 3}(\gamma^{\epsilon}_{\rho 3}\rho) - \frac{j\omega n\mu_{\phi 3}\epsilon_{z3}}{\epsilon_{\rho 3}{\gamma^{\epsilon}_{\rho 3}}^2\rho} C''_3 H^{(2)}_{\tau 3}(\gamma^{\mu}_{\rho 3}\rho)\right]\cos(n\phi)e^{-\gamma z}, \tag{3.18}$$

$$H_{\phi 3}(\rho,\phi,z) = \left[\frac{-\gamma n\epsilon_{z3}}{\epsilon_{\rho 3}{\gamma^{\epsilon}_{\rho 3}}^2\rho} C''_3 H^{(2)}_{\tau 3}(\gamma^{\mu}_{\rho 3}\rho) - \frac{j\omega\epsilon_{z3}}{\gamma^{\epsilon}_{\rho 3}} C''_1 H^{(2)\prime}_{\nu 3}(\gamma^{\epsilon}_{\rho 3}\rho)\right]\cos(n\phi)e^{-\gamma z} \tag{3.19}$$

$$H_{\rho 3}(\rho,\phi,z) = \left[\frac{-\gamma\mu_{z3}}{\mu_{\rho 3}\gamma^{\mu}_{\rho 3}} C''_3 H^{(2)\prime}_{\tau 3}(\gamma^{\mu}_{\rho 3}\rho) - \frac{j\omega n\epsilon_{\phi 3}\mu_{z3}}{\mu_{\rho 3}{\gamma^{\mu}_{\rho 3}}^2\rho} C''_1 H^{(2)}_{\nu 3}(\gamma^{\epsilon}_{\rho 3}\rho)\right]\sin(n\phi)e^{-\gamma z}. \tag{3.20}$$

The fields in region 2 can be represented in any basis, but for simplicity, Bessel and Neumann functions are chosen:

$$E_{z2}(\rho,\phi,z) = \left[C_1' J_{\nu 2}(\gamma_{\rho 2}^{\epsilon}\rho) + C_2' Y_{\nu 2}(\gamma_{\rho 2}^{\epsilon}\rho)\right]\cos(n\phi)e^{-\gamma z} \tag{3.21}$$

$$H_{z2}(\rho,\phi,z) = \left[C_3' J_{\tau 2}(\gamma_{\rho 2}^{\mu}\rho) + C_4' Y_{\tau 2}(\gamma_{\rho 2}^{\mu}\rho)\right]\sin(n\phi)e^{-\gamma z}, \tag{3.22}$$

$$\begin{aligned} E_{\phi 2}(\rho,\phi,z) = \Bigg[&\frac{\gamma n \mu_{z2}}{\mu_{\rho 2}{\gamma_{\rho 2}^{\mu}}^2\rho}\left[C_1' J_{\nu 2}(\gamma_{\rho 2}^{\epsilon}\rho) + C_2' Y_{\nu 2}(\gamma_{\rho 2}^{\epsilon}\rho)\right] + \\ &\frac{j\omega\mu_{z2}}{\gamma_{\rho 2}^{\mu}}\left[C_3' J_{\tau 2}'(\gamma_{\rho 2}^{\mu}\rho) + C_4' Y_{\tau 2}'(\gamma_{\rho 2}^{\mu}\rho)\right]\Bigg]\sin(n\phi)e^{-\gamma z} \end{aligned} \tag{3.23}$$

$$\begin{aligned} E_{\rho 2}(\rho,\phi,z) = \Bigg[&\frac{-\gamma\epsilon_{z2}}{\epsilon_{\rho 2}\gamma_{\rho 2}^{\epsilon}}\left[C_1' J_{\nu 2}'(\gamma_{\rho 2}^{\epsilon}\rho) + C_2' Y_{\nu 2}'(\gamma_{\rho 2}^{\epsilon}\rho)\right] - \\ &\frac{j\omega n\mu_{\phi 2}\epsilon_{z2}}{\epsilon_{\rho 2}{\gamma_{\rho 2}^{\epsilon}}^2\rho}\left[C_3' J_{\tau 2}(\gamma_{\rho 2}^{\mu}\rho) + C_4' Y_{\tau 2}(\gamma_{\rho 2}^{\mu}\rho)\right]\Bigg]\cos(n\phi)e^{-\gamma z}, \end{aligned} \tag{3.24}$$

$$\begin{aligned} H_{\phi 2}(\rho,\phi,z) = \Bigg[&\frac{-\gamma n\epsilon_{z2}}{\epsilon_{\rho 2}{\gamma_{\rho 2}^{\epsilon}}^2\rho}\left[C_3' J_{\tau 2}(\gamma_{\rho 2}^{\mu}\rho) + C_4' Y_{\tau 2}(\gamma_{\rho 2}^{\mu}\rho)\right] - \\ &\frac{j\omega\epsilon_{z2}}{\gamma_{\rho 2}^{\epsilon}}\left[C_1' J_{\nu 2}'(\gamma_{\rho 2}^{\epsilon}\rho) + C_2' Y_{\nu 2}'(\gamma_{\rho 2}^{\epsilon}\rho)\right]\Bigg]\cos(n\phi)e^{-\gamma z} \end{aligned} \tag{3.25}$$

$$\begin{aligned} H_{\rho 2}(\rho,\phi,z) = \Bigg[&\frac{-\gamma\mu_{z2}}{\mu_{\rho 2}\gamma_{\rho 2}^{\mu}}\left[C_3' J_{\tau 2}'(\gamma_{\rho 2}^{\mu}\rho) + C_4' Y_{\tau 2}'(\gamma_{\rho 2}^{\mu}\rho)\right] - \\ &\frac{j\omega n\epsilon_{\phi 2}\mu_{z2}}{\mu_{\rho 2}{\gamma_{\rho 2}^{\mu}}^2\rho}\left[C_1' J_{\nu 2}(\gamma_{\rho 2}^{\epsilon}\rho) + C_2' Y_{\nu 2}(\gamma_{\rho 2}^{\epsilon}\rho)\right]\Bigg]\sin(n\phi)e^{-\gamma z}. \end{aligned} \tag{3.26}$$

The boundary conditions yet to be applied are the continuity of the tangential field components at the boundaries:

$$E_{z1}(a,\phi,z) = E_{z2}(a,\phi,z) \qquad H_{z1}(a,\phi,z) = H_{z2}(a,\phi,z) \tag{3.27a}$$

$$E_{\phi 1}(a,\phi,z) = E_{\phi 2}(a,\phi,z) \qquad H_{\phi 1}(a,\phi,z) = H_{\phi 2}(a,\phi,z) \tag{3.27b}$$

$$E_{\phi 2}(b,\phi,z) = E_{\phi 3}(b,\phi,z) \qquad H_{\phi 2}(b,\phi,z) = H_{\phi 3}(b,\phi,z) \tag{3.27c}$$

$$E_{z2}(b,\phi,z) = E_{z3}(b,\phi,z) \qquad H_{z2}(b,\phi,z) = H_{z3}(b,\phi,z) \tag{3.27d}$$

Applying these boundary conditions leads to the following nonlinear eigenproblem:

$$\begin{bmatrix}
J_{\nu1}(\gamma_{\rho1}^{\epsilon}a) & 0 & -J_{\nu2}(\gamma_{\rho2}^{\epsilon}a) & -Y_{\nu2}(\gamma_{\rho2}^{\epsilon}a) \\
0 & J_{\tau1}(\gamma_{\rho1}^{\mu}a) & 0 & 0 \\
\frac{\gamma n\mu_{z1}}{\mu_{\rho1}{\gamma_{\rho1}^{\mu}}^2 a}J_{\nu1}(\gamma_{\rho1}^{\epsilon}a) & \frac{j\omega\mu_{z1}}{\gamma_{\rho1}^{\mu}}J'_{\tau1}(\gamma_{\rho1}^{\mu}a) & \frac{-\gamma n\mu_{z2}}{\mu_{\rho2}{\gamma_{\rho2}^{\mu}}^2 a}J_{\nu2}(\gamma_{\rho2}^{\epsilon}a) & \frac{-\gamma n\mu_{z2}}{\mu_{\rho2}{\gamma_{\rho2}^{\mu}}^2 a}Y_{\nu2}(\gamma_{\rho2}^{\epsilon}a) \\
\frac{-j\omega\epsilon_{z1}}{\gamma_{\rho1}^{\epsilon}}J'_{\nu1}(\gamma_{\rho1}^{\epsilon}a) & \frac{-\gamma n\epsilon_{z1}}{\epsilon_{\rho1}{\gamma_{\rho1}^{\epsilon}}^2 a}J_{\tau1}(\gamma_{\rho1}^{\mu}a) & \frac{j\omega\epsilon_{z2}}{\gamma_{\rho2}^{\epsilon}}J'_{\nu2}(\gamma_{\rho2}^{\epsilon}a) & \frac{j\omega\epsilon_{z2}}{\gamma_{\rho2}^{\epsilon}}Y'_{\nu2}(\gamma_{\rho2}^{\epsilon}a) \\
0 & 0 & \frac{\gamma n\mu_{z2}}{\mu_{\rho2}{\gamma_{\rho2}^{\mu}}^2 b}J_{\nu2}(\gamma_{\rho2}^{\epsilon}b) & \frac{\gamma n\mu_{z2}}{\mu_{\rho2}{\gamma_{\rho2}^{\mu}}^2 b}Y_{\nu2}(\gamma_{\rho2}^{\epsilon}b) \\
0 & 0 & \frac{-j\omega\epsilon_{z2}}{\gamma_{\rho2}^{\epsilon}}J'_{\nu2}(\gamma_{\rho2}^{\epsilon}b) & \frac{-j\omega\epsilon_{z2}}{\gamma_{\rho2}^{\epsilon}}Y'_{\nu2}(\gamma_{\rho2}^{\epsilon}b) \\
0 & 0 & J_{\nu2}(\gamma_{\rho2}^{\epsilon}b) & Y_{\nu2}(\gamma_{\rho2}^{\epsilon}b) \\
0 & 0 & 0 & 0
\end{bmatrix}$$

$$\begin{bmatrix}
0 & 0 & 0 & 0 \\
-J_{\tau2}(\gamma_{\rho2}^{\mu}a) & -Y_{\tau2}(\gamma_{\rho2}^{\mu}a) & 0 & 0 \\
\frac{-j\omega\mu_{z2}}{\gamma_{\rho2}^{\mu}}J'_{\tau2}(\gamma_{\rho2}^{\mu}a) & \frac{-j\omega\mu_{z2}}{\gamma_{\rho2}^{\mu}}Y'_{\tau2}(\gamma_{\rho2}^{\mu}a) & 0 & 0 \\
\frac{\gamma n\epsilon_{z2}}{\epsilon_{\rho2}{\gamma_{\rho2}^{\epsilon}}^2 a}J_{\tau2}(\gamma_{\rho2}^{\mu}a) & \frac{\gamma n\epsilon_{z2}}{\epsilon_{\rho2}{\gamma_{\rho2}^{\epsilon}}^2 a}Y_{\tau2}(\gamma_{\rho2}^{\mu}a) & 0 & 0 \\
\frac{j\omega\mu_{z2}}{\gamma_{\rho2}^{\mu}}J'_{\tau2}(\gamma_{\rho2}^{\mu}b) & \frac{j\omega\mu_{z2}}{\gamma_{\rho2}^{\mu}}Y'_{\tau2}(\gamma_{\rho2}^{\mu}b) & \frac{-\gamma n\mu_{z3}}{\mu_{\rho3}{\gamma_{\rho3}^{\mu}}^2 b}H_{\nu3}^{(2)}(\gamma_{\rho3}^{\epsilon}b) & \frac{-j\omega\mu_{z3}}{\gamma_{\rho3}^{\mu}}H_{\tau3}^{(2)\prime}(\gamma_{\rho3}^{\mu}b) \\
\frac{-\gamma n\epsilon_{z2}}{\epsilon_{\rho2}{\gamma_{\rho2}^{\epsilon}}^2 b}J_{\tau2}(\gamma_{\rho2}^{\mu}b) & \frac{-\gamma n\epsilon_{z2}}{\epsilon_{\rho2}{\gamma_{\rho2}^{\epsilon}}^2 b}Y_{\tau2}(\gamma_{\rho2}^{\mu}b) & \frac{j\omega\epsilon_{z3}}{\gamma_{\rho3}^{\epsilon}}H_{\nu3}^{(2)\prime}(\gamma_{\rho3}^{\epsilon}b) & \frac{\gamma n\epsilon_{z3}}{\epsilon_{\rho3}{\gamma_{\rho3}^{\epsilon}}^2 b}H_{\tau3}^{(2)}(\gamma_{\rho3}^{\mu}b) \\
0 & 0 & -H_{\nu3}^{(2)}(\gamma_{\rho3}^{\epsilon}b) & 0 \\
J_{\tau2}(\gamma_{\rho2}^{\mu}b) & Y_{\tau2}(\gamma_{\rho2}^{\mu}b) & 0 & -H_{\tau3}^{(2)}(\gamma_{\rho3}^{\mu}b)
\end{bmatrix}
\begin{bmatrix} C_1 \\ C_3 \\ C'_1 \\ C'_2 \\ C'_3 \\ C'_4 \\ C''_1 \\ C''_3 \end{bmatrix} = [0]. \tag{3.28}$$

With an assumption on the eigenvalue (the propagation constant γ), the above system of equations can be solved for frequency to plot the dispersion of the waveguide. We created a root-finding algorithm implementing Muller's method in Python to find the dispersion of the waveguide, where the determinant of the matrix is 0.

We must now narrow the scope of the problem to the case under study. Assume all regions are non-magnetic ($\bar{\bar{\mu}}_1 = \bar{\bar{\mu}}_2 = \bar{\bar{\mu}}_3 = \mu_0 I$, where I is the identity tensor), that the central region is vacuum ($\bar{\bar{\epsilon}}_1 = \epsilon_0 I$), and that the outer region (region 3) is gold (using the same Drude model for the permittivity of gold as before). Next, allow $\epsilon_{z2} = \epsilon_0$, let $\epsilon_{\rho2}$ and $\epsilon_{\phi2}$ vary and generally be different, and let $b = 120$ nm. Finally, assume $\gamma \approx 0$ to extract only the waveguide mode cutoff frequencies, or equivalently, the aperture resonance frequencies, where the approximation is used to avoid divide-by-zero errors. Notice that using an anisotropic permittivity leads to Bessel functions of complex order, which cannot be evaluated in MATLAB. Numerical approximation based on the gamma function leads to significant errors; however, the mpmath Python library can accurately evaluate Bessel and Neumann functions of complex order to arbitrary precision.

For $\epsilon_{\rho 2} = \epsilon_{\phi 2} = 1$, the solutions are independent of a, where $0 < a < b$, and we reproduce the unlined waveguide case while allowing the electric field to penetrate into the outer region. The fundamental TE_{11} mode cutoff frequency is reduced from 732 THz (for the case of no field penetration) to 521 THz. For a PEC waveguide to resonate at 521 THz, a radius of $b = 170$ nm would be required, which we call the effective radius. As the waveguide radius b is increased, the dispersion of the gold region causes the gap between the radius and effective radius to shrink. For our designed modal cutoff frequency of 193 THz, the effective radius is $b = 455$ nm, while the radius including field penetration is $b = 422$ nm.

Applying an ENNZ liner continues to reduce the cutoff frequency of the waveguide, and hence the miniaturization of the equivalent aperture. For the thin-liner case where $b = 120$ nm and $a = 100$ nm, the resonance frequency of 270 THz seen in simulation can be matched with a liner effective permittivity of $\epsilon_{\rho 2} = \epsilon_{\phi 2} = -0.24$. For the wagon-wheel case, assuming a uniaxial liner permittivity, the resonance frequency can be matched for an effective permittivity of $\epsilon_{\rho 2} = \epsilon_{\phi 2} = -0.986$, and the resonance frequency becomes extremely sensitive to the liner effective permittivity.

We now use the model to study the effects of a fully anisotropic liner permittivity on the HE_{11} resonance frequency, since the field profile of the wagon-wheel aperture contains azimuthal components within the liner. To separate the effects of the gold region's dispersion from the effects of anisotropy, we replace the gold region with a PEC, with the understanding that the field penetration simply increases the effective radius of the aperture and relaxes the condition that fields be entirely radial on $\rho = b$. For an aperture with $b = 140$ nm and $a = 120$ nm (*i.e.*, a thin-liner case), the frequency of the HE_{11} resonance is plotted with respect to the anisotropic ϕ and ρ liner permittivity components in Fig. 3.10a. Clearly, for a thin liner, the ϕ component has very little effect on the frequency-reduced HE_{11} modal cutoff frequency, which validates the isotropic model used by Pollock *et al.* [116].

If the inner radius is reduced to $a = 14$ nm, as plotted in Fig. 3.10b, the contribution from ϵ_ϕ is as important as the ϵ_ρ component given the higher

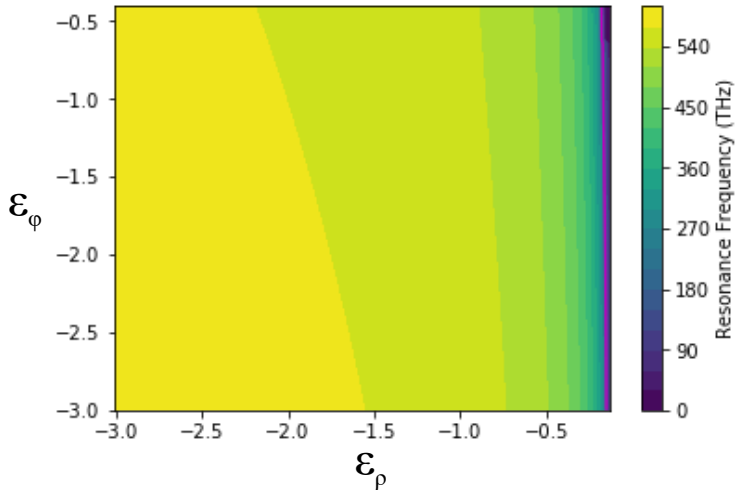

(a)

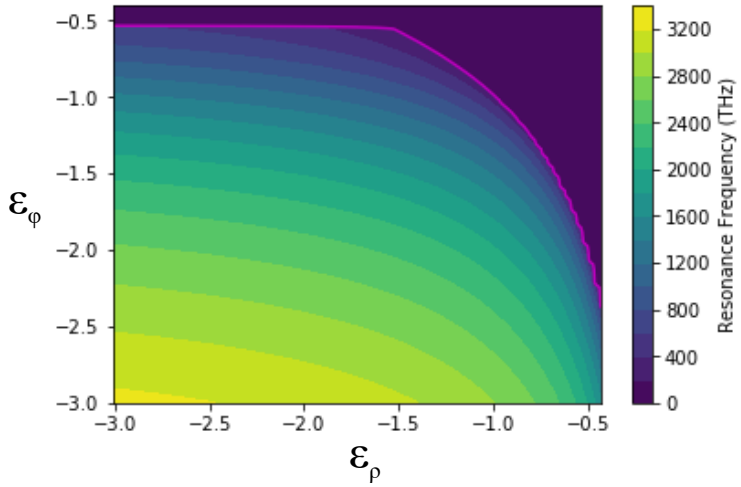

(b)

Figure 3.10: Surface plot of HE_{11} cutoff frequency with respect to anisotropic liner permittivity parameters for (a) a thin liner ($b = 140$ nm, $a = 120$ nm), and (b) a thick liner ($b = 140$ nm, $a = 14$ nm). The magenta line denotes 193 THz, or 1.55 µm, the wavelength of optical telecommunications. Reproduced from [155], CC BY 4.0.

filling factor of the aperture. As the permittivity falls to zero, the resonance frequency is reduced to DC, as was observed for the MTM-lined PEC waveguide. Frequency-reduced resonance occurs for either ϵ_ρ or ϵ_ϕ, whereas the isotropic case required only ϵ_ρ to be near zero. With fields penetrating into the PEC region, the liner thickness threshold at which anisotropy must be invoked is decreased, and even for a liner as thin as $b - a = 140 - 120 = 20$ nm, anisotropy significantly shifts the modal cutoff frequencies. The isotropic case is restored for a 10-nm-thick liner.

A slice taken from the lower left to the top right of Fig. 3.10b extracts the response for an isotropic liner permittivity. It can be seen that for a thick, isotropic liner, the resonance frequency saturates at 0 for a much higher absolute value of permittivity (*i.e.*, near $(-1, -1)$) than for either anisotropic parameter. The liner is therefore more sensitive to very small changes in effective permittivity.

Unfortunately, the results of this analysis cannot be intuitively applied to the wagon-wheel aperture since the resonant frequency cannot be uniquely mapped to an anisotropic effective permittivity value. Moreover, model for the wagon-wheel MTM-lined aperture should incorporate radial inhomogeneity, as the filling fraction of metal decreases significantly from the centre towards the edges.

3.1.6 Wagon-wheel Liner Equivalent Circuit

To apply the above results directly to the wagon-wheel MTS and predict its resonance frequency over a range of geometries, we must homogenize the liner region to an equivalent effective permittivity. Unfortunately, the ENNZ-liner circuit model developed by Baladi *et al.* to assist in designing miniaturized apertures for the microwave domain cannot be applied to the thick-liner wagon-wheel aperture as the liner cannot be accurately described as a coplanar stripline, and hence the TL-MTM theory cannot readily homogenize its effective material properties. Moreover, the analytical derivation for a homogenized liner presented above predicts only the resonance frequencies of the lined aperture, and the complex mode-matching problem required to predict

the full spectrum of the aperture has yet to be solved. Even with a solution to the mode-matching problem, the homogenized thick-liner derivation does not predict a resonance to describe the notch at 150 THz in Fig. 3.4.

Instead, we appeal to the concept of optical nanocircuits to derive a phenomenological equivalent-circuit that is able to model the behaviour of the wagon-wheel MTM-lined aperture near its fundamental resonance frequency [156]–[158]. In essence, optical nanocircuits emphasize the use of the full Drude model in deriving equivalent circuit impedances for metals, which includes the effects of both conduction currents and displacement currents. As a result, one finds that even without contributions from the magnetic fields, an inductance arises due to the momentum of the electron gas, called kinetic inductance. The analysis of dielectric elements and capacitive gaps does not change. Overall, this means metallic traces have additional intrinsic inductance at optical frequencies that often dominates over the Faraday (magnetic) inductance.

Although optical nanocircuit concepts have been used to describe a variety of nanostructures, they have rarely been used to describe MTSs, and in particular, aperture-based MTSs [159]–[161]. In fact, the majority of circuit models used to represent optical MTSs are fit entirely numerically, and rarely consider the actual geometry of the structure they model [162]. Our analysis draws on the well-known analogy between a plane wave meeting a periodic screen of scatterers and a guided wave meeting a diaphragm in a waveguide, and we derive approximate equivalent optical impedances for every element with full consideration of the displacement current [163], [164].

Intuitively, Fig. 3.11a shows how metallic regions are replaced by their equivalent kinetic inductance and resistance, whereas the gaps are replaced by equivalent capacitors. Considering the complicated layout, this phenomenological approach to building the circuit model allows significant intuition to be gained into how a number of parameter variations affect the aperture's scattering spectrum. A full description of the circuit model development and initial parameters is available in Appendix B. Initial parameters are derived using reasonable approximations, with the expectation that a good effective circuit model can be tuned numerically to describe the aperture over a range of

similar geometrical parameter values. As a result, this method is very general and can be applied to model almost any MTS layout.

The full final circuit model is shown in Fig. 3.11b. We invoke four-fold symmetry to describe just one-quarter of the aperture, where the horizontal symmetry doubles all element impedances and the vertical symmetry halves them. Elements on the vertical and horizontal symmetry planes (marked by the red dashed lines in Fig. 3.11a) are doubled or shorted out, respectively. With reference to Fig. 3.11b, we built the circuit model from three main elements coupled together: (i) the unlined aperture impedance, Z_a, (ii) the vertical nanowire on the symmetry plane acting as a resonant plasmonic monopole with impedance $2Z_w$, and (iii) a resonant loop with current i_3. The vertical nanowire is responsible for the main resonance, whereas the loop is responsible for the notch resonance. We now describe each element in more detail, from left to right.

The current source $j\omega D$ represents the uniform excitation across the unit cell, and in practice, is connected between the planes of symmetry. Since the unit cell is deeply subwavelength, all elements can be described as lumped equivalents, and a quasi-static regime can be assumed. For a resonant plasmonic circuit, however, this assumption is flawed as a resonant sinusoidal field/current distribution can exist on a miniaturized scale. We assume that this approximation can be corrected with numerical tuning as we cannot accurately describe the evolution of the current distribution with frequency.

In accordance with Fano theory, a Fano lineshape is the result of a coupling between some background continuum and a resonance [165]. In the case of the MTM-lined aperture, it is clear that the lineshape follows that of an unlined aperture away from resonance, so this background transmission should be modelled in the equivalent circuit. The impedance Z_a represents the impedance of the fundamental TE_{11} resonance of the unlined aperture below its cutoff frequency. Although this impedance is difficult to derive analytically, a good approximation is to assume a uniform current distribution on the metal surface and to find the impedance of that section from the self-reaction [164]. To this end, we assume that any current travelling near the aperture will interact

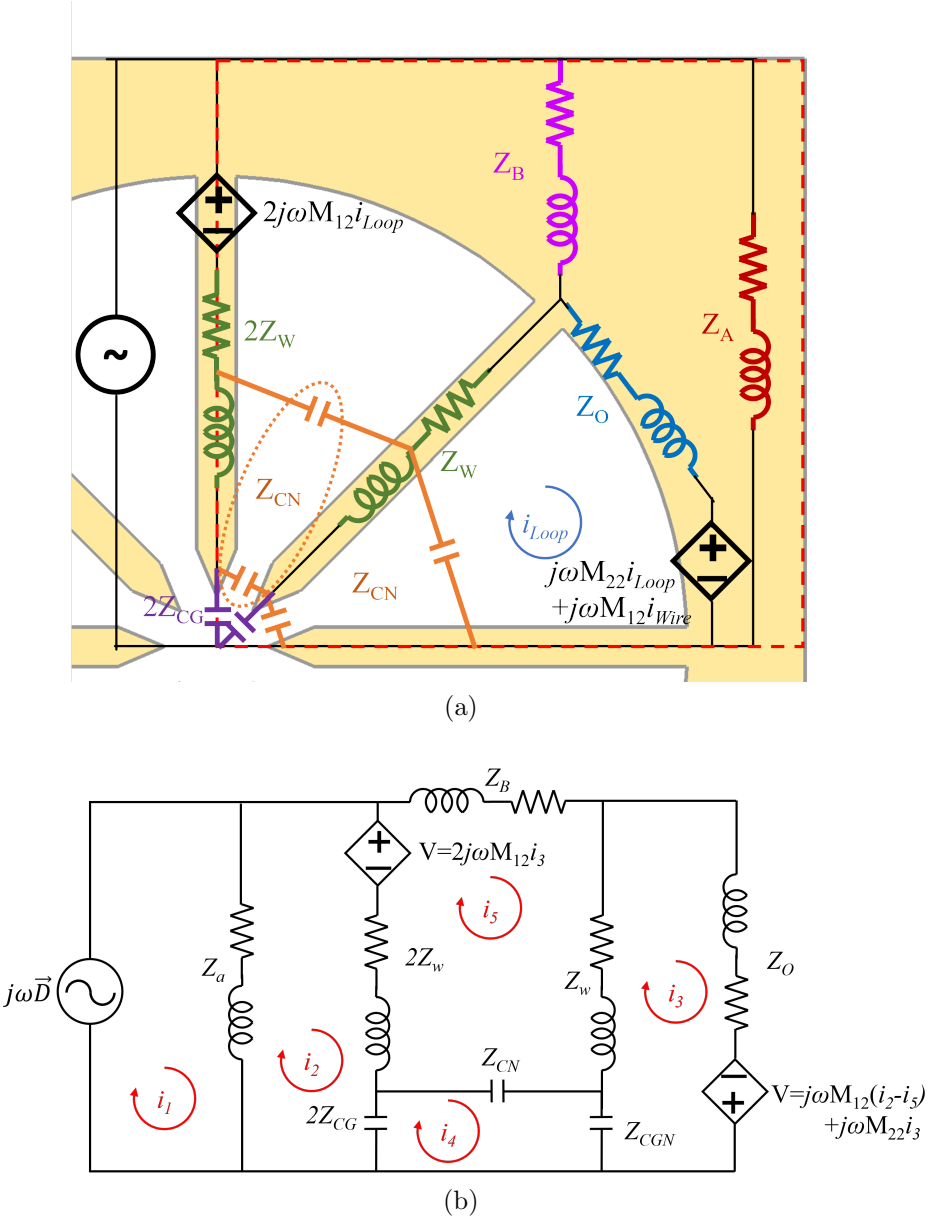

Figure 3.11: (a) Schematic showing the intuitive description of each part of the MTM-lined aperture as an equivalent lumped circuit element, and (b) the equivalent circuit model.

with the liner loading and that Z_a can be approximated by uniform currents travelling vertically between the symmetry planes over a width of half the unit cell period minus the radius, $p/2 - b$, and penetrating infinitely into the film (which is 50 nm or approximately two skin depths thick):

$$Z_a = \frac{p/2}{p/2 - b}\sqrt{\frac{\mu_0}{\epsilon(\omega)}}. \tag{3.29}$$

Along with the Drude model for $\epsilon(\omega)$, this equation effectively describes an inductor in series with a resistor.

Next, consider the nanowire impedance $2Z_w$. Since the width of the nanowire is much smaller than the skin depth, we assume that the fields are uniformly distributed throughout the nanowire cross-section. If the cross-sectional area of the nanowire is $A = tw$, and we ignore the pointed shape of the wire tips:

$$Z_w = \frac{l}{tw}\frac{1}{j\omega\epsilon(\omega)}, \tag{3.30}$$

where $l = b - g/[2\sin(\pi/N)]$ is the nanowire length to the tip. This is effectively the formula for the resistance of a rectangular wire, where the conductivity is described by the Drude model to create a complex impedance.

The first current-dependent voltage source represents the magnetic coupling between the vertical nanowire and the resonant loop, and M_{12} is derived from the Biot-Savart law and the quasi-static assumption of a triangular current distribution across the nanowire length.

The final element along i_2 is the capacitive impedance to ground at the tip of the nanowire. The Z_{CG} impedance is intended to represent the total combined charges induced on all the closely-spaced central nanowires except the nearest neighbours, which are represented by Z_{CN}. The complex geometry and the passage over the symmetry boundary make this capacitance impossible to separate analytically, hence we assume it is on the same order as Z_{CN}, for which we can make a more reasonable calculation. Z_{CN} represents the capacitance between each nanowire and its nearest neighbour, calculated by adding together the capacitance between the two wire tips and a radial capac-

itor extending from the end of the gap to the outer radius (see Appendix B):

$$C_N = \frac{\epsilon_0 t w}{2g\sin(\pi/N)} + \frac{N}{2\pi} t\epsilon_0 \ln\left(\frac{b - w/[2\sin(\pi/N)]}{g/[2\tan(\pi/N)]}\right). \tag{3.31}$$

Z_B represents the portion of the gold film that the currents feeding the oblique 45° nanowire travel through. Once again, this impedance cannot be directly separated from the other film impedances and we resort to an approximation based on the following assumed important parameters: (i) Z_B should grow with p as the length of the feeding region becomes longer, (ii) Z_B should scale inversely with b since the width of the feeding region decreases with b, and (iii) the frequency dispersion should follow the form of Z_a. This implies:

$$Z_B = \frac{p/2 - b/\sqrt{2}}{(b/2)} \sqrt{\frac{\mu_0}{\epsilon(\omega)}} \tag{3.32}$$

is a reasonable approximation.

Finally, the loop i_3 represents the interfering loop resonator that is seen just below the designed 193 THz resonance in the MTM-lined aperture. It consists of Z_w, Z_O, Z_{CGN}, and a mutual coupling term. Z_w is the same as in eq. (3.30), Z_O represents the impedance seen by a current travelling along the outside edge of the aperture, and Z_{CGN} is the parallel combination of Z_{CG} and Z_{CN}. The mutual coupling term represents both the magnetic coupling between the loop and its neighbour across the horizontal plane of symmetry, and the coupling between the monopole and the loop. For Z_O, we assume the exciting field is uniform along the thickness (z-direction), penetrates infinitely into the film in-plane, and that the length can be approximated as straight:

$$Z_O = \frac{2\pi b}{Nt} \sqrt{\frac{\mu_0}{\epsilon(\omega)}}. \tag{3.33}$$

The nearest-neighbour magnetic flux linkage M_{22} is derived from a COMSOL simulation of a single loop, fed by a 1 A current source at 193 THz. The magnetic flux is then integrated over the area that would hold the neighbouring loop.

With a full equivalent circuit for the aperture array, this circuit can be

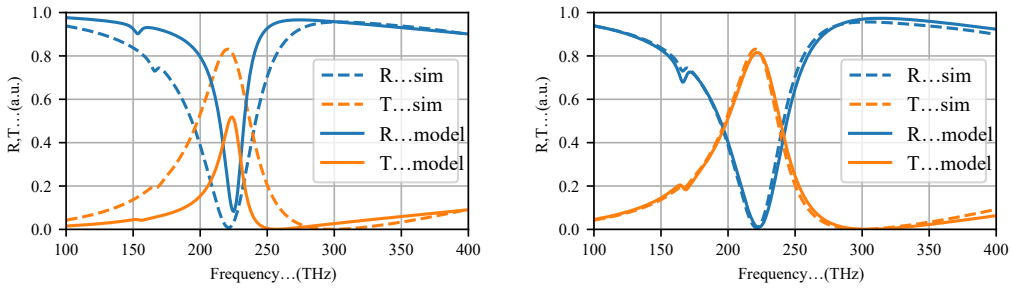

(a) (b)

Figure 3.12: Comparison of the reflection and transmission spectra of the circuit model to COMSOL simulations for (a) the nominal predicted circuit model, and (b) the tuned circuit model. For the simulations, the substrate was removed, the MTS was excited with a vertically polarized plane wave, and the nominal parameters were $b = 120$ nm, $p = 300$ nm, $t = 50$ nm, $w = g = 10$ nm, and $N = 8$.

inserted in shunt into a square parallel-plate waveguide with characteristic impedance $Z_0 = \sqrt{\mu_0/\epsilon_0}$. The transmission and reflection then take the form:

$$R = \left(\frac{-Z_0}{2Z_{MTS} + Z_0} \right)^2, \tag{3.34}$$

$$T = \left(\frac{2Z_{MTS}}{2Z_{MTS} + Z_0} \right)^2, \tag{3.35}$$

where Z_{MTS} is the total circuit model impedance as seen by the source.

The results for the nominal case are shown in Fig. 3.12a. Despite the number of approximations made, the resonance frequencies are well-predicted by the circuit model, though the overall transmission at resonance is significantly lower than in simulation. Analysis of the circuit shows that this is due to the current being higher in the loop than in the nanowire, despite being away from resonance, suggesting the impedance of the loop is too low.

To optimize the circuit model, we applied a linear multiplier to each circuit parameter and used a numerical optimization algorithm to find the multipliers that give the lowest difference between the model and the simulation spectra. Simplicial homology global optimisation (SHGO) is a fast optimization algorithm readily available through the scipy Python library that is particularly

Parameter	Z_w	Z_O	Z_a	M_{12}	C_N	C_G	$2Z_w$	Z_B	M_{22}
Multiplier	0.59	2.69	1.38	1.27	1.16	0.87	0.94	0.55	1.00

Table 3.1: Parameter multipliers used to match the circuit model to the simulation. The parameters are nominally unity.

suitable for low-dimension optimizations such as this one [166]. SHGO can return several "good" solutions, and since our circuit model is not perfect, the "best" solution it finds often cannot describe a parametric sweep accurately. To resolve this issue, we insert additional simulation data for other radii b into the algorithm to converge on a single solution.

The tuned spectrum is shown in Fig. 3.12b, and the tuning parameters required to match the spectra are listed in Table 3.1. Overall, the tuning required by the circuit is small, and no tuning parameter changes the impedance by a full order of magnitude.

Scaling Z_w, Z_O

The combination of multipliers on Z_w and Z_O shifts the impedance of the loop from the left branch to the right branch, which follows the near quarter-wavelength current distribution around the loop and our prediction that Z_O would be underestimated. The significant increase in Z_O is due to improper modelling of the radial decay of the assumed excitation field and having ignored the potentially significant magnetic self-inductance generated in the loop. Considering that adding the self-inductance leads to far too many degrees of freedom, the effect of scaling Z_O instead is a small increase in loss.

Scaling Z_a

Z_a is increased due to the overlap between Z_O and Z_a causing a double-counting.

Scaling M_{12}

M_{12} and $2Z_w$ are related as Z_{M12} was derived using a triangular current distribution, and $2Z_w$ was derived using a uniform current distribution. In practice,

the current is closer to a sinusoidal distribution, requiring an increase in Z_{M12} and a decrease in $2Z_w$.

Scaling C_N, C_G

C_N should be increased due to fringing fields, whereas the estimation of C_G, despite being on the correct order of magnitude, was too high.

Scaling Z_B

The multiplier on Z_B suggests that a denominator of b, rather than $b/2$, may better model the path feeding the diagonal wire.

Scaling M_{22}

Finally, scaling M_{22} makes little difference in the overall spectrum without changing its value by an order of magnitude or more. This is unsurprising as the value of M_{22} was taken directly from the numerical simulation. Since the rest of the multipliers were well within a factor of 10, the multiplier on M_{22} was left unchanged.

To further judge the effectiveness of the circuit model in describing the MTM-lined aperture, we compare the model to COMSOL simulation data as the parameters b, p, and w are swept. The results of this study are shown in Fig. 3.13 for reflectance, where the coloured curves represent COMSOL data for discrete parameter values, the grey mesh represents the circuit model with a continuous sweep of each parameter, and the black curves highlight where the circuit model has the same parameter value as the COMSOL curves for easier comparison.

Sweeping b

Fig. 3.13a shows the comparison for varied aperture radius b, where b was swept from 100–140 nm in increments of 10 nm. It is clear that the nanowire resonant frequency is well-predicted, and the full spectrum matches well as b is decreased. As b is increased, and the fill factor of the MTS grows, the approximations made to derive Z_a become increasingly problematic, leading

to a deviation of the spectrum at higher frequencies. Additionally, the small dip due to the loop resonance grows but does not match for larger b, which is likely due to not modelling the change in M_{22} as the loop area increases, the coupling of the loops from the neighbouring unit cell across the vertical axis of symmetry, and the assumptions on Z_O. A shift in b model enlarged or shrunk apertures due to over/undermilling with the HIM.

Sweeping p

The comparison for varied array pitch p is shown in Fig. 3.13b, where p was swept from 260–340 nm in increments of 20 nm. Outside of resonance, variations in p match similarly well to variations in b, and the loop resonance frequency is well-modelled. Nevertheless, there is a small overestimation of the nanowire resonant frequency shift with p, despite p not appearing in the nanowire impedance expressions. A small perturbation of each of Z_B or Z_a is unable to correct for this discrepancy, suggesting a competing variation of the resonance frequency is not modelled, or the discrepancy is due to a combined effect of Z_B and Z_a on the nanowire resonance. Given the result of the aperture radius sweep, the latter is more likely the case. The ion beam optics may drift between milled apertures, which can be modelled by a variation in p.

Sweeping w

Finally, the wire width w is varied from 5–15 nm in steps of 5 nm. Despite the significant implications of the wire width to the aperture geometry (in particular, the layout of the central region), the shift in the resonant frequency of the nanowire is well-modelled, as is the increased depth of the loop resonance. The small shift in both resonance frequencies is likely due to a shift in the resonant field distribution across each of Z_w and $2Z_w$ as the capacitive loading of the aperture centre decreases (smaller w) or increases (larger w). Smaller w models overmilling of the nanowires, whereas larger w models their undermilling.

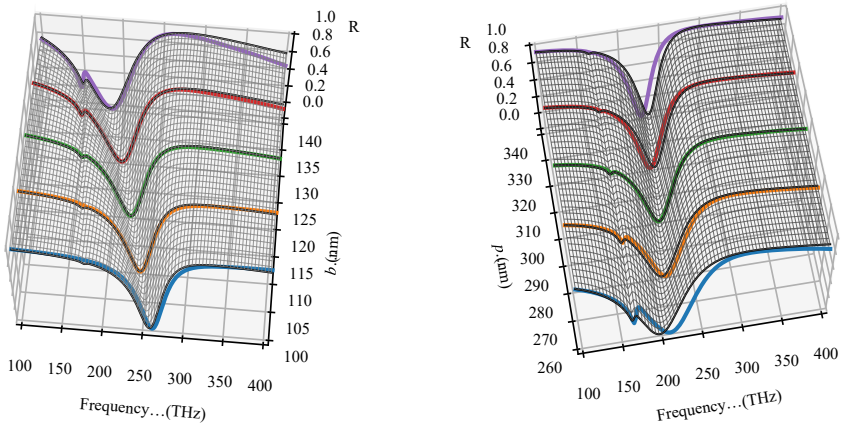

(a)

(b)

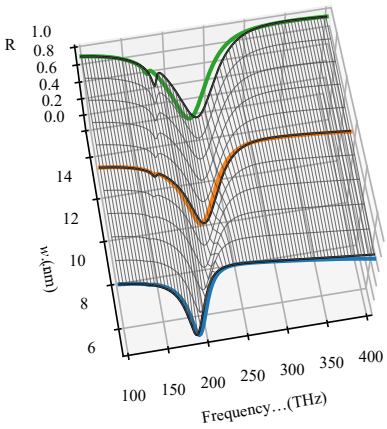

(c)

Figure 3.13: Comparison of the circuit model to COMSOL simulations for varied geometrical parameters. (a) $b = 100$–140 nm, (b) $p = 260$–340 nm, (c) $w = 5$–15 nm. The coloured curves represent the COMSOL simulation data, the grey mesh represents the circuit model data, and the black curves highlight the circuit model data where the circuit model can be compared directly to the COMSOL data.

Discussion

We have shown that our circuit model is able to accurately predict the transmission/reflection of MTM-lined apertures over a range of parameters and to well within the fabrication tolerances of the HIM. Moreover, a monopole coupled to a loop accurately describes the spectrum of the MTM-lined aperture with eight nanowires in the liner. This implies that with only four wires, the notch below the main aperture resonance should not exist, and this is indeed what was seen in Fig. 3.9 (with six wires the loop is excited symmetrically from the vertical nanowires, which suppresses its resonance). In fact, without the requirement of deeply subwavelength elements for MTM homogenization, a four-nanowire aperture performs better than the eight-wire aperture in terms of miniaturization and may be simpler to fabricate at the cost of additional losses.

Future directions for this model include modelling the thin plasmonic liner as T-shaped resonators and considering the film thickness more closely. The latter may require inspiration from the modal perspective, where the lossy propagation of the waveguide mode through the film can be modelled using a direct coupling coefficient between the top and bottom surfaces of the film [164]. Since our circuit model can predict both the scattering amplitude and phase, it is an excellent starting point for quickly developing and prototyping non-uniform arrays of apertures, as are required in many MTS applications. Modelling a nonuniform array would be as simple as widening the incident waveguide (using a geometric factor) and loading it with the model for two different apertures in parallel.

Throughout this section, we have shown that MTM-lined apertures can be scaled from the microwave domain to the NIR by modelling the plasmonic properties of the constituent metal at these frequencies. We modified the structure to include a thick liner in order to increase the miniaturization while enforcing an extremely small 10-nm minimum feature size and a 1:5 aspect ratio that is only achievable by HIM patterning. As we will show in the next chapter, the MTS spectrum relies strongly on the accurate reproduction

of these minute features. In order to design the MTM-lined apertures more quickly, we have suggested how an anisotropic homogenized liner model might be applied to produce the correct resonance frequencies, though such a model fails to account for all aspects of the resonant spectrum. Finally, we proposed an alternative perspective to describe the designed MTS that is based on coupled LSP resonators. Using this perspective, we derived an equivalent-circuit model using general simple techniques that accurately describes the MTM-lined aperture spectrum over a wide range of parameters.

3.2 Scaling MTM-lined Apertures to Visible Wavelengths

Throughout the previous section, we relied consistently on 10-nm features to create MTM-lined apertures that operate as strongly miniaturized resonators in the NIR regime. In this section, we aim to establish that consistent 10-nm features can improve the performance of miniaturized plasmonic resonator-based MTSs. With the operating principle understood to be based on coupled plasmonic resonators, we can make full use of the plasmonic effect to miniaturize the MTM-lined aperture further, improving the spatial resolution of field transformations and near-field imaging probes, and potentially increasing the near-field enhancement for particle trapping, surface-enhanced spectroscopy, and strong nonlinearities such as second and third harmonic generation. Moreover, we may shift the resonance frequency to the visible domain, where sensors can be made simpler through qualitative evaluation of the results, *i.e.*, by identifying the resonantly transmitted colour. We will see in the next chapter that increased miniaturization creates many new fabrication challenges to address.

To minimize the unit cell electrical size (p/λ_0, where p is the array period and λ_0 is the free-space wavelength), either the resonant frequency of the MTM-lined aperture must be minimized, or the pitch of the array must be reduced without a commensurate increase in the resonance frequency. In the parametric studies of the NIR MTM-lined aperture shown in Sec. 3.1.4, two major features decreased the unit cell electrical size: reducing the number of

wires and reducing the size of the aperture [92].

Decreasing the number of nanowires to decrease the electrical size is intuitive with the basic equivalent-circuit analogy, where the resonance is due to the nanowires modelled as inductors dominated by the kinetic inductance of the gold in series with the gap capacitance at the centre of the aperture. Reducing the number of wires inside the aperture decreases the number of inductors in parallel, increasing the overall inductance loading the aperture. Our circuit model in Sec. 3.1.6 showed that this interpretation is not strictly true, yet it gives an intuitive understanding of the loading. Similarly, the number of capacitors in series at the tips of the nanowires is reduced, increasing the effective capacitance of the aperture.

The same equivalent-circuit analogy can be applied to the change in aperture size. If we consider an aperture loaded with two nanowires, as the aperture shrinks, the overall capacitance decreases slowly and eventually saturates at the gap capacitance, while the inductance falls linearly. As a result, the resonance frequency $\omega = 1/\sqrt{LC}$ only increases at a rate of $\sim \sqrt{b}$, while the size decreases linearly with b, and the electrical size is decreased. When material dispersion is also introduced, the resonant frequency variation of an isolated gold nanoantenna is linear, but with a shallower slope than for a PEC [167]. Using the Drude dispersion model for the nanowire, the equivalent impedance of the nanowire diverges at the bulk plasma frequency of the metal, and hence the resonance frequency will always be below this value (though the actual frequency depends strongly on the nanoantenna geometry). Taking into account the fringing fields allows the derivation of the LSP capacitance and correctly predicts its resonance frequency [168].

Reducing the number of nanowires in the wagon-wheel aperture from 8 to 2 redshifts the resonance frequency from ∼200 THz to ∼150 THz. Although this frequency shift is only 25% and hence does not greatly reduce the electrical size, the effects of this shift on the aperture geometry are important. First, the symmetry of the aperture is reduced and the MTM-liner resonance becomes polarization-sensitive, allowing the design of different aperture responses for different polarizations, or polarization selectivity for applications such as ellip-

sometry and near-field sensing. Second, the central region of the liner can be made more compact. Enforcing the minimum feature size of 10 nm requires that the tip of each wire be $g = 10$ nm from its nearest neighbour, and under the constraint that the wire width $w = g$, the radius a of a circle enclosing the central region including the tapered nanowire tips and capacitive gaps can be calculated from the law of cosines:

$$a = \frac{g}{2\sqrt{1 - \cos(\pi/N)}}, \tag{3.36}$$

where N is the number of nanowires loading the aperture. For $N = 8$, this evaluates to a radius of 25.6 nm, whereas for $N = 2$, the central region is reduced to a radius of 5 nm, which allows the total aperture size to be reduced significantly. When designed to operate at a wavelength of 700 nm (near the edge of the visible regime) the aperture radius is 25 nm, where there is clearly insufficient space for 8 nanowires [169].

The nominal design and the transmittance/reflectance of the polarization-sensitive MTM-lined aperture, which we call the two-wire aperture, are shown in Fig. 3.14. The simulation was performed in Ansys Lumerical FDTD, where the $w = 10$ nm is the nanowire width and $g = 10$ nm is the minimum gap width based on fabrication constraints, and $b = 25$ nm is the aperture radius chosen to shift the resonance into the visible regime. The array pitch $p = 150$ nm is chosen for a small fill factor to potentially multiplex many apertures into one cell, and $t = 50$ nm is the film thickness chosen for opacity. The material model for gold is now a numerical fit to experimental data and the substrate was removed, while the nanowire tips are filleted to model the rounding that occurs in fabrication [170]. The designed LSP resonance is seen at 425 THz/700 nm when excited with a y-polarized incident plane wave, where there is a sharp decrease in reflection and a significant fraction of the incident power is absorbed by the MTS. For an x-polarized excitation, the plasmonic nanowires are not excited and the spectrum is that of an array of empty apertures, where the fundamental resonance frequency is well outside of the range of interest. We note that this result is similar to those seen in

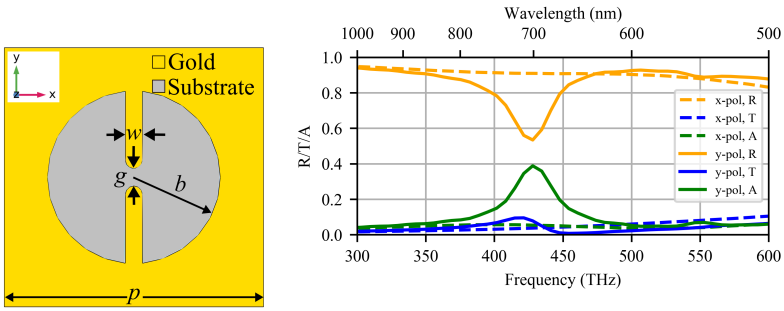

(a) (b)

Figure 3.14: (a) Optical two-wire MTM-lined aperture design for visible-frequency operation, and (b) the transmission, reflection and absorption spectra for a nominal design resonating at 425 THz/700 nm. Geometric parameters for this design are $w = g = 10$ nm, $b = 25$ nm, $p = 150$ nm, and the film thickness is $t = 50$ nm. Reproduced with permission from [169], ©2020 IEEE.

experiments on extraordinary transmission; however, the pitch of our array is much too small to excite propagating diffraction anomalies.

3.2.1 Two-wire Liner Equivalent Circuit Model

To guide our analysis of the two-wire MTM-lined aperture, we develop in detail an intuitive circuit model to conserve simulation time, using the same general procedure as in Sec. 3.1.6. The circuit model for the MTS, shown in Fig. 3.15, consists of a series-RLC resonator that represents the resonating nanowires in parallel with an RL branch that represents the subwavelength aperture and the surrounding gold screen. The nanowires are modelled by their kinetic inductance and ohmic resistance Z_w, which scales according to l/A, where l is the nanowire length and $A = tw$ is the nanowire cross-sectional area. Using the Drude model to absorb the conductivity into the permittivity model, and assuming a uniform field over the wire:

$$Z_w = \frac{b - g/2}{tw} \frac{1}{j\omega\epsilon(\omega)}. \tag{3.37}$$

The capacitor models the gap at the centre of the aperture as a uniform capacitor, plus the induced charges along the length of the nanowires modelled as a radial capacitor, augmented by an arbitrary factor to account for fringing

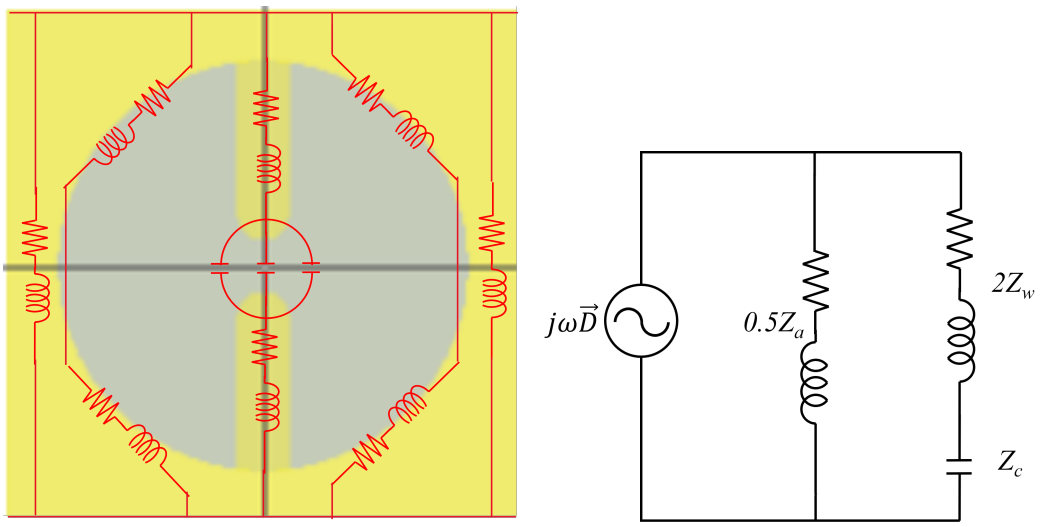

Figure 3.15: Circuit model describing the two-wire MTM-lined aperture. (a) Schematic overlay showing the physical source of each circuit element, and (b) the reduced circuit model derived to describe the MTS unit cell.

fields (starting value arbitrarily chosen to be 1.75):

$$C = 1.75\left(\frac{\epsilon_0 t w}{g} + 2t\epsilon_0\frac{\ln(b/(0.5g))}{\pi}\right). \tag{3.38}$$

Thus the intuitive explanation of the capacitor behaviour with b described above holds. The capacitor impedance $Z_c = 1/j\omega C$ decreases significantly as the nanogap width g is reduced and increases slowly as the aperture radius b is reduced, eventually saturating as the nanogap capacitance (which is unchanging) begins to dominate. Charges induced on the outside edge of the aperture create the fundamental TE_{11} resonant aperture electric-field profile, and if included, should be modelled as a part of the parallel subwavelength aperture impedance.

For the two-wire liner case, we take a slightly different approach to calculating Z_a as there are fewer interfering elements. The subwavelength aperture impedance Z_a effectively describes the fill factor of the unit cell (aperture area over unit cell area $F = \pi b^2/p^2$), where the kinetic inductance increases with the fill factor since the conduction currents are confined to a smaller area. More specifically, assuming t is larger than the skin depth and using one half the unit cell due to symmetry, we model Z_a as the parallel combination of the

current path around half the aperture perimeter (assumed straight) and half the uninterrupted solid path between the symmetry planes on either side of the aperture:

$$Z_a = \left(\left(\frac{\pi b}{t} \sqrt{\frac{\mu_0}{\epsilon(\omega)}} \right)^{-1} + \left(\frac{p}{0.5p - b} \sqrt{\frac{\mu_0}{\epsilon(\omega)}} \right)^{-1} \right)^{-1}, \tag{3.39}$$

with the total subwavelength aperture impedance being half the above. This model is a crude approximation that entirely ignores the field distribution within the nonresonant aperture, but provides sufficient accuracy when the aperture impedance is low and the kinetic inductance dominates, as is the case for plasmonic structures in the visible regime. A more accurate model could be derived from a variational solution with an assumed TE_{11} field profile within the aperture and uniform, plane-wave-like fields inside the gold [164].

As before, to model the scattering parameters of the MTS, this circuit can be inserted in shunt into a square parallel-plate waveguide with characteristic impedance $Z_0 = \sqrt{\mu_0/\epsilon_0}$. The shunt loading impedance Z_{MTS} is the total MTS circuit model impedance for the y-polarized case, and just Z_a for the x-polarized case. The calculated nominal spectra are shown in Fig. 3.16a, compared to a full-wave simulation in Lumerical FDTD for a nominal two-wire MTM-lined aperture with rounded wire tips, $b = 50$ nm, $p = 150$ nm, and $w = g = 10$ nm. This aperture is used as a second case to validate our circuit model as smaller apertures are more difficult to model due to the increased contributions from the solid film. The resonance frequency is well-predicted, as is the resonant magnitude. The subwavelength aperture impedance is somewhat lower than necessary, leading to a larger mismatch and hence higher x-polarized reflection in the solid red curve. Fig. 3.16b shows the calculated spectrum for the smaller MTM-lined aperture discussed above, with radius $b = 25$ nm and all other parameters the same as before. We see that once again, the resonance frequency is well-predicted; however, it is now the resonant (y-polarized) spectrum that matches less well in overall magnitude.

We now optimize the above results by adding constant, linear multipliers to each of the three impedance parameters. These multipliers do not

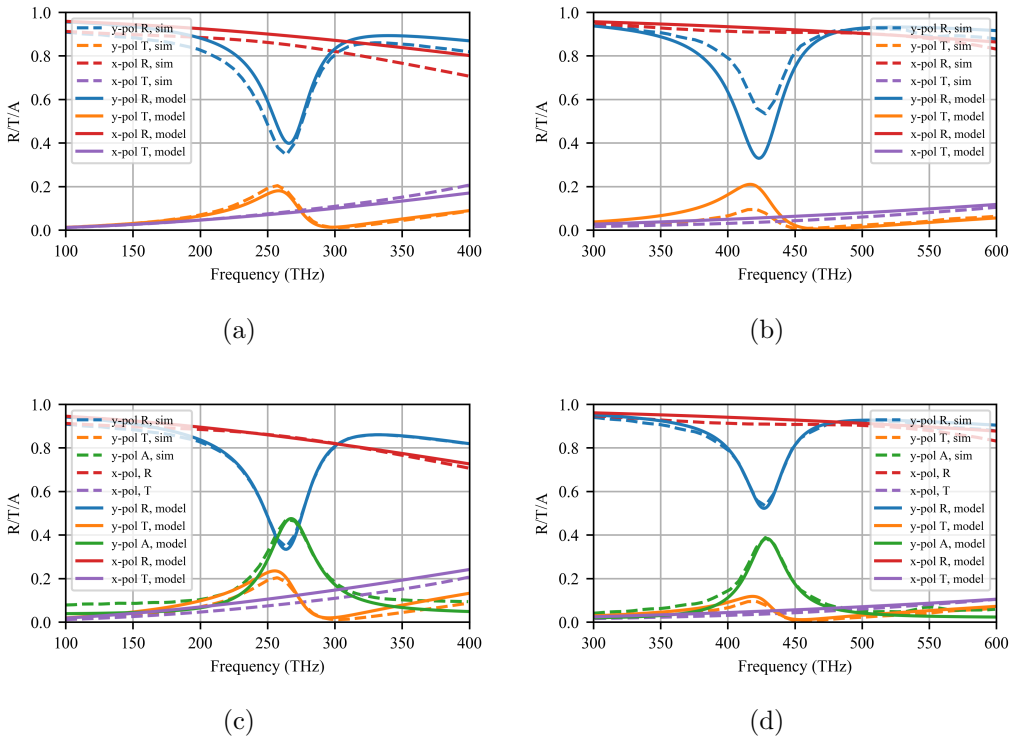

Figure 3.16: Comparison of reflection and transmission spectra from Lumerical FDTD simulations (dashed) and the MTM-lined aperture circuit model (solid), (a) for $b = 50$ nm, $p = 150$ nm, $t = 50$ nm, $w = g = 10$ nm and analytically derived circuit component values, (b) for $b = 25$ nm and analytically derived component values, (c) optimized circuit model for $b = 50$ nm and the circuit components scaled by $[1.22Z_c, 1.24Z_w, 1.25Z_a]$, and (d) optimized circuit model for $b = 25$ nm and the circuit components scaled by $[1.75Z_c, 1.90Z_w, 0.94Z_a]$. Simulation data taken from [169].

change the dispersion of the elements but allow the relative tuning of each element's value to better match the simulated spectrum. Fig. 3.16c shows the results of the tuned $b = 50$ nm circuit model, where the multipliers are $[1.22Z_c, 1.24Z_w, 1.25Z_a]$.

Case 1: $b = 50$ nm, tuning Z_a

Intuitively, this result suggests that the subwavelength aperture impedance Z_a has been underestimated, likely due to double-counting the smallest edge between apertures and the crude approximation of the first term in eq. (3.39).

Case 1: $b = 50$ nm, tuning Z_w

An increased nanowire impedance Z_w is due to only modelling the nanowire from the edge of the aperture, and neglecting the current path from the symmetry plane to the nanowire and any magnetic self-inductance. It should be noted that we have not modelled the resonant current distribution along the nanowire, which reduces the contribution of the nanowire to Z_w by a factor of up to 0.5.

Case 1: $b = 50$ nm, tuning Z_c

Finally, the overestimation of the capacitance is due to the arbitrary choice of the fringing capacitance multiplier. The multipliers on Z_c and Z_w must be similar to keep the resonance frequency constant.

The tuned results for $b = 25$ nm are shown in Fig. 3.16d. We might expect that since the resonant magnitude was overestimated, rather than underestimated like in the previous case, the required multipliers would trend below 1. This is only true for Z_a, which matches better here than in the previous case. Z_a has a large effect on the resonant magnitude, and scaling it upward in the previous case significantly increased the coupling to the nanowire resonance, which was then tempered with Z_c and Z_w multipliers greater than one. This is again the case for $b = 25$ nm, where the multipliers are $[1.75Z_c, 1.90Z_w, 0.94Z_a]$.

Case 2: $b = 25$ nm, tuning Z_a

Z_a is now dominated by the second term in eq. (3.39), and hence the effect of the overlap is reduced.

Case 2: $b = 25$ nm, tuning Z_w

Z_w now represents approximately one-sixth of the MTS period, and hence requires a larger scaling factor to model the contribution of the current path from the symmetry plane. We note that the majority of the impedance produced by the current path to the symmetry plane is concentrated where the currents must converge to feed the nanowire, which makes this impedance value scale weakly with both b and p. If we include a resonant field profile multiplier of 0.8, a total multiplier of $1.9Z_w$ is predicted for both cases studied.

Case 2: $b = 25$ nm, tuning Z_c

Finally, the capacitance C is overestimated as the two terms in eq. (3.38) are comparable, and the first term is overestimated as it models flat capacitor plates, not the rounded ones found in the simulation. Again, the multipliers on Z_c and Z_w are similar, which leads to a small resonant frequency shift.

Absorption curves are also shown in the bottom half of Fig. 3.16, where it is clear that the absorption is not particularly well-modelled, even for the nonresonant apertures. Since our model does not include any parameters that decouple the real and reactive components of each circuit element, increasing the loss would necessarily shift the spectra. Moreover, the poor matching of the red curves implies that the additional loss is also seen in the nonresonant spectra. Correcting this discrepancy would require adding a new parameter to the unlined aperture portion of the model to match the additional loss, such as including the coupling between apertures or Faraday inductance, which we leave for future work.

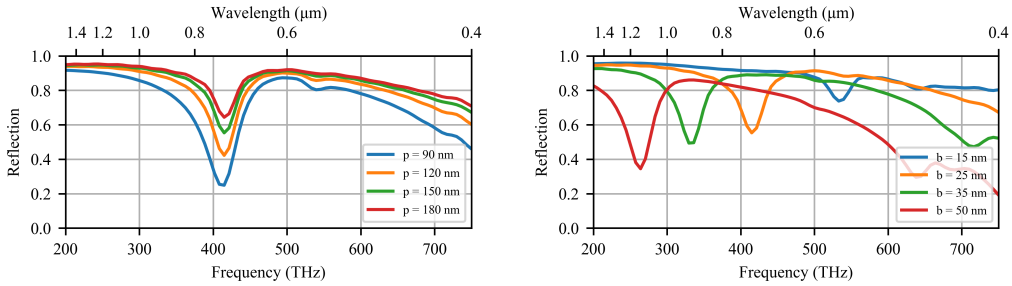

(a) (b)

Figure 3.17: Resonant (y-polarized incident wave) reflection spectra for two-wire MTM-lined aperture arrays with nominal feature sizes $b = 25$ nm, $p = 150$ nm, $w = g = 10$ nm, and $t = 50$ nm. (a) Parametric sweep of the periodicity p, and (b) parametric sweep of the aperture radius b.

3.2.2 Two-wire Parametric Studies

Let us now study the geometric parameters of the two-wire MTM-lined aperture to ensure the intuition extracted from the circuit model holds and establish the advantages of fine, 10-nm features. We begin with simple parametric studies linking back to the wagon-wheel MTM-lined aperture, then compare the performance to two conventional nanoantenna structures commonly used as MTS elements.

In a similar manner to the wagon-wheel MTM-lined aperture, the two-wire MTM-lined aperture has two primary geometric parameters that can be tuned to achieve the desired performance: the radius b and the array pitch p. The gap width g, the nanowire width w, and the film thickness t are instead a function of the fabrication method and fabrication quality. Fig. 3.17 shows the results of simulations performed in Lumerical FDTD to study the effect of each of these parameters on the resonant reflection spectra. We note that, due to the change in the simulated frequency range, Lumerical has modified the fitting parameters for the material model and the results may not agree exactly with those presented previously.

In comparison to the wagon-wheel aperture structure, Fig. 3.17a shows less variation of the resonance frequency as p is increased. This is due to the lower fill factors used in this sweep, which prevent the coupling of apertures to

their nearest neighbours. From the perspective of the circuit model developed above, the only factor that varies directly with p is the nonresonant aperture impedance, which increases with fill-factor, and in turn, increases the coupling to the plasmonic nanowire resonance. The small resonant frequency shift seen for the smallest periodicity studied ($p = 90$ nm) is likely due to inter-aperture magnetic coupling, which may be modelled in part by a small increase in the nanowire feed impedance. As the distance between apertures is diminished further, it may also be necessary to consider the capacitive coupling of the fringing fields at the gold film surface to accurately model the shift in resonance frequency.

The shift in resonant frequency with b, shown in Fig. 3.17b, is similar to what was seen for the wagon-wheel structure, where the resonant frequency varies less than linearly with b. Since a fit to real material parameters was used to model the gold, the $b = 15$ nm spectrum is an outlier that has been modified by non-Drude-like material dispersion (though the circuit model does predict its position accurately when the material model extracted from Lumerical is used). We have already shown that to accurately model a shift from $b = 50$ nm to $b = 25$ nm, the capacitor model should be modified to account for the rounding of the wire tips, and the nanowire model should be augmented by a nearly constant feed impedance. As the aperture grows, the logarithmic relation in eq. (3.38) controls the change in gap capacitance and the kinetic inductance increases linearly, which leads to a resonant frequency shift of the form $\omega_p \propto 1/\sqrt{b\ln(2b/g)}$. Without accounting for material dispersion, we substitute $b = 25$ nm, $\omega_{p1} = 410$ THz and $g = 10$ nm into this equation, then predict the resonant frequency for $b = 35$ nm to be 315 THz, and the resonant frequency for $b = 50$ nm to be 242 THz. Both of these predictions are quite close to their actual values calculated by full-wave simulation, which validates the intuition gained through the equivalent circuit model.

3.2.3 Comparison to Bowtie Nanoantennas

From another perspective, one could visualize the MTM-lined aperture as the limiting case of a bowtie-shaped aperture, where the bowtie has been flared

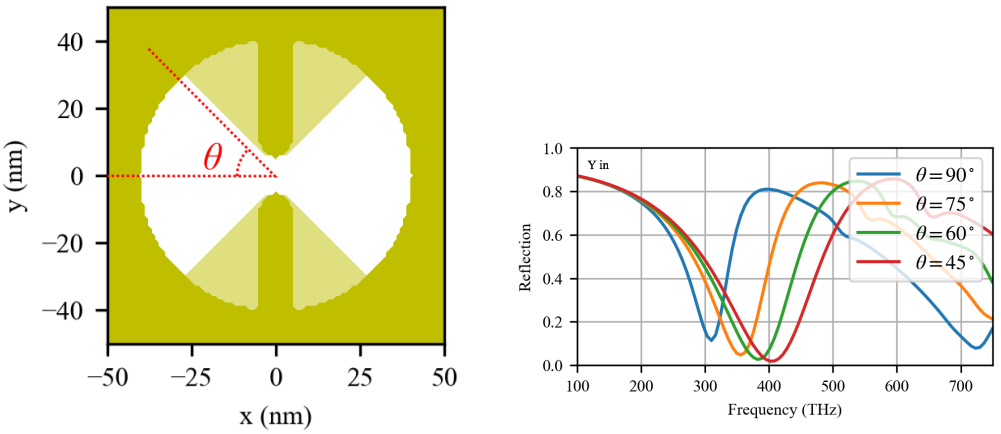

(a) (b)

Figure 3.18: (a) A schematic of the relation between a bowtie aperture ($\theta = 45°$) and a two-wire MTM-lined aperture ($\theta = 90°$). (b) Reflection spectra of the aperture shown in part (a), for various angles θ. The input is a y-polarized plane wave at normal incidence and $b = 40$ nm.

to full half-sectors. This concept is shown in Fig. 3.18a by overlaying the MTM-lined aperture with a conventional quarter-sector bowtie aperture. Due to symmetry, it is most convenient to describe the structure by the sector half-angle θ, as labelled in the figure, *i.e.*, $\theta = 90°$ for the two-wire MTM-lined aperture, and $\theta = 45°$ for the conventional bowtie aperture. Bowtie-shaped nanoapertures are commonly used as subwavelength elements to focus electric fields into a small volume at the centre of the aperture with large field enhancements. This technique finds use in applications such as subwavelength near-field microscopy [171], surface-enhanced Raman scattering, and fluorescence imaging [172]. The most important factor for these applications is the local field enhancement at the centre of the aperture as the signal strength is a function of powers of the local electric field strength, $|E|^x$. For subwavelength near-field microscopy, the miniaturization of the aperture is also important as it ultimately sets the limit on the achievable resolution of the near-field probe. Here, we look to establish that 10-nm features can improve miniaturization without a loss of field enhancement, which may improve near-field microscope resolution and the density of optical hotspots for sensing.

To compare the performance of the MTM-lined aperture MTS to that of a

bowtie nanoaperture antenna, we implemented the bowtie nanoaperture array shown in Fig. 3.18a in Ansys Lumerical FDTD and performed a sweep of the sector half-angle θ, with radius $b = 40$ nm, gap width $g = 10$ nm, minimum nanowire width $w = 10$ nm, and array pitch $p = 100$ nm. The 10-nm nanogap is present in all cases and the conductive tips are circularly rounded, hence all the studied structures would require fabrication by HIM. Nevertheless, the gap width is critical to the field enhancement, therefore, it should be held constant for a meaningful comparison.

The reflection spectra are shown in Fig. 3.18b for four θ angles, where it is clear that as the sector angle increases toward the MTM-lined aperture case, the resonance becomes redshifted. This implies a reduced electrical size as the aperture radius and unit cell period are constant, and hence better resolution when used as a near-field probe. From the equivalent-circuit perspective, a redshift is expected due to the kinetic inductance of Z_w scaling inversely with the cross-sectional area of the nanowires, which increases as θ decreases. Z_c decreases linearly with decreasing θ, which is slower than the change in Z_w. The resistance of the nanowires is also inversely proportional to the nanowire cross-sectional area, and a commensurate decrease in the transmission amplitude is observed (though not shown).

The electric-field profiles at resonance are shown in Fig. 3.19 for four sector angles θ. As the sector angle grows, the induced surface charge is pulled to the tips of the nanowires due to the lightning rod effect, causing an increase in the resonant local electric field magnitude at the centre of the aperture [173]. If we approximate the aperture nanowires as oblate spheroids with tip width w and length $b \sin\theta$, the MTM-lined aperture is expected to increase the field enhancement by a factor of 2 over the 45° bowtie case. Instead, an enhancement of only 20% is observed. Although our equivalent circuit does not model the field profile, the increased dissipation from the nanowire resistance is intuitively consistent with a damped field enhancement. Thus the improved field enhancement and miniaturization in the MTM-lined apertures are balanced by increased loss. Nevertheless, the MTM-lined aperture exhibits a 20% improvement in field enhancement over a comparable bowtie

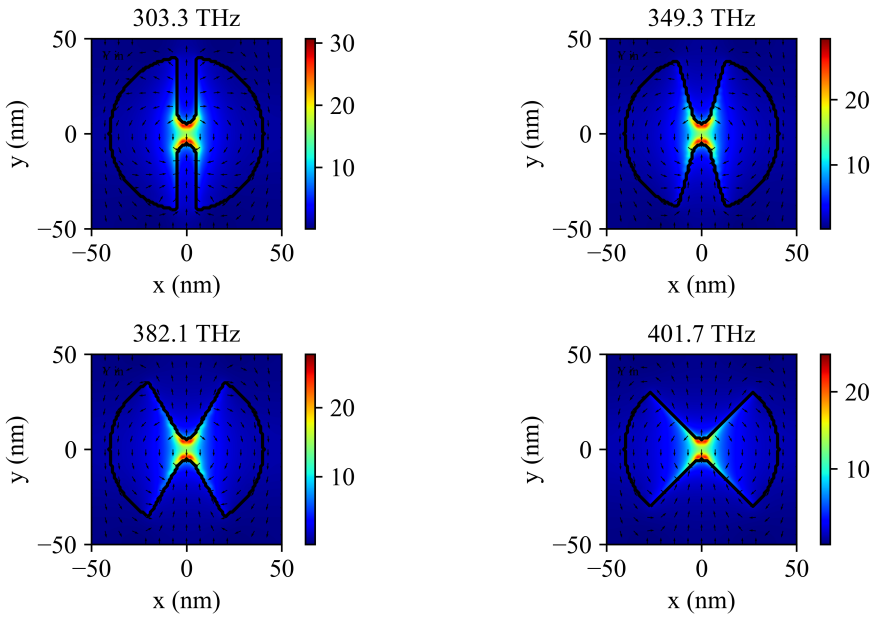

Figure 3.19: Electric-field profiles of the bowtie-shaped aperture arrays at resonance for a y-polarized, normally incident plane wave. The two-wire MTM-lined aperture is miniaturized by a factor of three quarters over the conventional bowtie antenna without a loss in field enhancement.

aperture, which implies 44% more signal in SEIRA applications, and twice the signal in SERS. The enhanced miniaturization can be used to pack apertures closer together for higher spatial resolution in near-field sensing and higher hotspot density in surface-enhanced sensing. The additional loss is undesirable in surface-enhanced fluorescence applications, where the active signal will be suppressed; however, in applications involving nonlinear processes, such as SERS, suppressing the scattering of the excitation is acceptable.

3.2.4 Comparison to V-shaped Nanoantennas

One of the first demonstrations of the generalized Snell's law, and indeed, one of the first demonstrations of MTS-based two-dimensional subwavelength optical field control, was the demonstration of anomalous refraction with V-shaped nanoantennas [106]. In this section, we show that two-wire MTM-lined apertures support equivalent resonances to V-shaped nanoantennas and can be designed for arbitrary scattered phase, but with improved miniaturiza-

tion/resolution.

The generalized Snell's law is created by augmenting Snell's law with a linearly varying scattered phase at the interface between two media that effectively allows the arbitrary redirection of the refracted wave, even when the two media are identical. This can be accomplished by discretizing the interface into subwavelength unit cells, then loading each cell with a resonator that scatters with a similar amplitude, but different phase than its neighbours. To create anomalous refraction, the scattered phase should vary linearly from 0 to 2π, and be extended periodically over the surface.

It is simple to prove that the limits on the co-polarized scattered phase shift for a single layer of nanoantennas are $-\pi/2 < \phi < \pi/2$ [174]. V-shaped nanoantennas circumvent this issue by scattering to the cross-polarization, where geometrical rotation of the nanoantenna by $\pi/2$ radians rotates the polarization by $\pi/2$ and introduces an additional geometric phase (also known as Pancharatnam-Berry phase) shift of $\pi/2$ in the scattered field [175]. Unfortunately, scattering to the cross-polarization also imposes a 25% limit on the scattering efficiency.

Pancharatnam-Berry phase is often understood to be an additional geometric phase accumulated during polarization transformations over a closed path on the Poincaré sphere. The total additional phase ϕ_G is equal to half the solid angle enclosed by the traced path [176]. Under this perspective, a single scattering MTS element is unable to draw a closed path, and hence geometric phase cannot be calculated. This is reconciled by comparing the path of two identical elements, one rotated with respect to the other by an angle ϕ. Each element draws an arc between the poles of the Poincaré sphere, and the arcs are separated azimuthally by the angle ϕ. This rotation on the Poincaré sphere is simple to understand using the Jones matrix formalism, where the principle axes of a scatterer are used to define the polarization basis [177]. The phase factor produced by the Jones formalism is 2ϕ, which is equal to the full solid angle between the arcs on the Poincaré sphere and is often interpreted as the geometric phase. The original definition by Berry of half the solid angle can be harmonized with the usual MTS definition by the understanding

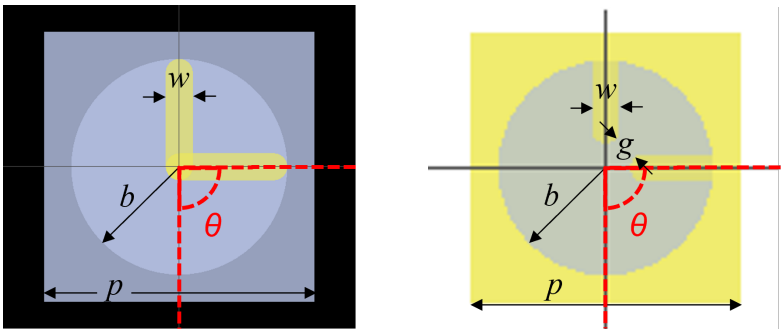

Figure 3.20: (a) V-shaped nanoaperture geometry, and (b) geometry of the asymmetric, two-wire MTM-lined nanoaperture.

from the previous paragraph, where half the geometric phase factor is due to Pancharatnam-Berry phase, and the other half is due directly to the rotation of the unit cell. Throughout this work, the full phase factor will be referred to as the geometric phase.

Consider the nominal V-shaped nanoantenna array shown in Fig. 3.20a with an arm length $b = 40$ nm, arm width $w = 10$ nm, thickness $t = 50$ nm, and period $p = 100$ nm. These dimensions are chosen for high packing density, which increases the maximum refraction angle of a phase-gradient MTS. The swept angle θ is the angle between the upper and lower halves of the antenna, as shown in Fig. 3.20a. To scatter to the cross-polarization, V-shaped nanoantennas make use of a pair of dipolar resonances supported by the structure, as shown in Fig. 3.21. The first resonance is the "antisymmetric" mode (Fig. 3.21a), which corresponds to a plasmonic bright mode and is excited by incident electric fields perpendicular to the antenna's axis of symmetry. For the case shown, the axis of symmetry is at 45° and the incident field is y-polarized, but the asymmetric resonance dominates. The second resonance is the "symmetric" mode (Fig. 3.21b), which corresponds to a plasmonic dark mode and is excited by incident electric fields parallel to the axis of symmetry. The total scattering amplitude and phase to the cross-polarization can then be tuned by changing the angle of the V-shape, the length of the antenna, and the polarization angle of the input wave.

Having previously modelled the nanowires loading the MTM-lined aperture

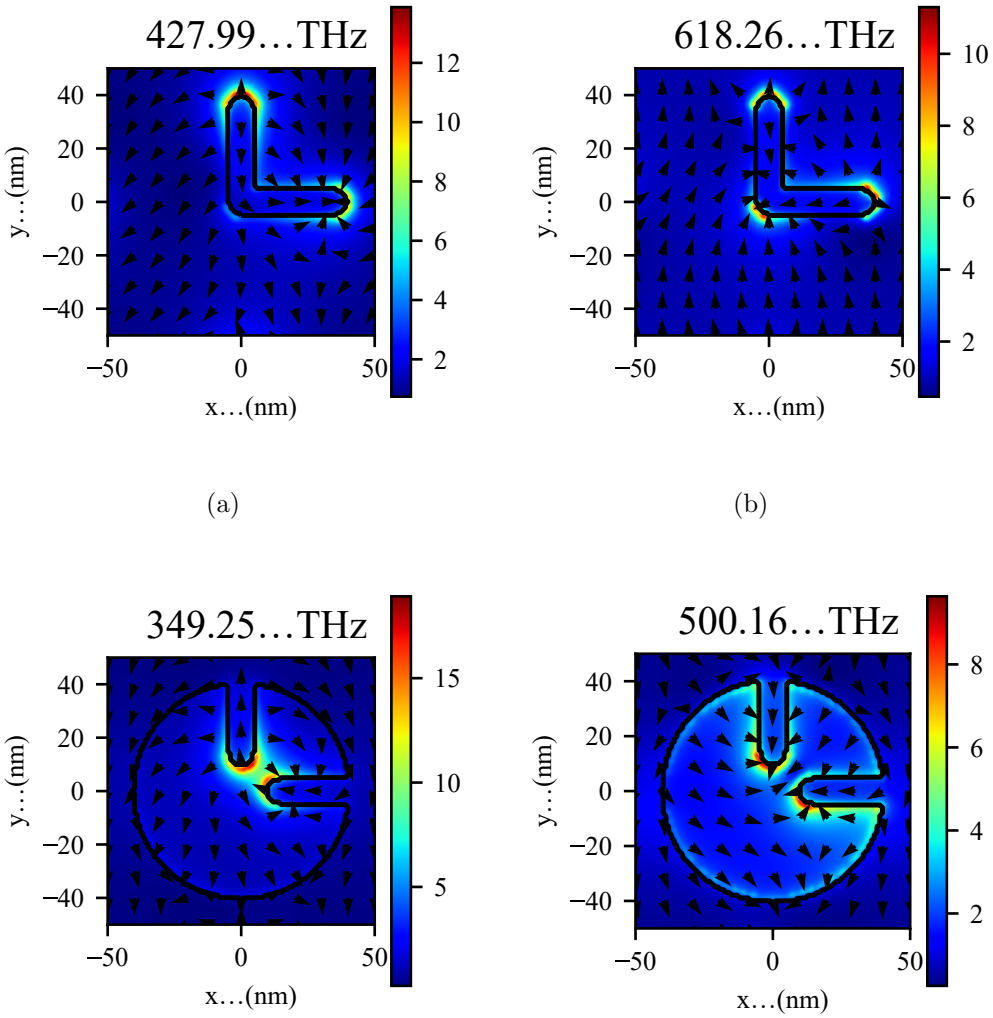

(a) (b)

(c) (d)

Figure 3.21: Electric-field profiles of a representative $\theta = 90°$ V-shaped nanoantenna at (a) its asymmetric resonance frequency, and (b) its symmetric resonance frequency. Resonant electric-field profiles for an asymmetric $\theta = 90°$ MTM-lined aperture, (c) at its asymmetric resonance frequency, and (d) at its symmetric resonance frequency. The incident field is y-polarized.

as resonant plasmonic monopoles, it is natural to suggest that an MTM-lined aperture also supports this pair of resonances, and hence, can create a controllable scattered phase. Fig. 3.20b shows how we can add a comparable asymmetry to the MTM-lined aperture. Indeed, similar symmetric and antisymmetric modes now exist if the nanowires are rotated about the centre of the aperture, as shown in Figs. 3.21c and 3.21d. The nominal MTM-lined aperture has a radius $b = 40$ nm, a wire and gap width $w = g = 10$ nm, a thickness $t = 50$ nm, and a period $p = 100$ nm to match the nanoantennas studied previously.

For simplicity, we have only rotated one-half of the nanoantenna/liner, but strictly speaking, the maximum scattering to the cross-polarization is expected when the structures are excited at 45° to their axes of symmetry. To remove the dependence on symmetry about the polarization angle, we choose to evaluate the response of our now asymmetric MTM-lined apertures to circularly polarized incident waves, though similar results could also be achieved by casting the data to symmetric linear polarizations. Since mirror symmetry is maintained, the response to right-hand circular polarization (RHCP) and left-hand circular polarization (LHCP) is identical in magnitude, but the rotation of the axis of symmetry presents as an additional positive or negative geometric phase $|\phi| = \theta$ over the entire spectrum, depending on the handedness of the input polarization.

Fig. 3.22 shows the scattered amplitude and phase spectra for various angles θ. Our study is limited to $\theta = 90°$ as enforcing the 10-nm gap width shortens the nanowires of the liner too far beyond this point. In general, the scattering amplitude of the nanoantenna array (Fig. 3.22a) is stronger than that of the MTM-lined aperture array (Fig. 3.22c) due to the fields not being limited to the aperture region and no additional loss within the solid film. For anomalous refraction, however, it is not the maximum scattering that is important. Instead, the scattering amplitude must normally be matched across all scattered phase angles (though other scattered field profiles may also be designed).

Comparing the scattered phase, the MTM-lined aperture (Fig. 3.22d)

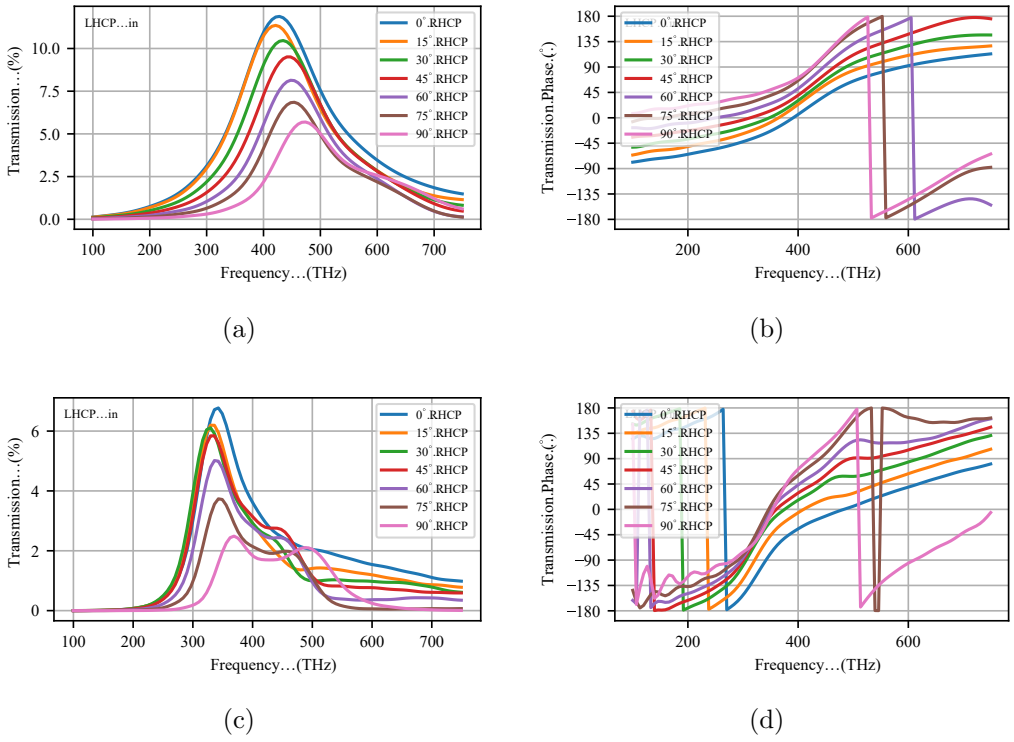

Figure 3.22: Scattered transmission spectrum (a) magnitude, and (b) phase for the V-shaped nanoantenna and various angles θ, and scattered transmission spectrum (c) magnitude, and (d) phase for the asymmetric MTM-lined aperture and various angles θ.

shows clear benefits since the goal is to find structures with a total phase variation of 180°. For the V-shaped nanoantenna (Fig. 3.22b), this phase variation is achieved at ∼650 THz, whereas for the MTM-lined aperture, the same phase variation is achieved at a much lower ∼500 THz. This increased level of miniaturization could improve the MTS scattering to oblique angles, which is limited by the size of the unit cell. Additionally, the minimum scattering amplitude at 500 THz for the MTM-lined aperture is ∼1%, which is on the same order as what is seen for the V-shaped nanoantenna case at 650 THz. Moreover, we observe that the scattered phase of the MTM-lined aperture is flat near the 500-THz resonance, which may be particularly useful for wider-bandwidth applications. In Ch. 5, we will use these results to create an MTS supporting anomalous refraction.

Although MTM-lined apertures can be designed to support the same interesting behaviours as V-shaped nanoantennas, these studies are only a starting point for the design of phase-gradient MTM-lined aperture MTSs. With proper tuning, V-shaped nanoantennas have nearly reached the limits of cross-polarized scattering efficiency [178]. Despite the limitations of the aperture area, we expect that additional tuning can increase the MTM-lined aperture's scattering efficiency significantly.

Nevertheless, the imposition of a 10-nm feature size increases the miniaturization, field enhancement, and bandwidth of two-wire MTM-lined aperture MTS elements over conventional nanoplasmonic resonators. This may be particularly useful for using circularly polarized waves to probe material chirality in a near-field imaging system, or using the scattered wave as an additional phase-contrast mechanism to enhance imaging resolution. We have presented general methods for tuning the shape of two-wire MTM-lined apertures to modify the resonance frequency and scattered phase, and developed an equivalent circuit model to facilitate the design.

3.3 Scaling MTM-Lined Discs to the MIR

As a final study case, we scale our MTM-lined aperture to the MIR domain and target the particular application of SEIRA. Increasing the size of the MTM-lined aperture array makes HIM a poor solution for fabrication due to the significantly increased patterning time. A different fabrication method must be chosen, and the fabrication challenges can be compared. A Ga^+ LMIS could be used, but makes for an ineffective comparison as the two methods share the majority of their challenges. Ga^+ FIB milling is a more mature technology offering increased reliability and patterning speed at the cost of reduced patterning resolution and increased implantation. We instead choose EBL as our patterning method, which a mature nanofabrication technique for high-resolution patterning that offers several compelling differences to HIM. These differences will be discussed in the next chapter.

Performing SEIRA spectroscopy in the fingerprinting region of the spectrum could lead to miniaturization of spectroscopic devices, more sensitive detection of lower concentration materials, and smaller required sample sizes. Since the SEIRA signal is proportional to the resonant electric-field intensity, the goal is to create maximum average field intensity enhancement over the MTS area. Using Babinet's principle, Baladi *et al.* inverted the MTM-lined aperture to create an MTM-lined disc [63]. They found that when the perimeter of a circular metallic disc is lined with a TL-MTM consisting of strong series capacitive loading and weak parallel inductive loading, plasmon-like resonant reflection can be induced well below the usual fundamental resonance frequency of the disc. Due to the miniaturized size at resonance, the liner region strongly confines and enhances the local electric fields, which causes the resonance frequency and reflectance to become very sensitive to nearby materials. Moreover, these properties do not rely on plasmonic metals, and may be useful for enhancing SEIRA signals in the long-wavelength MIR part of the fingerprinting region, where plasmonic enhancement is weak. We will specifically target an enhancement of the CO_2 absorption band at a wavelength of 15 µm (667 cm^{-1}), which is the absorption band responsible for CO_2's contributions

to the greenhouse effect.

When designed to operate in the microwave regime, the MTM-lined disc, shown in Fig. 3.23a, consists of a central solid disc (radius a) surrounded by an MTM region ($a < r < b$) and resonates at a frequency of 2.4 GHz (12.5 cm wavelength, $p = 1.8$ cm unit cell size). At resonance, the interdigitated capacitors loading the liner region (highlighted in green) exhibit strong field enhancement, and the resonant frequency can be tuned by changing the geometrical parameters of the capacitors (θ, t). Eight capacitors are arranged azimuthally for polarization isotropy.

Inspired by this design, we apply Babinet's principle to the wagon-wheel aperture, harnessing the plasmonic effect and extreme feature sizes to create strong field enhancement within simple straight capacitive nanogaps (highlighted green), as shown in Fig. 3.23b. However, this design still resonates in the NIR.

To target the MIR, we combine aspects of the NIR and the microwave MTM-lined discs by using a capacitively-loaded plasmonic liner. We begin with the NIR MTM-lined disc, which resonates at a wavelength of 1.55 µm. Targeting the MIR CO_2 absorption band at 15 µm, we scale the size of the structure by a factor of $\sim$10. This scaling maintains the thick liner region but scales the gap size and disc radius. As the disc grows, the resonance wavelength increases approximately linearly. However, due to material dispersion and the weaker miniaturization of the plasmonic effect, the 10$\times$ scaling does not tune the resonance wavelength directly to 15.5 µm. Hence, to tune the resonance down to 15 µm and miniaturize the resonant unit-cell further, we interdigitate the capacitive gaps, like in the microwave design. The number of interdigitations can be used to tune the gap capacitance and thus the resonant wavelength of the unit cell. This interdigitation also allows the field enhancement in the capacitive gaps to be spread out over the full unit-cell area, increasing its uniformity. Fig. 3.23c depicts the nominal design, with an interdigitated capacitor highlighted in green, and with geometric parameters as described below.

Gold is used for the metallic layer as it is a good conductor in the MIR

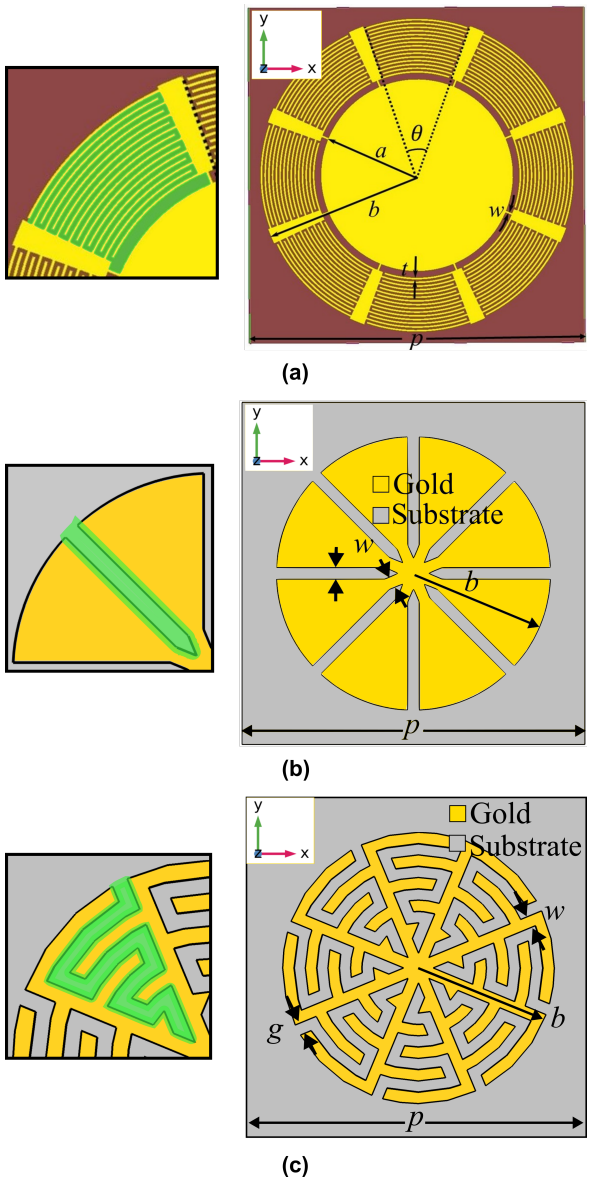

Figure 3.23: (a) Microwave MTM-lined disc, where θ is the angular interdigitated capacitor span, a is the radius of the inner solid disc, b is the disc radius including the liner, w is the inductive connecting trace width, t is the capacitor trace width, and p is the array pitch. (b) NIR MTM-lined disc, where b is the disc radius, w is the capacitive gap width and minimum central nanowire width, and p is the array pitch. (c) MIR MTM-lined disc, where b is the total disc radius, w is the nanowire width throughout the unit cell, g is the nanogap width throughout the unit cell, and p is the array pitch [179]. Each panel includes an inset with the capacitive gaps highlighted in green. (a) licensed under CC BY 4.0, modified with axis and highlighted gap insets [63], (c) ©IEEE 2020, modified with permission [179].

and will not degrade when stored in air. For the substrate, NaCl is readily available and transparent at 15 µm but sublimates under electron beam illumination, so is a poor substrate for this process. ZnSe and CdTe are potential alternatives; however, CdTe is potentially toxic and not supported by the University of Alberta nanoFAB Centre. The majority of other crystals do not have a transparency window that extends to a wavelength of 15 µm or are not compatible with the EBL lift-off process due to dissolving in water. ZnSe is therefore the substrate material of choice.

We apply the $\sim 10\times$ scaling to many of the geometric features to create the nominal design. The film thickness is held at $t = 50$ nm for ease of fabrication. The minimum feature size w is scaled from 10 nm to 100 nm, which decides the fabrication method. Although the NIR design required high-precision helium focused-ion-beam milling, we chose 100-kV EBL for the MIR design, as it can pattern a resist with features as small as 20 nm and has much higher throughput. Additionally, EBL liftoff is better suited to creating arrays of disconnected patches than creating arrays of apertures, hence the choice of MTM-lined discs over MTM-lined apertures. Next, the overall size of the unit cell is scaled by a factor of 10, resulting in a $p = 3$ µm pitch and a $b = 1.2$ µm patch radius. Finally, the straight nanogaps are meandered to tune the resonance wavelength to 15 µm. We continue to use eight azimuthal cells for polarization isotropy.

To validate our approach, we simulated the nominal structure depicted in Fig. 3.23c in COMSOL Multiphysics. The results are shown in Fig. 3.24a (solid curves), compared to an equivalent array of solid discs with equal radius b (dashed curves). Subject to the minimum feature size, 5 capacitive teeth (equivalently, 5 meanders of the gap) are required to tune the resonance to the desired 15-µm (20-THz) wavelength. The resonance profile exhibits an enhancement in reflection coefficient from 0.30 to 0.77 and a distinct Fano-shape, which allows increased contrast when an absorbing species is present and reduces the resonance bandwidth to better target the desired absorption line. Outside the resonant band, the MTM-lined MTS follows a similar trend to that of the unlined disc array. The unlined disc array reflectance increases

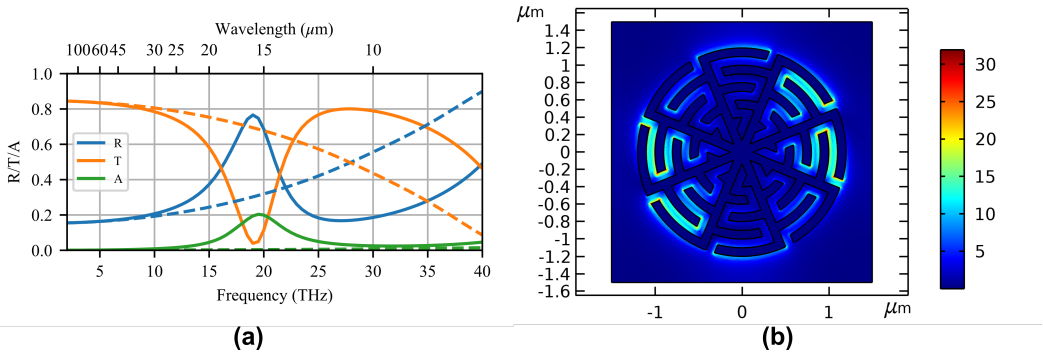

Figure 3.24: (a) Reflection, transmission, and absorption spectra for the nominal MTS-lined MTS structure (solid) and an equivalent unlined-disc array (dashed). (b) Electric-field enhancement ratio for the nominal MTM-lined MTS at the resonance wavelength of 15 µm. The nominal structure has $b = 1.2$ µm, $p = 3$ µm, and $g = w = 100$ nm. ©IEEE 2020, modified with permission to add scale bars to part (b) [179].

toward a resonance above 40 THz, which shows that the MTM loading is indeed able to miniaturize the discs and that no structural resonances unrelated to the MTM loading occur in the active spectral region.

Fig. 3.24b shows the ratio of the input electric-field magnitude to the resonant electric-field magnitude (*i.e.*, electric-field enhancement) at 15 µm/20 THz for a horizontally polarized excitation. Electric fields are enhanced over the entire liner region with a peak enhancement ratio greater than 30. Since this peak value may be subject to numerical inaccuracies and SEIRA signal enhancement is proportional to the electric-field *intensity* enhancement, a more meaningful measure of the field enhancement is the *average* electric field intensity enhancement factor, field intensity enhancement ratio (F_I), of 24.5, averaged over the full unit-cell area and film thickness (see Appendix D). The prevailing approach in the literature, which is to report the average intensity enhancement near a hotspot, creates ambiguity in the required averaging volume [28]. Although a solid circular disc array is a good comparison for miniaturization and to show the creation of a new resonance, F_I cannot be similarly compared as fewer degrees of freedom prevent tuning the unlined disc resonance to 15 µm with an equivalent footprint. To create a meaningful comparison using the F_I metric, we have designed an equivalent conventional

coupled-dipole array resonating at 15 µm, with equal feature sizes and the same unit-cell area. The coupled-dipole array design has a maximum field enhancement ratio of 44 and an F_I of 5.2, less than one quarter that of the MTM-lined disc. Additionally, the resonance is significantly less selective than the MTM-lined disc. More details on this dipole array are also included in Appendix D.

3.3.1 MIR Parametric Studies

Wire and Gap Width

SEIRA demands field enhancement at a targeted wavelength. Maximum field enhancement may occur at the resonance, antiresonance, or somewhere in-between based on material dispersion and coupling efficiency to the incident wave. As a result, targeting maximum reflectance at 15 µm (667 cm^{-1}, 20 THz) may not lead to ideal sensor performance. To study the field enhancement at 15 µm, we simulate the MTM-lined disc with varied gap width (g) and wire width (w). The study is limited to 80 nm as the minimum feature size due to fabrication constraints and because feature sizes below 80 nm shift the resonance wavelength well below 15 µm, decreasing the relevant average field enhancement. 80 nm is a conservative estimate of our maximum patterning resolution to simplify the EBL process development. Similarly, 120 nm is chosen as the maximum feature size as the resonance shifts as far as 20 µm. We once again use F_I to compare the simulations, and the results are presented in Fig. 3.25a. The outer radius $b = 6(w+g)$ and the pitch $p = 2.4b$ are allowed to vary to keep the fill factor, and hence resonance amplitude, constant.

In general, decreasing g is the most important factor in increasing F_I as the stored electric energy is forced into a smaller volume, which necessarily increases the local electric field intensity. Decreasing the gap size, however, also shifts the resonance wavelength away from 15 µm, which reduces F_I at 15 µm. The shift in resonance wavelength can then be compensated by a commensurate increase in the wire width w or a direct increase in b to ensure maximum field enhancement at 15 µm. With reference to Fig. 3.25, the

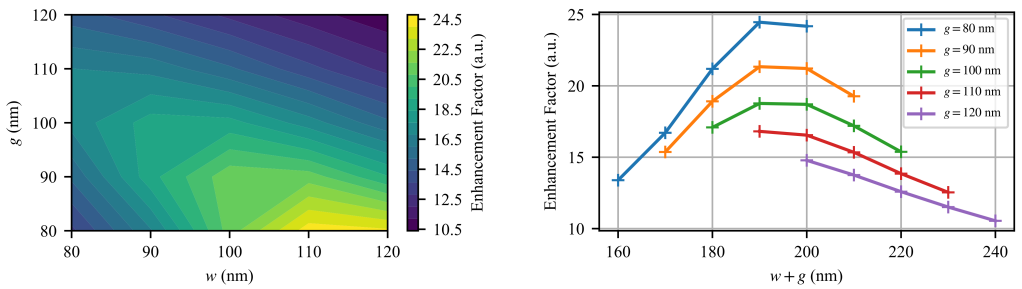

Figure 3.25: (a) Simulated average field intensity enhancement factor, F_I, at 15 µm (20 THz) with respect to the wire width w and the gap width g, and (b) with respect to the sum of w and g. Reproduced from [180], CC BY 4.0.

maximum reflection wavelength varies from 13.3 µm for smaller feature sizes to 20 µm for larger feature sizes, also presented later in Fig. 3.26b. For gap sizes above 100 nm, the gaps are too large to create a large F_I. These data suggest that for a maximum F_I, the sum of w and g approaches approximately 190 nm, as shown in Fig. 3.25b. Given the fabrication constraints, we chose to fabricate the $(g, w) = (80\text{ nm}, 110\text{ nm})$ design, which has the best F_I of the cases studied. The fabrication details and results will are detailed in Ch. 4. For these values of g and w, $b = 6(g + w) = 1140$ nm and $p = 2.4b = 2736$ nm.

Period and Radius

The MTM-lined disc may be tuned through geometric variations to target the absorption bands of other materials. Parametric simulations of the MIR MTM-lined disc reveal many features similar to the NIR MTM-lined aperture [92]. Decreasing the pitch (p) of the array leads to increased resonance amplitude as a function of the filling fraction (disc area divided by total unit-cell area), as shown in Fig. 3.26a. This study does not change the absolute field enhancement, and as a result, the F_I is increased as the filling fraction grows, *i.e.*, as the integrated averaging volume decreases.

Fig. 3.26b shows the simulated reflection spectra for MTM-lined MTSs with varied radius b. This sweep is accomplished by setting $w = g = 80$–120 nm, $b = 6(w + b)$, and $p = 2.4b$, which keeps the fill factor constant and hence the resonance amplitude does not change. These data show that

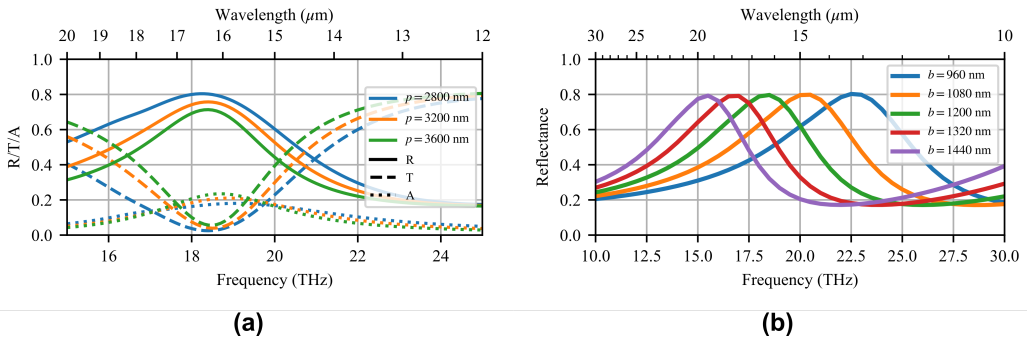

Figure 3.26: (a) Simulated R/T/A spectra for varied MTS pitch p, and (b) simulated reflection spectra for varied MTS disc radius b, while keeping the fill factor constant. Reproduced from [180], CC BY 4.0.

upscaling and downscaling the size of the disc (b) respectively redshifts and blueshifts the resonance. The study presented above for tuning the maximum F_I may also be repurposed to tune the resonant wavelength as the wire and gap widths control a large fraction of the overall unit-cell geometry and are hence extremely important to the MTS performance.

The MTM-lined disc MTS can thus be scaled intuitively from the NIR domain to the long-wavelength MIR, keeping its increased miniaturization and field enhancement properties. With control over the feature and disc sizes, we can tune the resonant band over the entire fingerprinting region to target any number of different materials. Moreover, the larger minimum feature size allows the MTSs to be fabricated by EBL, which provides many contrasting features to HIM nanofabrication. Nevertheless, this structure could also benefit from 10-nm features if designed to operate at a different frequency. The patterned nanogaps would further increase the gap field enhancement, and as a result, the overall F_I. Such a structure could be patterned in a two-step process, starting with the definition of circular patches by EBL, then the intricate patterning and edge definition by HIM.

3.4 Summary

We have explored the design of MTM-lined plasmonic resonators using extreme features as small as 10 nm to increase their plasmonic performance. Despite

the miniaturization effects of plasmonic metals in the optical regime, MTM-inspired plasmonic liners continue to increase the miniaturization and local field confinement inside MTS unit cells. An aperture with a thin plasmonic liner supports an HE_{11} mode at half its unloaded fundamental resonance frequency, with electric fields confined to within 30 nm of the aperture edge. The strong electric field confinement implies high sensitivity to materials loading the liner. Moreover, the controllable resonances, high surface area, and strong field enhancement may be ideal for nonlinear plasmonics. For example, plasmonic second harmonic generation may be possible by reducing the aperture symmetry.

Extending the liner region to encompass the majority of the aperture area allows the aperture to be miniaturized further, while the fields at resonance become focused at the centre of the aperture. This focusing allows the near-field probing area to be reduced to a diameter as small as 50 nm with strong scattering levels. We have shown that MTM-lined apertures can be tuned by a number of geometric factors, including a sweep of the liner thickness, which we will harness in Ch. 5 to create a superresolution imaging array that multiplexes near-field spatial information to the far-field scattered frequency spectrum.

We studied effects of plasmonic field penetration and anisotropy on ENNZ MTM-lined apertures with an effective-medium model, but found our results difficult to apply to the realized designs. Instead, we developed a simple and intuitive method to create an equivalent circuit model for the full MTS unit cell. The circuit model describes the MTS well over a range of geometrical parameters expected in fabrication, and could be used as a simple method to design and realize nonuniform MTSs for phase-gradient or imaging applications.

We also proposed that sensors based on the qualitative evaluation of resonance frequency (transmitted colour) could be made by scaling the MTM-lined aperture to resonate in the visible domain. This required reducing the loading to two nanowires, making the new aperture design comparable to conventional nanoplasmonic resonators such as bowtie nanoapertures and V-shaped

nanoantennas. We showed that MTM-lined apertures with 10-nm features outperform bowtie apertures with 10-nm nanogaps in terms of miniaturization without loss of field enhancement. This could be used for increasing the surface density of field hotspots for MTS arrays applied to surface-enhanced sensing. Both types of aperture would require the fine resolution of the HIM to fabricate. In comparison to V-shaped nanoantennas, two-wire MTM-lined apertures are better-miniaturized while supporting a full 360° of scattered phase, which could be used to increase the deflection angle of a phase-gradient MTS. We explore this idea in more detail in Ch. 5.

Finally, studied MTM-lined resonator MTSs as solutions to the low field enhancement observed in the long-wavelength MIR regime for SEIRA of CO_2. We designed an array of MTM-lined discs, which are the complement of MTM-lined apertures, with 100-nm features and strong capacitive liner loading. After tuning, the MTM-lined discs exhibit nearly 5× the average near-field intensity enhancement over a similar array of straight dipoles, which is directly proportional to their enhancement of SEIRA signals. The unit cells are insensitive to polarization, which makes them simpler to excite by a conventional FTIR microscope.

Chapter 4

Experimental Realization

In this chapter, we discuss the studies performed to fabricate the three MTS designs from the previous chapter, create a process flow for reliably patterning high-aspect-ratio 10-nm features into gold over large areas with the HIM, and show the basic optical characterization of the devices. Patterning with the HIM is inherently unreliable due to the enormous number of factors that can affect the patterning result. Alignment, patterning path, noise from the fab environment (particularly when the cryopumps are regenerated), and materials are just a few examples of the myriad variables that must be controlled to achieve 10-nm scale features in a reproducible manner. We begin by assessing the general factors inside the HIM that create problems during any FIB patterning process and show the results of a detailed study of the HIM beam parameters. We create a wagon-wheel MTS and characterize it, but it does not show the expected resonant response to optical illumination. The beam parameter studies are analyzed to identify the most important challenges that led to the characterization failure.

New samples are fabricated that address these challenges, and we fabricate a high-fidelity two-wire MTS. The MTS is fully characterized with polarized reflection measurements, and a representative simulation is produced.

We also develop a 100-keV EBL liftoff process to create low aspect ratio 100-nm features in gold for fabricating the MIR MTM-lined disc design. We later compare this process to the HIM. The fabricated MIR MTS is characterized by FTIR microscopy, showing excellent agreement with the simulated

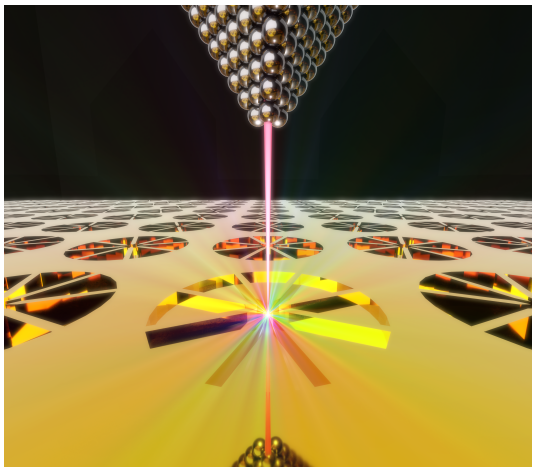

Figure 4.1: Schematic representation of the ion beam, selected from a single atom of the three-atom trimer, patterning the gold film surface (not to scale). Reproduced with permission from [182], ©2021 ACS.

designs.

4.1 HIM Milling – Sample-Ion Interactions

The direct-write approach of the HIM does not require a masking layer. Instead, the beam is rastered continuously over the area to be patterned, removing a small amount of material with each pass. The helium ion beam used for this study was the Zeiss Orion Nanofab Helium Ion Microscope housed at the University of Alberta nanoFAB Centre [149], [181]. This system uses a 30-keV GFIS comprising a cryogenically-cooled, atomically-sharp tungsten needle. The tip of the needle is fashioned into a three-atom "trimer", shown schematically in Fig. 4.1, from which the ion beam is extracted, and the extraction optics select the emission from a single atom to maintain a very low energy spread. The trimer degrades over time due to the adsorption of contaminants, lowering the beam current, and must be rebuilt periodically (typically every few weeks). Additionally, the cryogenic cooling dewar attached to the source must be refilled every 12 hours, which limits the total continuous patterning time at a 10-nm resolution since the filling process introduces vibrations. The extracted ions pass through several electrostatic lenses and apertures to focus the beam and to select the probe current and spot size.

To realize a nanoplasmonic MTS with the HIM, each periodic element must be created sequentially; *i.e.*, the beam is rastered once or a number of times over one unit cell before moving on to the next. The patterning parameters are related to one another as follows: the *number of passes* is determined by dividing the *target dosage* (total number of ions delivered to the patterned area, measured in charge per unit area) by the time-averaged dosage, while the time-averaged dosage is determined by multiplying the *beam current* (the number of ions delivered per second) by the *dwell time* (time spent on each pixel per pass). Additionally, the probe current is related to the physical spot size of the HIM beam and the metal film thickness determines the required target ion dosage for complete patterning. Poor beam focus causes undermilling (wider nanowires, slimmer nanogaps, and potentially incomplete milling), while drift during patterning displaces each successive raster across a single pattern, leading to a washing out of the patterned features. On a larger scale, drift modifies the pitch of the MTS array.

To characterize the encountered fabrication challenges, it is important to understand the interactions that may occur between the ion beam and the sample [183]. Described below are the most common interactions below along with the common mitigating strategies. In describing the HIM, a FIB-based technology, it is informative to make comparisons to the more familiar scanning electron microscope (SEM), as the HIM shares many of the same working principles [184]. Practically, the only difference between an SEM and the HIM system is the source (electrons or ions, respectively).

4.1.1 Secondary Electron Generation

Secondary electron generation occurs when an incoming ion transfers energy to the sample, causing it to emit electrons. This is analogous to secondary electron generation in an SEM and is the most common method for creating image contrast. Secondary electrons are emitted and blocked in a very similar manner to reflected photons, which leads to images with an optical appearance, *i.e.*, displaying a depth of field. Neutralization of the incoming ions and the emission of secondary electrons both lead to positive charging of the sample

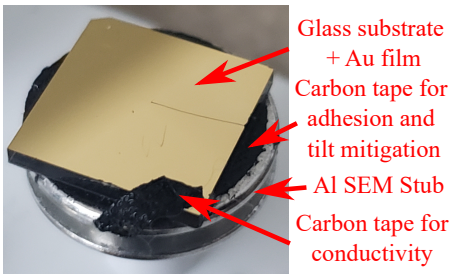

Figure 4.2: Sputtered gold sample mounted on an aluminum stub. The sample is affixed with double-sided, conductive carbon tape for mechanical security, and a second strip of carbon tape is affixed between the gold film surface and the stub to guarantee electrical conductivity. Reproduced with permission from [182], ©2021 ACS.

and can be mitigated either by conduction or by an electron flood gun to avoid major deflections of the beam by the charged surface. For gold films, which are the subject of the present work, the accumulated charge can be conducted away to ground using a strip of double-sided, conductive carbon tape affixed to the gold surface (Fig. 4.2). Unfortunately, the electron flood gun method, which is necessary for studying insulating samples or discontinuous conducting samples, affects the beam and worsens the maximum achievable resolution.

4.1.2 Sputtering

Due to the relatively large mass of an ion compared to an electron, the HIM will cause the sample to eject not only secondary electrons but may also sputter away parts of the sample. The effect of ejecting atoms from the sample is leveraged in this work to draw patterns by selectively sputtering the sample surface. The use of heavier ions increases the sputter rate and the use of lighter ions leads to a decrease in the surface interaction volume, which increases the maximum achievable patterning resolution. Sputter yield is closely related to beam energy, and for He^+ ions, higher sputter yield is observed for lower beam energies but with larger probe sizes [185]. The removed material must generally be redeposited elsewhere locally on the sample.

4.1.3 Ion-Activated Reactions

A well-known issue in particle microscopy is the cross-linking of hydrocarbons causing the growth of carbon films from contamination within the sample chamber (on sample surfaces or in the vacuum) [186]. While imaging, these films occlude desired features [187]. From a patterning perspective, however, this effect leads to a generally unpredictable reduction in sputter rate and rounded pattern edges/corners that reduce the reliability and quality of the patterning method. In the present studies, we will show that organic contaminants can be removed from a sample by treating it with a plasma-cleaning process immediately before loading it into the microscope vacuum chamber.

4.1.4 Implantation

Incoming ions will unavoidably penetrate the sample surface and implant inside the substrate, which can have several effects. Since helium is inert, it will not react chemically with the sample and will instead come to rest inside the substrate. For amorphous substrates, the gas will usually diffuse out of the sample over time without causing permanent damage. On the other hand, for crystalline substrates, the helium atoms may form nanobubbles and coalesce to cause swelling of the substrate [188]. The deformation of the substrate can modify structured features, thus careful control over the dosage or an amorphous substrate is necessary to avoid substrate expansion effects. Beam energy may also be lowered to reduce the implantation depth of the ions; however, this necessarily leads to an increased probe size and hence lower resolution, and care must be exercised to avoid implantation in the metal film.

4.2 Sample Pre-Processing

4.2.1 Sample Preparation

A solid understanding of the potential sample-ion interactions foreshadows a number of the challenges that will need to be addressed below. In the next section, we describe the early work done partially by the nanoFAB staff to set

the stage for the later studies required to fully develop the repeatable HIM fabrication procedure. The fabrication process flow includes three main steps: i) substrate preparation/cleaning, ii) film growth by physical vapour deposition (PVD), and iii) film patterning by HIM. The first step depends on the type of substrate used. In the following studies, the majority of the samples were prepared on square borofloat glass wafers that were cleaned in piranha solution immediately before loading into the PVD instrument. For the second step, we grew the majority of the films by electron-beam evaporation, which showed the best reliability for polycrystalline films. In preparation for the third step, we diced the wafers into smaller 1 cm^2 pieces. We first coated the gold films with photoresist to protect the film, then diced the wafers, and rinsed off the photoresist with acetone. Finally, we affixed the samples to aluminum stubs and loaded them into the HIM for patterning.

4.2.2 Pattern Development

The first samples were prepared by Dr. Aaron Hryciw at the nanoFAB Centre. Dr. Hryciw also made several patterning attempts that led us to believe that the 100-nm polycrystalline gold films on borosilicate glass exhibited significant sputter rate variation. He also noted that simple lines do not pattern well, and generally, two-dimensional shapes should be used.

Based on recommendations from Zeiss, the first patterns attempted were the primitive shapes required to construct the wagon-wheel MTM-lined aperture. 45-degree sectors were milled from the gold, as shown in Fig. 4.3, however, it is clear that some sectors – which were patterned serially – are poorly aligned around the expected common centre. This was due to the drift of the beam while patterning, which will always build up as more area is evacuated. This was first addressed by modifying the aperture design to include the minimum patterned area – the asterisk-shaped aperture introduced in Sec. 3.1.3.

While the asterisk-shaped apertures – and more generally, patterns consisting of a small milled area – could be patterned quickly and without significant beam drift, several challenges arose in patterning arrays of these apertures reliably. Fig. 4.4 shows examples of these challenges. In Fig. 4.4a, a grain defect

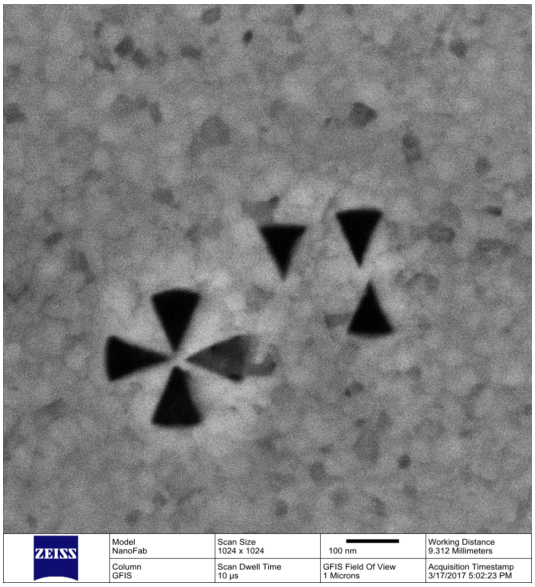

Figure 4.3: An HIM micrograph showing evacuated 45-degree sectors in the 100-nm gold film on borofloat. Image courtesy of Dr. Aaron Hryciw.

is visible due the variable sputter rate of the gold grains causing selective under/overetching of parts of the pattern. In Fig. 4.4b, the growth of thin films on the sample by ion-activated reactions is seen, reducing the effective sputter rate for milling the sample to the point where asterisk-shaped patterns are being deposited on the sample. This is useful for high-precision, bottom-up fabrication, but not for our purposes. Fig. 4.4c shows that the 10-nm gaps required to create strong field concentration and miniaturization are blown out by overmilling that occurs as the beam is rastered repeatedly through the asterisk centre. Addressing the first challenge highlighted above requires reducing the number of grains, which can be done by increasing the grain size or using thinner films. The second challenge requires additional fabrication steps outside of the HIM, and is addressed in Sec. 4.2.3. The third problem may be addressed by tuning the pattern milled by the HIM. Some attempts to tune the pattern are summarized next, and a detailed study of the patterning parameters follows in Sec. 4.3.

The main parameter causing the overmilling of the aperture center is the dosage of ions to the centre. In the first iterations of the pattern, the pattern was composed of 4 rectangles patterned sequentially and overlapping at the

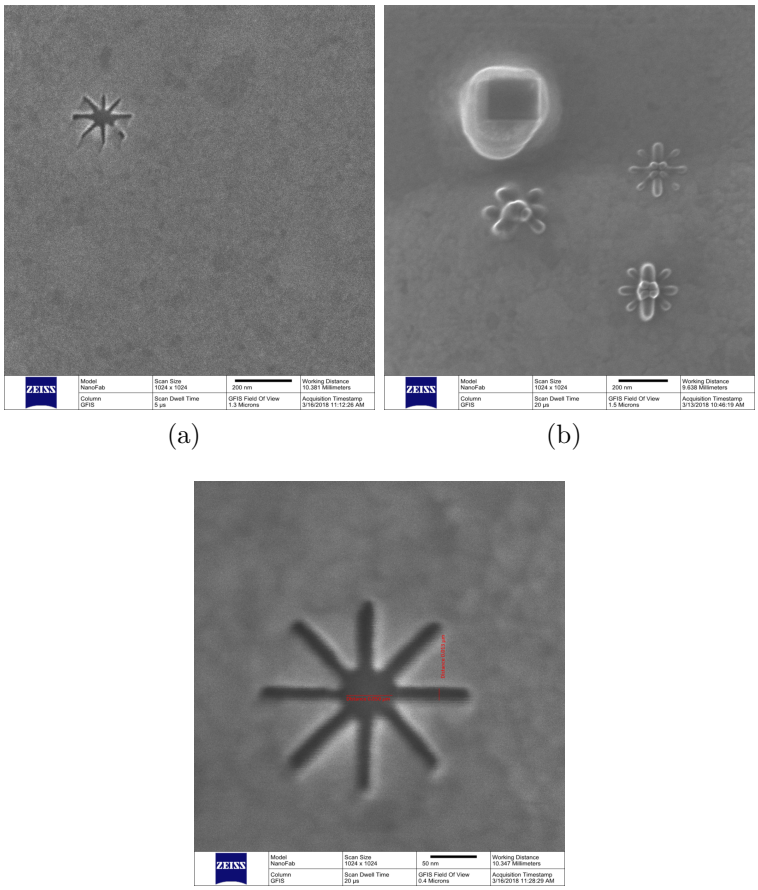

Figure 4.4: HIM micrographs showing the defects encountered while patterning asterisks into polycrystalline films. (a) grain defects due to varied crystal face orientations, (b) deposition of contamination films and substrate swelling, and (c) overmilling at the pattern centre.

centre. This serial patterning within a single aperture causes the centre to receive 4× the dosage of the asterisk arms. If the dosage is lowered, the asterisk arms do not get fully cleared, but if the dosage is increased, the centre gaps are widened. To address this, we created a pattern with the 4 rectangles unified into a single pattern. The difficulty with this type of pattern is that the raster direction cannot be changed over the pattern, hence the horizontal arms of the pattern may be aligned with the raster, whereas the vertical arms are perpendicular to the raster. This causes differences in redeposition and resolution between the arms that can be difficult to control. With proper alignment of the beam and careful minimization of the beam astigmatism, the

resolution is not significantly different on either axis. Redeposition is avoided by running a sufficiently high number of passes. Unfortunately, despite no longer delivering four times the necessary dosage to the aperture centre, the central gap is still often overmilled due to drift in focus/alignment and the high feature density.

The Fibics Nanopatterning and Visualization Engine (NPVE) software includes a greyscale patterning feature that may be useful for reducing the overdosage at the centre of the aperture. The greyscale patterning feature can be used to impose a spatially-dependent dosage profile on the pattern, which effectively allows a selective increase or decrease in the patterning depth. On an HIM image, the deeper features generally appear darker and hence a greyscale bitmap can be physically reproduced as a depth profile on the sample. In our case, the greyscale feature can be used to selectively reduce the dosage to the centre of the aperture. We created a bitmap in MATLAB, shown in Fig. 4.5, that selectively reduces the dosage to the sharp metallic tips inside the aperture to increase their fidelity in the final patterned shape. Unfortunately, we found that the greyscale patterning feature is very limited in speed. Between each pass, the system must generate a new pattern by masking all pixels below a particular threshold, then patterns the resulting binary image. The generation of this binary image takes much longer than a single pass and extends the patterning time of a single aperture by a factor of > 10. As a result, significant drift is incurred between passes and the final pattern becomes washed out. A new pattern generation software called FIB-o-mat was recently released that gives full control over the raster pattern, including an optimization function that reduces the overdosage of fine, closely spaced features as we have attempted to do here [40]. Deinhart *et al.* show a structure where feature sizes as small as 3 nm can be produced, though they admit to poor reproducibility. We expect that their raster pattern generation procedure, limited to a minimum feature size of 10 nm, could further improve the patterning results presented below.

Finally, moving to thinner, 50-nm films instead of the original 100-nm was necessary to more reliably pattern the 10-nm features. Despite the 10:1 aspect

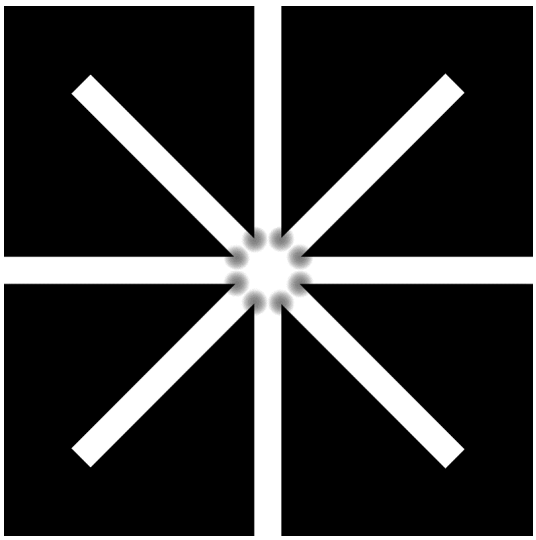

(a)

Figure 4.5: Grey-scale patterning bitmap generated in MATLAB.

ratio offering the best out-of-band rejection performance for resonant plasmonic MTS applications, thinner films require less time to pattern a single structure, which reduces the time for drift to accrue. These thinner films also exhibit fewer crystal grain boundaries, which reduces the number of defects. The simulation studies presented in Sec. 3.1.4 show only small changes in the aperture resonance for thinner films, and with the aforementioned fabrication benefits, the original aperture design can be patterned reliably without resorting to the asterisk. In turn, this allows us to show the fabrication of both fine nanowires and fine nanogaps.

4.2.3 Contamination Investigations

A number of the samples prepared over the course of these studies showed unexpected behaviours when illuminated by the HIM. Fig. 4.4b above shows one such case, where rather than milling the film, structures are grown on the film surface. This growth is a well-known issue in particle microscopy and can generally be attributed to hydrocarbon contamination introduced at some point in the fabrication process. Evidence of hydrocarbon contamination was seen on a number of the samples studied throughout this work. In particular, polycrystalline gold films grown on NaCl then transferred to copper TEM grids

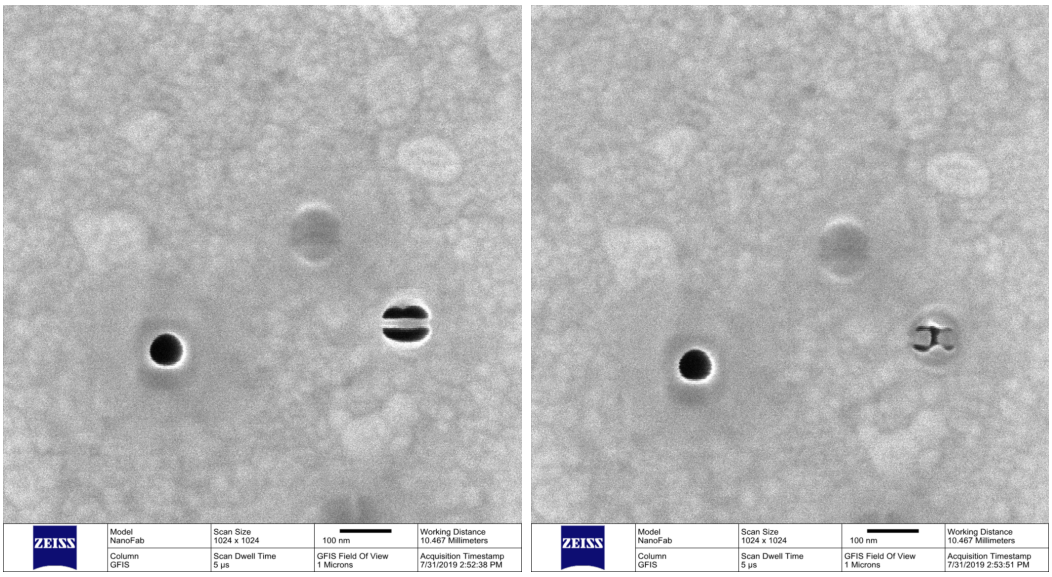

(a) (b)

Figure 4.6: HIM micrographs showing an aperture patterned in two steps: (a) an aperture with a continuous wire through the centre, and (b) after a vertical line was cut through the centre of the wire.

showed significant problems with contamination. This fabrication process is explained in more detail in Sec. 4.6.2.

While developing a milling pattern for the two-wire design, we found that patterns could reliably be milled through the film, but despite a well-aligned beam and low patterning time, the edges were not well-defined. Moreover, Fig. 4.6 shows that milling an aperture in two steps (in this case, milling an aperture with a single continuous wire, then milling the gap in between with a simple line path), caused significant unintended changes to the aperture geometry. To learn the composition of the contamination films and to find ways to prevent their growth, we characterized the films under SEM and TEM with the energy-dispersive x-ray (EDX) attachment. Specifically, did the NaCl substrate contribute to the grown structures or was the growth entirely due to hydrocarbon contamination?

EDX Analysis

Results of the SEM EDX analysis are shown in Fig. 4.7. Without the high mass of the ions to sputter away the growing contamination film, a filament

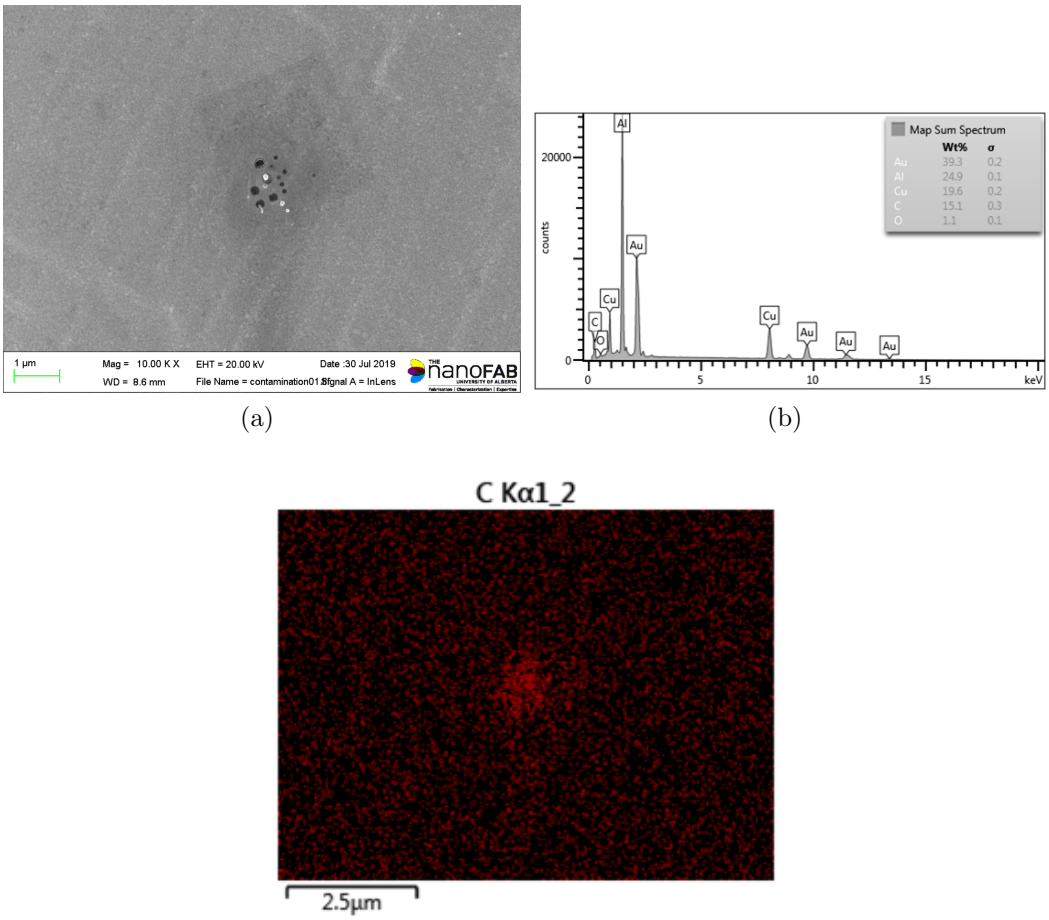

(a) (b)

(c)

Figure 4.7: SEM EDX results, showing (a) the imaged area, where imaging/focusing with the HIM and the SEM has grown contamination on the surface, (b) the collected EDX spectrum, showing contributions from Au, Cu, Al, O, and C, and (c) a map of the carbon signal, showing a strong localization of the carbon to the patterned area.

was formed where the electron beam was focused. This is a clear signature of carbon contamination, and indeed, the EDX results show the presence of Cu (the TEM grid), Au (the deposited film), Al (the SEM mounting stub), C (from contamination), and O (oxidation of the Cu, Al, or contamination). Additionally, the carbon map shows a significantly increased prevalence of carbon in the patterned area, whereas the other materials show reduced prevalence. No contribution is seen from the original NaCl substrate.

As a second validation, results from the TEM EDX analysis, which improve the resolution and remove the aluminum contribution, are shown in Fig. 4.8.

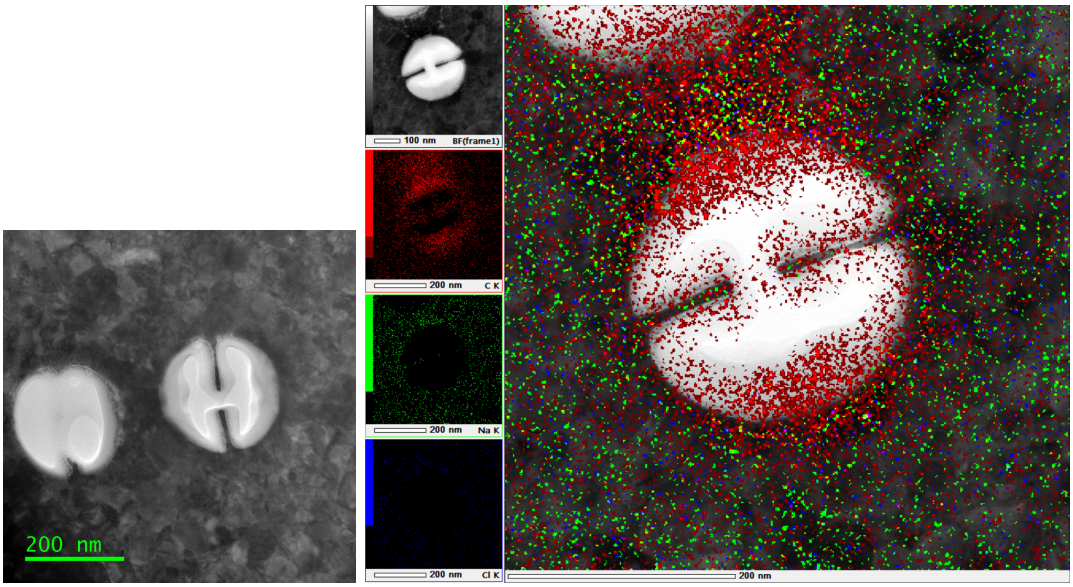

(a) (b)

Figure 4.8: Results of the TEM analysis of the gold films grown on NaCl. (a) TEM micrograph of an aperture patterned in two steps, (b) the EDX map of the patterned area, showing the C signature (red), the Na signature (green), and the Cl signature (blue). The signatures of gold and copper were also detected, but not plotted.

The increased contrast of the TEM to the atomic number of the material makes the contamination film stand out clearly. While the structure was milled into the gold with fairly high fidelity, a bright corona of contamination material is clear. Examining the EDX map of the sample (Fig. 4.8b), no signature from the Al stub remains and the contamination films are made entirely of carbon (red dots), and only a weak signature from the dissolved Na (green dots) Cl (blue dots) substrate is recorded on the gold regions.

With the contamination composition confirmed and with no clear source from the fabrication procedure, we looked into removing the carbon contamination in postprocessing using a plasma cleaner. We first tried the IBSS Chiaro Plasma Contamination Control System (IBSS), which uses a downstream plasma to sublimate surface contamination and is the least aggressive cleaning tool available [189]. Unfortunately, after processing with the IBSS, the fabrication results did not improve. The second available plasma cleaner was the Fischione 1020 plasma cleaner, which uses a direct Ar/O_2 plasma to

etch away the contamination on the sample surface [190]. The TEM images above were taken after this process was used, and it is clear that strands of carbon are no longer growing, however, the previously deposited contamination layers remain. Thus preprocessing a sample with an Ar/O_2 plasma before loading it into the HIM can avoid issues with carbon contamination. Since the Fischione system only supports TEM grids, any samples with substrates that required cleaning before patterning in the HIM were cleaned with the JEOL JAMP 9500F Auger Microprobe, which has an Ar/O_2 plasma cleaning process [191].

4.3 HIM Milling – Processing Parameters

In this section, we explore the impact of several key HIM parameters on the overall high-resolution, wide-area fabrication in decreasing order of importance. The quality of the resulting pattern for each set of parameters is gauged by the degree of over/undermilling, the time required to mill the unit-cell pattern, and the measured drift between individual unit cells. The source gas pressure was set to the software-defined maximum of 5×10^{-6} Torr to maximize the achievable beam current with a 10-µm gold aperture. Higher gas pressures are possible at the expense of trimer lifetime. A new trimer was built three days before the experiment, and the samples were plasma-cleaned immediately before loading into the HIM. In our experience, the current from a new trimer source grows 10%–20% over the first few days of usage before decaying over the following weeks due to the adsorption of contaminants to the source tip. The decay rate is generally unpredictable, but a current value of ∼60% of the maximum can often be maintained for two to three weeks. The best patterning results are achieved when using a fresh trimer as the increased current significantly reduces the patterning time and hence the time to accumulate drift.

We studied three samples with polycrystalline layer thicknesses of 50 nm, 70 nm, and 90 nm. Nominally, the beam current was set to 10.5 pA, which required a spot size control parameter of 3 (smaller numbers correspond to

larger spot/probe sizes), the dwell time was set to 3 µs, and the dosage was set to 4.5 nC/µm^2 to completely mill the 50-nm film. The number of passes varies with the above parameters, with a nominal 6 passes for a circular 0.25-nm-diameter pixel size. A theoretical estimate of the focused probe size from the NanoFab instrument manufacturer for these conditions is $d_{50} = 2.5$ nm. We prepared the gold films by sputtering on borofloat glass with a 10-nm chromium adhesion layer, diced the wafers into 1 cm^2 sections, and mounted them to aluminum stubs using carbon tape (as shown in Fig. 4.2).

4.3.1 Target Dosage

To increase the target dosage with a constant current and dwell time, the number of passes the beam makes across the pattern must increase. In fact, with all other variables held constant, a change in dosage is equivalent to a change in the number of passes (rounded to the nearest integer) since each pass is identical. We varied the dosage between 1.5 nC/µm^2 (2 passes) and 12 nC/µm^2 (12 passes) in steps of 1.5 nC/µm^2 for a nominal current and dwell time. The results shown in Fig. 4.9 exhibit a gradual shift from under- to overmilling as the dosage is increased, with the dosage required to clear the aperture increasing with film thickness. For the nominally 50-nm thick film, the minimum dosage to clear was 4.5 nC/µm^2, with a measured aperture diameter of $2b = 240$ nm, a nanowire width $w = 11$ nm, a nanogap width $g = 9$ nm, and some undermilling due to gold grain boundary effects. The 12-nC/µm^2 case was overmilled to a diameter of 251 nm, and the nanowires were entirely removed. For the 70-nm thick film, the minimum dosage to clear was 7.5 nC/µm^2, with an aperture diameter $2b = 236$ nm, nanowire width $w = 12$ nm, and nanogap width $g = 6$ nm. The 12-nC/µm^2 overmilled case had a minimum nanogap size of 14 nm, maximum wire width of 8 nm, and aperture diameter of 239 nm. The 90-nm thick film required a full 12 nC/µm^2 to clear, since the central region where the nanowires meet was not cleared for lower dosages. Although the measurements may be somewhat ill-defined due to the significant variation within the aperture, we measured an aperture diameter of $2b = 254$ nm, a nanowire width of $w = 12$ nm (where grain defects

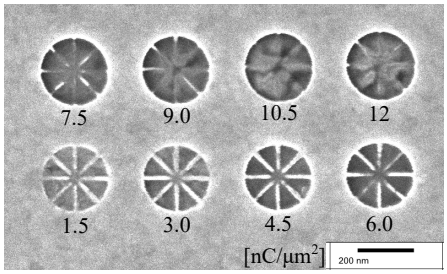

(a)

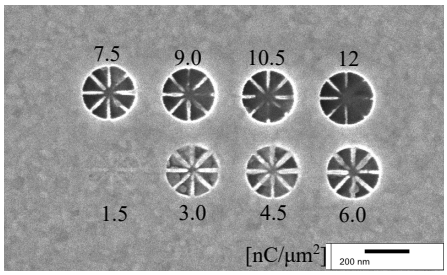

(b)

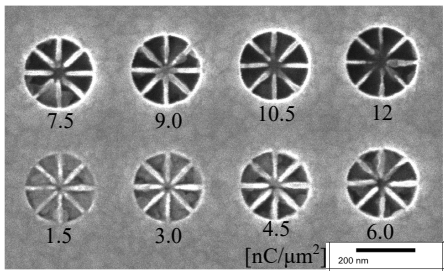

(c)

Figure 4.9: HIM micrograph of patterns with varying target dosage for (a) the 50-nm thick film, (b) the 70-nm thick film, and (c) the 90-nm thick film. From bottom-left to top-right, the dosage is increased from 1.5 nC/µm^2 to 12 nC/µm^2 in steps of 1.5 nC/µm^2. Reproduced with permission from [182], ©2021 ACS.

are not present), and a nanogap width $g = 10$ nm.

4.3.2 Beam Current and Spot Size

The spot size parameter controls the crossover position of the beam using the electrostatic condenser lens. Combined with the static current-limiting aperture, the beam current is largely fixed under normal operation since changes in the other relevant parameters may require realignment of the source. The current may also change based on the beam alignment, the helium gas pressure, and the quality of the trimer source. For milling, a higher current is desired

as patterning time is directly proportional to the current. A lower patterning time decreases the observed drift and hence increases the pattern quality.

For the present study, we increased the current in 1.5-pA increments from 1.5 pA to 15 pA. This corresponds to a spot size control parameter between 5.33 and 2.65 for a well-aligned beam and a three-day-old trimer source. Theoretical estimates of focused probe size from the NanoFab instrument manufacturer for these spot size control parameter values are 1 nm and 3 nm, respectively. This estimate does not include the effect of vibrations or sample-ion interactions, hence sputtered atoms may be ejected from a larger area. Since the digital size of each pattern pixel is constant but the physical size of the beam spot changes, overmilling is likely to occur.

The resulting patterns are shown in Fig. 4.10, where the dwell time was nominal and the dosage was the minimum dosage to clear, identified above. Due to the significant increase in patterning time for low currents (from 11–114 s for the 50-nm, 15-pA case to as high as 28 s–5 minutes for the 90-nm, 1.5-pA case), significant drift was observed between trials and the 1.5-pA case was omitted from the 90-nm case. It should also be noted that in the 90-nm case (Fig. 4.10c), the field of view was shifted between the 6.0 and 7.5 pA cases to avoid having the later trials drift to the point of overlapping (an example of drift causing overlapping is shown in Fig. 4.17).

A visual comparison between the patterned apertures shows that most current values were adequate to pattern for the 50-nm film, however, measurements of the aperture feature sizes show that 10.5 pA produced the best match to the intended design ($2b$ = 242 nm, w = 10 nm, g = 9 nm). For the 70-nm and 90-nm films, redeposition and grain defects make the comparisons difficult. In the 70-nm case, the least overmilling and best feature sizes ($2b$ = 242 nm, w = 13 nm) were seen for 12 pA (although the nanogaps were filled), and for the 90-nm case, the most accurate features were measured for 9 pA ($2b$ = 240 nm, w = 13 nm, g = 8 nm). Multiple trials found, however, that 10.5 pA was more reliable for the 90-nm case.

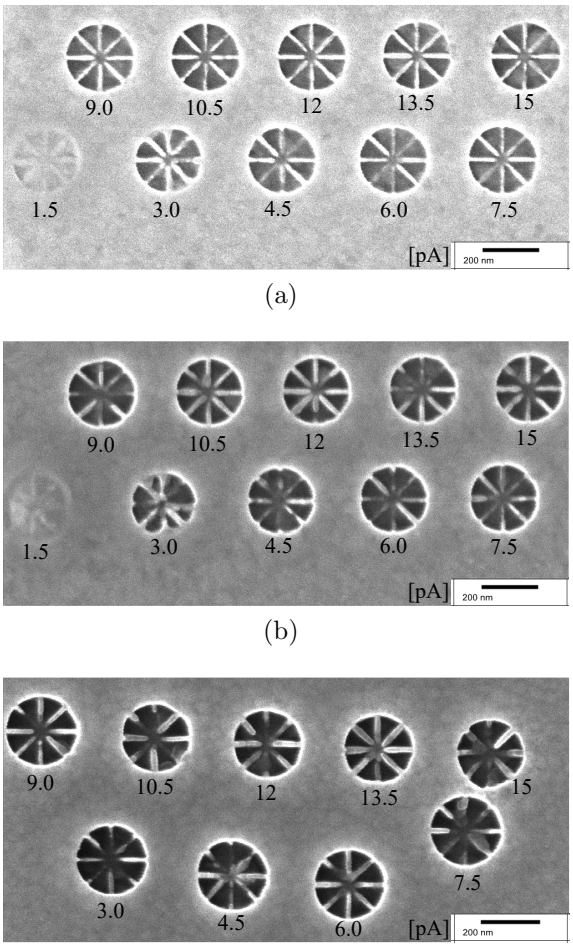

Figure 4.10: HIM micrograph showing patterning differences as the current is increased for (a) the 50-nm thick film, (b) the 70-nm thick film, and (c) the 90-nm thick film. From bottom-left to top-right, the current is increased from 1.5 pA to 15 pA in steps of 1.5 pA. Reproduced with permission from [182], ©2021 ACS.

4.3.3 Dwell Time

The dwell time is the time spent milling each pixel before moving to the next. To keep the dosage and current at their identified best values, the number of passes must change to compensate for any change in dwell time. The dwell time was varied between 0.5 µs and 5 µs in 0.5-µs increments, which corresponds to the number of passes decreasing from 27 to 3 for the 50-nm film, 39 to 4 for the 70-nm film, and 74 to 7 for the 90-nm film.

The resulting unit cells are shown in Fig. 4.11, where it is clear that dwell

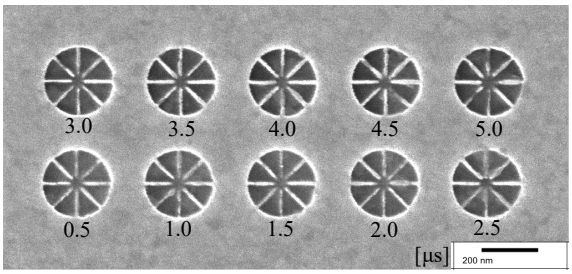

(a)

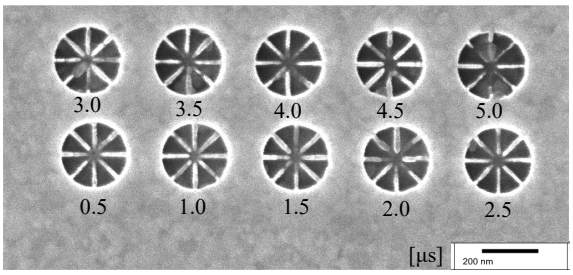

(b)

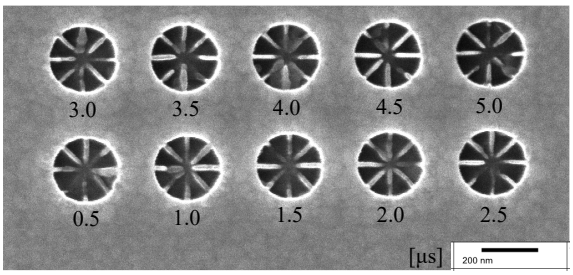

(c)

Figure 4.11: HIM micrographs that capture the effect of varying dwell times on the milled pattern for (a) the 50-nm thick film, (b) the 70-nm thick film, and (c) the 90-nm thick film. From bottom-left to top-right, the dwell time is increased from 0.5 µs to 5 µs in steps of 0.5 µs. Reproduced with permission from [182], ©2021 ACS.

time has the least effect on pattern quality. Nevertheless, the patterns for longer dwell times were generally overmilled, while the patterns for shorter dwell times exhibit undermilling at the pattern centre. Ideal dwell times for the 50-nm and 70-nm cases were 3 µs ($2b = 245$ nm, $w = 10$ nm, $g = 9$ nm) and 2.5 µs ($2b = 241$ nm, $w = 11$ nm, $g = 8$ nm), respectively. In the 90-nm case, the choice is unclear, however, dwell times between 2.5 µs ($2b = 242$ nm, $w = 13$ nm, $g = 10$ nm) and 4.5 µs ($2b = 240$ nm, $w = 14$ nm, $g = 9$ nm) showed the best results when ignoring grain effects.

4.3.4 Array Patterning

The parameters described above allow single structures to be reliably fabricated with sub-10-nm features; however, patterning large arrays with predictable spacing is also an important challenge to overcome. The most significant causes of pattern degradation were observed to be beam drift, grain boundaries, and redeposition. When patterning arrays, moving the stage introduces vibrations and instability in the processing chamber that stabilize over time. To gauge the reliability of array patterning, we define a figure-of-merit, F_{AF}, as the ratio of one side of the patterned area to the minimum feature size, and propose a ratio $F_{AF} > 400$ as a wide area. Fig. 4.12 shows small MTS arrays patterned into the 50-nm and 70-nm films, with a figure of merit of $F_{AF} = 1500/10 = 150$. Large-array patterning challenges become increasingly evident for thicker films as the patterning time necessarily increases, hence well-patterned large arrays with closely spaced elements were not achieved on the 90-nm film.

4.4 Wagon-Wheel MTS

4.4.1 Wagon-Wheel MTS Fabrication

As we have shown, the wagon-wheel aperture MTS unit cell is an ideal choice for exploring the limits of the HIM patterning capabilities due to the fine features and high aspect ratios required. The 10-nm features are necessary to sufficiently reduce the plasmonic resonance frequency of the gold nanowires loading the aperture, the 1:5 aspect ratio increases the opacity and enhances resonance contrast, and long-range reproducibility is required to pattern hundreds of identical cells to cover an illumination region of at least $(3\lambda_0)^2$ or $\sim 22\,\mu m^2$, which can be practically achieved with a focused, wide-band source.

While many small wagon-wheel MTSs were made, we only created a single large wagon-wheel MTS due to the long patterning time involved. The large-scale MTS was patterned as soon as good fabrication results were achieved, and before the full reproducible process was developed, hence the patterning

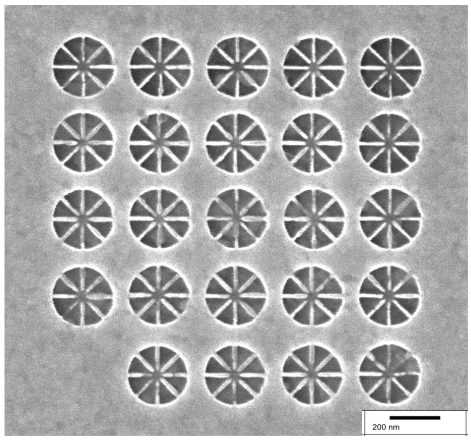

(a)

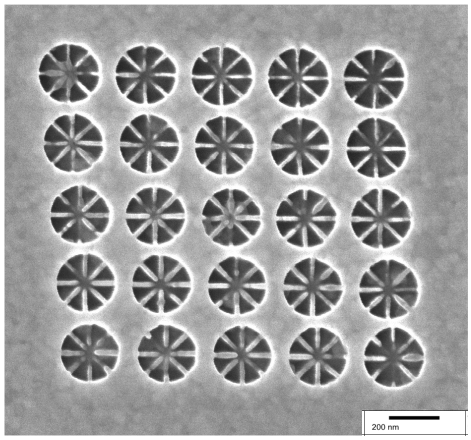

(b)

Figure 4.12: HIM micrographs depicting small-scale arrays for (a) the 50-nm film and (b) the 70-nm film. Problems associated with large-scale reproducibility become increasingly evident for thicker films. Beam drift between patterns, redeposition, and grain defects are all present. Reproduced with permission from [182], ©2021 ACS.

fidelity varied considerably over the array. Moreover, the array was patterned over several sessions with the HIM, where the current and spot size varied for each one. In the end, a 50-nm thick gold film was patterned with MTS elements over an area of approximately 15 µm×15 µm, on a borofloat substrate. Although the array is not continuous, this corresponds to a very high $F_{AF} = 1500$. A section of the MTS is shown in Fig. 4.13, and despite the low resolution, significant differences are seen between the array drift in each section, which indicates significant differences in the single-pattern drift as well.

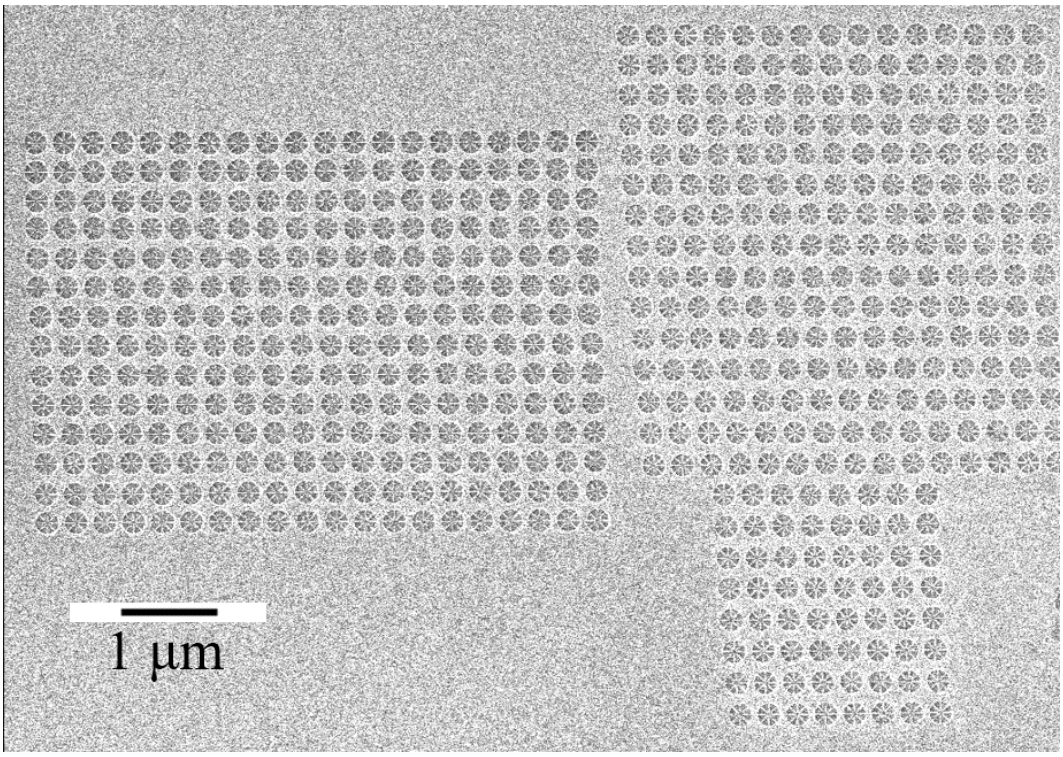

Figure 4.13: An HIM micrograph showing a section of the 15 µm×15 µm wagon-wheel MTS.

4.4.2 Wagon-Wheel MTS Characterization

The spectroscopy requirement for the structure is simply to show a contrast between a patterned area and an unpatterned area in either a transmission or a reflection measurement near the expected resonance frequency of the patterned design. Unfortunately, the resonance of the apertures is quite wide in bandwidth, and lasers used to test optical telecommunications devices cannot provide sufficient details to characterize the device.

Readily available spectroscopy equipment that supports the 1.55 µm operating wavelength includes a wide-bandwidth spectrophotometer, an ellipsometer, and an FTIR microscope. The ellipsometer and spectrophotometer are designed for material and thin film analysis, which does not require high spatial resolution. Their spot sizes can both be reduced to about 2 mm, which is much too large to illuminate a 15 µm×15 µm area. The FTIR microscope, on the other hand, is designed to map variations in material properties on a high-resolution scale, with an aperture as small as 10 µm×10 µm. Regrettably,

(a) (b)

Figure 4.14: Photographs of (a) the measured wagon-wheel MTS die, mounted on a Si chip with clamps and carbon tape, and (b) visible image of the patterned wagon-wheel MTS under the FTIR microscope.

the only available sources are centred in the MIR and the visible, making the signal-to-noise ratio (SNR) quite low in the NIR range.

The first step for characterizing the wagon-wheel MTS with the FTIR microscope was to find the 15 µm×15 µm (F_{AF} = 1500) patterned area on the 10 mm×10 mm chip. This was done by mounting the borofloat die on a larger Si chip with prepatterned alignment marks, as shown in Fig. 4.14a, and correlating the patterned location to the marks as they are also visible under the FTIR microscope. With this system, the patterned area was visible under the FTIR microscope, as seen in Fig. 4.14b, however, there was no contrast between the NIR signal of the patterned area and the unpatterned area. The SNR on the FTIR microscope may be improved by finding a better source or purchasing better optics that allow the 10 µm aperture to fill the entire detector area.

We made several other attempts to characterize the MTS with focused wide-band light sources that were much brighter in the required spectral range using a transmission experiment. This produced much clearer results, but only showed a moderate increase in transmission over the background for all wavelengths, with no clear resonant peak. We expect that the poor overall patterning fidelity caused a range of grain defects, overmilling of nanowires,

and undermilling/shorting of nanogaps that prevented a sufficient number of apertures from resonating to show contrast in experiment. Redeposition was not a clear issue due to the thickness of the film, but it may have contributed to the shorting of the nanogaps, which would be difficult to see on HIM images.

4.5 HIM Milling – Parameter Analysis

To understand why the fabricated wagon-wheel MTS did not respond in the experiment, we now study the observed fabrication defects in simulation to predict their effect on the resonant spectrum. Feature size, aspect ratio, and reliability are paramount to the performance of the wagon-wheel aperture prototype, and by extension, to any number of as yet unexplored finely-featured miniaturized plasmonic MTS elements. These features offer precise control over the plasmonic nanowire properties and the resonance contrast and hence will be the focus of the following analysis.

4.5.1 Target Dosage & Overmilling

Overdosing the sample overetches the nanowires in the gold film, and underdosing the sample underetches the nanogaps, electrically shorting out the nanogaps and suppressing the resonance. Further, overdosing the sample leads to extra damage to the substrate through implantation and sputtering. This is particularly clear in Fig. 4.9a, where the substrate contrast changes significantly as the structure is increasingly overmilled. Had the substrate merely charged up, it would appear entirely dark. Inspection of the lower-dosage cases reveals the polycrystalline grain structure of the underlying gold film, where some grains sputter much more readily than others due to ion channelling. Unfortunately, this grain structure is unpredictable and can cause undermilling in critical pattern areas. The minimum required dosage to clear increases approximately linearly with increasing film thickness, after overcoming a minimum necessary to clear the smaller grains. The increased aperture radius at higher dosages is generally due to drift (and not just overdosage) since it is seen in the thicker films.

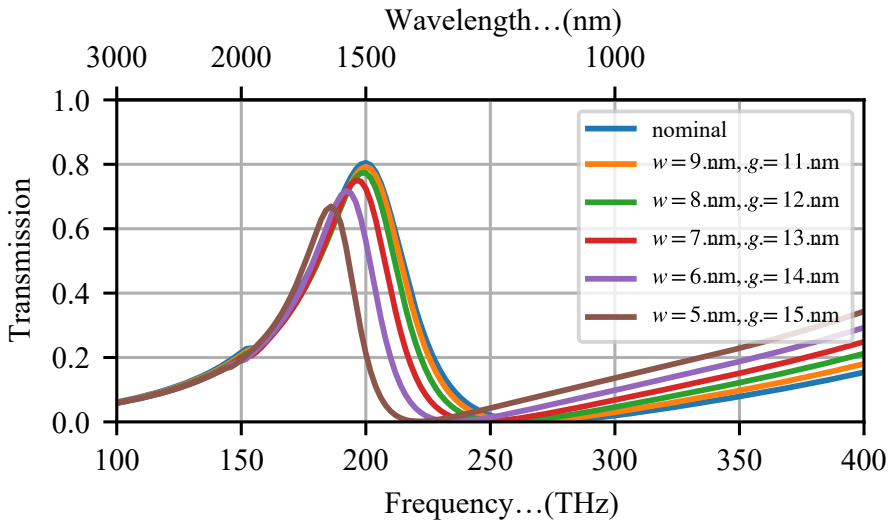

Figure 4.15: Simulation of the wagon-wheel aperture MTS transmission with reduced wire width $w = 10$–5 nm and correspondingly increased gap width $g = 10$–15 nm, representative of overmilling. From Reproduced with permission from [182], ©2021 ACS.

To understand the overmilling effects of overdosage, we simulate the wagon-wheel apertures with narrower nanowire widths w and correspondingly wider gap widths g. Fig. 4.15 shows the transmission for w decreased from 10 nm to 5 nm in 1 nm increments, where the resonant transmission magnitude falls to 0.64 and both the resonance and antiresonance frequencies are redshifted. The frequency shift is due to two competing mechanisms that create the resonance: i) thinner nanowires increase the inductive loading of the liner, which redshifts the resonance, while ii) the increased nanogap width g and decreased nanogap area both reduce the capacitive loading, which blueshifts the resonance. Combined, the increase in inductive loading dominates and hence causes a redshift. The small loop resonance is also redshifted, and the increased impedance makes it more difficult to excite. Overall, significant overmilling would be required to entirely suppress the resonance.

4.5.2 Grain Defects

To analyze the effect of grain defects on the MTS performance, a gold disc of radius $r = 20$ nm is added to the unit cell in simulation. The transmission spectra for several gold disc locations are shown in Fig. 4.16 for a vertically-polarized excitation, with the nominal simulation as reference. Interestingly, although the defects shift the resonance frequency by up to 15 THz, it is not until the defect connects all the wires at the centre of the aperture that the resonance is entirely suppressed. For the rest of the defects studied, transmission levels above 0.64 are observed at 185 THz, an enhancement that would be clear in our optical spectrometry experiment. The position of the antiresonance, however, is shifted more significantly, thus a minimum in transmission (or maximum in reflection) is unlikely to be clearly resolved in the experiment. Due to the strong fields at the nanowire tips, the spectra are most affected by grain defects at the centre of the aperture, where an analyte would be placed for sensing applications. This highlights the importance of the symmetry of the unit cell, which allows only small changes to the overall current distribution as up to three of the nanowires are shorted together. Hence the majority of grain defects seen experimentally, which connect only two nanowires, should have had a minimal effect on the transmitted spectrum.

Compared to the circuit model, the transmission magnitude falls similarly to that seen in Fig. 4.15 for overmilling, which suggests that certain grain defects cause an effective shortening of the nanowires and a decrease in the capacitive coupling of the nanowire tips. An interesting effect is also observed in defect #3 (red curve) that is corroborated by our equivalent circuit in Ch. 3: the defect connects the modelled monopole conductively to the modelled loop resonator, which significantly increases the coupling to the loop. Although the combination of overmilling and grain defects may cause the transmission magnitude to fall significantly, these two effects should not occur simultaneously as the overmilling is expected to remove any grain defects.

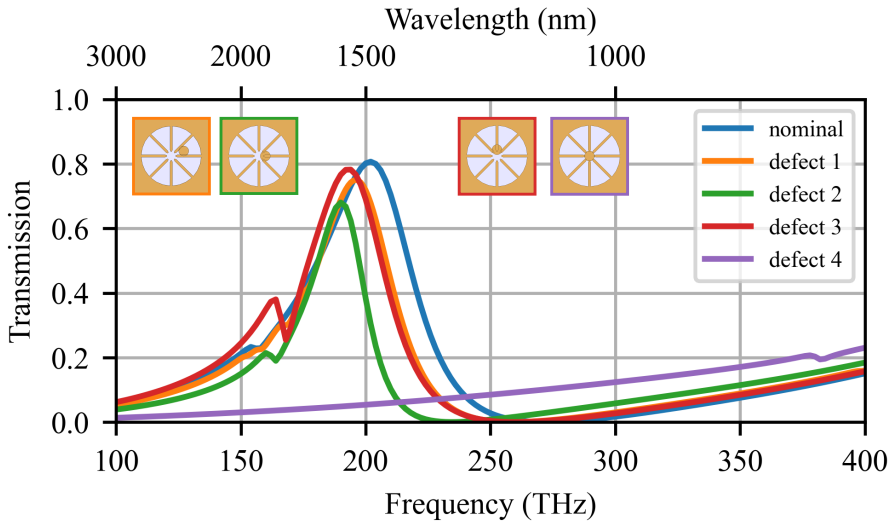

Figure 4.16: Simulation of the effect of a 20-nm radius grain defect placed in various locations on the wagon-wheel aperture MTS transmission performance. Insets show the defect location in the unit cell, with coloured borders to identify the associated curve. Reproduced with permission from [182], ©2021 ACS.

4.5.3 Current & Spot Size

For low current values, the patterning time becomes extremely long, and the accumulation of drift causes an undermilled wagon-wheel aperture. On the assumption that the chamber and sample have been adequately cleaned (i.e., there is no carbon film growth), increasing current leads to a simple increase in sputter rate. Unfortunately, the spot size must also be increased to match the current, and the surface interaction volume of the ion beam with the sample increases, decreasing the patterning resolution. Creating fine, 10-nm nanowires and nanogaps thus requires that the total surface interaction volume be smaller than the features themselves to avoid significant overmilling. Fig. 4.10 shows that this is the case for all the spot sizes studied; however, for lower currents, the gaps between wire tips are underdeveloped due to a smaller probe size and features smaller than 10 nm may be readily achievable. The best results are seen for current values between 9 pA and 12 pA in all cases. Sacrificing the minimum feature size for a decrease in patterning time may be desirable to avoid drift when it cannot be mitigated by other means. Notice that the inter-

pattern drift also significantly improves as the patterning time is decreased, particularly for the 90-nm case. Although not shown, a uniform undermilling over the pattern suppresses the resonance entirely, as was seen for a central grain.

4.5.4 Dwell Time & Redeposition

For thinner films, the effect of dwell time is reduced due to a lower dosage requirement. As the film thickness increases, the higher dosage and longer total patterning time can cause the accumulation of drift error and hence the first and last passes to become misaligned. Shorter passes (i.e., shorter dwell times) will be better aligned from one pass to the next, but the overall drift throughout the patterning of a single aperture remains constant since the dosage is constant. This effect must also be weighed against the redeposition of the sputtered gold atoms. A single pass will not provide the opportunity to resputter the gold that has been redeposited in a cleared area, but removing too little gold each pass may only sputter the redeposited material and not the original film.

The effects of redeposition are shown in Fig. 4.17 for the 90-nm film. In this case, the apertures are patterned in rows from top-right to bottom-left and a large drift is observed between patterns that cause successive rows to nearly overlap. The image acquired after the second row was patterned shows a large increase in the width of the nanowires of the first row and the centre of each aperture being filled in by the material displaced while milling the bottom row. In Fig. 4.11, the bottom-left apertures (those patterned first in the sequence) and the apertures in the thicker films show wider nanowires. This is evidence that the geometry of the present structure causes redeposition to occur on the protruding nanowires as adjacent unit cells are patterned, even when the patterns do not overlap. The apertures in Fig. 4.12b are also subject to redeposition, where the first apertures patterned (also bottom-left) show wider wires than the final ones. Many options exist to mitigate redeposition. The patterned area could be decreased to reduce the amount of redeposited material, the array pitch could be increased, or the MTS could be patterned

into a free-standing film such that the gold is redistributed over both sides of the film.

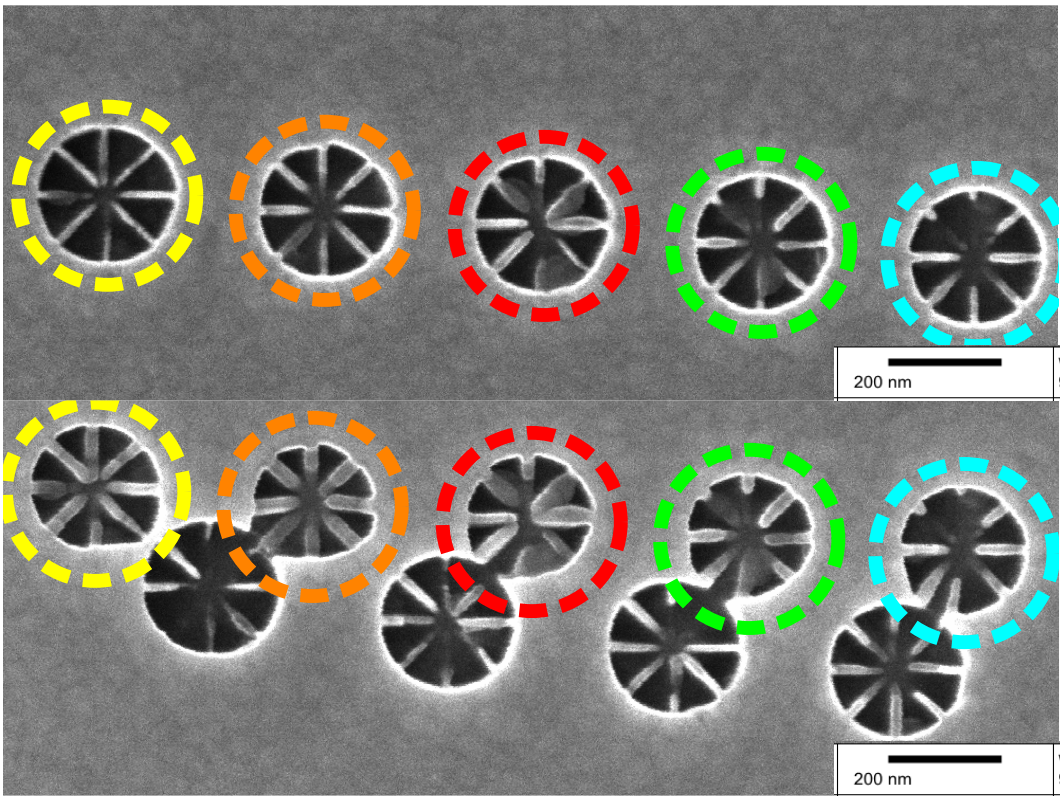

Figure 4.17: HIM micrographs of the 90-nm film showing the effects of redeposition on nearby unit cells. The top half shows 5 cells immediately after patterning, and the bottom half shows the same 5 cells after patterning nearby. Reproduced with permission from [182], ©2021 ACS.

To simulate the effects of redeposition, we increase the width of the wires w, with a commensurate decrease in the gap width g. If the wire width increases beyond $w = 20$ nm, the wires are shorted together and the resonance is suppressed. For intermediate cases, shown in Fig. 4.18, the resonance frequency is redshifted by an increasing amount w and g change, and the transmission magnitude stays constant within the vicinity of the resonance. The antiresonance frequency shifts less dramatically, with very low transmission at 275 THz in all cases. Both the redeposition effects and the grain defects are more pronounced in thicker films, hence a redshifting of the total spectrum can be expected in the experiment. While this simulation does not cover the case where the nanowires become shorted together, it is clear from our analysis of

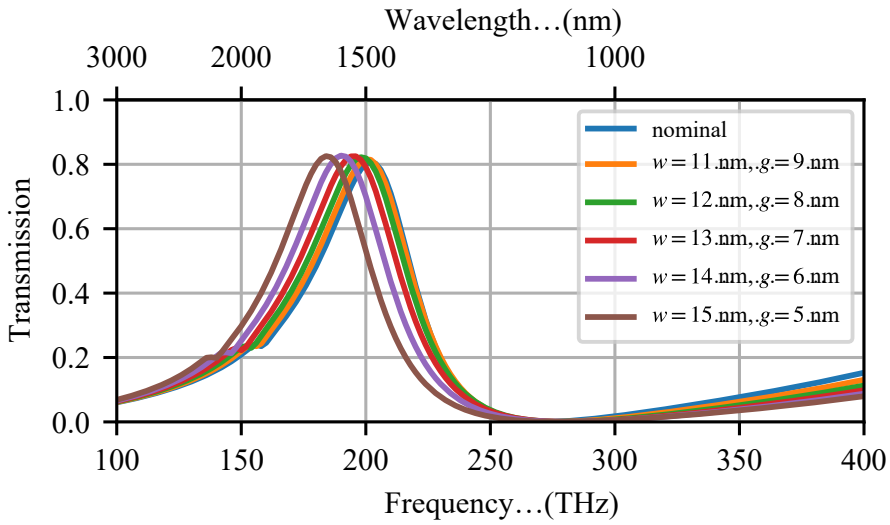

Figure 4.18: Transmission simulation of the effect of redeposition by increasing the wire width w from 10 nm to 15 nm in 1-nm increments, and decreasing the gap width g from 10 nm to 5 nm in 1-nm increments. Reproduced with permission from [182], ©2021 ACS.

Fig. 4.16 that this will suppress the resonance.

4.5.5 Pattern Drift

Drift is one of the most difficult problems to address as many causes of drift are inherent to the lab environment. Outside vibrations coupled into the system, stage instability, beam instability, and substrate charging are all difficult to avoid. The most effective method of mitigating drift for a single unit cell is to decrease the patterning time by increasing the current (and hence spot size). The faster a single pattern can be milled, the less drift can accumulate over the patterning time, which reduces undermilling and improves the minimum achievable feature size. A balance must be struck between spot size and drift to reliably achieve the desired features. Fig. 4.10 shows that the pattern quality is reduced beyond 12 pA and a patterning time of ∼20 s. The shortest patterning time for the 90-nm film is 28 s, over which time significant drift is accrued. Charging is implicitly mitigated by appropriate endpointing, where the dosage is chosen to be the minimum required to clear the gold, as any charge deposited

on the metal will be conducted away and few ions will impact and charge the substrate.

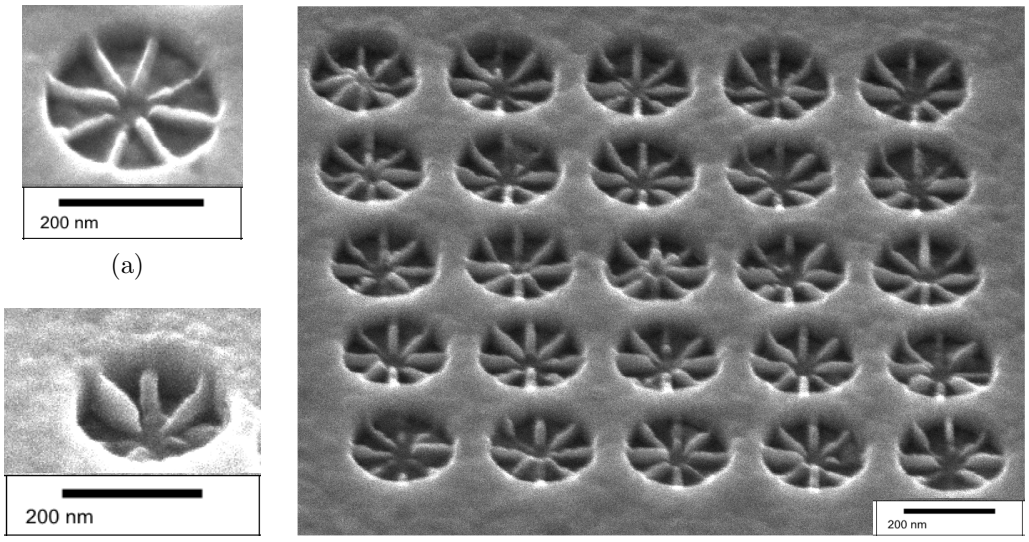

Figure 4.19: HIM micrograph showing (a) a cell patterned on the nominal 50-nm film, (b) a cell patterned on the 90-nm, and (c) the nominal 70-nm film small array, imaged at a 45° angle. Despite grain defects, the central area of each aperture is well-milled, and most wires are continuous. The wire thickness degrades towards the centre of the aperture, and approximate measurement of the depth shows each film lost 10 nm to the plasma cleaning process or deposition rate inaccuracy. Reproduced with permission from [182], ©2021 ACS.

Fig. 4.19c shows the 70-nm small array from Fig. 4.12b imaged at a 45° angle to show the topology of the fabricated features. Note that imaging the structure may have damaged some of the features, especially the thin, exposed nanowires. Due to the surface interaction volume being larger than the pixel size, the overall thickness of the nanowires is less than designed. However, almost all wires are continuous and the nanogaps at the tips are well-defined, despite the redeposition identified previously. Tuning the pixel size to be closer to the probe size may reduce overmilling, though overmilling will still occur due to vibrations and drift. Grain defects are present in the top-left and the central cells, but these defects are local and will have only a small effect on the overall MTS performance, as was shown in Fig. 4.16. Fig. 4.19 also allows an

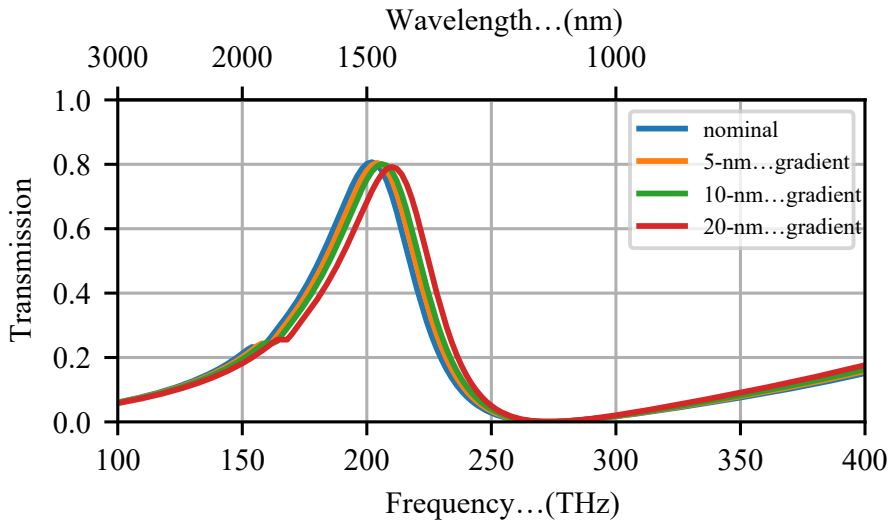

Figure 4.20: Transmission simulation with a thickness gradient applied to the nanowires. The labelled thickness is the difference between the nanowire thickness at the edge of the aperture (t = 50 nm) and at the nanowire tips at the centre of the aperture. Reproduced with permission from [182], ©2021 ACS.

approximate measurement for the depth of each aperture, which shows that each film is approximately 10 nm thinner than the nominal thickness due to the initial plasma cleaning.

To study the effects of the nanowires thinning toward the aperture centre, we applied a linear thickness gradient to the nanowires in simulation. The results in Fig. 4.20 show that although the wire thickness changes dramatically, the competing reduction in the capacitive coupling area holds the resonance frequency nearly constant. Since the wire thickness gradient defect is distributed over the majority of the patterned apertures, the overall effect on the MTS transmission should be uniform. With larger gradients, the resonance is blueshifted, which could compensate for other fabrication anomalies, such as redeposition and grain defects if the centre does not get shorted together.

4.5.6 Focus & Stigmation

Milling patterns while the beam is out of focus can simplify the process of focusing on a flat, featureless film. If the beam is focused to the wrong work-

ing distance the pattern is undermilled, even with ideal patterning parameters. Alternating patterning and refocusing on the milled pattern can tune the beam focus to create sharp patterns. Another challenge results from beam astigmatism, where patterns are sharp along one axis, but blurred along the other. As with focus, the issue can be resolved by patterning and then imaging while making small adjustments to the stigmation of the beam until a high-fidelity pattern is created. Alternating patterning and imaging to focus the beam is more sensitive than image focusing alone as the blurred, nm-scale features are sputtered away during the imaging process, then replenished with sharper patterned features that make judging the focus easier since the expected shape is known. The eight nanowires also make judging astigmatism simpler as the wires along the blurred axis are often entirely removed.

4.5.7 Array Drift

Problems with repeatability over a larger scale are caused by both defocusing and drift. When the pattern quality decreases across a large area of patterns, defocusing is the cause. Defocusing occurs when the working distance changes over the array area, either due to beam instabilities or sample tilt. Using too much carbon tape makes the sample difficult to remove from the stub, but using too little creates tilt. Correcting the sample tilt largely overcomes the defocusing problem. This can be done by modifying the mounting procedure to use an aluminum stub with mechanical clamps to hold the sample in place instead of putting carbon tape underneath the sample.

Drift was discussed above for a single pattern, but the time scales involved in creating large-area arrays exacerbate the problem. Improving drift over a long time scale requires increasing system stability by addressing environmental factors. This can be accomplished by leaving the room while patterning and using the microscope outside of peak facility hours to reduce sources of vibration, and/or allowing time for the system to stabilize after moving the stage. For example, the door to the room housing the HIM significantly skewed the beam. We found that closing the door to the room shifted the beam by $\sim$150 nm, and the beam shifted back when reopening the door. Moreover,

when processes requiring large pumps were started in the cleanroom next door, vibrations > 10 nm were observed and active patterning sessions were forced to stop. The drift introduced by the stage is reasonably well controlled if it is not moved for at least one hour prior to patterning. Once the stage has been moved to the desired area to be patterned, the beam should only be deflected within a fixed field of view (no stage motion or stitching).

Fig. 4.21 shows a large, 6 µm × 4.2 µm (20 × 14 unit-cell) array patterned into a 50-nm thick gold film over 100 minutes, after 100 minutes of stabilization time. This corresponds to a figure of merit of $F_{AF} = 6000/10 = 600$ or $F_{AF} = 4200/10 = 420$, both above the 400 defined earlier for wide-area nanopatterning. Unfortunately, we did not get the opportunity to characterize this MTS. Comparing the apertures on the right edge of the figure, a total drift of less than one half-period (< 150 nm), or, equivalently, a drift of ∼0.6 nm per 25-s aperture pattern, is observed. Another approach, used by Hahn *et al.* [38] to achieve a figure of merit of $F_{AF} = 10000/15 = 667$, is to pattern alignment marks near the desired MTS area that can be reimaged periodically to automatically correct for beam drift and stitch together larger arrays more accurately. Additionally, their results do not include nanogaps, making it clear that it is our combination of fine nanogaps *and* fine nanowires that have increased the fabrication challenge significantly.

To model the effects of array-scale drift on the overall MTS performance, the array pitch p can be varied. Since small variations in array pitch have little effect, the simulation results shown in Fig. 4.22 are computed in steps of 20 nm. This figure reproduces some of the data in Fig. 3.6, but on a linear scale. The reduced coupling between apertures as the pitch p increases results in lower bandwidth and a small blueshift of the resonance. Since the resonance mechanism of the MTS does not rely on a collective excitation of the apertures, the < 1-nm drift observed in Fig. 4.21 will have very little effect on the overall MTS performance. Even MTS structures that do rely on collective excitations may find a 0.3% tolerance on the array pitch tolerable (though realignment between rows may be necessary).

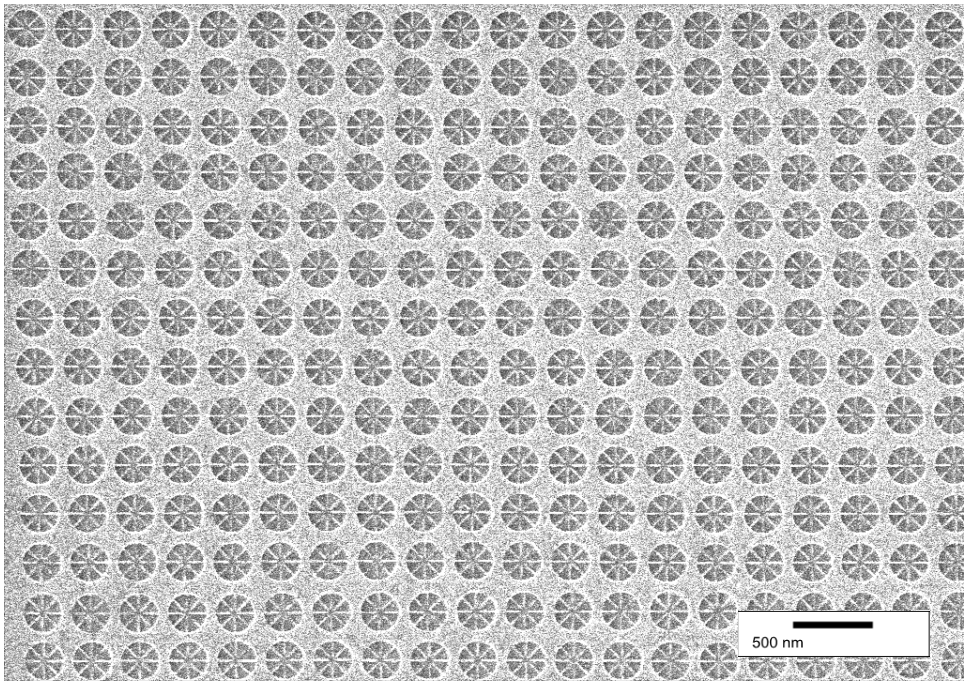

Figure 4.21: HIM micrograph depicting a large patterned array of $20 \times 14 = 280$ unit cells. Reproduced with permission from [182], ©2021 ACS.

4.6 Additional Process Development

We saw no resonance in the experiment, but the analysis presented above showed that simple overmilling of nanowires does not entirely remove the resonance. On the other hand, at least three mechanisms exist that can cause the nanowires to short together at the centre of the aperture: 1) grain defects, 2) redeposition, and 3) undermilling (drift, focus, dosage). In the following section, we develop procedures to mitigate these effects. Grain defects are mitigated by growing epitaxial films that exhibit a single grain orientation over the entire MTS area. Redeposition is mitigated partially by removing the substrate to allow the redeposited material to cover both sides of the film, but also by choices in the design of the realized pattern. The removal of the substrate also addresses the undermilling, as the contrast is significantly increased between fully milled and unmilled areas. Whereas the substrate is only a darker grey as it charges, no substrate is always entirely black.

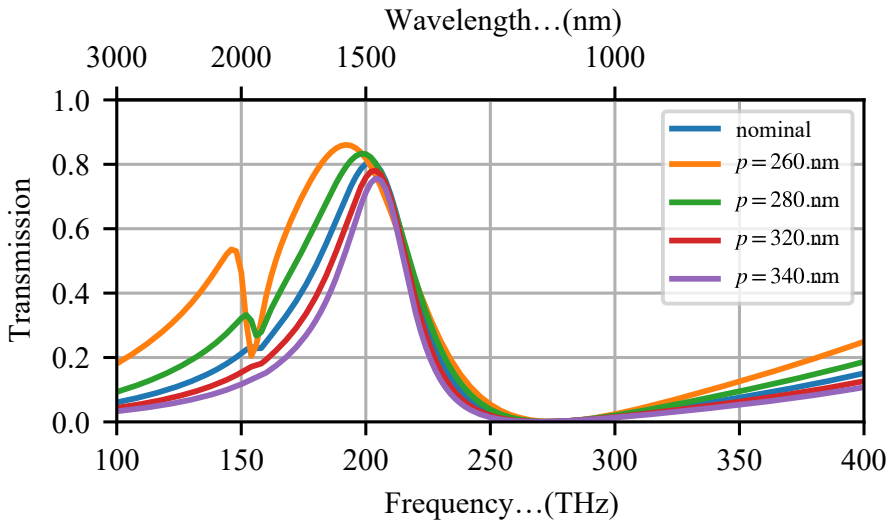

Figure 4.22: Simulation of array drift on the wagon-wheel aperture MTS transmission performance. The array pitch, p, is varied from 260 nm–340 nm in steps of 20 nm. Reproduced with permission from [182], ©2021 ACS.

4.6.1 Single-Crystal Gold Films

To mitigate the effects of the granular structure of the polycrystalline gold films on the HIM sputter rate, we studied growing epitaxial gold films in the nanoFAB Centre. Additionally, there has been a significant push to study many plasmonic structures fabricated in single-crystal gold films for their improved scattering properties, many of which could be improved with features as small as 10 nm [36], [76], [192]–[194]. A number of suitable processes exist based on vapour [195]–[198], liquid [192], [199], and solid-phase epitaxy [200], [201]. Liquid-phase epitaxy requires unavailable electrochemistry equipment, while the annealing required for solid-phase epitaxy can lead to undesired changes in film morphology. Hence we prefer to use vapour-phase epitaxy, which is more similar to our original deposition process. First, a suitable substrate must be found. It is simplest to grow epitaxial films on crystalline substrates that have a similar lattice parameter to the film crystal, which promotes adhesion and minimizes stress in the film. Gold has face-centred cubic (FCC) structure with a lattice constant of 4.08 Å [202]. Epitaxial growth of gold has been reported on LiF using a simple sputtering process on a heated

substrate, which is a simple cubic crystal with a well-matched lattice constant of 4.02 Å [203]. Epitaxial growth has also been reported on mica with a gold (111) crystal orientation and a 2.35-Å triangular lattice, matched to the (110) 4.5-Å hexagonal mica lattice [204]. Due to the lattice symmetry of mica, the epitaxial gold crystals may be grown in two different orientations, which can be problematic for growing large crystalline surfaces [205]. Deposition at higher temperatures causes one of the orientations to dominate.

Dr. Hryciw first attempted to grow an epitaxial film on a mica substrate (source unknown) that was readily available at the nanoFAB Centre, inspired by the process of Elbel *et al.* [196]. As shown in Fig. 4.23, our results were similar to others reported previously [206], where at room temperature, continuous polycrystalline films were grown, and at 400°C, larger epitaxial plateaus were grown but filled with large gaps and holes. We were unable to find a temperature at which a continuous, epitaxial film could be realized. Additionally, the films grown at room temperature showed significant problems with contamination. Despite no individual epitaxial plateau being sufficiently large to pattern a full array of apertures, patterning into a particular patch of the high-temperature-grown film was more consistent than in the previous polycrystalline films, allowing the creation of single particularly high-fidelity asterisks, as shown in Fig. 4.24. If this procedure were to be taken up again, perhaps an annealing step at the end would reduce the number of impurities and improve the structure of the film [197], [205].

The process of Fedotov *et al.* was more successful [195]. 1 cm^3 LiF crystals were sourced from United Crystals for the epitaxial film growth [207]. As directed, the crystals were cloven immediately before loading into the vacuum chamber for deposition. We set a razor blade on the edge of the crystal and hit the back of the razor blade with a small hammer, using a moderate amount of force. The razor blade needed to be held firmly against the crystal, otherwise, the blade would bounce off rather than cleave into the crystal between lattice planes. LiF was considerably more difficult to cleave than mica, and the cleaved surface of the crystal was rough. Nevertheless, numerous terraces large enough for plasmonic device fabrication were created. We deposited gold on

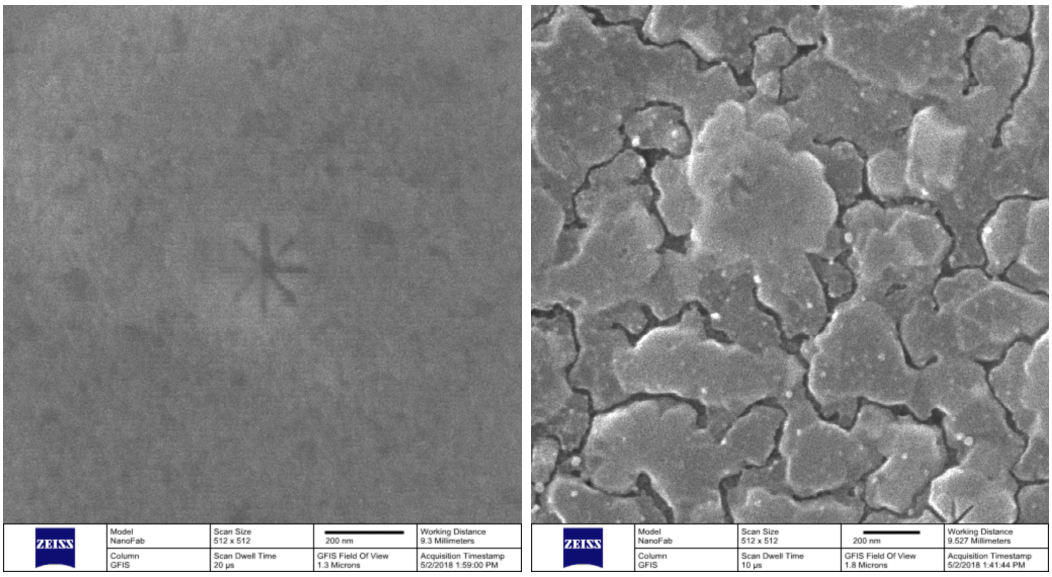

(a) (b)

Figure 4.23: HIM micrographs of the films grown on a mica substrate, (a) at room temperature, and (b) at 400°C.

LiF three times to grow a 100-nm thick film (courtesy of Dr. Hryciw), a 20-nm thick film, and a 65-nm thick film.

AFM Analysis

All three samples were inspected by atomic force microscope (AFM), x-ray diffraction (XRD), and HIM to determine their structural properties. Unfortunately, since there was no opportunity to mask the substrate during growth, a sharp edge for determining the film thickness cannot be found. The AFM results are shown in Fig. 4.25. The 100-nm film has a similar structure to the film grown at a high temperature on mica, though the gaps are thinner and more uniform. The 20-nm film also shows a similar profile, however, the gaps are smaller and the islands seem closer to coalescing to form a continuous film. The differences are likely due to temperature calibration as the first film was deposited shortly after the PVD system was installed and before it had been fully validated. Finally, the 65-nm film shows large areas of continuous film with small holes and low, 1-nm surface roughness. Here, the islands seen in Fig. 4.25b have coalesced, leaving small holes where dislocations were present

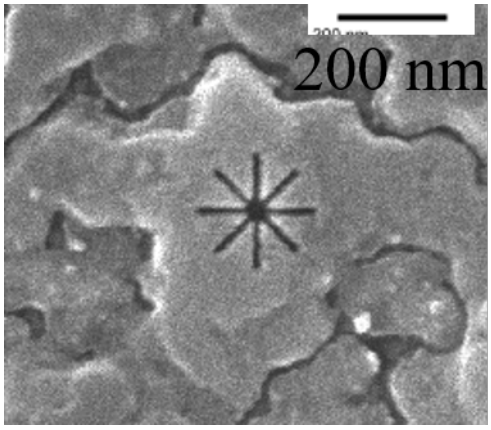

Figure 4.24: HIM micrograph showing a well-patterned asterisk aperture patterned into a gold film grown on mica at high temperatures.

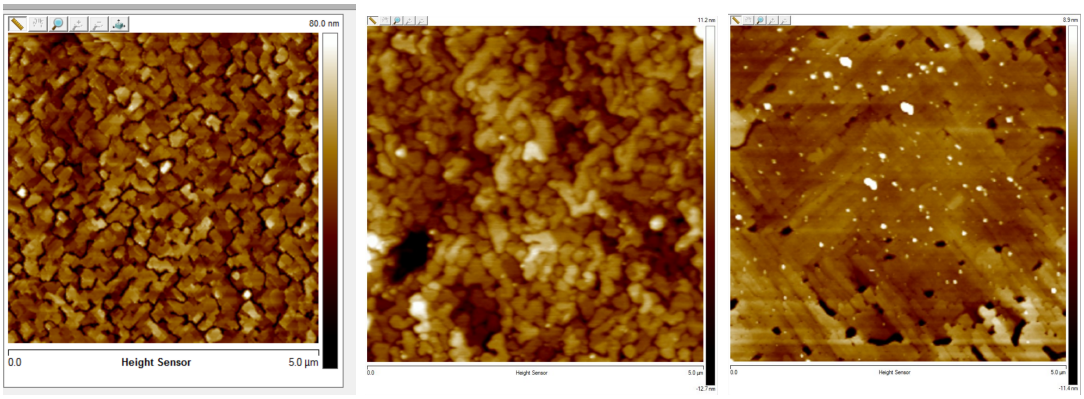

(a) (b) (c)

Figure 4.25: AFM micrographs of the various films grown on LiF, (a) the 100-nm film, courtesy of Dr. Aaron Hryciw, (b) the 20-nm, discontinuous film, and (c) the nearly continuous 65-nm film.

and continuing to the growth of a very flat film surface. Other parts of the surface of the 65-nm specimen produce AFM micrographs more similar to those presented for the 100-nm and 20-nm samples, which is due to temperature variations over the sample surface as LiF has low thermal conductivity. If repeated, the high-temperature soaking time should be increased to improve the uniformity of the film.

XRD Analysis

Next, we confirmed the crystal structure of the films grown on LiF with XRD analysis, and the results are shown in Fig. 4.26. The 100-nm film shows clear

peaks for many gold crystal orientations, indicating that the film is polycrystalline and thus was discarded. The 20-nm film was too thin to collect a strong XRD signal, and the spectrum is dominated by the LiF substrate. The 65-nm film shows a large peak at the LiF (200) angle, a smaller peak near the Au (200) angle, and a very small peak at the other Au (111) crystal angle, indicating a strong preference for the Au (100) orientation in the film. The sample was difficult to mount onto the XRD stage as the bottom surface of the cleaved crystal was not flat, which led to some misalignment of the results. The Au (200) peak is shifted and wide, which indicates that some dislocations were formed during the coalescence of the film, either due to the poorly cleaved surface or displacement/rotation misfits [205], [208]. When compared to the results achieved by Fedotov *et al.*, a similar arrangement of the relative peak intensities is seen. Additional tuning of the deposition parameters, the cleaving procedure, and the XRD measurement may improve these results, but our 65-nm film is of sufficient quality to eliminate grain defects in HIM milling.

HIM Analysis

Finally, the films were inspected with the HIM. A solid conductive path could not be established on the 20-nm film due to its low continuity. To image the sample, the electron flood gun was activated to dissipate the deposited charge. The collected micrograph is shown in Fig. 4.27a. While the contrast is not particularly clear, islands of gold can be seen across the surface of the sample, along with a clear cleavage boundary of the underlying LiF crystal. Fig. 4.27b shows the results for the 65-nm film, where the film is largely flat. Some pitting is visible, and gaps are seen along crystal cleavage boundaries in other parts of the film. Otherwise, the film is largely continuous and no grain contrast is seen. The detailed processing parameters in Appendix E have hence been validated for the epitaxial growth of gold on LiF in the nanoFAB Centre.

4.6.2 Substrate Removal

As mentioned previously, the implantation of helium into a crystalline substrate can cause the substrate to swell as the helium diffuses and coalesces

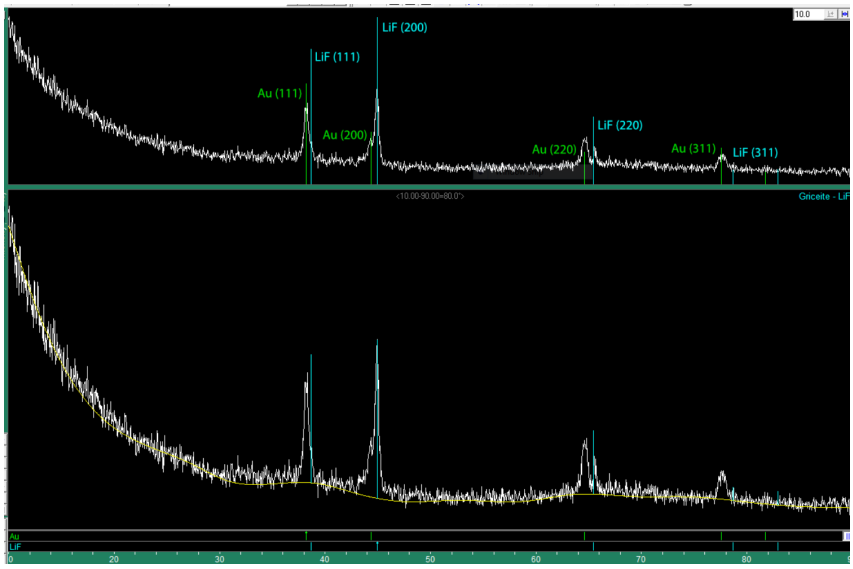

(a)

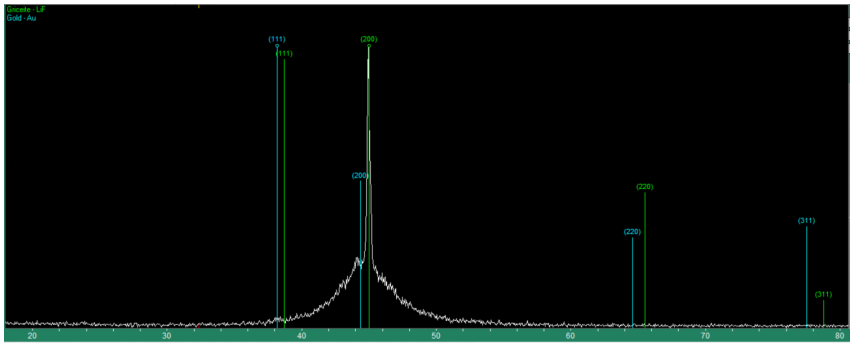

(b)

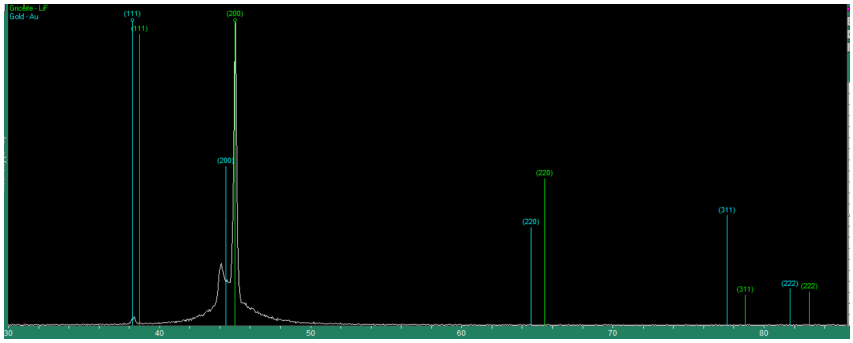

(c)

Figure 4.26: XRD spectra for (a) the 100-nm film on LiF, courtesy of Dr. Aaron Hryciw, (b) the 20-nm film on LiF, and (c) the 65-nm film on LiF.

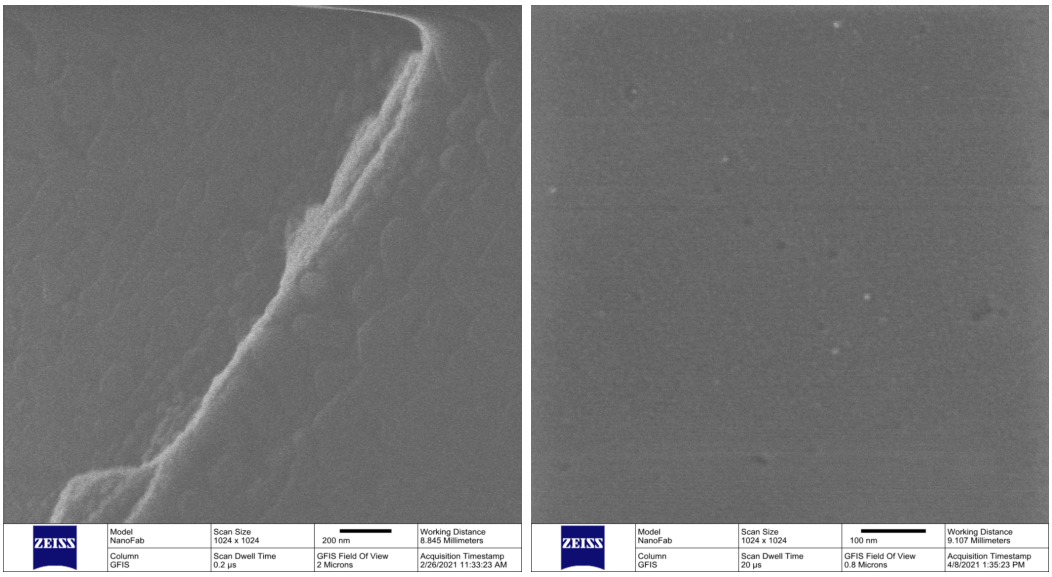

(a) (b)

Figure 4.27: HIM micrographs of (a) the 20-nm film on LiF, and (b) the 65-nm film on LiF.

into bubbles within the crystal. In an amorphous substrate, the reduced order causes the helium to prefer to diffuse out of the substrate rather than collect into nanobubbles. When patterning films that were grown on LiF, this problem becomes increasingly obvious as more gold is milled away. An example of an overmilled single aperture is shown in Fig. 4.28a. The film has buckled and a rectangular bubble has appeared next to the aperture, while the aperture wires have been destroyed. This problem accrues as more apertures are milled, and the bright area in Fig. 4.28b, taken at a 45° angle, shows a bubble formed under a small array of apertures. Thus to reliably pattern subwavelength features into this nearly epitaxial film over a wide area, the crystalline substrate must be removed and the film must either be transferred to an amorphous substrate or simply left free-standing.

In the present study, we left the film free-standing by mounting flakes of the film onto copper TEM grids. Since our example uses a continuous film of gold, we do not need the structural support of a substrate (as would be required for a nanoantenna array), though transferring the film to an amorphous substrate is a common procedure [192], [193], [209]. This allows us to avoid the

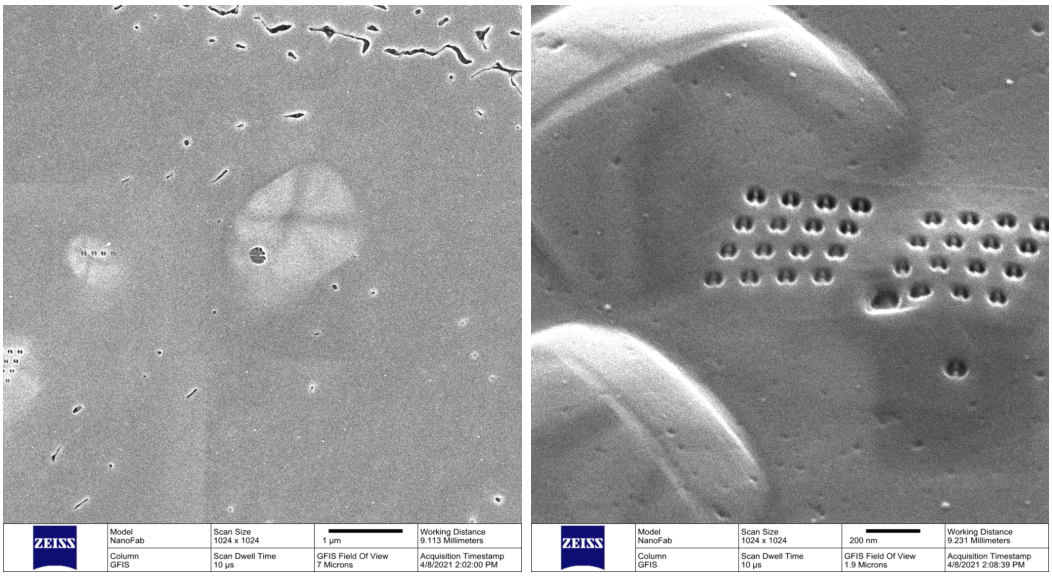

(a) (b)

Figure 4.28: HIM micrographs of the films grown on LiF, showing (a) a bubble created by the overmilling of a single aperture taken normal incidence, and (b) a bubble created by patterning a small array of apertures taken at a 45° angle to accentuate the topography.

complications of substrate charge accumulation and sputtered material can be redeposited on both sides of the film. The drawbacks of this approach are that the film may flex where there is no support and films of contaminants may be grown on both sides of the metal. Interestingly, we found that the film can be driven into a mechanical membrane resonance while patterning when the film is thin or poorly supported by the grid, but that the thicker film areas or those close to the grid boundaries could not. Such a patterned membrane could be used as an optically controlled or probed capacitive sensor for temperature, pressure, or photoacoustic applications.

As a first test case, we deposited films on NaCl rock salt crystals for substrate removal as NaCl is very soluble in water. In a similar manner to the LiF crystals, the NaCl 1 cm^3 crystals were cleaved immediately before loading into the evaporation chamber, and 50 nm of gold was deposited. Since we intended to remove the substrate, no adhesion layer was required. The TEM grids are small, so the film was cut into smaller sections using a razor blade prior to dissolving the substrate. The crystal was then slowly lowered into a

beaker of de-ionized (DI) water, and the film was able to lift off and float on the water surface as the crystal dissolved. The copper TEM grids were then used to fish the films off the water surface and were dried with filter paper. This produced many TEM grids with free-standing gold films well-adhered to them. Unfortunately, when these samples were brought to the HIM, their patterning was inconsistent and produced very odd shapes. This observation was addressed in Sec. 4.2.3 above.

LiF has much lower solubility than NaCl in water. Datasheets often list the solubility of LiF in HF as well, which is much higher than its solubility in water, but still lower than NaCl's [210]. As a second test case, the LiF sample with the thin 20-nm film was processed with HF first. We found that the lower solubility of LiF made the process of slowly lowering the crystal into the HF ineffective, and the film did not lift off immediately. Instead, the sample was submerged entirely in HF for 5 minutes then carefully removed, and without drying, transferred to a beaker of water. As soon as the crystal made contact with the water, the gold film lifted off and floated on the water's surface. Since the film was discontinuous, it shattered into numerous small pieces, and no single piece was large enough to fish out with a TEM grid. With the same process applied to the 65-nm thick sample, a few sections of the film separated and were easily retrieved with TEM grids.

The samples prepared this way were reliable to pattern, showing no problems with contamination, grain defects, or charging/swelling. These films were used for the final results presented in Sec. 4.7.

4.7 Two-Wire MTS

4.7.1 Two-Wire MTS Fabrication

Throughout this chapter, we have discovered the most important factors to create reproducible, fine features over a wide area with the HIM. Patterns milled in a single step are more reliable as redeposition and contamination can be better controlled. Structures exhibiting symmetry are more robust to grain defects, but these defects can be eliminated with single-crystal films.

Crystalline substrates must be avoided, and careful choice of the ion dosage is required to use insulating amorphous substrates. Poor cleanliness is difficult to address at later stages in the fabrication process, requiring destructive plasma cleaning, and should thus be eliminated as early as possible. Time permitting, the microscope should be allowed to stabilize as long as possible between loading, moving the stage, and patterning to reduce drift. As the patterning area increases, the mounting procedure of the sample on the microscope stub becomes increasingly important and methods to eliminate tilt must be applied.

For the patterning parameters, the dosage to clear must be established first to minimize overmilling. The current and spot size should then be tuned simultaneously to achieve the desired feature size over a cell in the minimum patterning time to avoid drift. Finally, the dwell time should be tuned to minimize the redeposition on nearby features.

Combining these recommendations, we patterned the ∼65-nm thick epitaxial film that was grown on LiF and transferred to a TEM grid. A mechanical clamp was used to secure the grid in place on the SEM stub, reduce tilt, and maintain conductivity. In this case, no contamination growth was observed, hence the plasma-cleaning step was omitted. The pattern used was the two-wire MTM-lined aperture design, and each aperture was milled in a single step (unlike what was shown in Fig. 4.6). The nominal array feature sizes were an aperture radius of $b = 40$ nm, a gap and wire size of $g = w = 10$ nm, and an array pitch of $p = 120$ nm. The relatively large pitch was chosen to reduce the effect of redeposition on the nanowires. The fabrication was performed shortly after a new trimer was formed and the gas pressure was increased from the nominal imaging pressure of 2×10^{-6} Torr to 5×10^{-6} Torr, resulting in a current of 9 pA. Although the current varied during patterning, the nominal patterning time for a single aperture was ∼10 s. Otherwise, the beam parameters were chosen based on the best results achieved in Sec. 4.3.

One final important modification to the fabrication process was the inclusion of the drift-correction feature of NPVE. This feature images an area with alignment marks near the patterned area and uses an image recognition algo-

rithm to estimate the degree of drift of the beam, then attempts to recenter the beam before continuing with the patterning process. This feature was simple to integrate into our patterning workflow by choosing to pattern near an area of the film where holes were formed during film growth (along a poorly cleaved crystal boundary of the LiF substrate), and we corrected the drift every 60 s. Due to the high current used while milling, the continuous scanning of the reference area changed the shape of the holes by parasitic milling and redeposition, and the reference image had to be recollected when the image processing algorithm failed. This led to some dislocations of the array, but overall, the drift-correction feature removed a significant amount of the drift normally observed while patterning large arrays. An option to automatically reset the reference when the comparison algorithm certainty becomes low would allow these additional dislocations to be removed. The imaging and drift correction, along with the slowly decaying current from the source, slowed the patterning speed to an average of about 15 s per aperture.

We fabricated a 4.8×4.2 µm^2 array of 40×35 MTS cells in approximately six continuous hours of patterning, with the result shown in Fig. 4.29. The full array is composed of smaller 5×5 arrays to minimize the effect of drift and redeposition on nearest neighbour apertures. From these images, the patterned features measure $b = \sim$35 nm, $w = \sim$15 nm, $g = \sim$10 nm, and $p =$ 120 nm, with variations of these dimensions on the order of < 1 nm. With the 10-nm feature size, the reliability figure-of-merit is $F_{AF} = (480, 420)$. We attribute the difference between the nominal and patterned feature sizes to the redeposition of gold as later apertures are milled, which may be partially corrected by overmilling the apertures, or, if the array drift is sufficiently well-controlled, can be corrected in a second pass. This is much more practical over very small arrays.

4.7.2 Two-Wire MTS Characterization

The two-wire MTS shown in Fig. 4.29, with nominal array feature sizes of $b =$ 40 nm, $g = w = 10$ nm, and $p = 120$ nm, was characterized in reflection mode using a home-made microscope assembled by Kyle Scheuer in the DeCorby

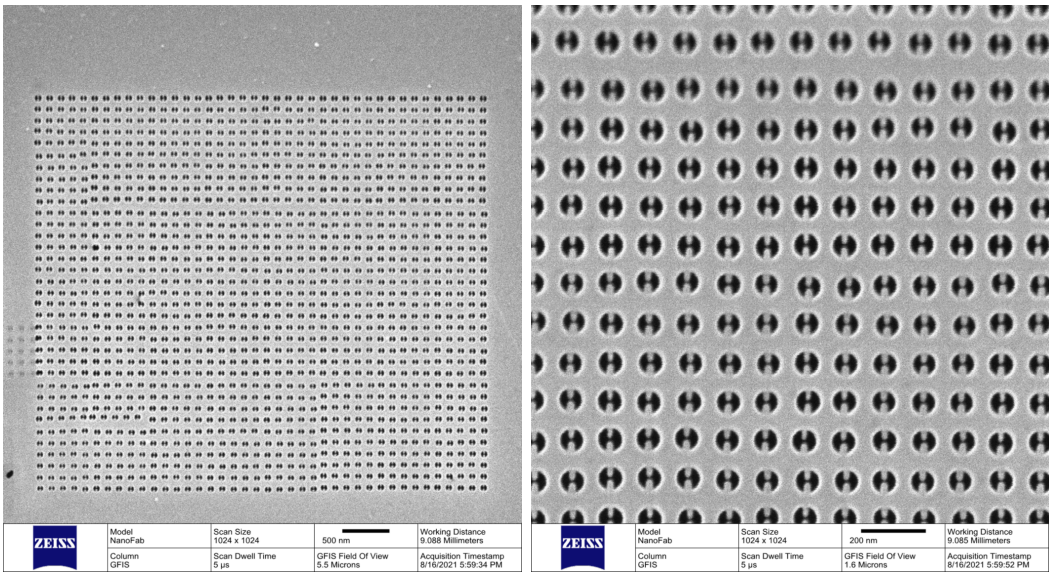

(a) (b)

Figure 4.29: HIM micrographs showing (a) the 40 × 35-cell MTS array, and (b) the same array magnified to better resolve the features.

lab at the University of Alberta. The details of the microscope layout and components are available in Appendix E. With low stage control precision, it was difficult to ensure that the MTS was fully illuminated during measurement.

The whole SEM stub used during fabrication was mounted to the microscope stage, and carbon tape was affixed to the very edge of the TEM grid to ensure the grid did not move while the clamp was removed. Since the MTS is polarization-sensitive, the goal of the measurement was to observe a contrast between opposite linearly polarized spectra to see the full effect of the resonant nanowire loading. The measurement was first attempted with a polarizer on the input beam between the neutral density filter and the first beamsplitter, however, a small misalignment of the polarizer's rotation axis caused the beam to scan in a circle on the sample as the polarizer was rotated. This, in turn, led to collecting the MTS spectrum for only a fraction of the measured polarization angles but minimized the optical power on the MTS. With the polarizer on the output, the MTS spectrum can always be collected, though some small differences in power levels may occur due to the movement of the beam on the output collection fibre face. Using a large-core collection fibre

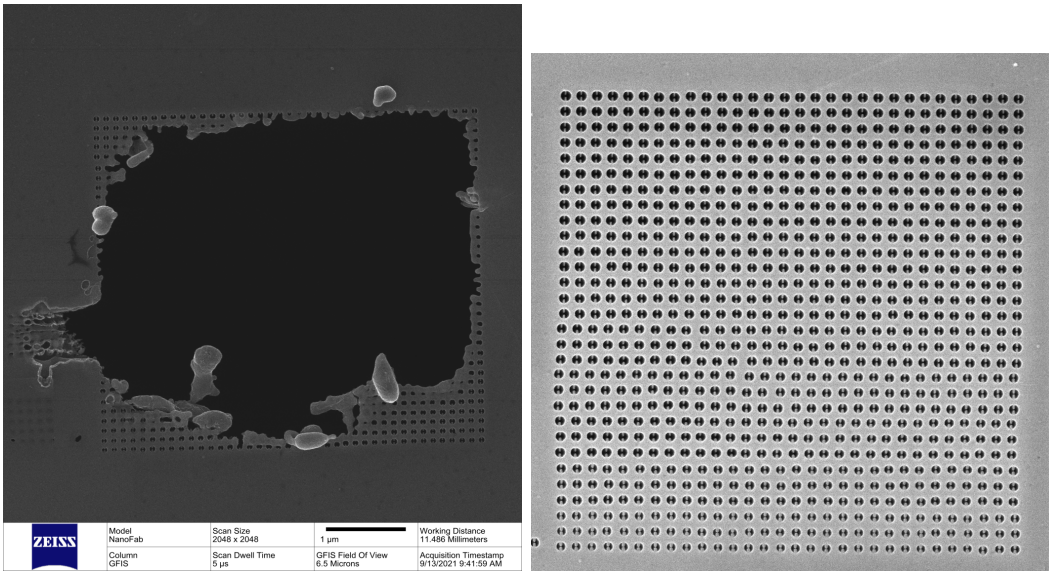

(a) (b)

Figure 4.30: (a) Melted two-wire MTM-lined aperture MTS from Fig. 4.29a after illumination, and (b) second patterned array, fabricated under suboptimal current and stability conditions.

minimizes this effect.

Another challenge that arose during our first attempt to measure the MTS spectrum was the power deposited by the supercontinuum source. The simulations in Ch. 3 showed that, at resonance, the loss in the MTS is significant. Despite the neutral density filter, the ohmic heating by the source caused the MTS to be melted away, as shown in Fig. 4.30a. The source power (*i.e.*, duty cycle) was reduced to 20% for subsequent experiments to avoid melting the MTS, though a preferable approach would be to use a wavelength-scanned (or filtered) laser and measure less of the spectrum at a time. Two more MTS arrays were fabricated (the best is shown in Fig. 4.30b), but with poorer feature fidelity as the trimer was older and a lower maximum current could be achieved.

Background reflection spectra were collected for the gold film and polarizer angles between 0°–180° in steps of 10°, and from 180°–360° in steps of 30°. If no alignment issues are present, the second half of the polarization angles should be identical to the first half, and hence are redundant and were reduced to save time. We note that the spectral response of a number of the optical

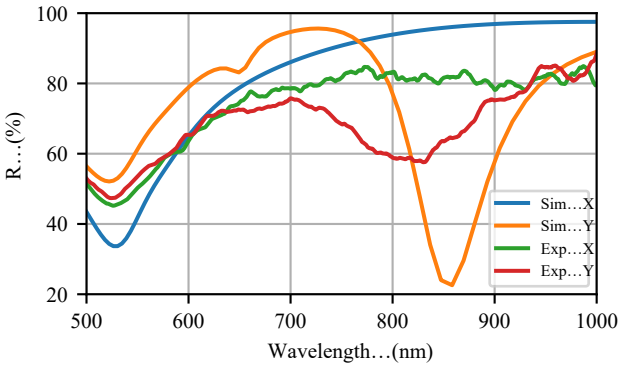

Figure 4.31: Experimental data normalized to the raw gold film background compared to nominal simulation data. The experimental data were smoothed using a 31-sample Savitzky-Golay filter, and the nominal geometric parameters were $b = 40$ nm, $g = w = 10$ nm, $p = 120$ nm, and $t = 65$ nm.

elements in the beam path (particularly the beamsplitters) were not uniform over all polarization angles, and hence the background spectra varied wildly for orthogonal polarizations. The stage was then moved to center the beam on the MTS, and spectra were collected for the same polarizer angles. The normalized reflection measurement is the ratio between the MTS reflectance and the background reflectance, which removes the effect of all the optical elements common to both measurements and leaves just the MTS spectrum.

To find the array axes with respect to the polarizer angle, we compared each normalized measurement to its orthogonal polarization angle. The polarizer proved to be well-aligned to the array axes, and the maximum difference was found to occur between the 0° and 90° cases. These cases are plotted in Fig. 4.31, where the data were smoothed through a 31-sample Savitzky-Golay filter. For comparison, the simulation data for the nominal MTS design and a thickness $t = 65$ nm are also overlaid, normalized to a simulated solid 65-nm thick gold layer background spectrum. In the vicinity of the designed resonance, the experimental reflection of the surface is significantly lower when excited with a vertically-polarized beam than with a horizontally-polarized beam. This is clear evidence that the MTS is operating as designed, though fabrication tolerances and experimental inaccuracies have shifted the resonance and reduced its strength.

Next, we consider the differences between the experiment and the simulation. First, we address the nonresonant x-polarized spectrum since it is independent of the fine, 10-nm features and has fewer confounding factors. When comparing to the simulation, there are three main features to be matched: i) the location of the material-based absorption peak of gold at ∼500 nm, ii) the level of the gold absorption peak at ∼500 nm, and iii) the overall reflectance.

The location of the gold absorption peak (or equivalently, the minimum reflectance) is controlled by the filling fraction of the array and the gold film thickness, where thicker films and smaller apertures marginally blueshift the observed minimum. Rough measurements made on Fig. 4.30b show that the designed aperture radius was well-patterned in experiment, and the radius varies from ∼39–41 nm. Additional simulations with a 40-nm aperture radius match the reflectance minimum wavelength best for a film thickness of 65 nm.

With the film thickness and aperture radius set, no geometric variables remain to match the nonresonant absorption level. We expect that the difficulties in evaluating the alignment of the optical beam to the patterned MTS area caused a fraction of the collected signal to be collected from the solid unpatterned surface near the MTS, rather than the MTS itself. To account for this difference, a scaling factor is added to the simulated spectrum:

$$R = (1 - BG_{ratio})R_0 + BG_{ratio}, \tag{4.1}$$

where R_0 is the original simulated spectrum and the total has been normalized to the background spectrum (hence BG_{ratio} is constant with frequency). This correction could be avoided by using a digital stage with more precise spatial control and aligning to the location on the sample with the minimum total reflectance.

Eq. (4.1) is only able to increase the reflection amplitude and hence even with the above corrections, the x-polarized spectra will never match from 650–1000 nm. We note that, curiously, the experimental scattered power is nearly constant over this range and never exceeds 85%, even over all polarization angles. Due to gold's high conductivity in the NIR, all variations of b and t

in simulation show nearly 100% reflectance at 1000 nm. Moreover, a change in the surface conductivity (which would model the potential damage to the film by the HIM) does not substantially improve the agreement. As a result, a shift in the alignment of the microscope between the background and the MTS measurement must have caused a uniform ∼15% drop in the collected power, and we introduce a power normalization factor P_{Exp} to correct the expected power level. With the correction factors, P_{Exp} and BG_{ratio}, the nonresonant experimental spectrum can be reliably matched to the x-polarized simulation spectrum.

Finally, the resonant spectrum (y-polarized excitation) must be matched. We showed in Fig. 4.19 that, when patterning fine features with the HIM, some overmilling of 10-nm wires is difficult to avoid. This leads to a thickness gradient along the wire or a uniform decrease in the wire thickness. In the present case, the low current during fabrication exacerbated this issue, significantly overmilling the nanowires. Fig. 4.32 shows an inspection of the MTS after the optical measurement with an incidence angle of 45°, such that the profile of the nanowires can be seen. A rough estimate of the film thickness in these images is t_f =∼62 nm, which is close to the thickness expected from the previous simulations, and the nanowire thickness is approximately $t_w = 42$ nm. The nanogap widths were measured to vary between $g = 11$–14 nm, and the nanowire widths were measured to vary between $w = 11$–13 nm. Despite the high resolution of these images, no grain contrast is observed, confirming the sufficiently high crystal quality of the gold film (as compared to, *e.g.*, Fig. 4.6 deposited on NaCl). Additionally, the wires are significantly more rounded than those originally modelled in simulation.

The simulation model that incorporates all the geometrical variations of the fabricated MTS is shown in Fig. 4.33, with the geometrical parameters summarized in Table 4.1. The simulation model is divided into four 2×2 sections that represent the extremes of the geometric variations observed. With b, w, and g corrected, the resonant minimum reflection continues to maintain a very low value near 20%, and it is the incorporation of the overmilling of the nanowires (*i.e.*, t_w) that corrects this discrepancy. To highlight this change, a

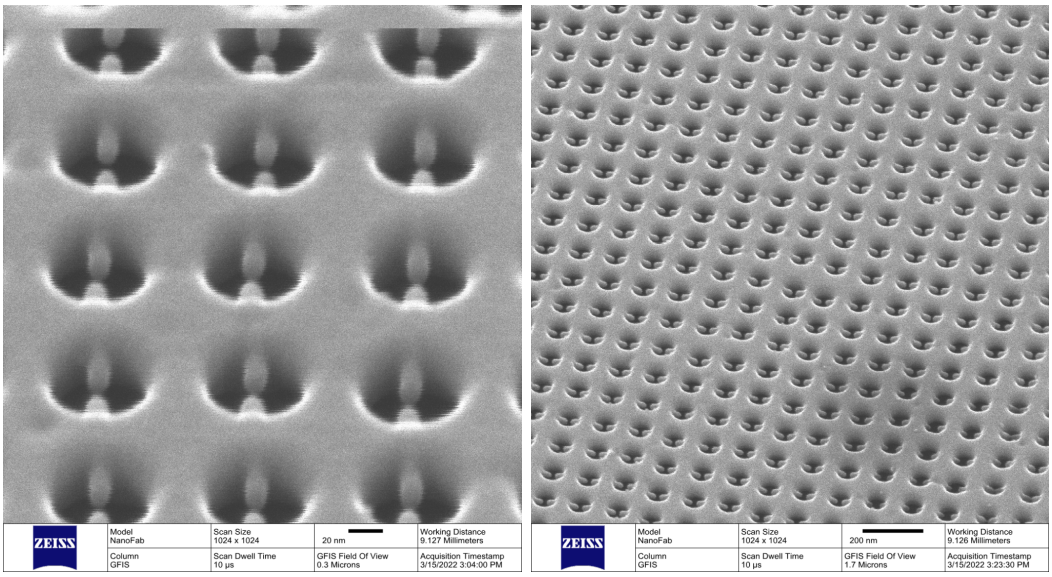

(a) (b)

Figure 4.32: Profile view of the fabricated MTS array at 45° oblique incidence, (a) parallel to the patterned nanowires, and (b) rotated with respect to the nanowires.

Aperture	b	w	g	t_f	t_w	p
1	39	13	11	65	40	120
2	39	11	14	65	40	120
3	41	13	11	65	40	120
4	41	11	11	65	40	120

Table 4.1: Geometric parameters used in the nonuniform simulation model.

cutaway is shown in Fig. 4.33b, where the top, bottom and front surfaces of an aperture have been hidden.

Fig. 4.34 shows the spectra computed in COMSOL, matched to the experimental data for both incident polarizations, where $BG_{ratio} = 0.26$ and $P_{Exp} = 1.17$ have been tuned numerically for the best possible agreement. The resonance frequency was shifted by the variation in b, g, and w, though the overall bandwidth below 80% reflection is not significantly increased. Shifting t_f does not change the resonance frequency, which agrees well with our circuit model derived in Sec. 3.2.1, but instead reduces the resonance amplitude by increasing the real part of the nanowire impedance at resonance. We believe that the ∼10% difference between 550–750 nm for the y-polarized excitation would

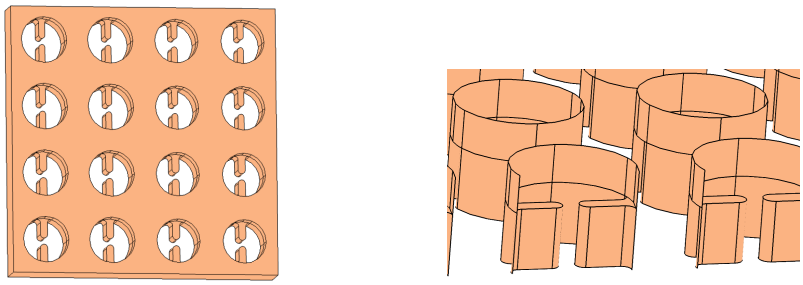

(a) (b)

Figure 4.33: (a) Simulation model layout incorporating fabrication variation. The array is divided into four 2×2 cells, and (b) shows a cutaway highlighting the reduced nanowire thickness.

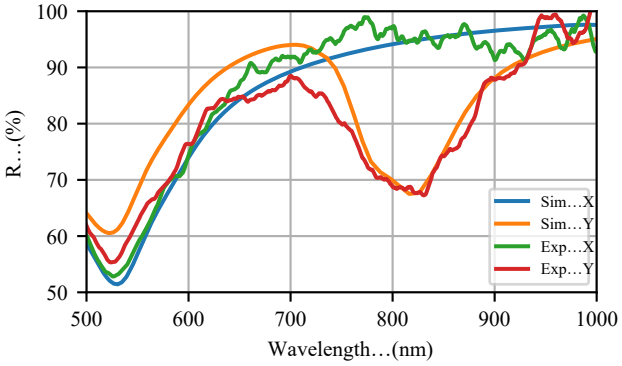

Figure 4.34: Final simulation results, tuned to match the experimentally acquired spectra. $BG_{ratio} = 0.26$ and $P_{Exp} = 1.17$.

be resolved by considering the rounding of all edges observed in Fig. 4.32.

Despite imperfect fabrication conditions, we have shown experimentally that polarization-sensitive resonances can be excited in a two-wire MTM-lined aperture MTS at optical frequencies. With the small shifts in plasmonic resonance frequency, sweeping the wavelength of a probe beam within the nanoaperture resonance band may allow faster, parallel resonant imaging of a sample surface or liquid analyte. Intentionally reducing the nanowire thickness also more tightly localizes the enhanced electric field at resonance, providing more precise control over the location of electromagnetically trapped particles for characterization by SERS or SEIRA.

Even with reduced source power, the apertures in the bottom-right of Fig. 4.32b show evidence of melting. These particular apertures were clearly

overmilled originally, creating thinner wires and inducing additional ohmic losses that were not present in the better-patterned cells. When sufficient fabrication fidelity cannot be achieved, near-field excitation or probing of the MTM-lined aperture MTS with a monochromatic or filtered source may be ideal [211]. For applications where the high temperatures may be desired, such as heat-assisted magnetic recording, a passivation layer could be used to increase the MTS durability [212].

4.8 MIR MTS

4.8.1 EBL Process

A recent collaboration between the Quantum NanoFab Facility (QNF) at Waterloo University and the nanoFAB Centre at the University of Alberta allows researchers at the University of Alberta access to QNF's 100 kV EBL system. This system has much better reproducibility than the HIM but has lower patterning resolution and the aspect ratio is limited since the preferred fabrication technique is lift-off.

In this section, we describe the EBL process used to fabricate the MIR MTS and the challenges faced in its development. This fabrication project was one of the first to make use of the collaboration between the QNF and the nanoFAB, hence no standard operating procedure was in place. Moreover, ZnSe was a new material to both groups and thus some process development was required. We modelled the liftoff process after the standard polymethyl methacrylate (PMMA) bilayer procedure used with the nanoFAB Centre's RAITH150 Two EBL system [213].

The EBL exposure process is shown pictographically in Fig. 4.35 and these steps were performed by the nanoFAB and QNF staff. The sample is first coated in a layer of PMMA 495K resist (the number referring to the molecular weight of the polymer), then a layer of PMMA 950k is added on top. The PMMA 495K is easier to dissolve during the later liftoff process, while the PMMA 950K layer is more durable. Next, a layer of Electra 92 is added as a conductive layer to dissipate charge during the EBL exposure. The sample was

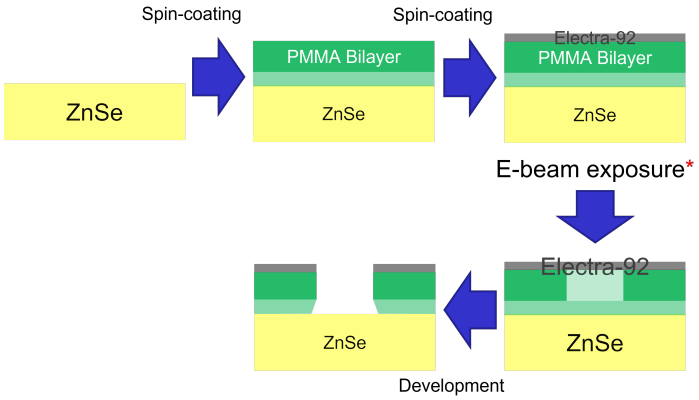

Figure 4.35: Pictographic representation of the EBL exposure process.

then shipped to Waterloo for the electron beam exposure and returned to the University of Alberta for development, where the Electra 92 is also rinsed off. This process leaves holes in the shape of the desired patterns where the PMMA resist was exposed and the polymer was broken down. The majority of the exposure process is identical to the standard operating procedure already in place, other than the electron dosage required to clear the PMMA resist during exposure to the 100 kV electron beam since it is not available locally. The second half of the fabrication process, the liftoff, consists of two steps. First, gold is deposited across the whole sample using electron beam evaporation, and second, the PMMA layer is dissolved in acetone with sonication to remove the gold from the areas that were not exposed to the electron beam. Full details are available in Appendix E.

Three 12.5 mm×1 mm round, polished ZnSe windows were purchased from Edmund Optics [214]. The first chip was used to validate the compatibility of the EBL lift-off process with the new materials and to find the required electron beam dosage for clearing the PMMA. The layout consisted of two 0.2 mm×0.2 mm arrays of discs side-by-side, one with nominal MTM loading ($w = g = 100$ nm, $b = 2.4$ µm) and the other unloaded. Nine of these array pairs were patterned with dosages ranging from 600 µC/cm^2 to 1400 µC/cm^2 in steps of 100 µC/cm^2. No problems arose in the coating of the sample with PMMA or Electra 92. During EBL exposure, the operator found that the high transparency of ZnSe throughout the MIR caused errors with the

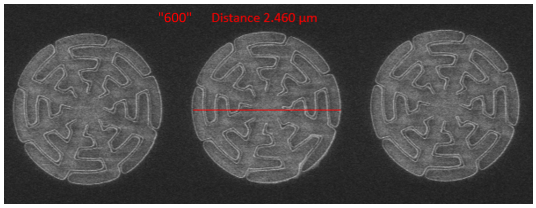

(a)

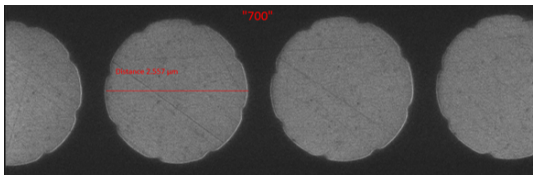

(b)

Figure 4.36: HIM micrographs of the overexposed patterns on the first sample after development for (a) an electron beam dosage of 600 µC/cm^2, and (b) an electron beam dosage of 700 µC/cm^2.

height alignment laser of the EBL system. These errors led to overdosage of the sample that destroyed the majority of the finely patterned features but were resolved by the operator for future experiments. Fig. 4.36 shows HIM micrographs of the developed PMMA resist for dosages of 600 µC/cm^2 and 700 µC/cm^2, where it is clear that the overdosage of the pattern has increased the overall radius of the disc, and that when the features were not entirely removed, their size was significantly altered. At the maximum dosage of 1400 µC/cm^2, the discs merged. A second sample was prepared and exposed to reduced electron beam dosages ranging from 400 µC/cm^2 to 800 µC/cm^2 in steps of 50 µC/cm^2 for further study. The exposure results were similar, with the complete overexposure of the MTS unit cells above 650 µC/cm^2.

The liftoff process was performed on both samples to validate the remaining processing steps. Specifically, the adhesion of gold to a ZnSe substrate has not been studied in detail in the literature, although there exist indications that ZnSe makes for an excellent adhesion layer between gold and ThF_4 [215]. Unfortunately, the minimum thickness to create a continuous gold film was not reported. Gold was deposited onto the sample by electron-beam evaporation, during which the crystal thickness monitor failed at a thickness of 37.8 nm, and the shutter was eventually closed at a thickness near 40 nm.

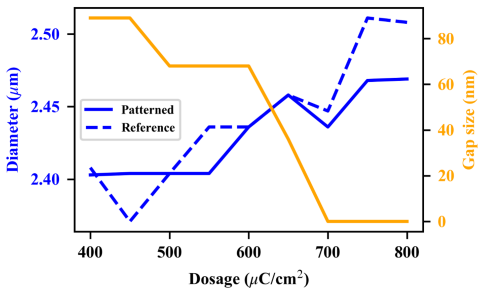

Figure 4.37: Geometric parameters of second MTM-lined disc arrays fabricated by EBL for electron beam dosages of 400–800 µC/cm^2.

The samples were placed in an acetone bath overnight to dissolve the PMMA bilayer, then transferred to a smaller beaker for sonication to dislodge the gold layer. The first sample was dried during the transfer process to inspect the chip and ensure the MTS elements were still intact, but this drying process caused the delaminated film to stick to the substrate, and the film proved impossible to remove entirely. Nevertheless, the desired MTS elements were well-adhered to the substrate and did not delaminate even after several minutes of sonication. The second chip was sonicated without drying, and the gold layer was easily removed.

4.8.2 MIR Fabrication Analysis

The second sample was inspected in the HIM to confirm the expected feature sizes. The use of the HIM here is important as the sample is insulating, and will accumulate charge as it is imaged. For an ion beam, this charge is guaranteed to be positive and can thus be neutralized with a low-energy flood of electrons across the surface. This does, however, reduce the ion dosage that can be applied while imaging, and hence reduces the achievable image quality. The measured feature sizes are summarized in Fig. 4.37, where the nominal feature sizes are a diameter of 2.4 µm, and a gap size of 100 nm. The lowest dosages approximate the nominal feature sizes best.

Despite choosing 100 nm as the minimum feature size to leave a large margin for fabrication difficulties, these results show that gaps as small as 70 nm can be fabricated with the process described here. With this in mind, for the

third and final prototype, the minimum feature size was tuned to 80 nm to increase the intensity enhancement factor, F_I. The gap size was reduced to $g = 80$ nm, the wire size was increased to $w = 110$ nm to compensate for the shift in resonance frequency, and the overall unit cell diameter was shifted to $b = 2280$ nm to keep the same number of meanders in the gap. Each array was exposed to an electron beam dosage between 200 and 600 µC/cm^2 in 50 µC/cm^2 increments (centered at 400 µC/cm^2 based on the results above). Arrays with dosages below 450 µC/cm^2 were underexposed and became underdeveloped, which caused them to lift off entirely in the final sonication step.

Helium ion micrographs of the fabricated arrays on the third and final sample are shown in Fig. 4.38. Measurements of the unit-cell features are plotted against the EBL dosage in Fig. 4.39 for the patterned (MTM-loaded) and reference arrays. The pattern with a dosage of 450 µC/cm^2 approximates the designed feature size ($w, g = 110, 80$) best, and also has the highest total sum of feature sizes at 195 nm. Unfortunately, some of the capacitor fingers at this dosage are underdeveloped and those fingers have lifted during the lift-off process. The sum of the feature sizes is nearly constant over the full dosage range, hence all the fabricated patterns will exhibit strong field enhancement near 15 µm; however, the 600 µC/cm^2 may provide the strongest absorption enhancement due to the smaller gap size as a result of overdosing the wires.

The patterned cell size grows monotonically with the dosage and reaches the designed cell size (diameter = 2280 nm) at a dosage of 500 µC/cm^2, and shows a trend towards overdosing at higher dosage values. The reference discs show a less regular trend than the patterned arrays. Differences may be due to: i) difficulties in measuring the disc size through the exact centre of the circle as there is no clear reference, ii) less intricate patterning, which may have led to a smaller effect of dosage on the overall structure, or iii) difficulties with the sample alignment during the EBL process, which may have changed the actual dosage delivered to each array.

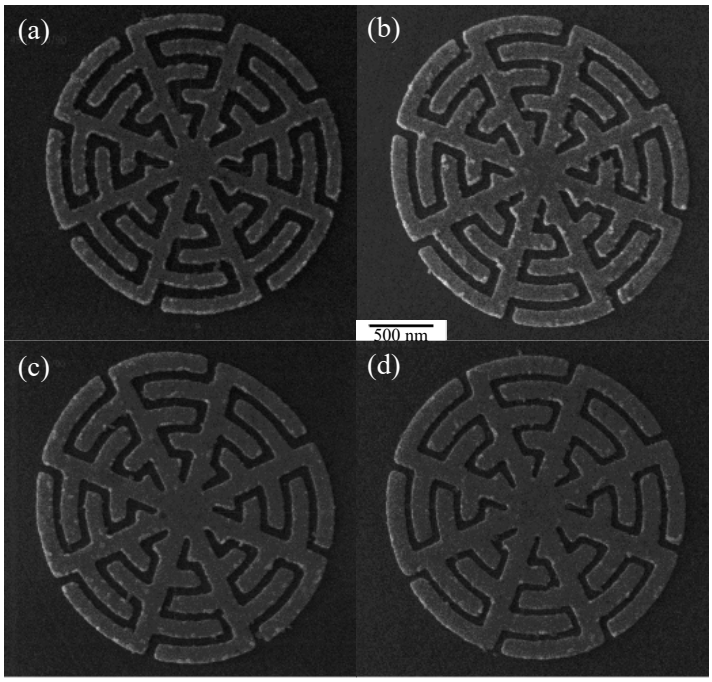

Figure 4.38: HIM micrographs of patterned MTM-lined discs for dosages (a) 450 µC/cm^2, (b) 500 µC/cm^2, (c) 550 µC/cm^2, and (d) 600 µC/cm^2. Reproduced from [180], CC BY 4.0.

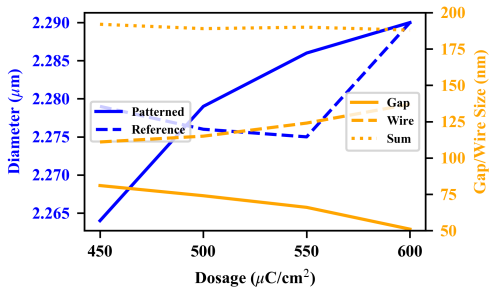

Figure 4.39: Geometric parameters of MTM-lined disc arrays fabricated by EBL for electron beam dosages of 450-600 µC/cm^2. Reproduced from [180], CC BY 4.0.

4.8.3 MIR MTS Characterization

The same FTIR microscope used above to characterize the wagon-wheel MTS was also used to characterize the MTM-lined disc MTSs patterned by EBL. A consequence of working in the long-wavelength MIR domain is that the FTIR microscope is limited to frequencies above 600 cm^{-1} due to the loss in the refractive optics. As a result, the full simulated spectrum cannot be observed in the spectroscopic measurements. To better visualize the resonance, we have fabricated a shifted, $g = 80$ nm/$w = 80$ nm set of patterned and reference arrays. Additionally, since the eventual measurement of CO_2 necessitates separating the optical path from the sensing medium, we excite the MTS from the backside of the substrate, as discussed in more detail in Ch. 5. To compare such a measurement to simulation, the reflection off the top surface of the substrate is artificially added to the simulation results. If we assume that the coherence is low and all higher-order reflections off the MTS are captured by the detector, the reflectance becomes a converging geometric series with sum [216]:

$$R = R_{ZnSe} + \frac{T_{ZnSe}^2 R_{MTS}}{1 - R_{ZnSe} R_{MTS}}, \tag{4.2}$$

where R is the reflectance seen in the measured spectrum, T_{ZnSe} and R_{ZnSe} are the normal-incidence reflectance at the air-ZnSe interface calculated by simulation (or equivalently by the Fresnel equations), and R_{MTS} is the normal-incidence reflectance off the ZnSe-MTS/ZnSe-air interface calculated by simulation. Assuming the ZnSe is lossless, $T_{ZnSe} = 1 - R_{ZnSe}$ and equation 4.2 becomes:

$$R = R_{ZnSe} + \frac{(1 - R_{ZnSe})^2 R_{MTS}}{1 - R_{ZnSe} R_{MTS}}. \tag{4.3}$$

Reflection spectra for the reference solid disc arrays (labelled "ref") are shown in Fig. 4.40a, where the experimental spectra are coloured, and the simulation spectra are shown in black. In the absence of a solid gold film to use as a reflectance standard, the total reflectance of the bare ZnSe surface was used as the background signal to remove environmental absorption. To

recreate this standard from simulation data, the reflectance of the MTS can be replaced by the reflectance of ZnSe in equation 4.3:

$$R = R_{ZnSe} + \frac{(1 - R_{ZnSe})^2 R_{ZnSe}}{1 - R_{ZnSe}^2}. \tag{4.4}$$

This normalization (eq. (4.4): $R_{ZnSe} = 0.17 \rightarrow R = 0.28$) leads to a maximum reflection of ∼250% instead of the conventional 100%. The solid curves are the $(g, w) = 80/80$ nm case, labelled "80", while the dashed curves are the $(g, w) = 80/110$ nm case, labelled "110". Only arrays with a successful liftoff procedure are included: 500 µC/cm^2 in blue, 550 µC/cm^2 in orange, and 600 µC/cm^2 in green. The simulated and measured spectra match very well over the plotted range, while the difference in reflection magnitude is due to the dispersion of ZnSe at lower frequencies, the variety of incidence angles present in the experiment, and experimental losses not modelled in the simulation, such as scattering from rough surfaces. It is clear that only resonances modelled in the simulation are present, and hence any enhancement in reflection is due entirely to the addition of the MTM liner. Few differences are seen when comparing the data for different dosages, which is expected given the size of the discs varies by only 15 nm. The small variations in amplitude are attributed to temperature differences in the cryogenically cooled detector for each measurement. Moreover, the signal amplitude decays in the refractive KBr optics and the sensitivity of the detector is reduced toward lower frequencies (higher wavelengths), which reduces the SNR of the measurement and the signal decays entirely beyond 500 cm^{-1}. No enhanced absorption due to CO_2 is seen.

Reflection spectra for the patterned MTS arrays, labelled "pat", are shown in Fig. 4.40b using the same conventions as before. Once again, the spectra match well over the measured range, with the reflection amplitude significantly increasing near 15 µm, as designed. Despite variations in the patterned feature sizes, the reflection of the MTS arrays is nearly unchanging at resonance, showing that the MTM-lined disc array is insensitive to fabrication discrepancies resulting from overdosage. The curves split towards higher fre-

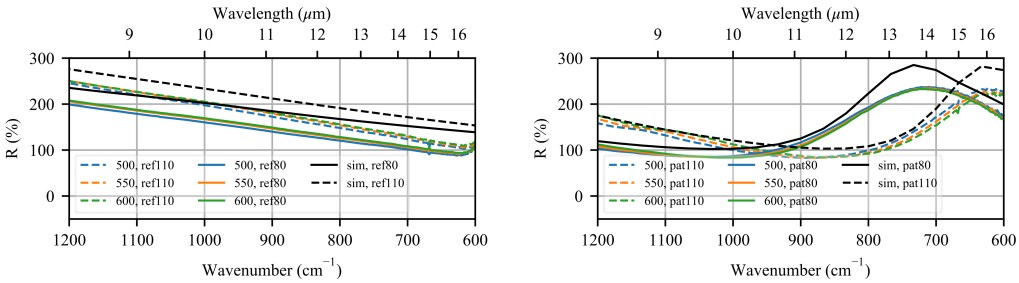

Figure 4.40: Relative reflection spectra of (a) the fabricated reference disc arrays (coloured) and the simulated reference disc array (black), and (b) the fabricated MTM-lined disc arrays (coloured) and the simulated MTM-lined disc array (black) normalized to the total reflectance of the bare ZnSe surface (eq. (4.4): $R = \sim 0.28$). The dashed curves correspond to the $(g, w) = 80/110$ nm case, while the solid curves correspond to the $(g, w) = 80/80$ nm case. The spectra have been normalized to remove source and environmental effects. Reproduced from [180], CC BY 4.0.

quencies, which is attributed to the geometric variations observed under HIM. The small differences in the spectra outside the resonant band can again be attributed to thermal variations. Furthermore, in these measurements, the predicted absorption at 15 µm is dominated by environmental CO_2 present in the microscope optical path and not absorption enhanced by the MTS, hence no clear absorption enhancement is seen in the normalized spectra. We will show in the next chapter that absorption enhancement can be observed when CO_2 is deliberately introduced to the MTS surface.

4.9 Summary

EBL and FIB are both mature technologies that have been compared countless times in the past. In general, EBL is preferred in applications where its speed and reliability are required. In our case, the entire EBL exposure of 18, 200×200 µm^2 patterns took only 96 minutes, whereas the HIM required the same amount of time to pattern a 6×4.2 µm^2 area without added realignment time. On the other hand, FIB is preferred in situations where EBL is impossible, such as direct modification of a sample for TEM analysis.

In our designs, we made deliberate choices to eliminate one or the other as

a potential fabrication candidate. Nevertheless, both processes required similar development steps to arrive at a sufficiently high fabrication quality. The validation of the substrates for each process required repeated fabrication attempts. In both cases, the particle beam dosage was crucial to reproducing the designed features. Due to the HIM being a younger technology, significantly more development time was dedicated to processes both inside and outside the microscope, but the development of the EBL process also took several tries before a usable device was created. With the results presented in this thesis, we hope to shrink the gap in development time for future researchers as nm-scale features continue to be explored in nanoplasmonic research. The HIM process consists of significantly fewer steps, and a plasmonic MTS prototype could reasonably be created within a single day, particularly if the epitaxial films have already been fabricated. Although HIM may never be as fast or as reliable as EBL, we have shown that HIM remains a viable solution when extremely fine features are required, even over a large patterning area.

Overall, the patterns created by EBL performed much better than those patterned by HIM. If the wagon-wheel MTS were refabricated on the free-standing, single-crystal film, the shorting between the central wires and the grain defects could be eliminated. We saw that the wagon-wheel design is less sensitive to the wire thickness gradient than the two-wire design, and better performance can be expected. More appropriate characterization tools that better support the wavelengths and scales of interest would also be beneficial. For example, a near-field probe would better characterize the variation in electromagnetic responses between apertures, and the true ratio of shorted to unshorted cells could be ascertained. Despite the poor fabrication conditions, the geometric features two-wire-aperture MTS were fairly accurately reproduced, with a variation on the order of only 2 nm. This variation is large when the designed features are on the order of 10 nm, but we believe that under ideal fabrication conditions, where tilt has been eliminated, the source is fresh, and the system has been stabilized, overmilling of the nanowires can be successfully mitigated. These conditions will be much easier to achieve once the nanoFAB has moved the microscope to a quieter area away from

the cleanroom, which is planned for this coming year. Redeposition must still be addressed through the pattern design, but a tuned raster pattern using FIB-o-mat is likely to be able to address this issue as well by patterning the nanowires and nanogap last.

Chapter 5

Applications

Innumerable applications involving plasmonics may benefit from improving the minimum reliable feature size from the 20 nm achievable with a Ga^+ FIB to the 10-nm feature size possible with the HIM. We chose three to be studied, one for each MTM-lined resonator designed in Ch. 3 based on their characteristic enhanced features. In this chapter, we suggest the implementation of a subwavelength imaging MTS with wagon-wheel MTM-lined apertures in the NIR domain, a phase-gradient beam steering MTS with two-wire MTM-lined apertures in the visible domain, and a CO_2-sensing SEIRA MTS using the MIR MTM-lined disc. We verify the absorption enhancement of the MTM-lined discs experimentally, and suggest how a functionalization layer could significantly improve the MTS's performance.

5.1 NIR Imaging of Subwavelength Features

Observing subwavelength structures under an optical microscope is typically challenging due to the Abbe diffraction limit, $d = \lambda/2\text{NA}$, where NA is the numerical aperture, which limits the maximum achievable resolution [47]. In biosensing and imaging applications, real-time observation of subwavelength cells is important to their identification and characterisation. Electron-beam microscopy can reach higher resolutions, but requires more expensive and bulky equipment, conducting samples, and may damage fragile biological samples. Therefore, we aim here to bring subwavelength information about individual MTM-lined apertures to the image plane of a microscope.

The microwave implementation of the ENNZ-lined apertures was previously applied to imaging conducting features on a subwavelength scale [47]. A nonuniform array of 5 ENNZ-lined apertures was designed with different inductors for each aperture, excited by a parallel-plate horn antenna and fed with a coaxial cable. This allowed the resonance frequency of each adjacent aperture to be shifted, such that the transmission spectrum showed peaks at 5 distinct frequencies, each one corresponding to a single aperture in space. Obstacles could be detected in front of each aperture individually by examining changes to the transmitted spectrum, at a resolution better than $\lambda_0/6$.

Such an imaging device can be implemented in the NIR domain with the combination of the thin liner and wagon-wheel structures [217]. The goal is to use a sufficient number of different apertures, X, to bring the total period of the array, $X \cdot p$, above the diffraction limit. In this way, each pixel on a diffraction-limited microscope image corresponds to a single supercell of the MTS. An image can be collected by exciting the MTS at the resonance frequency of a particular aperture inside the supercell, where contrast is created by the amplitude of the reflected or transmitted signal. Each pixel on the image therefore corresponds to a single aperture on a subwavelength scale. X images, each taken at the resonance frequency of a different aperture in the supercell, may then be combined to create a single image with subwavelength-resolution in one dimension and grayscale amplitude contrast.

For example, take the 9×9 aperture array with period $\lambda_0/6$ and subwavelength distribution of reflecting obstacles shown in Fig. 5.1a. Each pixel in a diffraction-limited microscope image will image approximately 9 apertures, as shown by the white dividing lines, and hence $X = 3$. As a result, a diffraction-limited reflection-mode image of the obstacles will be 3×3 pixels, each quantized into 9 levels based on the number of apertures covered by obstacles, as shown in Fig. 5.1b. To improve the resolution, each pixel is divided into $X = 3$ columns and the apertures in each column are assigned a different resonance frequency, denoted by the colours in Fig. 5.1c. An image taken at one resonance frequency probes only the corresponding apertures, and hence creates an image with 3 reflection levels for each pixel. Figs. 5.1c–5.1e show

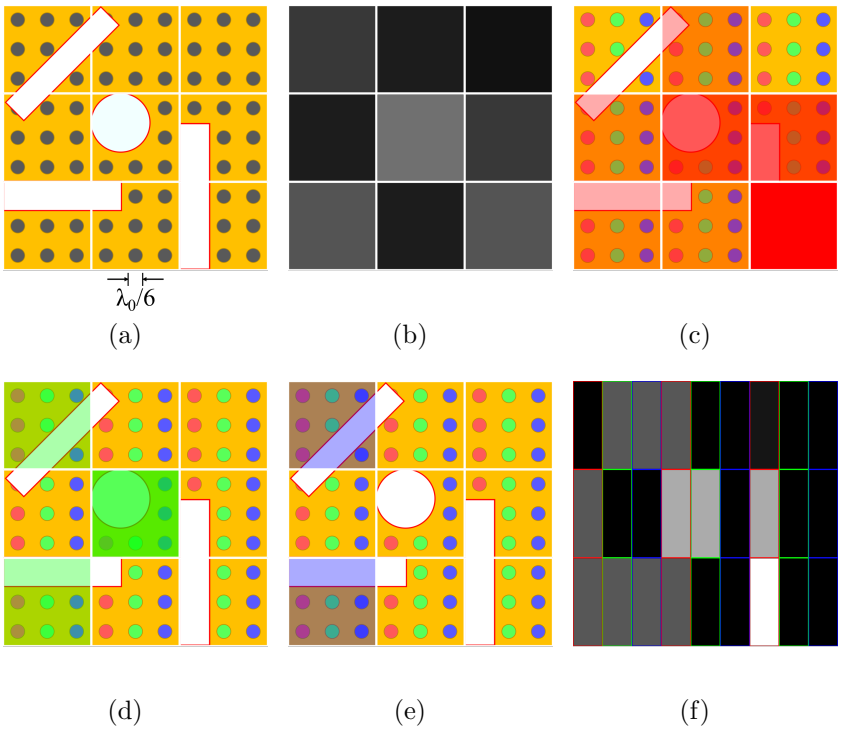

Figure 5.1: Subwavelength imaging mechanism example, where (a) a random distribution of reflecting subwavelength obstacles (shown in white) is imaged using an aperture array with a period of $\lambda_0/6$, and with a diffraction-limited microscope in reflection mode. (b) the diffraction-limited image. The subwavelength-resolution image is divided into three images, each excited at the resonance frequency of a particular set of apertures, denoted by (c) red, (d) green, and (e) blue. (f) the image with subwavelength resolution in the horizontal direction.

the collected images for each resonance frequency, and Fig. 5.1f shows the concatenated grayscale image. All obstacles can now be better-localized in the horizontal direction to a resolution of $\lambda_0/6$. In reality, each resonant frequency corresponds to a different wavelength, and the resolution must be referenced to the shortest probing wavelength.

While it is simple to modify the resonance frequency of the ENNZ-lined apertures in the microwave domain by changing their loading inductance, in the optical domain, the resonance frequency is controlled by changing the liner thickness or the aperture size. With a nominal period $p = 300$ nm, a minimum resonance wavelength of $\sim$1550 nm ($d > 755$ nm), and since the resonances generally have a broader bandwidth in the NIR, we aim to design at least

three individual resonances within the 100 THz to 400 THz band. Next, individual unit cells were simulated to create a library from which to choose the resonances. Aperture outer radius b was swept from 100 nm to 140 nm, and inner radius a was swept from 10 nm to $a = b - 20$ nm. Finally, the total MTS is pieced together from the required library cells. In the microwave case, the unit cell library was able to create 5 individual resonances in the design band, while overlapping each adjacent resonance with the antiresonance of the previous one for minimal coupling. In the NIR domain, however, the resonant bandwidth is much too large for such a scheme, and instead, the resonances are overlapped at -3 dB.

The results of this study are summarized in Fig. 5.2. Aperture 1 measures $(b, a) = (120, 10)$ nm and resonates at 193 THz, aperture 2 measures $(b, a) = (130, 90)$ nm and resonates at 240 THz, and aperture 3 measures $(b, a) = (110, 90)$ nm and resonates at 280 THz. Fig. 5.2b shows the response of each of the above apertures in uniform, $p = 300$-nm arrays, and the -3 dB point is plotted as a red dotted line to show the designed overlap location. When combined in the way shown in Fig. 5.2a, the overall transmission response (plotted in Fig. 5.2c) shows three distinct peaks, one corresponding to each aperture, with a very minimal shift in frequency. This is expected due to the low inter-aperture coupling, however, the transmission off-resonance is much lower than the -3-dB overlap may have suggested. This is due to the nonuniformity of the array: if each aperture is independent of its neighbours, the more effective comparison would be to an array with its neighbours filled in, *i.e.*, a uniform array with $p = (900, 300)$ nm in the (x, y) directions. This reduced fill factor would certainly decrease the resonant transmission, but also reduce the resonant bandwidth. Overall, the resonances are much better-separated in this scheme at the cost of resonant transmission. With a period p of 300 nm and a maximum operating frequency of 280 THz ($\lambda_0 = 1071$ nm), this array is capable of improving the resolution of a microscope to at least $\lambda_0/3.6$ in one dimension, but in practice, the strong confinement of the fields to the nanogaps would improve the probing resolution further, particularly in the case of the wagon-wheel.

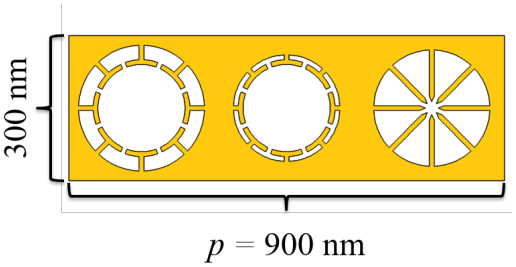

(a)

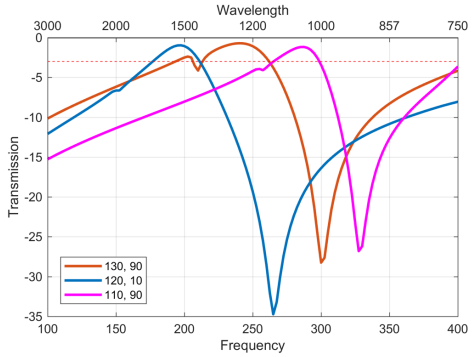

(b)

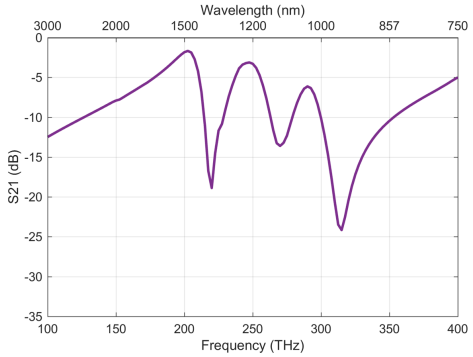

(c)

Figure 5.2: (a) Overall structure of the 3×1 imaging array, (b) the transmission of each of the three apertures individually, with −3 dB marked with a red dotted line, and (c) the overall transmission response of the structure depicted in (a). Adapted with permission from [217].

The most straightforward implementation of the MTS in an imaging system would be as a substrate for a liquid sample in a conventional microscope. The MTS could be excited by either a filtered lamp or a tunable laser, and images would be collected near the resonance frequency of each aperture that capture the subwavelength obstacles in their vicinity. The three images could then be combined into a single image with improved lateral resolution in one axis with excellent surface sensitivity.

Another implementation of this MTS in the optical domain would be at the tip of a scanning near-field optical microscope (SNOM) probe. A campanile probe configuration is most similar to the horn antenna used in the microwave domain, though the role of the source and detector are switched: in the microwave domain, it is simple to make subwavelength sources, whereas in the optical domain, laser sources are large and must harness the plasmonic effect for subwavelength focusing [218]. Nevertheless, the benefits of the two structures are the same: increased sensing throughput through spectral multiplexing. A campanile probe takes an optically-transparent dielectric and patterns it into a square-pyramidal shape. Two facets are then coated in metal, creating a tapered waveguide to focus the source. The tip is typically fashioned into a small gap, but we would instead fashion a 3×1 imaging array onto the pyramid tip, significantly enhancing the scattering in three bands with very little cross-talk. In turn, this would allow the scanning speed to be increased dramatically. This implementation is not limited to comparable MTM-lined apertures, and in fact, almost any SNOM probe normally patterned with a FIB may benefit from the increased resolution of the HIM. Without the large-area requirement, the HIM, along with the results of this thesis, would have comparable patterning speed, better resolution, and less surface damage than the conventional Ga^+ FIB.

5.2 Phase-Gradient Visible MTS

In Ch. 3, we showed how adding asymmetry to the two-wire MTM-lined aperture allows the scattered phase angle of the MTS to be designed. In this

section, we develop this idea further by designing a nonuniform, 8×1 unit-cell array that implements a phase gradient, scattering to an angle of 48.5°.

Refraction at an interface between two materials is generally governed by Snell's Law:

$$\sin(\theta_t) n_t = \sin(\theta_i) n_i, \tag{5.1}$$

where θ_t, n_t are transmittance angle and the transmission medium refractive index, and θ_i, n_i are the incident angle and the incident medium refractive index. An MTS element along the interface can locally change the scattered phase, leading to interference between the scattered field from the MTS element and its neighbours. Like in the case of a Fresnel lens, this discretization of the scattered phase at the interface between two media can be used to emulate the effect of arbitrary dielectric inclusions. In the case of refraction, an MTS is designed such that the scattered phase is a linear taper along the surface. Refraction is then governed instead by the generalized Snell's law [106]:

$$\sin(\theta_t) n_t - \sin(\theta_i) n_i = \frac{\lambda_0}{2\pi} \frac{d\Phi}{dx}. \tag{5.2}$$

Therefore, the refraction angle is limited by the maximum phase gradient, and hence by the size of the unit cell used to discretize the phase gradient since a smaller unit cell allows a steeper phase gradient to be produced. Moreover, the phase gradient is a continuous function that must be discretized by individual MTS cells, meaning smaller unit cells are useful over shallower phase gradients to improve efficiency by reducing discretization errors.

Many approaches exist for designing a phase-gradient MTS. Since we have previously characterized the MTS elements using reflection/transmission magnitudes and phase, a design based on scattering parameters is appropriate. Additional corrections normally required to address inter-cell coupling can be omitted because the unit cells only interact weakly with their nearest neighbours.

Under these assumptions, the design process is as follows: i) develop a unit-cell library with a variety of scattered amplitudes and phases, ii) choose

a number of unit cells with constant scattering amplitude and a linear phase gradient that encompasses at least 180° at the design frequency, and iii) combine the chosen unit cells into a nonuniform array, rotating a cell by 90° where necessary to impart an additional 180° of geometric phase.

For our simple proof of concept, we choose design parameters that are largely already met by the simulations presented in Ch. 3. In these simulations, the 2-wire MTM-lined aperture was able to achieve a 180° phase range at 500 THz, and hence we choose this as the design frequency. To show the benefit of miniaturization, we choose the number of unit cells to be 8, the same as used in the paper by Yu *et al.* [106]. For a linear phase gradient, this corresponds to the deflection of a normally incident, circularly polarized plane wave to an angle of $\sin^{-1}(\lambda/p) = 48.5°$, which is approximately the maximum angle shown by Yu *et al.*, yet we do not make use of the miniaturization potential of a substrate. Since the majority of the scattering amplitude curves in Fig. 3.22c cross at 1.15% and 500 THz, this is chosen as the target scattering amplitude. In summary, we are looking for 5 unique unit-cells with scattered amplitudes of 1.15% and phases 0°, 45°, 90°, 135°, and 180° at 500 THz, and the phase angles −45°, −90°, and −135° will be created with a rotation.

5.2.1 Unit Cell Library

The unit cell library begins with an interpolation of the data shown previously in Fig. 3.22d to find cells that scatter at phases of 45°, 90°, and 135°, which can be done with θ angles of 22.5°, 45°, and 62.5°, respectively. For the 0° and 180° cases (θ = 0°, 90°), the scattering amplitude at 500 THz is too high, and an additional tuning parameter must be introduced. To reduce the scattering amplitude while keeping the scattered phase the same, the gap at the centre of the aperture can be displaced vertically by a small distance g, as shown in Fig. 5.3a, to separate the symmetric and asymmetric resonances in frequency. The effect of this displacement on the scattered amplitude and phase is shown in Figs. 5.3b and 5.3c, respectively, for the θ = 90° case. Particularly at 500 THz, the phase varies very little with g, but as expected, the symmetric and asymmetric resonances separate and depress the scattering

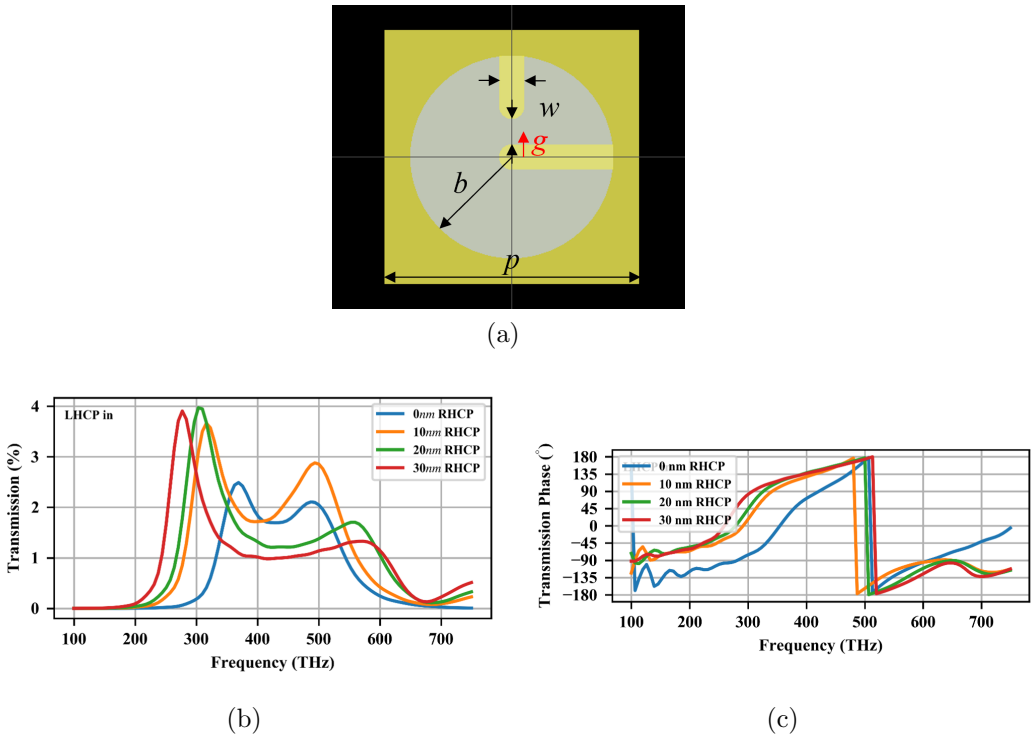

Figure 5.3: (a) Geometry of the displaced gap simulation, where g now refers to the distance by which the gap is displaced, (b) the scattered transmission magnitude for various gap displacements g, and (c) the scattered transmission phase for various gap displacements g.

amplitude to 1.15% when $g = 35$ nm, nearly entirely removing the second nanowire. A similar simulation was used to depress the scattering amplitude of the 0° scattered phase case to 1% for $g = 20$ nm and $\theta = 0°$.

5.2.2 Nonuniform Array

Next, we combine the chosen unit cells into a nonuniform MTS with a linear phase taper across the array, as shown in Fig. 5.4a. The scattering amplitude and phase across the spectrum are shown in Figs. 5.4b and 5.4c, where the colours correspond to the labels above. The scattering amplitude curves corresponding to the −135°, −90°, and −45° cases overlap exactly with those corresponding to the 45°, 90°, and 135° cases since the only difference between the two is a geometric phase factor. With additional tuning, the 0° case could be improved to overlap more closely with the scattering amplitude of the other curves, but it was found that achieving a phase shift of 0° with

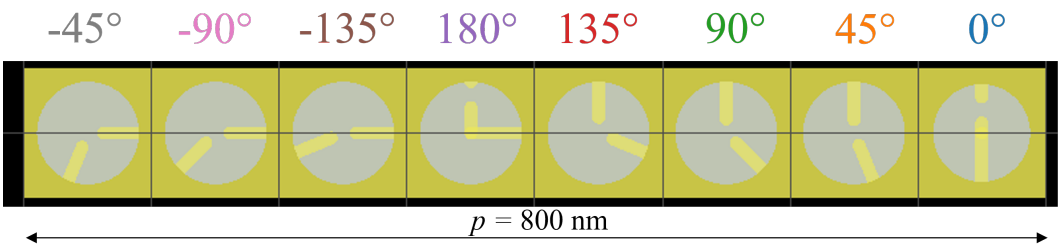

(a)

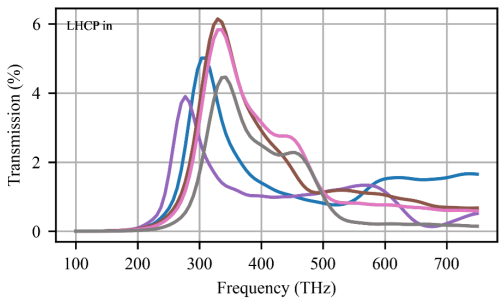

(b)

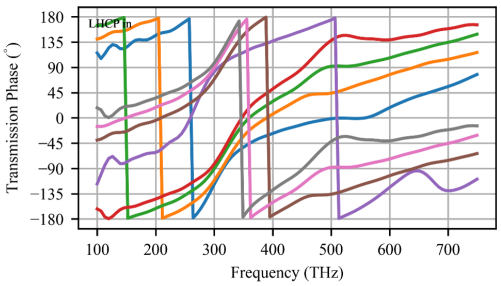

(c)

Figure 5.4: (a) Layout of the non-uniform phase-gradient MTS, with the scattered phase of each cell labeled above, (b) scattered transmission magnitude for each individual unit cell, where the curve colours correspond to the labels above, and (c) the scattered transmission phase for each individual unit cell, where the curve colours correspond to the labels above. (a) adapted with permission from [219].

the proper scattering amplitude was challenging. If additional degrees of freedom are required, varying the aperture radius b over the array may be able to achieve this goal more accurately.

Finally, the entire MTS is simulated to confirm the anomalous refraction. The real part of the scattered electric field is shown in Fig. 5.5, where the source is an LHCP, normally incident plane wave from the bottom of the domain. The scattered field is calculated by casting the resulting fields onto an RHCP basis for the top-half plane, and onto the LHCP basis for the bottom-half plane, since the reflection swaps the handedness of the wave. The black dashed lines are plotted at the designed 48.5°, showing that the scattered field is plane-wave-like and travels in the expected direction. Performing a Fourier transform of the fields on the output port (at the top of the plotted region) allows the power fraction and scattering efficiency to be calculated.

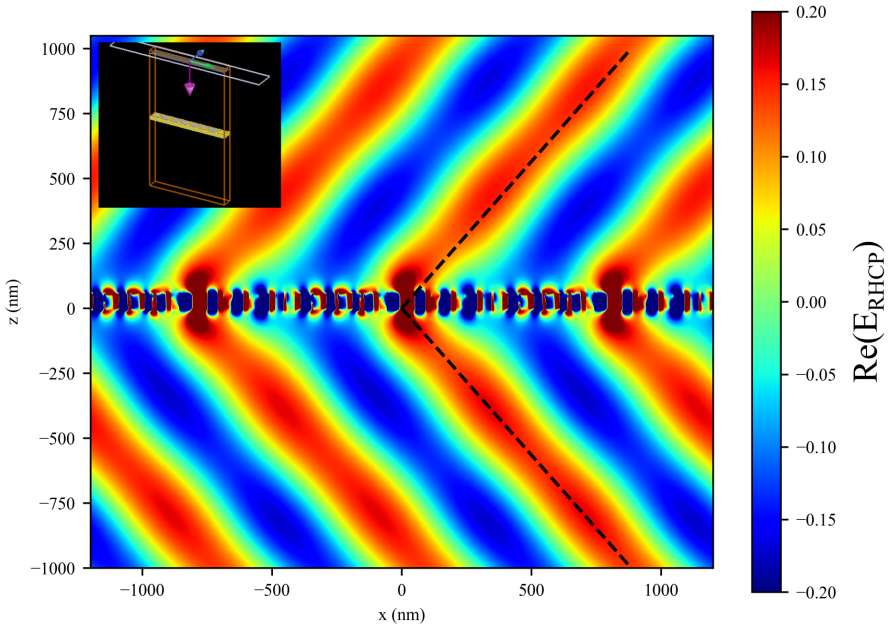

Figure 5.5: Real part of the RHCP scattered electric field of the phase-gradient MTS for a normally-incident, LHCP plane wave, showing the clear scattering to an angle of 48.5°, denoted by the dashed black lines. The inset shows the simulation setup, where the purple arrow is the propagation direction of the incident wave.

∼2.38% of the incident power is scattered to the 48.5° direction on either side of the MTS, which is 100× more than is scattered to any other direction. As one might expect, this efficiency is comparable to that achieved in the first demonstrations by gold nanoantennas. Moreover, the unit cell electrical size is $\lambda/6$ at 500 THz, which is comparable to some of the first demonstrations of anomalous refraction with V-shaped nanoantennas, but we have achieved this size without the wavelength-shortening effect of a substrate [220]. An implementation of this MTS on an SNOM probe could allow phase contrast to be used to enhance the collected image.

5.3 Long-Wavelength MIR SEIRA of CO_2

In Sec. 3.3, we designed MTM-lined disc MTS elements for maximum field enhancement at a wavelength of 15 µm to target the bending absorption band of CO_2. In Sec. 4.8, we fabricated the MTSs and verified its resonant frequency experimentally. In this section, we load the MTS with CO_2 to demonstrate SEIRA at the target wavelength. We design a custom glass gas cell for the experiment with the MTS on the inside, and compare the experimental results to simulation using an electromagnetic material model for pure CO_2 derived from atmospheric absorption lines that models the effects of the FTIR microscope on the measured results.

5.3.1 Experimental Setup

The experimental setup consisted of the custom glass gas cell loaded onto the Nicolet Continμum FTIR microscope stage, connected to gas cylinders and a venting valve via 1/4" plastic tubing. A schematic of the gas cell with illumination is shown in Fig. 5.6, and the inset shows a cartoon of the MTS exciting nearby CO_2 molecules (not to scale). The ZnSe window was epoxied to the glass cell. The microscope was focused onto the bottom surface of the yellow ZnSe substrate, where the MTS is patterned. 100% CO_2 or 100% N_2 gas was fed in from one side, and the pressure was measured with the regulator attached to the gas cell inlet. The output was vented outside the lab through a 1/4" plastic tube. The measurement was prepared by opening the N_2 valve and the venting valve for 2 minutes to purge the gas cell of air. The valves were then closed, the cell was left for 2 minutes to stabilize, and a measurement was taken. The same procedure was used to take measurements with CO_2. The 10-PSI (170 kPa relative to vacuum) CO_2 measurement was taken with both the CO_2 and the venting valves open. Without mass flow controllers, this setup did not allow precise control over gas mixing or gas pressure and was chosen as a simple, cheap, but effective means to load the MTS with a known quantity of CO_2.

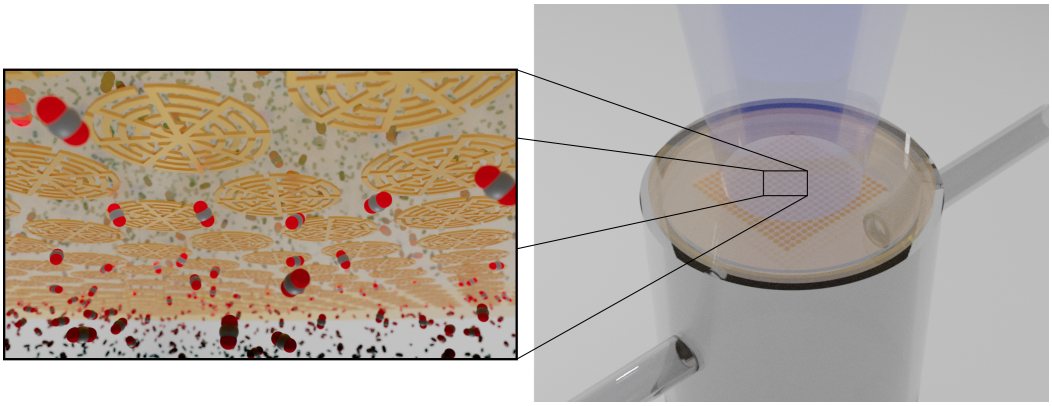

Figure 5.6: Schematic of the fabricated gas cell, with inset showing a cartoon of the excitation of CO_2 by the MTS (not to scale). The microscope illumination is shown in blue, the ZnSe substrate is shown in yellow with the MTS patterned on the inside surface, and the glass gas cell is clear with two gas inlets. Adapted from [180], CC BY 4.0.

5.3.2 Modelling CO_2

The CO_2 model was derived based on data from the HITRAN database [221]. The HITRAN database is a high-resolution compilation of molecular absorption properties for a wide variety of materials. The absorption spectrum was calculated for a temperature of 300K, 26 PSI (280 kPa relative to vacuum), 100% CO_2 molar fraction, a thickness of 100 cm, and frequencies from 580–760 cm^{-1} at a resolution of 0.01 cm^{-1} [222]. The absorbance was then extracted using Beer's law $I = I_0 e^{-\alpha z}$, where I is the output irradiance after travelling through the material layer, I_0 is the input irradiance, α is the absorbance, and z is the thickness of the material layer. Next, the absorbance was related to the extinction coefficient κ_1 using the well-known equation $\alpha = 2\omega\kappa_1/c$, where ω is the radial frequency and $c = 3 \times 10^8$ is the speed of light [216].

Since the complex refractive index is a causal, time-invariant spectrum, the real part of the refractive index was derived from the extinction coefficient using the Kramers-Krönig relations [223]:

$$n_1(\omega) - 1 = \frac{2}{\pi} \mathrm{P} \int_0^\infty \frac{\omega' \kappa_1(\omega')}{\omega'^2 - \omega} d\omega', \tag{5.3}$$

where P denotes the Cauchy principal value integral.

With the full complex refractive index, plotted in Fig. 5.7, the instrument

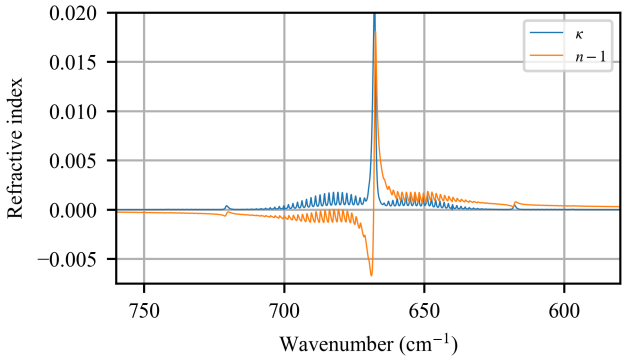

Figure 5.7: High-resolution complex refractive index model for CO_2. Reproduced from [180], CC BY 4.0.

response was modelled next. The instrument response reduces the sample resolution of the modelled spectrum and convolves the spectrum with an apodization function to suppress the sidelobes of resonant peaks. The apodization function used was the Happ-Genzel function [224]:

$$A(x) = 0.54 + 0.46 \cos \frac{\pi x}{X}. \tag{5.4}$$

The FTIR measurement resolution is a function of the maximum path difference inside the interferometer. To model the smaller path difference (and hence lower resolution), the real and imaginary parts of the complex refractive index spectrum were individually inverse Fourier cosine-transformed to the spatial domain, truncated at the same path distance of 0.25 cm that was used in measurement, multiplied by the Happ-Genzel apodization function, then Fourier cosine transformed back to the frequency domain:

$$\kappa_2 = \mathcal{F}(A(x)\mathcal{F}^{-1}(\kappa_1)), \tag{5.5}$$

$$n_2 = \mathcal{F}(A(x)\mathcal{F}^{-1}(n_1)). \tag{5.6}$$

The resampled and apodized complex refractive index is plotted in Fig. 5.8 and was directly imported into COMSOL as an interpolated function.

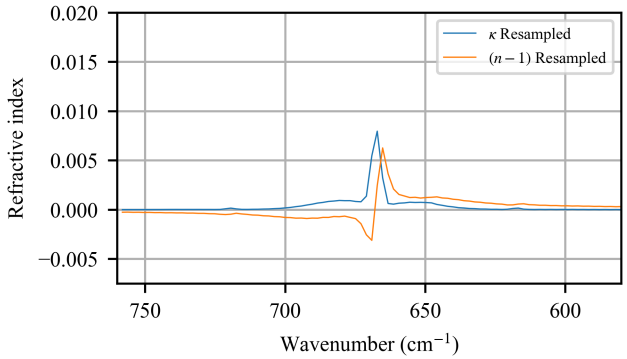

Figure 5.8: Resampled and apodized complex refractive index model for CO_2. Reproduced from [180], CC BY 4.0.

5.3.3 CO_2 Sensing Experiment

Creating a gas sensor from a SEIRA-enabled surface proves difficult as CO_2 does not adsorb (stick) well to gold surfaces, the molecular density of gases is low compared to liquid and solid analytes, and ambient CO_2 must be removed from the optical path. Low adsorption may be ideal for a real-time sensor to reduce the time between measured adsorption events, but will inevitably reduce the sensor sensitivity [225]. Functionalization of the gold surface, where a linking molecule is added to chemisorb the target molecule to the gold, is often the preferred solution for increasing the density of excited molecules [98], [226], [227]; however, such sensors may be single-use or require regeneration cycles. Additionally, the incorporation of high-surface-area materials such as metal-organic framework nanocomposites has been suggested to increase CO_2 adsorption [27], [228]. Nevertheless, functionalization may be important in the future to improve the sensitivity of the MTM-lined disc MTS to a variety of materials.

Here, we aim to validate the absorption enhancement of physisorbed CO_2 by the MTM-lined disc MTS, and hence develop a repeatable method of measuring the absorption enhancement for high concentrations of CO_2. A sealed glass gas cell is designed to support positive pressure and the MTS was fabricated on the inside surface of the gas cell window to improve the adsorption of CO_2. The cell was loaded with either 100% N_2 or 100% CO_2 (the gases

were not mixed) under variable pressure conditions to increase the adsorption of CO_2 on the MTS. A far-field, microscope-focused reflection measurement is used and the MTS is excited from the substrate side (see Methods for more details). The relative reflection results of this experiment are plotted in Fig. 5.9a.

The pressure of both cylinders feeding the gas cell was set to 26 PSI with the exhaust valve closed, and a back-pressure of 10 PSI was measured with the exhaust valve open. For the background case, the gas cell was evacuated of CO_2 with a continuous flow of N_2. Any absorption in the baseline is due to incomplete purging of the microscope optical path and its effect is removed by the difference operation. In the solid curves, the reflection is measured under a continuous flow of CO_2 and an approximate pressure of 10 PSI, measured at the gas cell inlet. Under these conditions, the measured reflection is decreased for the MTS cases (orange and red), while the reflection increases for the bare ZnSe case (in blue), meaning the nanoscale nearfields of the MTSs can induce significant absorption by the surrounding CO_2. When the pressure is increased by a factor of 1.64 to 26 PSI, the differential reflectance improves to -2.5% for the 600 µC/cm^2 case. The 600 µC/cm^2 case shows the most absorption enhancement due to the smaller gap widths observed in Fig. 4.38d increasing the overall field enhancement at resonance. Despite wider gaps, the 500 µC/cm^2 case shows a small absorption enhancement that increases with increasing pressure. Unfortunately, the 550 µC/cm^2 MTS was destroyed while creating the gas cell.

A representative simulation of the experimental results is shown in Fig. 5.9b, where the dashed curves are the experimental data and the solid curves are the simulation data. CO_2 is introduced using the model derived in Sec. 5.3.2. This resampling method effectively models what occurs in the FTIR, where the ultimate resolution is decided by the length of the interferogram.

A comparison of the simulation to the experimental data suggests an agreement in the trends when the CO_2 model is applied, particularly at the resonance. A detailed analysis (see Appendix F) of the signal-to-noise ratio shows that the main observed resonance features are significant. For the bare ZnSe case (in blue), the small rise in reflection at 670 cm^{-1} is seen due to an index

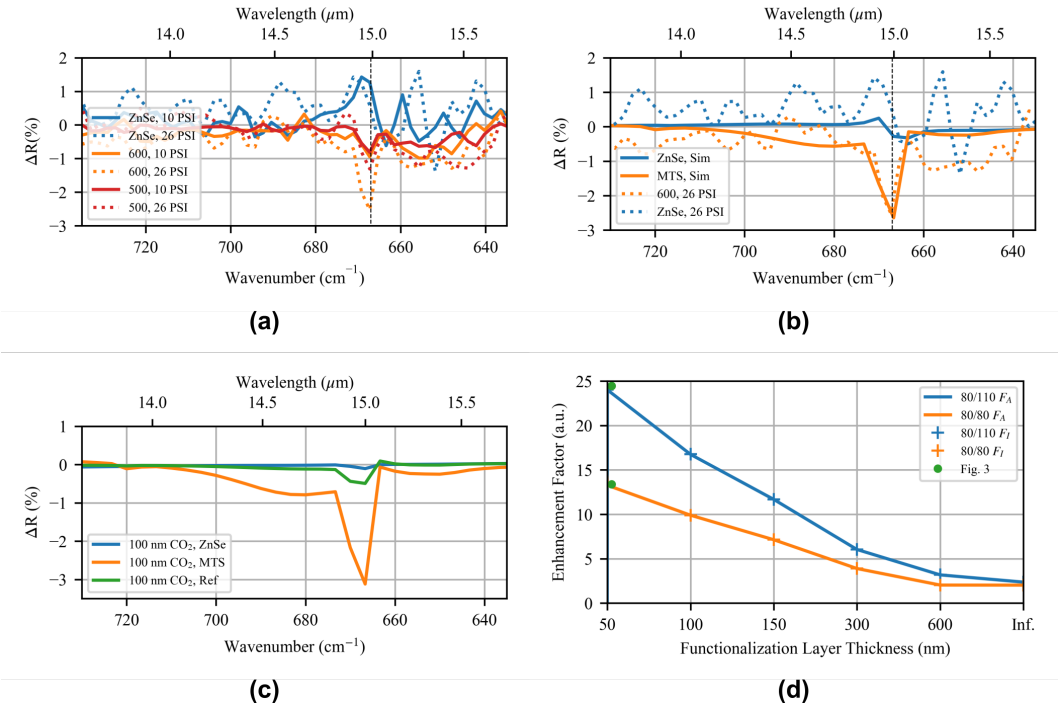

Figure 5.9: (a) Differential MTS reflection data when the gas cell is filled with different pressures of CO_2 (10 PSI solid, 26 PSI dotted), relative to the case with N_2 filling. Bare ZnSe is plotted in blue, the case of 600 μC/cm^2 in orange, and 500 μC/cm^2 in red. (b) Differential reflection data for the 26 PSI case (dotted) plotted against the differential reflection data for a representative simulation with a CO_2 model (solid). (c) Simulated differential reflectance for a 100-nm functionalization layer of CO_2 at 26 PSI, bare ZnSe vs. MTS vs. reference disc array. (d) Calculated field intensity enhancement factor, F_I, and absorption enhancement factor, F_A, for the two fabricated cases and various functionalization layer thicknesses. The green dots reproduce the data in Fig. 3.25, and *Inf.* represents a full half-space of CO_2, as in the experiment. Reproduced from [180], CC BY 4.0.

mismatch at resonance with the addition of the CO_2 model, while the drop in reflection is due to both absorption and increased transmission. With the presence of the MTS, the resonant evanescent fields are confined very near to the MTS surface and hence absorption is strongly enhanced, both at 667 cm^{-1} and along the band wings. Interestingly, the left band wing is enhanced in simulation, whereas the right band wing is enhanced in the experiment. This is due to the fabrication tolerances marginally shifting the resonance location. In simulation, the contrast enhancement ratio (*i.e.*, $\Delta R_{MTS}/\Delta R_{ZnSe}$ at 667 cm^{-1}) is 9.34, much less than the 24.5 that was predicted from the intensity enhancement in Fig. 3.25. If the top-surface reflection is not added, the contrast enhancement ratio decreases further to 6.26.

5.3.4 Functionalization Layer

To improve the observed contrast enhancement ratio, we consider numerically the case of a thin physical adsorption layer. As discussed above, a functionalization layer that can increase the concentration of CO_2 near the surface of the sample may increase the sensitivity. To model the functionalization layer, the CO_2 material model is removed from all but the top 100 nm of the sample and replaced with air. In this case, the MTS will continue to strongly enhance the absorption near the surface and contributions to absorption from outside the surface will be suppressed. Conversely, the unenhanced fields near the bare ZnSe will absorb weakly in the thin CO_2 region, and penetrate far into the lossless air region where they were previously increasing absorption and decreasing the contrast enhancement ratio. As a result, the measurement volume with the MTS could be significantly decreased and the contrast between the MTS and the bare ZnSe surface significantly increased.

The results of this study are shown in Fig. 5.9c, without adding in the top-surface reflection. For the bare ZnSe surface (in blue), a small reflection differential of -0.11% is seen. For the MTS case (in orange), the strong field enhancement within the top 100 nm of the sample continues to enhance the absorption by the CO_2, and a -3.11% dip in reflection is seen at the absorption resonance for a contrast enhancement ratio of 29.2. The case of reference discs

is also shown (in green), where there is very little enhancement wihtout the MTM liner. With the top-surface reflection, the contrast enhancement ratio increases to 33.1, however, the reflection dip decreases to -1.5%. The absorption enhancement factor, F_A, which is equal to F_I when chemical changes are ignored, is:

$$F_A = F_I = \frac{1}{V}\int_V \frac{|E_{MTS}|^2}{|E_0|^2}dV = \frac{1}{V}\int_V Q_{MTS}^{\mathrm{CO_2}}\left(\frac{Q_{ZnSe}^{\mathrm{CO_2}}|E_0|^2}{|E_{ZnSe}|^2}\right)^{-1}dV, \tag{5.7}$$

where $E_{MTS/ZnSe}$ is the total electric field, E_0 is the incident electric field, and $Q^{\mathrm{CO_2}}$ is the power absorbed in the carbon dioxide region V. $Q^{\mathrm{CO_2}}$ is calculated from total fields:

$$Q = \frac{1}{2}\Re(j\omega\bar{D}\cdot\bar{E}^*). \tag{5.8}$$

The absorption enhancement factor, F_A, is plotted in Fig. 5.9d at 15 µm for varying functionalization layer thicknesses and the two fabricated MTS designs. For a 50-nm thick functionalization layer, the results of Fig. 3.25 are nearly reproduced (a small variation is present due to the differences between CO_2 and air). F_A decreases for increasing functionalization film thicknesses until the full transmitted wave is absorbed. The simulations show that in a practical environment, the MTS performs better than F_A suggests as it is $\Delta R_{MTS}^{\mathrm{CO_2}}$ and $\Delta R_{ZnSe}^{\mathrm{CO_2}}$ that are being compared (which is largely a result of the difference between $Q_{MTS}^{\mathrm{CO_2}}$ and $Q_{ZnSe}^{\mathrm{CO_2}}$). Reflections off the bare ZnSe surface reduce $|E_{ZnSe}|^2$ below 1 near the surface, suppressing $Q_{ZnSe}^{\mathrm{CO_2}}$. Additionally, more energy is stored within the MTS metal regions due to the small index mismatch between the carbon dioxide and air, and hence increased Q_{MTS} further amplifies the differential reflection amplitude. Due to the 100% CO_2 concentration used, a meaningful calculation of sensitivity cannot be made.

An additional improvement to the MTS sensor would be to make use of the high permittivity of the ZnSe substrate for attenuated total reflectance spectroscopy, exciting the MTS at a grazing angle under total internal reflection conditions and removing the reflection off the top of the substrate [132]. A quantum-cascade laser applied directly to the ZnSe surface would remove

interference from atmospheric CO_2 while significantly improving the signal-to-noise ratio, and air may then be applied to the open surface of the MTS and absorption enhancement may be inferred from the reflected signal. This method allows a stronger excitation of the MTS and is more amenable to integration into other systems. Additionally, if the ZnSe layer is made thin, the beam can be made to excite the MTS several times before proceeding to the detector to increase the interaction length and hence the sensitivity of the device. Finally, the experiment could be improved by using mass flow controllers to regulate the gas concentrations inside the cell. Increasing the FTIR scan resolution to clearly distinguish the strong absorption peak at 15 µm would significantly enhance the minimum amount of CO_2 detected.

5.4 Summary

We have proposed implementations of MTM-lined resonator MTSs for applications in superresolution imaging, beam steering, and long-wavelength SEIRA of CO_2. Simulations show that label-free superresolution of $\lambda_0/3.6$ or better can be achieved in the NIR by multiplexing spatial information to the frequency domain using a nonuniform array of subwavelength MTM-lined apertures with closely-spaced resonant frequencies. With a sufficient number of cells to bring the array periodicity above the diffraction limit, scattering from a subwavelength aperture can be distinguished from those around it in a microscope image. Such label-free MTSs may be useful as reusable sensors for imaging biological samples to identify cells and proteins, and can be easily integrated into a conventional microscope.

With the two-wire MTM-lined aperture, we designed a phase-gradient MTS that scatters a circularly-polarized incident wave to an angle of 48.5° with a polarization conversion and an efficiency of 2.38% in simulation. The phase gradient was achieved by breaking the symmetry of the unit cell and by moving the location of the gap between the wires. Conventional V-shaped nanoantennas perform similarly to our designed MTS in terms of deflection angle and scattering efficiency, however, they require a substrate to achieve the same

degree of miniaturization. This makes them unsuitable for microfluidic applications where a fluid could be sensed by passing it through the apertures. Otherwise, a substrate could be added to the MTM-lined apertures to increase the deflection angle further. Moreover, the resonance in the visible range could allow sensor data to be observed qualitatively, simplifying the equipment required for measurement.

Finally, we demonstrated SEIRA of CO_2 at a wavelength of 15 µm using a field-enhancing MTM-lined disc MTS. We created a custom glass gas cell for the experiment and derived a representative electromagnetic model for CO_2. The experimental results matched well with simulations, where an enhancement ratio of 9.34 was observed. We showed that the majority of the enhanced absorption occurs within 100 nm of the MTS surface, and hence the sampling volume could be significantly reduced without loss of signal. Although our measurements show very little sensitivity, our results are a significant step toward miniaturized, real-time gas sensors in the long-wavelength MIR regime. Simple modifications to our experiment could significantly improve the results.

Chapter 6

Conclusion

6.1 Summary

In this thesis, we suggest that the fabrication of gold plasmonic MTSs employing features as small as 10 nm with long-range order should be possible by HIM milling. Our results showed for the first time that even in a noisy practical environment, feature sizes on the order of 10 ± 1 nm can be reliably achieved over wide areas and with high aspect ratios. Although we have shown two specific designs, this work significantly lowers the barrier to the future development of other plasmonic MTS structures with fine features, bringing the total process development times from raw materials to working prototypes significantly closer to those of EBL.

Using concepts related to plasmonics, we have shown that MTM-lined apertures and discs can be scaled from the microwave domain to the optical domain by making use of fine nanopatterned features, where they exhibit improved miniaturization and field enhancement performance. Three designs were proposed and investigated: (1) a wagon-wheel aperture for operation in the NIR, (2) a polarization-sensitive two-wire aperture for operation in the visible, and (3) a larger MTM-lined disc for operation in the MIR.

The wagon-wheel design exemplifies the fine features, high aspect ratio, complex geometry, and long-range order that can only be achieved with the HIM. For the design, lumped magnetic inductors were replaced with plasmonic kinetic inductors, and the ENNZ-lined aperture theory was extended to describe the resonances of the new aperture design. To describe the full scatter-

ing spectrum, we derived an equivalent circuit model using general principles that apply to any number of nanoplasmonic resonators. Our results show that MTM liners can be intuitively applied in the optical regime to miniaturize plasmonic nanoapertures and to tune their resonance properties. Using this structure, we studied how the ion beam parameters of the HIM can be tuned to improve patterning reliability, and analyzed the results in simulation to find the most impactful parameters on the MTS performance. The most important problems were those that led to the undermilling of the fine nanogaps at the centre of the aperture, namely grain defects, redeposition, and poor substrate contrast. Many nanoplasmonic sensors and imaging devices could be improved using the MTM-lined aperture MTS's enhanced miniaturization and local field intensities. We suggested a super-resolution imaging MTS that is simple to integrate into a conventional microscope and achieves a resolution of at least $\lambda_0/3.6$ in simulation. Moreover, we suggest how this MTS could be implemented on a near-field probe to increase the scanning throughput by a factor of three without loss in resolution.

The two-wire design aimed to maximize miniaturization through the use of fine, 10-nm features, and to shift the aperture resonance frequency into the visible regime. Using the same approach as for the wagon-wheel design, we derived an equivalent-circuit model for the two-wire aperture. An analogy to conventional plasmonic bowtie apertures and plasmonic V-shaped nanoantennas showed that the two-wire MTM-lined aperture increases miniaturization without sacrificing field enhancement in the gap region. Moreover, adding asymmetries between the nanowires allows the scattered phase to be controlled. We successfully addressed the difficulties identified in fabricating the wagon-wheel structure by depositing epitaxial gold films on LiF and removing the supporting substrate. Using these films, several prototype two-wire MTM-lined aperture MTSs were fabricated and we showed experimentally that they respond differently to orthogonal polarizations, with an excellent match to comparable simulations. We harnessed the miniaturization and phase control of the asymmetric two-wire MTM-lined apertures to demonstrate in simulation a phase-gradient MTS that refracts a normal-incidence plane wave to an

angle of 48.5° with an efficiency above 2%. Due to the enhanced miniaturization imparted by 10-nm features, the phase-gradient MTS achieved a wide redirection angle without a substrate, making it easier to pattern with the HIM.

To target the application of MIR SEIRA, the MIR MTM-lined disc MTS was designed for maximum average field enhancement F_I using a larger, 100-nm feature size achievable using EBL nanofabrication. We established that miniaturization and field enhancement can be achieved even in the underserved long-wavelength MIR regime. Using a combination of plasmonic and microwave equivalent-medium approaches that merged plasmonic nanowires and meandered capacitive gaps, we demonstrated an average field intensity enhancement of nearly 5× over a conventional nanodipole array. The development of the EBL fabrication process was generally much simpler than the HIM process, though a number of different processing steps were required and the fabricated MTSs were much larger. The fabricated MTSs were characterized by FTIR and found to match simulations very well. We designed and integrated a gas cell into the FTIR microscope, and experimentally demonstrated SEIRA of CO_2 at its 15-µm bending vibration resonance. Although the demonstrated sensitivity was low, we suggested how an experiment including an appropriate functionalization layer could significantly improve the observed absorption enhancement and numerically validated our results. This study represents an important step toward real-time, miniaturized gas sensors, and a first demonstration of significant field enhancement for the extension of SEIRA techniques to characterize molecules in the fingerprinting region using long-wavelength MIR.

6.2 Outlook

6.2.1 Short-Term

Although the results presented in this thesis show promise, some studies have shown better patterning resolution of nanogaps on a small scale than we have, and we do not achieve the theoretical maximum resolution predicted in Ch. 2.

Immediate extensions of this work should look to improve the minimum patterned feature size and study the HIM operation under a wider range of processing conditions that may be necessary for future arbitrary plasmonic element nanofabrication. For the MIR MTS, a more viable proof of concept is desired. Some potential studies include:

1. The measurement of the fabricated wagon-wheel MTS by SNOM. This method would allow a more detailed understanding of the fabrication defects present in each aperture, and their effect on the overall aperture performance. Moreover, the strong field enhancement at the nanowire tips could be confirmed experimentally.

2. Moving the HIM to a quieter environment will significantly improve not only the reliability but also the minimum achievable feature size. 10 nanometres is extremely small, and any disturbance can significantly deteriorate the patterning result. Part of the difficulty in achieving the results we obtained was having to cut patterning sessions short due to vibrations of heavy equipment and general fab activity levels. Once the HIM has been moved, the improvement in noise should be evaluated.

3. Implementation of the FIB-o-mat toolbox on our HIM [40]. This could improve the maximum resolution of our patterning and the achieved aspect ratio. Larger aspect ratios could be used to extend the applications of arbitrarily-shaped MTS elements by allowing the possibility of creating longitudinal resonances in the apertures to emulate magnetic dipoles at normal incidence.

4. Electrochemical methods of creating epitaxial gold flakes have proven to be both flexible and reliable [209]. Patterning such gold flakes deposited on TEM grids or a suitable flat substrate may improve the focus drift seen when patterning the samples presented in this thesis.

5. The wagon-wheel structure could be refabricated with an epitaxial film and characterized. The lower operating frequency alleviates some of

the concerns with the melting of the structure, however, the additional milling required when fabricating may also deliver sufficient heat to melt the sample. Proper design of the raster pattern with FIB-o-mat could likely be used to alleviate this effect.

6. The loop resonance identified in the spectrum of the wagon-wheel aperture is Ch. 3 can produce a magnetic dipolar response at off-normal incidence angles. A more detailed study of this resonance, and its coupling to the dominant electric-dipolar nanowires, could be rich ground for demonstrating a wider variety of MTS properties.

7. CO_2 sensitivity could be improved by cryogenically cooling the sample to promote adsorption, or using a high-surface-area adsorbent such as a metal-organic framework. Xylenes are liquid, and hence would support a much higher surface density than a gas, and could demonstrate significantly enhanced absorption. Finally, a chemically-active functionalization layer is the standard choice for SEIRA, but these layers shift the molecular resonance wavelengths. We have shown that the MTM-lined disc MTS is scalable, making it simple to redesign for the wavelength range required.

8. The subwavelength imaging array and the phase-gradient MTSs presented in Ch. 5 could be fabricated and characterized.

6.2.2 Long-Term

Longer-term development should look to extend the capabilities presented here to new domains not targeted by this work. Such studies might include:

1. Adding additional deposition steps after patterning. This could be used to deposit two-dimensional or other nonlinear materials and study their properties with the strong near-field enhancement offered by the MTM-lined aperture designs or to create reconfigurable MTSs. Potential applications include all-optical switches, magnetic memory devices, and enhanced photon-mixing devices. Patterning a second metallic layer could

also be used to add a wider variety of resonant features to the MTS spectrum, such as longitudinal magnetic dipolar resonances.

2. A number of other material platforms could benefit from the high-resolution patterning of the HIM. Even in cases where directional etchants are available, it may not always be possible to create a mask with sufficiently high precision using any method other than HIM.

3. Scaling the HIM is a big challenge. Moreover, gold is not compatible with conventional complementary metal-oxide-semiconductor processes. Despite the very slow throughput, the HIM is ideal for extremely specialized, low-volume fabrication and prototyping. Some approaches to increasing the throughput include:

   Using HIM just as a finishing tool. The wagon-wheel aperture could be made by (1) depositing some kind of conductive disc, *e.g.*, silver or aluminum (though it must be a material that won't inter-diffuse with the intended aperture metal), (2) using the HIM to mill just the areas required for nanowires, (3) use some kind of conformal deposition process such as atomic layer deposition to deposit the required gold layer over the entire surface, (4) (potentially optional) etch away the excess gold over the aperture area, (5) chemically etch away the filling material. This may increase the overall process time but also reduce the time using the HIM, which reduces drift and redeposition (and the redeposited metal will be etched anyhow) and may decrease the overall fabrication time for larger surfaces than the ones studied here.

   Masking the target surface and defocusing the He^+ beam. Conventional plasma etching systems are unable to create features as small as the HIM due to significantly larger energy spread, even with light ions. If the surface of the sample were masked at a sufficiently high resolution, a defocused ion beam with maximized current providing a collimated illumination of the sample may be able to pattern a wider area of the sample at once.

4. Patterning at an angle and using depth profiles could be used to create chiral MTS elements at a very high resolution. Such MTSs could be used to probe the chirality of molecules with unprecedented sensitivity or for polarization conversion.

6.3 Contributions

Below, I list the publications I authored or contributed to over the course of this work.

6.3.1 Journal Publications

(J8) **M. Semple**, K. G. Scheuer, R. G. DeCorby, and A. K. Iyer, "Complex 10-nm Resolution Nanogap and Nanowire Geometries for Plasmonic Metasurface Miniaturization". ***(Under Review, Jul 2022).*** (14 pages)

(J7) **M. Semple** and A. K. Iyer, "Surface-Enhanced Mid-Infrared Absorption Spectroscopy Using Miniaturized-Disc Metasurface". *Sci Rep*, vol. 11, 23557, Dec 2021. (13 pages)

(J6) A. K. Iyer, B. P. Smyth, **M. Semple**, and C. Barker, "Going Remote: Teaching Microwave Engineering in the Age of the Global Pandemic and Beyond". *IEEE Microwave Magazine*, vol. 22, no. 11, pp. 64–77, Oct 2021. (14 pages)

(J5) **M. Semple**, A. C. Hryciw, P. Li, E. Flaim, and A. K. Iyer, "Patterning of Complex, Nanometer-Scale Features in Wide-Area Gold Nanoplasmonic Structures Using Helium Focused Ion Beam Milling". *ACS Applied Materials and Interfaces*, vol. 13, no. 36, pp. 43209–43220, Sep 2021. (12 pages)

(J4) A. Bhardwaj, D. Pratap, **M. Semple**, A. K. Iyer, A. M. Jayannavar, S. A. Ramakrishna, "Properties of waveguides filled with anisotropic

metamaterials". *Comptes Rendus. Physique*, vol. 21, no. 7–8, pp. 677–711, Jan 2021. ***Invited*** (35 pages)

(J3) E. Baladi, **M. Semple**, and A. K. Iyer, "A Fano-Reflection Metafilm Composed of Metamaterial-Lined Discs". *IEEE Access*, vol. 8, pp. 117018–117027, Jun 2020. (10 pages)

(J2) E. Baladi, **M. Semple**, and A. K. Iyer, "Single-Layer Dual-Band Polarization-Selective Metafilm with Independently Controlled and Closely Spaced Shielding Bands". *IEEE Transactions on Antennas and Propagation*, vol. 68, no. 3, pp. 1448–1457, Mar 2020. ***Invited*** (10 pages)

(J1) **M. Semple**, E. Baladi, and A. K. Iyer, "Optical Metasurface Based on Subwavelength Nanoplasmonic Metamaterial-Lined Apertures". *IEEE Journal of Selected Topics in Quantum Electronics Special Issue on Metamaterial Photonics and Integration*, vol. 25, no. 3, pp. 1–8, Jan 2019. (8 pages)

6.3.2 Conference Proceedings

(C14) **M. Semple** and A. K. Iyer, "Asymmetric Metamaterial-Lined Apertures for Plasmonic Phase-Gradient Optical Metasurfaces". *2022 USNC-URSI National Radio Science Meeting*, Boulder, CO, p. 58, Jan 2021. (Online) ***Invited*** (1 page)

(C13) A. K. Iyer, B. P. Smyth, **M. Semple**, and C. J. Barker, "Strategies for the fully remote delivery of a microwave engineering course with a hands-on lab component". *Proc. IEEE 2021 Antennas and Propagation Society and URSI USNC International Symposium*, Singapore, abstract no. 2824, Dec 2021. (Online) ***Invited*** (1 page)

(C12) **M. Semple** and A. K. Iyer, "A Study of Asymmetric Epsilon-Negative and Near-Zero Metamaterial-Lined Plasmonic Nanoapertures as Metasurface Unit Cells". *2021 USNC-URSI National Radio Science Meeting*, Boulder, CO, p. 55, Jan 2021. (Online) ***Invited*** (1 page)

(C11) **M. Semple** and A. K. Iyer, "Electron-Beam Lithography Fabrication Process Development For A Mid-IR Plasmonic Metasurface With Fine Features". *Metamaterials'2020*, New York, NY, pp. X-511–X-513, Sep 2020. (Online) ***Invited*** (3 pages)

(C10) **M. Semple** and A. K. Iyer, "Mu-Negative and Near-Zero Lined Disks for Surface-Enhanced Mid-Infrared Spectroscopy". *2020 IEEE AP-S Symposium on Antennas and Propagation and USNC-URSI Radio Science Meeting*, Montreal, QC, pp. 749–750, Jul 2020. (Online) (2 pages)

(C9) **M. Semple** and A. K. Iyer, "Design and Simulation of Polarization-Sensitive ENNZ-Lined Apertures for Visible-Light Metasurfaces". *14^{th} European Conference on Antennas and Propagation, EuCAP 2020*, Copenhagen, Denmark, Mar 2020. (3 pages)

(C8) **M. Semple** and A. K. Iyer, "Nanometre-Scale Fabrication of Optical Metasurfaces Using Helium Ion Milling". *2019 IEEE AP-S Symposium on Antennas and Propagation and USNC-URSI Radio Science Meeting*, Atlanta, GA, Jul 2019. (1 page)

(C7) E. Baladi, **M. Semple**, and A. K. Iyer, "Imaging of Subwavelength Features in the Far-Field Using Resonant Metasurfaces: Design from Microwave to Infrared Frequencies". *URSI EM Theory Symposium 2019*, San Diego, CA, May 2019. ***Invited*** (4 pages)

(C6) **M. Semple**, E. Baladi, and A. K. Iyer, "Advances in Metasurfaces Based on Metamaterial-Lined Apertures and Discs". *2019 USNC-URSI National Radio Science Meeting*, Boulder, CO, Jan 2019. ***Invited*** (1 page)

(C5) **M. Semple**, A. C. Hryciw, and A. K. Iyer, "Asterisk Metasurface at 193 THz". *2018 IEEE AP-S Symposium on Antennas and Propagation and USNC-URSI Radio Science Meeting*, Boston, MA, pp. 1463-1464, Jul 2018. ***Invited*** (2 pages)

(C4) **M. Semple**, A. C. Hryciw, and A. K. Iyer, "Asterisk-shaped-aperture array optical metasurfaces at telecommunications wavelengths". *2018*

USNC-URSI National Radio Science Meeting, Boulder, CO, Jan 2018. ***Invited*** (1 page)

(C3) **M. Semple**, A. C. Hryciw, and A. K. Iyer, "Compact Aperture Arrays Demonstrating EOT at Telecommunications Wavelengths". *2017 MRS Fall Meeting and Exhibit*, Boston, MA, Nov 2017. (1 page)

(C2) E. Baladi, **M. Semple**, and A. K. Iyer, "High-Resolution Optical Imaging Using ENNZ-Metamaterial-Lined Aperture Arrays". *2017 MRS Fall Meeting and Exhibit*, Boston, MA, Nov 2017. (1 page)

(C1) **M. Semple**, E. Baladi, J. G. Pollock, and A. K. Iyer, "Optical Implementation of a Miniaturized ENNZ-Metamaterial-Lined Aperture Array". *2017 IEEE AP-S Symposium on Antennas and Propagation and USNC-URSI Radio Science Meeting*, San Diego, CA, Jul 2017. (1 page)

6.3.3 Technical Reports

(T2) **M. Semple** and A. K. Iyer, "Patterning nanoscale features with the Zeiss Orion Helium Ion Microscope", *NanoFAB Centre*, Edmonton, AB, Dec. 2018.

(T1) **M. Semple**, B. P. Smyth, and A. K. Iyer, "Characterization of the Conductivity and Roughness Properties of the Voltera V-One Conductive Ink at Microwave Frequencies", *Voltera*, Kitchener, ON, Jul 2017.

References

[1] E. Tseng, S. Colburn, J. Whitehead, *et al.*, "Neural nano-optics for high-quality thin lens imaging," *Nature Communications*, vol. 12, no. 1, p. 6493, Dec. 2021. DOI: 10.1038/s41467-021-26443-0. 1

[2] B. Xu, H. Li, S. Gao, *et al.*, "Metalens-integrated compact imaging devices for wide-field microscopy," *Advanced Photonics*, vol. 2, no. 06, p. 066 004, Nov. 2020. DOI: 10.1117/1.AP.2.6.066004. 1

[3] L. Huang, S. Zhang, and T. Zentgraf, "Metasurface holography: from fundamentals to applications," *Nanophotonics*, vol. 7, no. 6, pp. 1169–1190, Jun. 2018. DOI: 10.1515/nanoph-2017-0118. 1

[4] G. Y. Lee, J. Y. Hong, S. H. Hwang, *et al.*, "Metasurface eyepiece for augmented reality," *Nature Communications*, vol. 9, no. 1, pp. 1–10, Dec. 2018. DOI: 10.1038/s41467-018-07011-5. 1

[5] R. Camacho-Morales, L. Xu, N. Dimitrov, *et al.*, "Infrared upconversion imaging in nonlinear metasurfaces," *Advanced Photonics*, vol. 3, no. 03, p. 036 002, Jun. 2021. DOI: 10.1117/1.AP.3.3.036002. 1

[6] M. Faraji-Dana, E. Arbabi, A. Arbabi, S. M. Kamali, H. Kwon, and A. Faraon, "Compact folded metasurface spectrometer," *Nature Communications*, vol. 9, no. 1, p. 4196, Dec. 2018. DOI: 10.1038/s41467-018-06495-5. 1

[7] F. Yesilkoy, E. R. Arvelo, Y. Jahani, *et al.*, "Ultrasensitive hyperspectral imaging and biodetection enabled by dielectric metasurfaces," *Nature Photonics*, vol. 13, no. 6, pp. 390–396, Jun. 2019. DOI: 10.1038/s41566-019-0394-6. 1

[8] N. A. Rubin, G. D'Aversa, P. Chevalier, Z. Shi, W. T. Chen, and F. Capasso, "Matrix Fourier optics enables a compact full-Stokes polarization camera," *Science*, vol. 365, no. 6448, Jul. 2019. DOI: 10.1126/science.aax1839. 1

[9] N. Meinzer, W. L. Barnes, and I. R. Hooper, "Plasmonic meta-atoms and metasurfaces," *Nature Photonics*, vol. 8, no. 12, pp. 889–898, Nov. 2014. DOI: 10.1038/nphoton.2014.247. 1, 12, 13

[10] J. Hu, S. Bandyopadhyay, Y.-h. Liu, and L.-y. Shao, "A Review on Metasurface: From Principle to Smart Metadevices," *Frontiers in Physics*, vol. 8, p. 502, Jan. 2021. DOI: 10.3389/fphy.2020.586087. 1

[11] F. Ding, Y. Yang, R. A. Deshpande, and S. I. Bozhevolnyi, "A review of gap-surface plasmon metasurfaces: fundamentals and applications," *Nanophotonics*, vol. 7, no. 6, pp. 1129–1156, Jun. 2018. DOI: 10.1515/nanoph-2017-0125. 1

[12] P. Genevet, F. Capasso, F. Aieta, M. Khorasaninejad, and R. Devlin, "Recent advances in planar optics: from plasmonic to dielectric metasurfaces," *Optica*, 2017. DOI: 10.1364/OPTICA.4.000139. 1

[13] G. Di Domenico, D. Weisman, A. Panichella, D. Roitman, and A. Arie, "Large-Scale Inverse Design of a Planar On-Chip Mode Sorter," *ACS Photonics*, vol. 9, no. 2, pp. 378–382, Feb. 2022. DOI: 10.1021/acsphotonics.1c01539. 1

[14] D. Z. Zhu, E. B. Whiting, S. D. Campbell, D. B. Burckel, and D. H. Werner, "Optimal High Efficiency 3D Plasmonic Metasurface Elements Revealed by Lazy Ants," *ACS Photonics*, vol. 6, no. 11, pp. 2741–2748, Nov. 2019. DOI: 10.1021/acsphotonics.9b00717. 1

[15] D. H. Werner, E. B. Whiting, L. Kang, and S. D. Campbell, "Meta-atom library generation via an efficient multi-objective shape optimization method," *Optics Express, Vol. 28, Issue 16, pp. 24229-24242*, vol. 28, no. 16, pp. 24 229–24 242, Aug. 2020. DOI: 10.1364/OE.398332. 1

[16] N. Li, J. Cadusch, A. Liu, A. J. Barlow, A. Roberts, and K. B. Crozier, "Algorithm-Designed Plasmonic Nanotweezers: Quantitative Comparison by Theory, Cathodoluminescence, and Nanoparticle Trapping," *Advanced Optical Materials*, vol. 9, no. 19, p. 2 100 758, Oct. 2021. DOI: 10.1002/ADOM.202100758. 1

[17] P. K. Venuthurumilli, Z. Zeng, and X. Xu, "Inverse Design of Near-Field Transducer for Heat-Assisted Magnetic Recording Using Topology Optimization," *IEEE Transactions on Magnetics*, vol. 57, no. 8, Aug. 2021. DOI: 10.1109/TMAG.2021.3090659. 1

[18] Y. Cui, Y. He, Y. Jin, *et al.*, "Plasmonic and metamaterial structures as electromagnetic absorbers," *Laser & Photonics Reviews*, vol. 8, no. 4, pp. 495–520, Jul. 2014. DOI: 10.1002/LPOR.201400026. 2

[19] A. Monti, A. Alù, A. Toscano, and F. Bilotti, "Optical invisibility through metasurfaces made of plasmonic nanoparticles," *Journal of Applied Physics*, vol. 117, no. 12, p. 123 103, Mar. 2015. DOI: 10.1063/1.4916257. 2

[20] J. Kim, S. Choudhury, C. DeVault, *et al.*, "Controlling the Polarization State of Light with Plasmonic Metal Oxide Metasurface," *ACS Nano*, vol. 10, no. 10, pp. 9326–9333, Oct. 2016. DOI: 10.1021/acsnano.6b03937. 2

[21] N. Yu, F. Aieta, P. Genevet, M. A. Kats, Z. Gaburro, and F. Capasso, "A Broadband, Background-Free Quarter-Wave Plate Based on Plasmonic Metasurfaces," *Nano Letters*, vol. 12, no. 12, pp. 6328–6333, Dec. 2012. DOI: 10.1021/nl303445u. 2

[22] L. Liu, X. Zhang, Z. Zhao, *et al.*, "Batch Fabrication of Metasurface Holograms Enabled by Plasmonic Cavity Lithography," *Advanced Optical Materials*, vol. 5, no. 21, p. 1 700 429, Nov. 2017. DOI: 10.1002/adom.201700429. 2

[23] X. Ni, A. V. Kildishev, and V. M. Shalaev, "Metasurface holograms for visible light," *Nature Communications*, vol. 4, no. 1, pp. 1–6, Nov. 2013. DOI: 10.1038/ncomms3807. 2

[24] J. Zhang, M. ElKabbash, R. Wei, S. C. Singh, B. Lam, and C. Guo, "Plasmonic metasurfaces with 42.3% transmission efficiency in the visible," *Light: Science & Applications 2019 8:1*, vol. 8, no. 1, pp. 1–13, Jun. 2019. DOI: 10.1038/s41377-019-0164-8. 2

[25] X. Ni, S. Ishii, A. V. Kildishev, and V. M. Shalaev, "Ultra-thin, planar, Babinet-inverted plasmonic metalenses," *Light: Science & Applications 2013 2:4*, vol. 2, no. 4, e72–e72, Apr. 2013. DOI: 10.1038/lsa.2013.28. 2

[26] J. Langer, D. Jimenez de Aberasturi, J. Aizpurua, *et al.*, "Present and Future of Surface-Enhanced Raman Scattering," *ACS Nano*, vol. 14, no. 1, pp. 28–117, Jan. 2020. DOI: 10.1021/acsnano.9b04224. 2, 19

[27] X. Chong, Y. Zhang, E. Li, *et al.*, "Surface-Enhanced Infrared Absorption: Pushing the Frontier for On-Chip Gas Sensing," *ACS Sensors*, vol. 3, no. 1, pp. 230–238, Jan. 2018. DOI: 10.1021/acssensors.7b00891. 2, 167

[28] F. Neubrech, C. Huck, K. Weber, A. Pucci, and H. Giessen, "Surface-Enhanced Infrared Spectroscopy Using Resonant Nanoantennas," *Chemical Reviews*, vol. 117, no. 7, pp. 5110–5145, Apr. 2017. DOI: 10.1021/acs.chemrev.6b00743. 2, 18, 83

[29] M. Mesch, B. Metzger, M. Hentschel, and H. Giessen, "Nonlinear Plasmonic Sensing," *Nano Letters*, vol. 16, no. 5, pp. 3155–3159, May 2016. DOI: 10.1021/acs.nanolett.6b00478. 2

[30] V. P. Drachev, A. V. Kildishev, J. D. Borneman, *et al.*, "Engineered nonlinear materials using gold nanoantenna array," *Scientific Reports 2018 8:1*, vol. 8, no. 1, pp. 1–9, Jan. 2018. DOI: 10.1038/s41598-017-19066-3. 2

[31] H. Gao, Z. Zhao, Y. Guo, *et al.*, "Super-resolution imaging with a Bessel lens realized by a geometric metasurface," *Optics Express, Vol. 25, Issue 12, pp. 13933-13943*, vol. 25, no. 12, pp. 13 933–13 943, Jun. 2017. DOI: 10.1364/OE.25.013933. 2, 3

[32] M. Horák, V. Křápek, M. Hrtoň, *et al.*, "Limits of Babinet's principle for solid and hollow plasmonic antennas," *Scientific Reports*, vol. 9, no. 1, pp. 1–11, Mar. 2019. DOI: 10.1038/s41598-019-40500-1. 2

[33] N. Zhou, E. C. Kinzel, and X. Xu, "Nanoscale ridge aperture as near-field transducer for heat-assisted magnetic recording," *Applied Optics, Vol. 50, Issue 31, pp. G42-G46*, vol. 50, no. 31, G42–G46, Nov. 2011. DOI: 10.1364/AO.50.000G42. 2

[34] M. Hrtoň, A. Konečná, M. Horák, T. Šikola, and V. Křápek, "Plasmonic Antennas with Electric, Magnetic, and Electromagnetic Hot Spots Based on Babinet's Principle," *PHYSICAL REVIEW APPLIED*, vol. 13, p. 54 045, 2020. DOI: 10.1103/PhysRevApplied.13.054045. 2

[35] L. Scipioni, D. C. Ferranti, V. S. Smentkowski, and R. A. Potyrailo, "Fabrication and initial characterization of ultrahigh aspect ratio vias in gold using the helium ion microscope," *Journal of Vacuum Science & Technology B, Nanotechnology and Microelectronics: Materials, Processing, Measurement, and Phenomena*, vol. 28, no. 6, C6P18–C6P23, Nov. 2010. DOI: 10.1116/1.3517514. 3, 22

[36] Y. Wang, M. Abb, S. A. Boden, J. Aizpurua, C. H. De Groot, and O. L. Muskens, "Ultrafast nonlinear control of progressively loaded, single plasmonic nanoantennas fabricated using helium ion milling," *Nano Letters*, vol. 13, no. 11, pp. 5647–5653, Nov. 2013. DOI: 10.1021/nl403316z. 3, 22, 124

[37] M. Melli, A. Polyakov, D. Gargas, *et al.*, "Reaching the theoretical resonance quality factor limit in coaxial plasmonic nanoresonators fabricated by helium ion lithography," *Nano Letters*, vol. 13, no. 6, pp. 2687–2691, Jun. 2013. DOI: 10.1021/nl400844a. 3, 22

[38] C. Hahn, A. Hajebifard, and P. Berini, "Helium focused ion beam direct milling of plasmonic heptamer-arranged nanohole arrays," *Nanophotonics*, vol. 9, no. 2, pp. 393–399, Feb. 2019. DOI: 10.1515/nanoph-2019-0385. 3, 22, 28, 122

[39] H. Kollmann, X. Piao, M. Esmann, *et al.*, "Toward Plasmonics with Nanometer Precision: Nonlinear Optics of Helium-Ion Milled Gold Nanoantennas," *Nano Letters*, vol. 14, no. 8, pp. 4778–4784, Aug. 2014. DOI: 10.1021/nl5019589. 3, 22, 28

[40] V. Deinhart, L. M. Kern, J. N. Kirchhof, *et al.*, "The patterning toolbox FIB-o-mat: Exploiting the full potential of focused helium ions for nanofabrication," *Beilstein Journal of Nanotechnology*, vol. 12, no. 1, pp. 304–318, Apr. 2021. DOI: 10.3762/bjnano.12.25. 3, 22, 97, 177

[41] F. Ding, A. Pors, and S. I. Bozhevolnyi, "Gradient metasurfaces: a review of fundamentals and applications," *Reports on Progress in Physics*, vol. 81, no. 2, p. 026 401, Feb. 2018. DOI: 10.1088/1361-6633/aa8732. 3

[42] W. T. Chen, K.-Y. Yang, C.-M. Wang, *et al.*, "High-Efficiency Broadband Meta-Hologram with Polarization-Controlled Dual Images," *Nano Letters*, vol. 14, no. 1, pp. 225–230, Jan. 2014. DOI: 10.1021/nl403811d. 3

[43] G. Zheng, H. Mühlenbernd, M. Kenney, G. Li, T. Zentgraf, and S. Zhang, "Metasurface holograms reaching 80% efficiency," *Nature Nanotechnology*, vol. 10, no. 4, pp. 308–312, Apr. 2015. DOI: 10.1038/nnano.2015.2. 3

[44] X. Li, L. Chen, Y. Li, *et al.*, "Multicolor 3D meta-holography by broadband plasmonic modulation," *Science Advances*, vol. 2, no. 11, e1601102, Nov. 2016. DOI: 10.1126/sciadv.1601102. 3

[45] R. Zhao, L. Huang, and Y. Wang, "Recent advances in multi-dimensional metasurfaces holographic technologies," *PhotoniX*, vol. 1, no. 1, p. 20, Dec. 2020. DOI: 10.1186/s43074-020-00020-y. 3

[46] G. H. Yuan, E. T. Rogers, and N. I. Zheludev, "Achromatic super-oscillatory lenses with sub-wavelength focusing," *Light: Science & Applications*, vol. 6, no. 9, e17036–e17036, Sep. 2017. DOI: 10.1038/lsa.2017.36. 3

[47] E. Baladi and A. K. Iyer, "Far-field Magnification of Subdiffraction Conducting Features using Metamaterial-Lined Aperture Arrays," *IEEE Transactions on Antennas and Propagation*, vol. 66, no. 7, pp. 3482–3490, 2018. DOI: 10.1109/TAP.2018.2829822. 3, 12, 14, 153, 154

[48] P. Salami and L. Yousefi, "Far-Field Subwavelength Imaging Using Phase Gradient Metasurfaces," *Journal of Lightwave Technology*, vol. 37, no. 10, pp. 2317–2323, May 2019. DOI: 10.1109/JLT.2019.2902544. 3

[49] F. Hong and R. Blaikie, "Plasmonic Lithography: Recent Progress," *Advanced Optical Materials*, vol. 7, no. 14, p. 1 801 653, Jul. 2019. DOI: 10.1002/adom.201801653. 3

[50] A. Datta and X. Xu, "Optical and thermal designs of near field transducer for heat assisted magnetic recording," *Japanese Journal of Applied Physics*, vol. 57, no. 9S2, 09TA01, Sep. 2018. DOI: 10.7567/JJAP.57.09TA01. 3

[51] C. Huck, F. Neubrech, J. Vogt, *et al.*, "Surface-Enhanced Infrared Spectroscopy Using Nanometer-Sized Gaps," *ACS Nano*, vol. 8, no. 5, pp. 4908–4914, May 2014. DOI: 10.1021/nn500903v. 3

[52] H. Shi, X. Zhu, S. Zhang, G. Wen, M. Zheng, and H. Duan, "Plasmonic metal nanostructures with extremely small features: new effects, fabrication and applications," *Nanoscale Advances*, vol. 3, no. 15, pp. 4349–4369, Jul. 2021. DOI: 10.1039/D1NA00237F. 3

[53] P. Anger, P. Bharadwaj, and L. Novotny, "Enhancement and Quenching of Single-Molecule Fluorescence," *Physical Review Letters*, vol. 96, no. 11, p. 113 002, Mar. 2006. DOI: 10.1103/PhysRevLett.96.113002. 3

[54] M. S. Tame, K. R. McEnery, Ş. K. Özdemir, J. Lee, S. A. Maier, and M. S. Kim, "Quantum plasmonics," *Nature Physics*, vol. 9, no. 6, pp. 329–340, Jun. 2013. DOI: 10.1038/nphys2615. 3

[55] T. Abir, M. Tal, and T. Ellenbogen, "Second-Harmonic Enhancement from a Nonlinear Plasmonic Metasurface Coupled to an Optical Waveguide," *Nano Letters*, vol. 22, no. 7, pp. 2712–2717, Apr. 2022. DOI: 10.1021/acs.nanolett.1c04584. 3

[56] P.-Y. Chen, C. Argyropoulos, G. D'Aguanno, and A. Alù, "Enhanced Second-Harmonic Generation by Metasurface Nanomixer and Nanocavity," *ACS Photonics*, vol. 2, no. 8, pp. 1000–1006, Aug. 2015. DOI: 10.1021/acsphotonics.5b00205. 3

[57] A. Ahmadivand, M. Semmlinger, L. Dong, B. Gerislioglu, P. Nordlander, and N. J. Halas, "Toroidal Dipole-Enhanced Third Harmonic Generation of Deep Ultraviolet Light Using Plasmonic Meta-atoms," *Nano Letters*, vol. 19, no. 1, pp. 605–611, Jan. 2019. DOI: 10.1021/acs.nanolett.8b04798. 3

[58] A. C. Lesina, P. Berini, and L. Ramunno, "Origin of third harmonic generation in plasmonic nanoantennas," *Optical Materials Express*, vol. 7, no. 5, p. 1575, May 2017. DOI: 10.1364/OME.7.001575. 3

[59] O. Hess, J. B. Pendry, S. A. Maier, R. F. Oulton, J. M. Hamm, and K. L. Tsakmakidis, "Active nanoplasmonic metamaterials," *Nature Materials*, vol. 11, no. 7, pp. 573–584, Jul. 2012. DOI: 10.1038/nmat3356. 3

[60] Y. Chen, Z. Shu, S. Zhang, *et al.*, "Sub-10 nm fabrication: methods and applications," *International Journal of Extreme Manufacturing*, vol. 3, no. 3, p. 032 002, Jul. 2021. DOI: 10.1088/2631-7990/ac087c. 3

[61] G. Rosolen, L. J. Wong, N. Rivera, B. Maes, M. Soljačić, and I. Kaminer, "Metasurface-based multi-harmonic free-electron light source," *Light: Science & Applications*, vol. 7, no. 1, p. 64, Dec. 2018. DOI: 10.1038/s41377-018-0065-2. 3

[62] E. Baladi, J. G. Pollock, and A. K. Iyer, "New approach for extraordinary transmission through an array of subwavelength apertures using thin ENNZ metamaterial liners," *Optics Express*, vol. 23, no. 16, p. 20 356, Aug. 2015. DOI: 10.1364/OE.23.020356. 3, 14, 15, 16, 17, 35, 36

[63] E. Baladi, M. Semple, and A. K. Iyer, "A Fano-Reflection Metafilm Composed of Metamaterial-Lined Discs," *IEEE Access*, vol. 8, pp. 117 018–117 027, 2020. DOI: 10.1109/ACCESS.2020.3003852. 3, 21, 79, 81

[64] ——, "Single-Layer Dual-Band Polarization-Selective Metafilm with Independently Controlled and Closely Spaced Shielding Bands," *IEEE Transactions on Antennas and Propagation*, vol. 68, no. 3, pp. 1448–1457, Mar. 2020. DOI: 10.1109/TAP.2019.2948574. 3, 21

[65] R. H. Ritchie, "Plasma Losses by Fast Electrons in Thin Films," *Physical Review*, vol. 106, no. 5, pp. 874–881, Jun. 1957. DOI: 10.1103/PhysRev.106.874. 9

[66] R. H. Ritchie and H. B. Eldridge, "Optical Emission from Irradiated Foils. I," *Physical Review*, vol. 126, no. 6, pp. 1935–1947, Jun. 1962. DOI: 10.1103/PhysRev.126.1935. 9

[67] I. R. Hooper and W. L. Barnes, "The Basics of Plasmonics," *Handbook of Surface Science*, vol. 4, pp. 37–74, Jan. 2014. DOI: 10.1016/B978-0-444-59526-3.00002-1. 9

[68] E. Kretschmann and H. Raether, "Notizen: Radiative Decay of Non Radiative Surface Plasmons Excited by Light," *Zeitschrift für Naturforschung A*, vol. 23, no. 12, pp. 2135–2136, Jan. 1968. DOI: 10.1515/zna-1968-1247. 9

[69] A. Otto, "Excitation of nonradiative surface plasma waves in silver by the method of frustrated total reflection," *Zeitschrift für Physik A Hadrons and nuclei*, vol. 216, no. 4, pp. 398–410, Aug. 1968. DOI: 10.1007/BF01391532. 9

[70] H. Ditlbacher, J. R. Krenn, G. Schider, A. Leitner, and F. R. Aussenegg, "Two-dimensional optics with surface plasmon polaritons," *Applied Physics Letters*, vol. 81, no. 10, p. 1762, Aug. 2002. DOI: 10.1063/1.1506018. 9

[71] E. Devaux, T. W. Ebbesen, J. C. Weeber, and A. Dereux, "Launching and decoupling surface plasmons via micro-gratings," *Applied Physics Letters*, vol. 83, no. 24, p. 4936, Dec. 2003. DOI: 10.1063/1.1634379. 9

[72] S. Kasani, K. Curtin, and N. Wu, "A review of 2D and 3D plasmonic nanostructure array patterns: fabrication, light management and sensing applications," *Nanophotonics*, vol. 8, no. 12, pp. 2065–2089, Oct. 2019. 10

[73] B. Shen, V. Linko, K. Tapio, *et al.*, "Plasmonic nanostructures through DNA-assisted lithography," *Science Advances*, vol. 4, no. 2, eaap8978, Feb. 2018. DOI: 10.1126/sciadv.aap8978. 10

[74] V. J. Sorger, R. F. Oulton, R. M. Ma, and X. Zhang, "Toward integrated plasmonic circuits," *MRS Bulletin*, vol. 37, no. 8, pp. 728–738, Aug. 2012. DOI: 10.1557/mrs.2012.170. 10

[75] T. J. Davis, D. E. Gómez, and A. Roberts, "Plasmonic circuits for manipulating optical information," *Nanophotonics*, vol. 6, no. 3, pp. 543–559, Oct. 2016. DOI: 10.1515/nanoph-2016-0131. 10

[76] S. Linden, "Fabrication of plasmonic slot waveguides in single-crystalline gold films and freestanding photonic metasurfaces by focused ion beam milling (Conference Presentation)," in *Advanced Fabrication Technologies for Micro/Nano Optics and Photonics XIII*, G. von Freymann, E. Blasco, and D. Chanda, Eds., vol. 11292, SPIE, Mar. 2020, p. 6. DOI: 10.1117/12.2550461. 10, 124

[77] A. V. Krasavin, P. Ginzburg, G. A. Wurtz, and A. V. Zayats, "Nonlocality-driven supercontinuum white light generation in plasmonic nanostructures," *Nature Communications*, vol. 7, no. 1, pp. 1–6, May 2016. DOI: 10.1038/ncomms11497. 10

[78] N. C. Panoiu, W. E. I. Sha, D. Y. Lei, and G.-C. Li, "Nonlinear optics in plasmonic nanostructures," *Journal of Optics*, vol. 20, no. 8, p. 083 001, Aug. 2018. DOI: 10.1088/2040-8986/aac8ed. 10

[79] S. G. Rodrigo, F. de Leon-Perez, and L. Martin-Moreno, "Extraordinary Optical Transmission: Fundamentals and Applications," *Proceedings of the IEEE*, vol. 104, no. 12, pp. 2288–2306, 2016. DOI: 10.1109/JPROC.2016.2580664. 10

[80] T. Debogovic, J. Perruisseau-Carrier, and J. Bartolic, "Partially Reflective Surface Antenna With Dynamic Beamwidth Control," *IEEE Antennas and Wireless Propagation Letters*, vol. 9, pp. 1157–1160, 2010. DOI: 10.1109/LAWP.2010.2098386. 10

[81] J. R. Cooper, S. Kim, and M. M. Tentzeris, "A Novel Polarization-Independent, Free-Space, Microwave Beam Splitter Utilizing an Inkjet-Printed, 2-D Array Frequency Selective Surface," *IEEE Antennas and Wireless Propagation Letters*, vol. 11, pp. 686–688, 2012. DOI: 10.1109/LAWP.2012.2204715. 10

[82] M. Sazegar, Y. Zheng, C. Kohler, *et al.*, "Beam Steering Transmitarray Using Tunable Frequency Selective Surface With Integrated Ferroelectric Varactors," *IEEE Transactions on Antennas and Propagation*, vol. 60, no. 12, pp. 5690–5699, Dec. 2012. DOI: 10.1109/TAP.2012.2213057. 10

[83] J. Ji, J. G. O'Connell, D. J. D. Carter, and D. N. Larson, "High-Throughput Nanohole Array Based System To Monitor Multiple Binding Events in Real Time," *Analytical Chemistry*, vol. 80, no. 7, pp. 2491–2498, Apr. 2008. DOI: 10.1021/ac7023206. 10

[84] S. Wu, P. Guo, W. Huang, S. Xiao, and Y. Zhu, "Dielectric Thickness Detection Sensor Based on Metallic Nanohole Arrays," *The Journal of Physical Chemistry C*, vol. 115, no. 31, pp. 15 205–15 209, Aug. 2011. DOI: 10.1021/jp2030472. 10

[85] Z.-L. Yang, Q.-H. Li, B. Ren, and Z.-Q. Tian, "Tunable SERS from aluminium nanohole arrays in the ultraviolet region," *Chemical Communications*, vol. 47, no. 13, p. 3909, Apr. 2011. DOI: 10.1039/c0cc05311b. 10, 11, 15

[86] F. J. Garcia-Vidal, L. Martín-Moreno, and J. B. Pendry, "Surfaces with holes in them: new plasmonic metamaterials," *Journal of Optics A: Pure and Applied Optics*, vol. 7, no. 2, S97–S101, Feb. 2005. DOI: 10.1088/1464-4258/7/2/013. 10

[87] J. V. Coe, J. M. Heer, S. Teeters-Kennedy, H. Tian, and K. R. Rodriguez, "Extraordinary Transmission of Metal Films with Arrays of Subwavelength Holes," *Annual Review of Physical Chemistry*, vol. 59, no. 1, pp. 179–202, 2008. DOI: 10.1146/annurev.physchem.59.032607.093703. 10

[88] D. V. Labeke, D. Gérard, B. Guizal, F. I. Baida, and L. Li, "An angle-independent Frequency Selective Surface in the optical range," *Optics Express*, vol. 14, no. 25, pp. 11 945–11 951, Dec. 2006. DOI: 10.1364/OE.14.011945. 10

[89] B. Munk and John Wiley & Sons., *Frequency selective surfaces : theory and design*. John Wiley, 2000, p. 410. 10

[90] A. Degiron and T. W. Ebbesen, "The role of localized surface plasmon modes in the enhanced transmission of periodic subwavelength apertures," *Journal of Optics A: Pure and Applied Optics*, vol. 7, no. 2, S90, 2005. DOI: 10.1088/1464-4258/7/2/012. 10

[91] S. B. Glybovski, S. A. Tretyakov, P. A. Belov, Y. S. Kivshar, and C. R. Simovski, "Metasurfaces: From microwaves to visible," *Physics Reports*, vol. 634, pp. 1–72, May 2016. DOI: 10.1016/j.physrep.2016.04.004. 11, 22

[92] M. Semple, E. Baladi, and A. K. Iyer, "Optical Metasurface Based on Subwavelength Nanoplasmonic Metamaterial-Lined Apertures," *IEEE Journal of Selected Topics in Quantum Electronics*, vol. 25, no. 3, pp. 1–8, May 2019. DOI: 10.1109/JSTQE.2019.2896277. 11, 30, 32, 34, 36, 37, 38, 39, 40, 60, 85

[93] K.-H. Kim, G.-H. Jung, S.-J. Lee, H.-G. Park, and Q.-H. Park, "Ultrathin Capacitive Metasurfaces for Strong Electric Response," *Advanced Optical Materials*, vol. 4, no. 10, pp. 1501–1506, Oct. 2016. DOI: 10.1002/adom.201600146. 11

[94] S. Chang, X. Guo, and X. Ni, "Optical Metasurfaces: Progress and Applications," *Annu. Rev. Mater. Res*, vol. 48724, no. 1, pp. 1–7, 2018. DOI: 10.1146/annurev-matsci-070616. 12

[95] H.-T. Chen, A. J. Taylor, and N. Yu, "A review of metasurfaces: physics and applications," *Reports on Progress in Physics*, vol. 79, no. 7, p. 076 401, Jul. 2016. DOI: 10.1088/0034-4885/79/7/076401. 12

[96] S. Zhang, C. L. Wong, S. Zeng, *et al.*, "Metasurfaces for biomedical applications: Imaging and sensing from a nanophotonics perspective," *Nanophotonics*, vol. 10, no. 1, pp. 259–293, Jan. 2021. DOI: 10.1515/nanoph-2020-0373. 12

[97] S. Gwo, C.-Y. Wang, H.-Y. Chen, *et al.*, "Plasmonic Metasurfaces for Nonlinear Optics and Quantitative SERS," *ACS Photonics*, vol. 3, no. 8, pp. 1371–1384, Aug. 2016. DOI: 10.1021/acsphotonics.6b00104. 12

[98] C. Wu, A. B. Khanikaev, R. Adato, *et al.*, "Fano-resonant asymmetric metamaterials for ultrasensitive spectroscopy and identification of molecular monolayers," *Nature Materials*, vol. 11, no. 1, pp. 69–75, Nov. 2012. DOI: 10.1038/nmat3161. 12, 167

[99] A. Ishikawa, S. Hara, T. Tanaka, Y. Hayashi, and K. Tsuruta, "Cross-Polarized Surface-Enhanced Infrared Spectroscopy by Fano-Resonant Asymmetric Metamaterials," *Scientific Reports*, vol. 7, no. 1, pp. 1–8, Dec. 2017. DOI: 10.1038/s41598-017-03545-8. 12

[100] S. M. Kamali, E. Arbabi, A. Arbabi, and A. Faraon, "A review of dielectric optical metasurfaces for wavefront control," *Nanophotonics*, vol. 7, no. 6, pp. 1041–1068, Jun. 2018. DOI: 10.1515/nanoph-2017-0129. 12

[101] C.-N. Chiu and W.-Y. Wang, "A Dual-Frequency Miniaturized-Element FSS With Closely Located Resonances," *IEEE Antennas and Wireless Propagation Letters*, vol. 12, pp. 163–165, 2013. DOI: 10.1109/LAWP.2013.2245092. 12

[102] J. P. Wong, M. Selvanayagam, and G. V. Eleftheriades, "Design of unit cells and demonstration of methods for synthesizing Huygens metasurfaces," *Photonics and Nanostructures - Fundamentals and Applications*, vol. 12, no. 4, pp. 360–375, Aug. 2014. DOI: 10.1016/J.PHOTONICS.2014.07.001. 12

[103] C. Pfeiffer and A. Grbic, "Bianisotropic Metasurfaces for Optimal Polarization Control: Analysis and Synthesis," *Physical Review Applied*, vol. 2, no. 4, p. 044 011, Oct. 2014. DOI: 10.1103/PhysRevApplied.2.044011. 12

[104] W. Zhou and T. W. Odom, "Tunable subradiant lattice plasmons by out-of-plane dipolar interactions," *Nature Nanotechnology 2011 6:7*, vol. 6, no. 7, pp. 423–427, May 2011. DOI: 10.1038/NNANO.2011.72. 13

[105] G. Vecchi, V. Giannini, and J. Gómez Rivas, "Shaping the fluorescent emission by lattice resonances in plasmonic crystals of nanoantennas," *Physical Review Letters*, vol. 102, no. 14, p. 146 807, Apr. 2009. DOI: 10.1103/PHYSREVLETT.102.146807/FIGURES/5/MEDIUM. 13

[106] N. Yu, P. Genevet, M. A. Kats, *et al.*, "Light propagation with phase discontinuities: Generalized laws of reflection and refraction," *Science*, vol. 334, no. 6054, pp. 333–337, Oct. 2011. DOI: 10.1126/science.1210713. 13, 72, 159, 160

[107] M. Decker, M. Wegener, M. W. Klein, and S. Linden, "Circular dichroism of planar chiral magnetic metamaterials," *Optics Letters, Vol. 32, Issue 7, pp. 856-858*, vol. 32, no. 7, pp. 856–858, Apr. 2007. DOI: 10.1364/OL.32.000856. 13

[108] M. Decker, N. Feth, C. M. Soukoulis, S. Linden, and M. Wegener, "Retarded long-range interaction in split-ring-resonator square arrays," *Physical Review B - Condensed Matter and Materials Physics*, vol. 84, no. 8, p. 085 416, Aug. 2011. DOI: 10.1103/PHYSREVB.84.085416/FIGURES/9/MEDIUM. 13

[109] M. C. Gwinner, E. Koroknay, F. Liwei, *et al.*, "Periodic Large-Area Metallic Split-Ring Resonator Metamaterial Fabrication Based on Shadow Nanosphere Lithography," *Small*, vol. 5, no. 3, pp. 400–406, Feb. 2009. DOI: 10.1002/SMLL.200800923. 13

[110] A. E. Nikolaenko, F. De Angelis, S. A. Boden, *et al.*, "Carbon nanotubes in a photonic metamaterial," *Physical Review Letters*, vol. 104, no. 15, p. 153 902, Apr. 2010. DOI: 10.1103/PHYSREVLETT.104.153902/FIGURES/5/MEDIUM. 13

[111] W. Wu, E. Kim, E. Ponizovskaya, *et al.*, "Optical metamaterials at near and mid-IR range fabricated by nanoimprint lithography," *Applied Physics A 2007 87:2*, vol. 87, no. 2, pp. 143–150, Feb. 2007. DOI: 10.1007/S00339-006-3834-3. 13

[112] A. B. Dahlin, "Size Matters: Problems and Advantages Associated with Highly Miniaturized Sensors," *Sensors (Basel, Switzerland)*, vol. 12, no. 3, pp. 3018–3036, Mar. 2012. DOI: 10.3390/s120303018. 14, 15

[113] J. G. Pollock and A. K. Iyer, "Experimental Verification of Below-Cutoff Propagation in Miniaturized Circular Waveguides Using Anisotropic ENNZ Metamaterial Liners," *IEEE Transactions on Microwave Theory and Techniques*, vol. 64, no. 4, pp. 1297–1305, Apr. 2016. DOI: 10.1109/TMTT.2016.2532872. 14

[114] M. Soljacic, E. Lidorikis, J. D. Joannopoulos, and L. V. Hau, "Electromagnetically induced transparency in microcavities," in *Optical Science and Technology, the SPIE 49th Annual Meeting*, E. W. Taylor, Ed., Oct. 2004, p. 174. DOI: 10.1117/12.562304. 15

[115] H. A. Bethe, "Theory of Diffraction by Small Holes," *Physical Review*, vol. 66, pp. 163–182, Oct. 1944. DOI: 10.1103/PhysRev.66.163. 15

[116] J. G. Pollock and A. K. Iyer, "Below-Cutoff Propagation in Metamaterial-Lined Circular Waveguides," *IEEE Transactions on Microwave Theory and Techniques*, vol. 61, no. 9, pp. 3169–3178, Sep. 2013. DOI: 10.1109/TMTT.2013.2274780. 15, 16, 33, 40, 45

[117] M. F. Limonov, M. V. Rybin, A. N. Poddubny, and Y. S. Kivshar, "Fano resonances in photonics," *Nature Photonics*, vol. 11, no. 9, pp. 543–554, Sep. 2017. DOI: 10.1038/nphoton.2017.142. 15, 213

[118] A. K. Iyer and G. V. Eleftheriades, "Negative-Refractive-Index Transmission-Line Metamaterials," *Negative-Refraction Metamaterials: Fundamental Principles and Applications*, pp. 1–52, Aug. 2005. DOI: 10.1002/0471744751.CH1. 16

[119] R. Pilot, R. Signorini, C. Durante, L. Orian, M. Bhamidipati, and L. Fabris, *A review on surface-enhanced Raman scattering*, Jun. 2019. DOI: 10.3390/bios9020057. 18

[120] A. Ishikawa, S. Hara, T. Tanaka, X. Zhang, and K. Tsuruta, "Robust plasmonic hot-spots in a metamaterial lattice for enhanced sensitivity of infrared molecular detection," *Applied Physics Letters*, vol. 111, no. 24, p. 243 106, Dec. 2017. DOI: 10.1063/1.5004703. 19, 20

[121] N. Li, H. Yin, X. Zhuo, B. Yang, X. M. Zhu, and J. Wang, "Infrared-Responsive Colloidal Silver Nanorods for Surface-Enhanced Infrared Absorption," *Advanced Optical Materials*, vol. 6, no. 17, p. 1 800 436, Sep. 2018. DOI: 10.1002/adom.201800436. 19, 20

[122] A. Tittl, A. Leitis, M. Liu, *et al.*, "Imaging-based molecular barcoding with pixelated dielectric metasurfaces," *Science*, vol. 360, no. 6393, pp. 1105–1109, Jun. 2018. DOI: 10.1126/science.aas9768. 19, 20

[123] V. Di Meo, A. Caporale, A. Crescitelli, *et al.*, "Metasurface based on cross-shaped plasmonic nanoantennas as chemical sensor for surface-enhanced infrared absorption spectroscopy," *Sensors and Actuators, B: Chemical*, vol. 286, pp. 600–607, May 2019. DOI: 10.1016/j.snb.2019.02.014. 19, 20

[124] F. Neubrech, A. Pucci, T. W. Cornelius, S. Karim, A. García-Etxarri, and J. Aizpurua, "Resonant plasmonic and vibrational coupling in a tailored nanoantenna for infrared detection," *Physical Review Letters*, vol. 101, no. 15, p. 157 403, Oct. 2008. DOI: 10.1103/PhysRevLett.101.157403. 19

[125] Y. Chang, D. Hasan, B. Dong, *et al.*, "Surface-Enhanced Infrared Absorption-Based CO2 Sensor using Photonic Crystal Slab," in *Proceedings of the IEEE International Conference on Micro Electro Mechanical Systems (MEMS)*, vol. 2019-January, Institute of Electrical and Electronics Engineers Inc., Jan. 2019, pp. 141–144. DOI: 10.1109/MEMSYS.2019.8870896. 19, 20

[126] W. Yue, V. Kravets, M. Pu, C. Wang, Z. Zhao, and Z. Hu, "Multiple-resonant pad-rod nanoantennas for surface-enhanced infrared absorption spectroscopy," *Nanotechnology*, vol. 30, no. 46, p. 465 206, Sep. 2019. DOI: 10.1088/1361-6528/ab3b69. 19, 20

[127] D. Hasan and C. Lee, "Hybrid Metamaterial Absorber Platform for Sensing of CO2 Gas at Mid-IR," *Advanced Science*, vol. 5, no. 5, p. 1 700 581, May 2018. DOI: 10.1002/ADVS.201700581. 19

[128] K. B. Crozier, M. Ye, K. B. Crozier, and K. B. Crozier, "Metasurface with metallic nanoantennas and graphene nanoslits for sensing of protein monolayers and sub-monolayers," *Optics Express, Vol. 28, Issue 12, pp. 18479-18492*, vol. 28, no. 12, pp. 18 479–18 492, Jun. 2020. DOI: 10.1364/OE.394564. 19

[129] N. J. Bareza, K. K. Gopalan, R. Alani, B. Paulillo, and V. Pruneri, "Mid-infrared Gas Sensing Using Graphene Plasmons Tuned by Reversible Chemical Doping," *ACS Photonics*, vol. 7, no. 4, pp. 879–884, Apr. 2020. DOI: 10.1021/ACSPHOTONICS.9B01714. 19

[130] M. Janneh, "(INVITED)Surface enhanced infrared absorption spectroscopy using plasmonic nanostructures: Alternative ultrasensitive on-chip biosensor technique," *Results in Optics*, vol. 6, p. 100 201, Jan. 2022. DOI: 10.1016/j.rio.2021.100201. 19

[131] C. D'Andrea, J. Bochterle, A. Toma, *et al.*, "Optical nanoantennas for multiband surface-enhanced infrared and raman spectroscopy," *ACS Nano*, vol. 7, no. 4, pp. 3522–3531, Apr. 2013. DOI: 10.1021/nn4004764. 19

[132] R. Adato, S. Aksu, and H. Altug, "Engineering mid-infrared nanoantennas for surface enhanced infrared absorption spectroscopy," *Materials Today*, vol. 18, no. 8, pp. 436–446, Oct. 2015. DOI: 10.1016/j.mattod.2015.03.001. 19, 171

[133] K. Weber, M. L. Nesterov, T. Weiss, *et al.*, "Wavelength scaling in antenna-enhanced infrared spectroscopy: Toward the far-IR and THz region," *ACS Photonics*, vol. 4, no. 1, pp. 45–51, Jan. 2017. DOI: 10.1021/acsphotonics.6b00534. 19

[134] D. J. McCaa, "Spectral Radiance Measurements of Exhaust Plumes from Scale Model Rocket Engines," *Applied Optics, Vol. 7, Issue 5, pp. 899-903*, vol. 7, no. 5, pp. 899–903, May 1968. DOI: 10.1364/AO.7.000899. 21

[135] Q. NIU, Z. HE, and S. DONG, "IR radiation characteristics of rocket exhaust plumes under varying motor operating conditions," *Chinese Journal of Aeronautics*, vol. 30, no. 3, pp. 1101–1114, Jun. 2017. DOI: 10.1016/J.CJA.2017.04.003. 21

[136] D. E. Kashirskii, O. V. Egorov, O. K. Voitsekhovskaya, and O. V. Shefer, "Modeling absorption spectra for detection of the combustion products of jet engines by laser remote sensing," *Applied Optics, Vol. 55, Issue 14, pp. 3814-3823*, vol. 55, no. 14, pp. 3814–3823, May 2016. DOI: 10.1364/AO.55.003814. 21

[137] M. Karlowatz, M. Kraft, and B. Mizaikoff, "Simultaneous Quantitative Determination of Benzene, Toluene, and Xylenes in Water Using Mid-Infrared Evanescent Field Spectroscopy," *Analytical Chemistry*, vol. 76, no. 9, pp. 2643–2648, May 2004. DOI: 10.1021/AC0347009. 21

[138] F. Laible, C. Dreser, D. P. Kern, and M. Fleischer, "Time-effective strategies for the fabrication of poly- and single-crystalline gold nanostructures by focused helium ion beam milling," *Nanotechnology*, vol. 30, no. 23, p. 235 302, Jun. 2019. DOI: 10.1088/1361-6528/ab0506. 22

[139] X. Chen, H. R. Park, M. Pelton, *et al.*, "Atomic layer lithography of wafer-scale nanogap arrays for extreme confinement of electromagnetic waves," *Nature Communications*, vol. 4, no. 1, pp. 1–7, Sep. 2013. DOI: 10.1038/ncomms3361. 22

[140] J. Rhie, D. Lee, Y.-M. Bahk, *et al.*, "Control of optical nanometer gap shapes made via standard lithography using atomic layer deposition," *Journal of Micro/Nanolithography, MEMS, and MOEMS*, vol. 17, no. 02, p. 1, May 2018. DOI: 10.1117/1.jmm.17.2.023504. 22

[141] I. C. Huang, J. Holzgrafe, R. A. Jensen, J. T. Choy, M. G. Bawendi, and M. Loncar, "10 nm gap bowtie plasmonic apertures fabricated by modified lift-off process," *Applied Physics Letters*, vol. 109, no. 13, p. 133 105, Sep. 2016. DOI: 10.1063/1.4963689. 22

[142] L.-J. Black, Y. Wang, C. H. de Groot, A. Arbouet, and O. L. Muskens, "Optimal Polarization Conversion in Coupled Dimer Plasmonic Nanoantennas for Metasurfaces," *ACS Nano*, vol. 8, no. 6, pp. 6390–6399, Jun. 2014. DOI: 10.1021/nn501889s. 22

[143] Y. Chen, K. Bi, Q. Wang, *et al.*, "Rapid Focused Ion Beam Milling Based Fabrication of Plasmonic Nanoparticles and Assemblies via "Sketch and Peel" Strategy," *ACS Nano*, vol. 10, no. 12, pp. 11 228–11 236, Dec. 2016. DOI: 10.1021/acsnano.6b06290. 22

[144] G. Gervinskas, G. Seniutinas, L. Rosa, and S. Juodkazis, "Arrays of Arbitrarily Shaped Nanoparticles: Overlay-Errorless Direct Ion Write," *Advanced Optical Materials*, vol. 1, no. 6, pp. 456–459, Jun. 2013. DOI: 10.1002/adom.201300027. 22

[145] G. Seniutinas, G. Gervinskas, A. Balčytis, *et al.*, "Nanoscale precision in ion milling for optical and terahertz antennas," G. von Freymann, W. V. Schoenfeld, R. C. Rumpf, and H. Helvajian, Eds., vol. 9374, International Society for Optics and Photonics, Mar. 2015, 93740P. DOI: 10.1117/12.2082344. 22

[146] Zeiss, *ORION NanoFab - Helium Ion Microscope (HIM) move beyond sub-10nanometer imaging of charged specimens and nanofabrication applications.* [Online]. Available: https://www.zeiss.com/microscopy/int/products/multiple-ion-beam/orion-nanofab-for-materials.html. 22

[147] *Helium Ion Microscope (Zeiss Orion NanoFAB with Ga FIB) — nanoFAB.* [Online]. Available: https://www.nanofab.ualberta.ca/capabilities/our-equipment/helium-ion-microscope-zeiss-orion/. 23

[148] J. Gierak, "Focused ion beam technology and ultimate applications," *Semiconductor Science and Technology*, vol. 24, no. 4, p. 043 001, Mar. 2009. DOI: 10.1088/0268-1242/24/4/043001. 23, 24

[149] J. Notte and J. Huang, "The Helium Ion Microscope," in *NanoScience and Technology*, Springer Verlag, 2016, pp. 3–30. DOI: 10.1007/978-3-319-41990-9_1. 24, 25, 90

[150] I. Shorubalko, L. Pillatsch, and I. Utke, "Direct–write milling and deposition with noble gases," in *NanoScience and Technology*, Springer Verlag, 2016, pp. 355–393. DOI: 10.1007/978-3-319-41990-9_15. 25, 26

[151] M. Gittinger, K. Höflich, V. Smirnov, H. Kollmann, C. Lienau, and M. Silies, "Strongly coupled, high-quality plasmonic dimer antennas fabricated using a sketch-and-peel technique," *Nanophotonics*, vol. 9, no. 2, pp. 401–412, Feb. 2020. DOI: 10.1515/nanoph-2019-0379. 28

[152] N.-H. Shen, T. Koschny, M. Kafesaki, and C. M. Soukoulis, "Optical metamaterials with different metals," *Physical Review B*, vol. 85, no. 7, p. 075 120, Feb. 2012. DOI: 10.1103/PhysRevB.85.075120. 30

[153] "Borofloat 33 - Optical Properties Datasheet," Home Tech SCHOTT North America, Inc, Tech. Rep. [Online]. Available: https://www.schott.com/en-gb/products/borofloat-p1000314/downloads. 30

[154] M. Semple, A. C. Hryciw, and A. K. Iyer, "Asterisk Metasurface at 193 THz," *2018 IEEE Antennas and Propagation Society International Symposium and USNC/URSI National Radio Science Meeting, AP-SURSI 2018 - Proceedings*, pp. 1463–1464, 2018. DOI: 10.1109/APUSNCURSINRSM.2018.8608428. 30, 32

[155] A. Bhardwaj, D. Pratap, M. Semple, A. K. Iyer, A. M. Jayannavar, and S. Anantha Ramakrishna, "Properties of waveguides filled with anisotropic metamaterials," *Comptes Rendus Physique*, vol. 21, no. 7-8, pp. 677–711, 2021. DOI: 10.5802/CRPHYS.19. 46

[156] N. Engheta, "From RF Circuits to Optical Nanocircuits," *IEEE Microwave Magazine*, vol. 13, no. 4, pp. 100–113, May 2012. DOI: 10.1109/MMM.2012.2189991. 48

[157] M. Staffaroni, J. Conway, S. Vedantam, J. Tang, and E. Yablonovitch, "Circuit analysis in metal-optics," *Photonics and Nanostructures - Fundamentals and Applications*, vol. 10, no. 1, pp. 166–176, Jan. 2012. DOI: 10.1016/j.photonics.2011.12.002. 48

[158] A. Sakurai, B. Zhao, and Z. M. Zhang, "Resonant frequency and bandwidth of metamaterial emitters and absorbers predicted by an RLC circuit model," *Journal of Quantitative Spectroscopy and Radiative Transfer*, vol. 149, pp. 33–40, Dec. 2014. DOI: 10.1016/J.JQSRT.2014.07.024. 48

[159] L. P. Wang, Z. M. Zhang, W. S. Cai, *et al.*, "Phonon-mediated magnetic polaritons in the infrared region," *Optics Express, Vol. 19, Issue S2, pp. A126-A135*, vol. 19, no. 102, A126–A135, Mar. 2011. DOI: 10.1364/OE.19.00A126. 48

[160] X. Jin, "Enhanced optical transmission through ridge nanoapertures for near-field applications," Ph.D. dissertation, 2006, p. 178. 48

[161] N. Zhou, "Optical nano-apertures for near and far field applications," Ph.D. dissertation, 2015, p. 151. 48

[162] A. Dorodnyy, S. M. Koepfli, A. Lochbaum, and J. Leuthold, "Design of CMOS-compatible metal–insulator–metal metasurfaces via extended equivalent-circuit analysis," *Scientific Reports 2020 10:1*, vol. 10, no. 1, pp. 1–12, Oct. 2020. DOI: 10.1038/s41598-020-74849-5. 48

[163] F. Medina, F. Mesa, and R. Marques, "Extraordinary Transmission Through Arrays of Electrically Small Holes From a Circuit Theory Perspective," *IEEE Transactions on Microwave Theory and Techniques*, vol. 56, no. 12, pp. 3108–3120, Dec. 2008. DOI: 10.1109/TMTT.2008.2007343. 48

[164] R. F. Harrington, *Time-harmonic electromagnetic fields*. Wiley-IEEE Press, 2001. 48, 49, 58, 64, 218

[165] B. Lv, R. Li, J. Fu, *et al.*, "Analysis and modeling of Fano resonances using equivalent circuit elements," *Scientific Reports 2016 6:1*, vol. 6, no. 1, pp. 1–6, Aug. 2016. DOI: 10.1038/srep31884. 49

[166] *scipy.optimize.shgo — SciPy v1.8.0 Manual*. [Online]. Available: https://docs.scipy.org/doc/scipy/reference/generated/scipy.optimize.shgo.html. 54

[167] L. Novotny, "Effective Wavelength Scaling for Optical Antennas," *Physical Review Letters*, vol. 98, no. 26, p. 266 802, Jun. 2007. DOI: 10.1103/PhysRevLett.98.266802. 60, 225

[168] N. Engheta, A. Salandrino, and A. Alù, "Circuit Elements at Optical Frequencies: Nanoinductors, Nanocapacitors, and Nanoresistors," *Physical Review Letters*, vol. 95, no. 9, p. 095 504, Aug. 2005. DOI: 10.1103/PhysRevLett.95.095504. 60

[169] M. Semple and A. K. Iyer, "Design and Simulation of Polarization-Sensitive ENNZ-Lined Apertures for Visible-Light Metasurfaces," *14th European Conference on Antennas and Propagation, EuCAP 2020*, Mar. 2020. DOI: 10.23919/EUCAP48036.2020.9135978. 61, 62, 65

[170] E. D. Palik, *Handbook of Optical Constants of Solids*. 1st ed. Elsevier, 1991, vol. 1. 61

[171] M. Mivelle, T. S. Van Zanten, L. Neumann, N. F. Van Hulst, and M. F. Garcia-Parajo, "Ultrabright Bowtie Nanoaperture Antenna Probes Studied by Single Molecule Fluorescence," *Nano Letters*, vol. 12, no. 11, pp. 5972–5978, Nov. 2012. DOI: 10.1021/NL303440W. 70

[172] V. Flauraud, T. S. van Zanten, M. Mivelle, C. Manzo, M. F. Garcia Parajo, and J. Brugger, "Large-Scale Arrays of Bowtie Nanoaperture Antennas for Nanoscale Dynamics in Living Cell Membranes," *Nano Letters*, vol. 15, no. 6, pp. 4176–4182, Jun. 2015. DOI: 10.1021/acs.nanolett.5b01335. 70

[173] P. F. Liao and A. Wokaun, "Lightning rod effect in surface enhanced Raman scattering," *The Journal of Chemical Physics*, vol. 76, no. 1, p. 751, Oct. 1998. DOI: 10.1063/1.442690. 71

[174] A. Arbabi and A. Faraon, "Fundamental limits of ultrathin metasurfaces," *Scientific Reports*, vol. 7, no. 1, p. 43 722, Dec. 2017. DOI: 10.1038/srep43722. 73

[175] Z. Bomzon, V. Kleiner, and E. Hasman, "Pancharatnam–Berry phase in space-variant polarization-state manipulations with subwavelength gratings," *Optics Letters*, vol. 26, no. 18, p. 1424, Sep. 2001. DOI: 10.1364/OL.26.001424. 73

[176] M. V. Berry, "Quantal phase factors accompanying adiabatic changes," *Proceedings of the Royal Society of London. A. Mathematical and Physical Sciences*, vol. 392, no. 1802, pp. 45–57, Mar. 1984. DOI: 10.1098/rspa.1984.0023. 73

[177] W. Luo, S. Xiao, Q. He, S. Sun, and L. Zhou, "Photonic Spin Hall Effect with Nearly 100% Efficiency," *Advanced Optical Materials*, vol. 3, no. 8, pp. 1102–1108, Aug. 2015. DOI: 10.1002/adom.201500068. 73

[178] Q. Lévesque, M. Makhsiyan, P. Bouchon, *et al.*, "Plasmonic planar antenna for wideband and efficient linear polarization conversion," *Applied Physics Letters*, vol. 104, no. 11, p. 111 105, Mar. 2014. DOI: 10.1063/1.4869127. 78

[179] M. Semple and A. K. Iyer, "Mu-Negative and Near-Zero Lined Disks for Surface-Enhanced Mid-Infrared Spectroscopy," in *2020 IEEE International Symposium on Antennas and Propagation and North American Radio Science Meeting, IEEECONF 2020 - Proceedings*, Institute of Electrical and Electronics Engineers Inc., Jul. 2020, pp. 749–750. DOI: 10.1109/IEEECONF35879.2020.9329893. 81, 83

[180] ——, "Surface-enhanced mid-infrared absorption spectroscopy using miniaturized-disc metasurface," *Scientific Reports*, vol. 11, no. 1, p. 23 557, Dec. 2021. DOI: 10.1038/s41598-021-02984-8. 85, 86, 147, 150, 165, 166, 167, 169, 239

[181] *nanoFAB - Fabrication and Characterization Facility*. [Online]. Available: https://www.nanofab.ualberta.ca/. 90

[182] M. Semple, A. C. Hryciw, P. Li, E. Flaim, and A. K. Iyer, "Patterning of Complex, Nanometer-Scale Features in Wide-Area Gold Nanoplasmonic Structures Using Helium Focused Ion Beam Milling," *ACS Applied Materials & Interfaces*, vol. 13, p. 38, 2021. DOI: 10.1021/ACSAMI.1C09295. 90, 92, 104, 106, 107, 109, 113, 115, 117, 118, 119, 120, 123, 124

[183] C. A. Volkert and A. M. Minor, "Focused Ion Beam Microscopy and Micromachining," *MRS Bulletin*, vol. 32, no. 5, pp. 389–399, May 2007. DOI: 10.1557/mrs2007.62. 91

[184] L. A. Giannuzzi and F. A. Stevie, "A review of focused ion beam milling techniques for TEM specimen preparation," *Micron*, vol. 30, no. 3, pp. 197–204, Jun. 1999. DOI: 10.1016/S0968-4328(99)00005-0. 91

[185] S. Tan, R. Livengood, D. Shima, J. Notte, and S. McVey, "Gas field ion source and liquid metal ion source charged particle material interaction study for semiconductor nanomachining applications," *Journal of Vacuum Science & Technology B, Nanotechnology and Microelectronics: Materials, Processing, Measurement, and Phenomena*, vol. 28, no. 6, C6F15–C6F21, Nov. 2010. DOI: 10.1116/1.3511509. 92

[186] P. Hirsch, M. Kässens, M. Püttmann, and L. Reimer, "Contamination in a scanning electron microscope and the influence of specimen cooling," *Scanning*, vol. 16, no. 2, pp. 101–110, 1994. DOI: 10.1002/sca.4950160207. 93

[187] G. Hlawacek, I. Ahmad, M. A. Smithers, and E. S. Kooij, "To see or not to see: Imaging surfactant coated nano-particles using HIM and SEM," *Ultramicroscopy*, vol. 135, pp. 89–94, Dec. 2013. DOI: 10.1016/j.ultramic.2013.07.010. 93

[188] R. Livengood, S. Tan, Y. Greenzweig, J. Notte, and S. McVey, "Subsurface damage from helium ions as a function of dose, beam energy, and dose rate," *Journal of Vacuum Science & Technology B: Microelectronics and Nanometer Structures*, vol. 27, no. 6, p. 3244, Dec. 2009. DOI: 10.1116/1.3237101. 93

[189] *Chiaro High-Vacuum – ibss Group*. [Online]. Available: https://ibssgroup.com/en/products/chiaro-high-vacuum/. 101

[190] *Model 1020 — Fischione*. [Online]. Available: https://www.fischione.com/products/contamination-solutions/model-1020-plasma-cleaner. 102

[191] *JAMP-9500F Field Emission Auger Microprobe — Products — JEOL Ltd.* [Online]. Available: https://www.jeol.co.jp/en/products/detail/JAMP-9500F.html. 102

[192] J.-S. Huang, V. Callegari, P. Geisler, *et al.*, "Atomically flat single-crystalline gold nanostructures for plasmonic nanocircuitry," *Nature Communications*, vol. 1, no. 1, p. 150, Dec. 2010. DOI: 10.1038/ncomms1143. 124, 130

[193] R. Méjard, A. Verdy, O. Demichel, *et al.*, "Advanced engineering of single-crystal gold nanoantennas," *Optical Materials Express, Vol. 7, Issue 4, pp. 1157-1168*, vol. 7, no. 4, pp. 1157–1168, Apr. 2017. DOI: 10.1364/OME.7.001157. 124, 130

[194] K. Chen, G. Razinskas, H. Vieker, *et al.*, "High-Q, low-mode-volume and multiresonant plasmonic nanoslit cavities fabricated by helium ion milling," *Nanoscale*, vol. 10, no. 36, pp. 17 148–17 155, Sep. 2018. DOI: 10.1039/c8nr02160k. 124

[195] V. A. Fedotov, T. Uchino, and J. Y. Ou, "Low-loss plasmonic metamaterial based on epitaxial gold monocrystal film," *Optics Express*, vol. 20, no. 9, p. 9545, Apr. 2012. DOI: 10.1364/OE.20.009545. 124, 125

[196] N. Elbel, "Preparation and characterization of epitaxial gold films deposited on mica by direct current magnetron sputtering," *Journal of Vacuum Science & Technology B: Microelectronics and Nanometer Structures*, vol. 13, no. 5, p. 2119, Sep. 1995. DOI: 10.1116/1.588086. 124, 125

[197] M. H. Dishner, M. M. Ivey, S. Gorer, J. C. Hemminger, and F. J. Feher, "Preparation of gold thin films by epitaxial growth on mica and the effect of flame annealing," *Journal of Vacuum Science & Technology A: Vacuum, Surfaces, and Films*, vol. 16, no. 6, p. 3295, Nov. 1998. DOI: 10.1116/1.581536. 124, 125

[198] M. J. Hall and M. W. Thompson, "Epitaxy and twinning in foils of some noble metals condensed upon lithium fluoride and mica," *British Journal of Applied Physics*, vol. 12, no. 9, pp. 495–498, Sep. 1961. DOI: 10.1088/0508-3443/12/9/312. 124

[199] Z. Guo, Y. Zhang, Y. DuanMu, L. Xu, S. Xie, and N. Gu, "Facile synthesis of micrometer-sized gold nanoplates through an aniline-assisted route in ethylene glycol solution," *Colloids and Surfaces A: Physicochemical and Engineering Aspects*, vol. 278, no. 1-3, pp. 33–38, Apr. 2006. DOI: 10.1016/J.COLSURFA.2005.11.075. 124

[200] V. Švorčík, O. Kvítek, O. Lyutakov, J. Siegel, and Z. Kolská, "Annealing of sputtered gold nano-structures," *Applied Physics A 2010 102:3*, vol. 102, no. 3, pp. 747–751, Aug. 2010. DOI: 10.1007/S00339-010-5977-5. 124

[201] D. Pashley, "The nucleation, growth, structure and epitaxy of thin surface films," *Advances in Physics*, vol. 14, no. 55, pp. 327–416, Jul. 1965. DOI: 10.1080/00018736500101071. 124

[202] A. Maeland and T. B. Flanagan, "LATTICE SPACINGS OF GOLD–PALLADIUM ALLOYS," *Canadian Journal of Physics*, vol. 42, no. 11, pp. 2364–2366, Nov. 1964. DOI: 10.1139/p64-213. 124

[203] H. J. Ullrich, A. Uhlig, G. Geise, H. Horn, and H. Waltinger, "Precise determination of the lattice constant of LiF by means of X-ray divergent beam (pseudo Kossel-) technique via computer graphics and multiple intersections," *Microchimica Acta 1992 107:3*, vol. 107, no. 3, pp. 283–293, May 1992. DOI: 10.1007/BF01244483. 125

[204] POPPA H, HEINEMANN K, and ELLIOT AG, "Epitaxial Orientation Studies of Gold on uhv-Cleaved Mica during Early Stages of Nucleation and Growth," *Journal of Vacuum Science and Technology*, vol. 8, no. 3, p. 471, Dec. 2000. DOI: 10.1116/1.1314581. 125

[205] C. E. Chidsey, D. N. Loiacono, T. Sleator, and S. Nakahara, "STM study of the surface morphology of gold on mica," *Surface Science*, vol. 200, no. 1, pp. 45–66, Jan. 1988. DOI: 10.1016/0039-6028(88)90432-3. 125, 128

[206] X. Y. Zheng, Y. Ding, L. A. Bottomley, D. P. Allison, and R. J. Warmack, "Discontinuous gold island films on mica," *Journal of Vacuum Science & Technology B: Microelectronics and Nanometer Structures Processing, Measurement, and Phenomena*, vol. 13, no. 3, p. 1320, Jun. 1998. DOI: 10.1116/1.587846. 125

[207] *Lithium Fluoride Crystal, LiF Crystal*. [Online]. Available: https://www.unitedcrystals.com/LiF.html. 125, 233

[208] M. H. Jacobs, D. W. Pashley, and M. J. Stowell, "The formation of imperfections in epitaxial gold films," *The Philosophical Magazine: A Journal of Theoretical Experimental and Applied Physics*, vol. 13, no. 121, pp. 129–156, 1966. DOI: 10.1080/14786436608211992. 128

[209] E. Krauss, R. Kullock, X. Wu, *et al.*, "Controlled Growth of High-Aspect-Ratio Single-Crystalline Gold Platelets," *Crystal Growth & Design*, vol. 18, no. 3, pp. 1297–1302, Mar. 2018. DOI: 10.1021/acs.cgd.7b00849. 130, 177

[210] P. A. Bond and V. M. Stowe, "SOLUBILITIES IN HYDROGEN FLUORIDE," *Journal of the American Chemical Society*, vol. 53, no. 1, pp. 30–34, Jan. 2002. DOI: 10.1021/JA01352A004. 132

[211] Y. Chen, Y. Chen, J. Chu, and X. Xu, "Bridged Bowtie Aperture Antenna for Producing an Electromagnetic Hot Spot," *ACS Photonics*, vol. 4, no. 3, pp. 567–575, Mar. 2017. DOI: 10.1021/acsphotonics.6b00857. 142

[212] O. Quevedo-Teruel, H. Chen, A. Díaz-Rubio, *et al.*, "Roadmap on metasurfaces," *Journal of Optics*, vol. 21, no. 7, p. 073 002, Jul. 2019. DOI: 10.1088/2040-8986/ab161d. 142

[213] *PMMA EBL Lift Off Procedure - nanoFAB Knowledge Base - nanoFAB Confluence*. [Online]. Available: https://confluence.nanofab.ualberta.ca/display/NFCORE/PMMA+EBL+Lift+Off+Procedure. 142

[214] *12.5mm Dia. x 1mm Thickness, Uncoated, ZnSe Window — Edmund Optics*. [Online]. Available: https://www.edmundoptics.com//p/125mm-dia-x-1mm-thickness-uncoated-znse-window/23137/. 143, 235

[215] A. M. Ledger, "Inhomogeneous interface laser mirror coatings," *Applied Optics, Vol. 18, Issue 17, pp. 2979-2989*, vol. 18, no. 17, pp. 2979–2989, Sep. 1979. DOI: 10.1364/AO.18.002979. 144

[216] Eugene Hecht, *Optics*, 5th ed. Essex: Pearson Education Limited, 2016. 148, 165

[217] E. Baladi, M. Semple, and A. K. Iyer, "Imaging of subwavelength features in the far-field using resonant metasurfaces: Design from microwave to infrared frequencies," *2019 URSI International Symposium on Electromagnetic Theory, EMTS 2019*, May 2019. DOI: 10.23919/URSI-EMTS.2019.8931490. 154, 157

[218] G. Calafiore, A. Koshelev, T. P. Darlington, *et al.*, "Campanile Near-Field Probes Fabricated by Nanoimprint Lithography on the Facet of an Optical Fiber," *Scientific Reports*, vol. 7, no. 1, Dec. 2017. DOI: 10.1038/S41598-017-01871-5. 158

[219] M. Semple and A. K. Iyer, "Asymmetric Metamaterial-Lined Apertures for Plasmonic Phase-Gradient Optical Metasurfaces," in *USNC-URSI NRSM*, Boulder, CO, 2022, pp. 58–58. 162

[220] X. Ni, N. K. Emani, A. V. Kildishev, A. Boltasseva, and V. M. Shalaev, "Broadband Light Bending with Plasmonic Nanoantennas," *Science*, vol. 335, no. 6067, pp. 427–427, Jan. 2012. DOI: 10.1126/science.1214686. 163

[221] I. E. Gordon, L. S. Rothman, C. Hill, *et al.*, "The HITRAN2016 molecular spectroscopic database," *Journal of Quantitative Spectroscopy and Radiative Transfer*, vol. 203, pp. 3–69, Dec. 2017. DOI: 10.1016/j.jqsrt.2017.06.038. 165

[222] C. S. Goldenstein, V. A. Miller, R. Mitchell Spearrin, and C. L. Strand, "SpectraPlot.com: Integrated spectroscopic modeling of atomic and molecular gases," *Journal of Quantitative Spectroscopy and Radiative Transfer*, vol. 200, pp. 249–257, Oct. 2017. DOI: 10.1016/J.JQSRT.2017.06.007. 165

[223] "Kramers-Kronig Relations in Optical Materials Research," *Kramers-Kronig Relations in Optical Materials Research*, 2005. DOI: 10.1007/B138913. 165

[224] P. R. Griffiths and J. A. De Haseth, "Fourier Transform Infrared Spectrometry: Second Edition," *Fourier Transform Infrared Spectrometry: Second Edition*, pp. 1–529, Jun. 2006. DOI: 10.1002/047010631X. 166

[225] S. I. Rae and I. Khan, "Surface enhanced Raman spectroscopy (SERS) sensors for gas analysis," *Analyst*, vol. 135, no. 6, pp. 1365–1369, May 2010. DOI: 10.1039/b924537e. 167

[226] F. Cheng, X. Yang, and J. Gao, "Ultrasensitive detection and characterization of molecules with infrared plasmonic metamaterials," *Scientific Reports*, vol. 5, no. 1, p. 14 327, Sep. 2015. DOI: 10.1038/srep14327. 167

[227] M. Oliverio, S. Perotto, G. C. Messina, L. Lovato, and F. De Angelis, "Chemical Functionalization of Plasmonic Surface Biosensors: A Tutorial Review on Issues, Strategies, and Costs," *ACS Applied Materials and Interfaces*, vol. 9, no. 35, pp. 29 394–29 411, Sep. 2017. DOI: 10.1021/acsami.7b01583. 167

[228] X.-J. Yu, Y.-M. Xian, C. Wang, *et al.*, "Liquid-Phase Epitaxial Growth of Highly Oriented and Multivariate Surface-Attached Metal–Organic Frameworks," *Journal of the American Chemical Society*, vol. 141, no. 48, pp. 18 984–18 993, Dec. 2019. DOI: 10.1021/jacs.9b08169. 167

[229] A. Vaccari, A. C. Lesina, L. Ramunno, and P. Berini, "On the convergence and accuracy of the FDTD method for nanoplasmonics," *Optics Express, Vol. 23, Issue 8, pp. 10481-10497*, vol. 23, no. 8, pp. 10 481–10 497, Apr. 2015. DOI: 10.1364/OE.23.010481. 210

[230] N. Marcuvitz, *Waveguide Handbook*. IET Digital Library, Jan. 1986. DOI: 10.1049/PBEW021E. 213

[231] D. Gall, "Electron mean free path in elemental metals," *Journal of Applied Physics*, vol. 119, no. 8, p. 085 101, Feb. 2016. DOI: 10.1063/1.4942216. 216

[232] E. C. Jordan and K. G. Balmain, *Electromagnetic Waves and Radiating Systems*, 2d ed., ser. Prentice-Hall Electrical Engineering Series. Englewood Cliffs, New Jersey: Prentice-Hall, 1968. 219

[233] N. W. Ashcroft and N. D. Mermin, *Solid State Physics*, Dorothy Garbose Crane, Ed. Saunders College Publishing, 1976, p. 833. DOI: 10.1119/1.11117. 222

[234] W. Frei, "How to Identify and Resolve Singularities in the Model when Meshing — COMSOL Blog," COMSOL, Tech. Rep., Oct. 2013. [Online]. Available: https://www.comsol.com/blogs/how-identify-resolve-singularities-model-meshing/. 228

[235] *SuperK COMPACT - NKT Photonics*. [Online]. Available: https://www.nktphotonics.com/products/supercontinuum-white-light-lasers/superk-compact/. 234

[236] *Thorlabs - RC02FC-P01 Protected Silver Reflective Collimator, 450 nm - 20 µm, Ø2 mm Beam, FC/PC*. [Online]. Available: https://www.thorlabs.com/thorproduct.cfm?partnumber=RC02FC-P01. 234

[237] *FS-ND ND Filter Set*. [Online]. Available: https://www.newport.com/p/FS-ND. 234

[238] *Thorlabs - BSW26R 25 mm x 36 mm 50:50 UVFS Plate Beamsplitter, Coating: 350 - 1100 nm, t = 1 mm*. [Online]. Available: https://www.thorlabs.com/thorproduct.cfm?partnumber=BSW26R. 234

[239] *Carl Zeiss Microscopy, LLC - Objective Assistant - Objective EC Epiplan-Neofluar 100x/0.90 BD DIC M27*. [Online]. Available: https://www.micro-shop.zeiss.com/en/us/shop/objectives/422392-9961-000/Objective-EC-Epiplan-Neofluar-100x-0.90-BD-DIC-M27. 234

[240] *Ultra Broadband Polarizer*. [Online]. Available: https://www.meadowlark.com/ultra-broadband-polarizer-p-86?mid=6. 234

[241] *Thorlabs - BS025 10:90 (R:T) Non-Polarizing Beamsplitter Cube, 400-700 nm, 1"*. [Online]. Available: https://www.thorlabs.com/thorproduct.cfm?partnumber=BS025. 234

[242] *Thorlabs - CS895MU Kiralux 8.9 MP Monochrome CMOS Camera, USB 3.0 Interface*. [Online]. Available: https://www.thorlabs.com/thorproduct.cfm?partnumber=CS895MU. 234

[243] *Thorlabs - F810FC-635 635 nm FC/PC Collimation Package, NA = 0.25, f = 35.41 mm*. [Online]. Available: https://www.thorlabs.com/thorproduct.cfm?partnumber=F810FC-635. 234

[244] *Thorlabs - M134L01 Ø600 µm, 0.50 NA, High OH, FC/PC to SMA905 Fiber Patch Cable, 1 m*. [Online]. Available: https://www.thorlabs.com/thorproduct.cfm?partnumber=M134L01. 235

[245] *QE Pro Spectrometer — High Sensitivity — Ocean Insight*. [Online]. Available: https://www.oceaninsight.com/products/spectrometers/high-sensitivity/Custom-Configured-qe-pro-series/. 235

[246] S. Ellis, "Advantages of Infinity-Corrected Optics in FT-IR Microspectroscopy," Thermo Fisher Scientific, Madison, WI, Tech. Rep., 2007, pp. 1–3. [Online]. Available: https://assets.thermofisher.com/TFS-Assets/CAD/Application-Notes/D10261~.pdf. 236

[247] *Nicolet™ Continuum™ Infrared Microscope*. [Online]. Available: https://www.thermofisher.com/order/catalog/product/IQLAADGAAGFABGMADW. 236

[248] S. Boyd and M. Kansiz, "Highest Available Signal-To-Noise Performance, Delivering Superior Sensitivity and Analytical Performance," Agilent Technologies, Inc., Tech. Rep., Mar. 2011, pp. 1–6. 238

[249] H. Ku, "Notes on the use of propagation of error formulas," *Journal of Research of the National Bureau of Standards, Section C: Engineering and Instrumentation*, vol. 70C, no. 4, p. 263, Oct. 1966. DOI: 10.6028/jres.070C.025. 238

Appendix A

Simulation Procedure

Below are the general procedures used throughout this thesis to simulate periodic MTSs throughout this project. Often, the results presented have been confirmed through simulations in both COMSOL and Ansys Lumerical FDTD, which each have particular advantages and disadvantages.

A.1 COMSOL Multiphysics

The general procedure used to simulate MTSs in COMSOL is as follows:

1. Two boxes are drawn with width and height equal to the MTS period p, and depth approximately $\lambda/4$.

2. A 2D working plane is added, and the MTS layout is drawn on the working plane.

3. The working plane is extruded by the film thickness t_f (or t, depending on the case).

4. Two additional boxes are added to each end of the simulation with cubic shape and side length p. These boxes will be assigned to perfectly matched layers and were required to make COMSOL automatically assign periodic meshing operations.

5. Material models are applied, usually air to the top $\lambda/4$ box, gold to the extruded layer (and air filling the apertures), and some substrate material to the bottom $\lambda/4$ box.

6. The RF module is used for the physics interface.

7. Boundary conditions are applied. These include the definition of two perfectly matched layers, assigned to the end cubic domains. The transverse outer boundaries are assigned Floquet periodic boundaries, and the longitudinal boundaries between the perfectly matched layer and the air/substrate are assigned domain-backed periodic port conditions.

8. The finer or extra-fine physics-based meshing is normally used, though some manual adjustments are made to increase convergence.

9. The frequency-domain study feature is used, along with several parametric sweep features to study changes in geometry and material parameters.

A.2 Limitations of COMSOL

COMSOL is a very powerful simulation software and has very few drawbacks. 3D modelling of the desired structure is very simple and easy to troubleshoot as the modelling steps can be built sequentially. Material models can be defined in any number of ways, and COMSOL will automatically infer the required expression. Additionally, COMSOL's built-in analysis tools are very robust and cover the large majority of use cases with simple, pre-defined expressions.

Some of the points above have drawbacks, however. It is very difficult to evaluate expressions not covered by COMSOL's built-in analysis functions, requiring slicing of the data, recomputation of the model, and a good understanding of the model object structure. The generation of material models is confusing and mismatches in the input values often lead to errors. Moreover, the material database lacks electromagnetic properties for many common materials. Additionally, the finite element method requires a significant amount of memory for finely-meshed simulations, which requires simulating on high-power computers. Finally, since each frequency point is solved individually, acquiring a high-resolution spectrum often takes a significant amount of time.

A.3 Ansys Lumerical FDTD

In Lumerical, the user interface only offers a fraction of the options available. A fully-featured scripting language is offered as an alternative, more powerful approach to designing and running simulations. The scripting language interfaces with both Python and MATLAB for data analysis and visualization. For this thesis, the Python interface was used. A script generally does the following:

1. All the simulation parameters are loaded into a dictionary.
2. If a parametric sweep is to be run, one simulation file is created for each parameter.
3. Three boxes representing the substrate, the film, and, if necessary, an input material, are created. Their transverse size is larger than p since the simulation domain will define the true edges.
4. The film is "patterned" by adding an aperture, then nanowires. The nanowires are rounded by using a polygon shape and calculating the required vertices in Python. Their mesh order must also be overridden to ensure they appear above the etched aperture.
5. An image of the simulation setup is saved, which only works when the user interface is open. If it is hidden, a black image will be saved instead.
6. An FDTD simulation object is added. Transverse boundaries are made periodic and symmetric (when possible), and the longitudinal boundaries are made to be perfectly matched layers.
7. A mesh override is added to ensure sufficient resolution at the nanogaps.
8. A "grating_s_params" object is added, which includes a source and monitors.
9. A field profile monitor is added at the aperture plane to monitor the resonant aperture fields.

10. An index monitor is added at the aperture plane to create a dataset that can be used to plot the contours of the geometry.

A.4 Limitations of Lumerical

The main advantage of Lumerical FDTD is that it can solve all frequencies of a spectrum simultaneously as it is a time-domain technique. Moreover, for MTS applications, often a single reflection is enough to characterize the device and the solution converges quickly once the majority of the power has left the simulation domain. Additionally, the robust scripting functions make automating simulations and custom analysis much simpler. The material model library is fairly complete and includes the most popular experimentally-determined material properties.

As far as drawbacks, FDTD isn't any better than finite element at calculating large field enhancement [229]. The hexahedral meshing makes changes of scale impossible, and when defining a fine mesh, the mesh size must be propagated throughout the entire simulation domain, which can dramatically increase simulation time. The user interface for Lumerical is also notoriously poor, particularly for 3D modelling. The lack of boolean operations for 3D modelling can make certain layouts particularly difficult to produce. Since the material properties are defined in the frequency domain, a time-domain equivalent fit must be generated, but somehow the generation of this model can (seemingly randomly) change. This can cause significant issues when comparing data, particularly when the simulation bandwidth is changed. This issue can often be avoided by manually setting all the material fitting parameters, but since the fitting parameters are not saved in the simulation file, some simulations cannot be reproduced. Finally, the continuous-wave normalization used by the software prevents coincident sources from having their power correctly calculated. There are probably no practical situations where coincident sources are required. When attempting to excite nonlinearities, it is preferable to keep the probe and pump beams at different incidence angles.

Appendix B

Wagon-Wheel MTS Equivalent Circuit

B.1 Intuitive Equivalent Circuit Model Construction

Here, we derive an intuitive circuit model to describe the wagon-wheel MTM-lined MTS's scattering spectrum. A normal-incidence plane wave on a periodic array can be modelled as a square parallel-plate waveguide, and the MTS acts as a waveguide discontinuity with impedance Z_t loading the waveguide in parallel. The reflectance and transmittance of the MTM-lined aperture surface, when loaded into a parallel-plate waveguide with $(Z, \beta) = (Z_0, \beta_0)$, where (Z_0, β_0) are the free-space impedance and propagation constant, are thus:

$$R = |S_{11}|^2 = \left| \frac{-Z_0}{2Z_t + Z_0} \right|^2, \tag{B.1}$$

$$T = |S_{21}|^2 = \left| \frac{2Z_t}{2Z_t + Z_0} \right|^2. \tag{B.2}$$

We begin our construction of the equivalent circuit model for the wagon-wheel MTM-lined aperture by dividing the aperture into a quarter by symmetry, taking the top-right corner for analysis. As shown in Fig. 3.11a, this reduces the aperture to two wires: one vertical and one at a 45° angle. We then inspect the current distribution across the aperture at resonance (193 THz), finding a resonant monopolar (quarter-wavelength) current distribution across

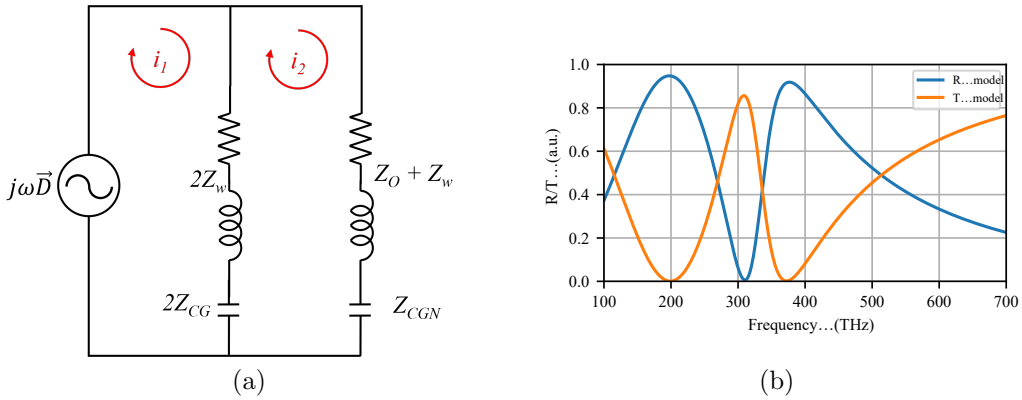

(a) (b)

Figure B.1: (a) Circuit model representing a resonant monopole and a resonant loop, and (b) the spectrum produced by the circuit model with circuit elements derived from rough approximations. Two reflective resonances are observed.

the vertical nanowire, and a similar but weaker current distribution as a loop from the centre of the aperture, across the oblique nanowire, and down the outside of the aperture. Inspecting the current near the notch in the spectrum (150 THz), the currents in the loop are stronger than those in the vertical nanowire, making the source of the notch clear. We also remove the substrate for ease of analysis, though it could be included through an effective permittivity in the capacitive impedances derived below.

The first step is thus to construct a circuit model that represents two parallel resonators as shown in Fig. B.1a, where one represents the monopole and the other the loop. The monopole is modelled as a series RLC resonator to produce a short-circuit at resonance, where we consider the feed to be the top symmetry plane. The resistance is the ohmic resistance of the nanowire, and the inductance is the kinetic inductance of the nanowire with total impedance $2Z_w$ due to symmetry. The capacitance represents some combination of the capacitive gaps at the centre of the aperture, denoted $2Z_{CG}$. The loop is modelled the same way, with the additional series impedance from the path along the edge of the aperture with impedance Z_O, and a potentially different capacitance Z_{CGN}. Connecting this model directly in parallel with the monopole is unlikely to correctly model the full spectrum, but we will correct this layout in a future step once the model is more complete.

Using rough representative circuit element values, the transmission/reflection

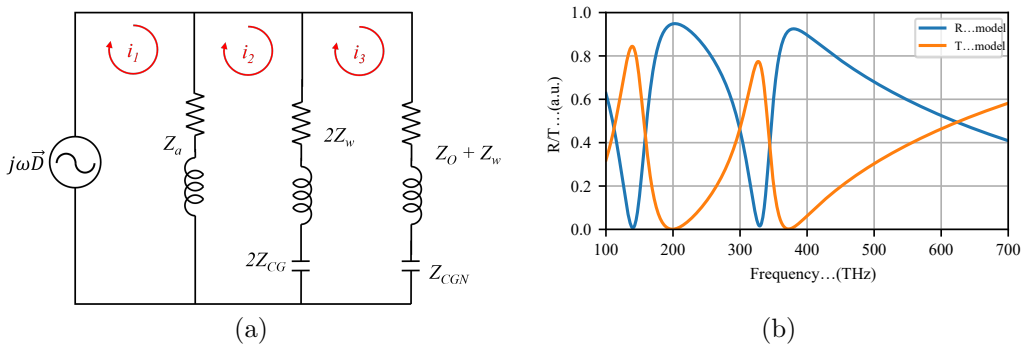

Figure B.2: (a) Circuit model after adding a parallel nonresonant aperture impedance Z_a, and (b) the spectrum produced by the circuit model with circuit elements derived from rough approximations. Two asymmetric, Fano-shaped transmissive resonances are observed.

of the first model are shown in Fig. B.1b. The resonances are within the correct frequency range but cause increased reflection instead of increased transmission. This is due to the resonators having high impedance outside of resonance, and low impedance at resonance. To change the default behaviour to reflection, a parallel low-impedance element must be added. To decide this impedance we appeal to Fano theory for asymmetric resonances, which states that the coupling between a discrete state (resonance) and a continuum leads to an asymmetric resonance of the type observed in the MTM-lined aperture, with strong transmission, followed by strong extinction (reflection) [117]. Throughout Ch. 3, we compared the spectra of MTM-lined apertures to comparable unlined apertures and observed that the spectra nearly match away from resonance. The default behaviour of the screen without resonances should thus be that of an unlined aperture, which can be represented as a series inductor and resistor when well below its resonance frequency (and should be augmented with a parallel capacitor when the aperture resonance is relevant) [230]. The augmented circuit is shown in Fig. B.2a.

Again, using rough representative circuit element values, the transmission/reflection of the second model are shown in Fig. B.2b. The parallel aperture impedance Z_a has not changed the reflective short-circuit resonance frequencies but has added transmission maxima before each one, characteristic

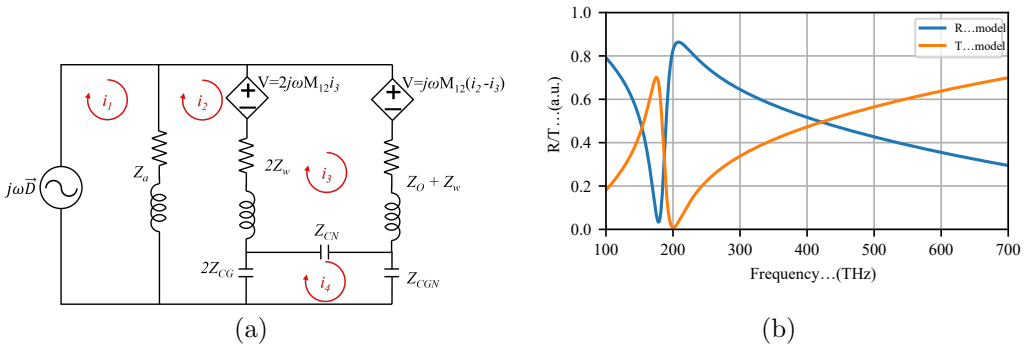

Figure B.3: (a) Circuit model after adding capacitive and inductive coupling elements, and (b) the spectrum produced by the circuit model with circuit elements derived from rough approximations. The two resonances have been merged into one.

of the Fano lineshape. Knowing that the two resonators are coupled through the central capacitors, we add a capacitor Z_{CN} linking the two resonators. To model the inductive coupling, one might normally use a transformer. In our case, however, the two resonators already share the currents driving the magnetic coupling, hence it is more convenient to represent the generated feedback by a pair of voltage-dependent current sources with mutual inductance M_{12}. The coupled circuit is shown in Fig. B.3a.

The transmission/reflection of the third model are shown in Fig. B.3b, where the capacitive coupling has caused the two resonances to merge, and the inductive coupling has induced a small redshift of the resonance frequency. To separate the resonances, we model the true geometry of the resonant loop by removing its connection to the top node (representing the top symmetry plane) and connecting it to ground (representing the bottom symmetry plane). This removes the source from the loop resonator and forces it to be excited parasitically through the coupling elements. The adjusted circuit is shown in Fig. B.4a.

As shown in Fig. B.4b, the rearrangement of the resonant loop restored the two resonances, however, the loop resonance is much more strongly excited in this circuit model than in the simulation. This is due to the loop supporting only current i_3, which forces the excitation of the loop for any current induced

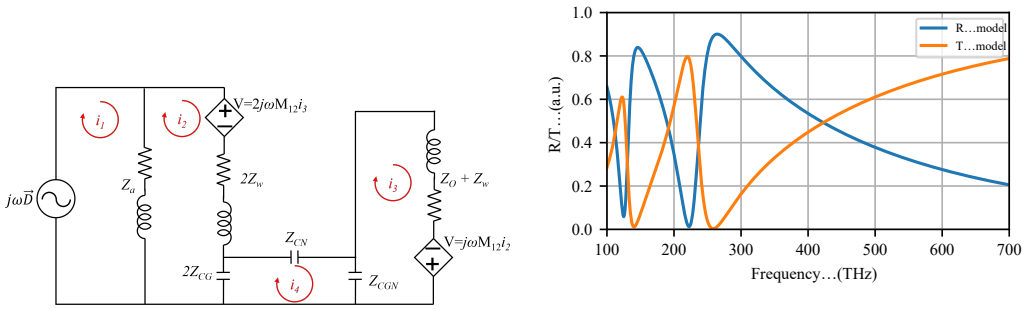

(a) (b)

Figure B.4: (a) Circuit model after rearranging the layout of the loop resonator, and (b) the spectrum produced by the circuit model with circuit elements derived from rough approximations. The two separated resonances have reappeared at approximately the correct frequencies.

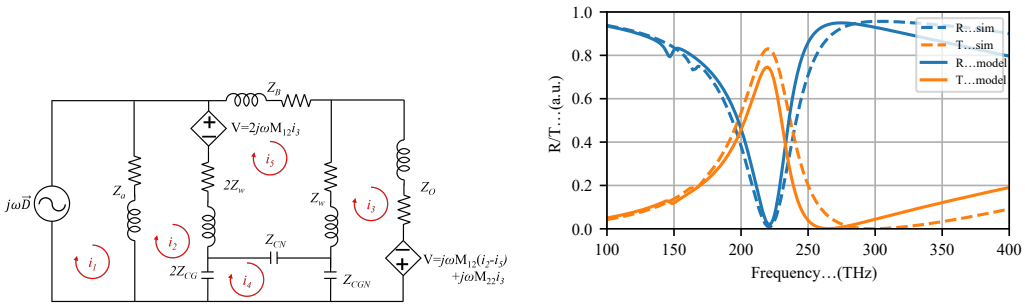

(a) (b)

Figure B.5: (a) The final circuit model after adding the loop feeding element Z_B, and (b) the spectrum produced by the circuit model with circuit elements derived from rough approximations, compared to the spectrum computed in COMSOL. The circuit model is able to match all the features of the spectrum.

by the coupling terms. We term the current i_3 as the "odd" mode of the loop resonator and propose that currents feeding the base of the oblique nanowire may also excite an "even" mode on the loop resonator. Hence the loop inductance must be separated into its two constituent elements, Z_w and Z_O, and an inductive feeding element Z_B added in between. Additionally, the inductive coupling between the loop resonator and its mirror image across the horizontal symmetry boundary should be modelled, which manifests as an additional M_{22} term in the coupling source. This constitutes the final circuit model shown in Fig. B.5a.

With rough approximations, the final circuit model can closely match the spectrum of the MTM-lined aperture simulation, as shown in Fig. B.5b. Analytical values for the circuit elements are derived below, and the circuit model is numerically tuned in Ch. 3 to find a near-perfect match to the simulation data.

B.2 Analytical Calculations for Initial Values

In this section, we analytically derive the initial values of each element in the circuit model, with a number of choice assumptions to simplify the calculations.

B.2.1 $\mathbf{Z_w}$

The nanowire impedance seen by the displacement current source is derived from the plane wave impedance of the metal, ignoring Faraday inductance as the kinetic inductance of the nanowires dominates. Due to the miniaturized nature of our aperture, we will assume a quasi-static regime. We begin Ohm's law for the displacement current under harmonic excitation, where the metal conductivity is included by using the Drude model for the metal's permittivity:

$$\bar{J}(\omega) = (\sigma(\omega) + j\omega\epsilon_0)\bar{E} = j\omega\epsilon\bar{E}. \tag{B.3}$$

The second term is often omitted for good conductors at lower frequencies, and the plane-wave impedance leads to the conventional wire impedance $Z = V/I = l/(\sigma w \delta_s)$, where δ_s is the skin depth. In our case, however, the displacement currents contribute a meaningful additional component to the impedance, and hence must be treated. As an approximation, since the wire is much thinner than the skin depth, we will consider the electric field to be uniform throughout the wire. It should be noted that at this scale, surface effects should generally be considered. Although surface effects can rarely be decoupled from other factors in the conductivity, it can be intuitively understood as an effective reduction of the mean free path of conduction electrons due to scattering off the surfaces and grain boundaries of the conductor between regular Drude collisions [231]. In the ideal simulation case, where surface

roughness is not modelled and all surfaces are flat, collisions with the surface boundary are purely elastic reflections, hence this effective reduction of τ need not be considered in attempting to reproduce the simulation results with a circuit model. The cross-section that encompasses all the currents is the one that is normal to the electric field, so to derive the total current, we set the x-dimension integration width to $w < \delta_s$ and the z-dimension width to t:

$$I = \int_0^w \int_0^t (j\omega\epsilon) E_0 dz dx = wt(j\omega\epsilon) E_0 \tag{B.4}$$

The potential difference across the wire (length $l = b - g/[2\sin(\pi/N)]$) is simple to calculate from the uniform field at the surface of the conductor:

$$V = -\int_0^l E_0 dy = -lE_0 \tag{B.5}$$

The impedance of the nanowire is thus:

$$Z = \frac{l}{wt(j\omega\epsilon)}, \tag{B.6}$$

where the negative has been absorbed by the implicit understanding that the voltage and current are measured in opposite directions.

When a resonant field profile is present, the effective impedance of the nanowire is reduced. The effective impedance can be derived from the total power:

$$P = Z_{w,eff} I_0^2 = Z_w \int I^2(x) dx, \tag{B.7}$$

For a perfect quarter-wavelength distribution, this equation evaluates to $Z_{w,eff} = 0.5 Z_w$. In practice, the resonant field profile extends beyond each end of the nanowire, which increases the effective impedance.

B.2.2 $\mathbf{Z_O}$

For the outside edge of the aperture, no dimension is deeply subwavelength, and hence we must consider the skin effect on the fields decaying inside the metal. Let us consider a current travelling around the edge of the aperture

from one wire to the next, where the field decays into the metal away from the aperture (in the r direction) but is constant in the z, ϕ directions. Since the arclength is small, we will consider the section to be straight and of length $2\pi b/N$ to ensure our impedance has a closed-form solution. This will underestimate the impedance Z_O. Allow the radial direction to be the x-direction, then the electric field inside the metal can be expressed as:

$$E = E_0 e^{j\omega t - j\omega\sqrt{\mu_0\epsilon}x}\hat{y} \tag{B.8}$$

Now consider a cross-section normal to the field that carries current J. We can find the total current by integrating over the cross-section:

$$I = \int_0^t \int_0^\infty j\omega\epsilon E_0 e^{-j\omega\sqrt{\mu_0\epsilon}x} dx dz. \tag{B.9}$$

$$I = t\sqrt{\frac{\epsilon}{\mu_0}} E_0 \tag{B.10}$$

and the potential, calculated the same way as before, is:

$$V = -\int_0^{2\pi b/N} E_0 dl = 2\pi b/N E_0 \tag{B.11}$$

And hence, by Ohm's law, the impedance is:

$$Z_O = \frac{2\pi b/N}{t}\sqrt{\frac{\mu_0}{\epsilon(\omega)}}, \tag{B.12}$$

which is the plane wave impedance inside the metal scaled by the "wire" dimensions.

B.2.3 $\mathbf{Z_a}$

Z_a represents the impedance of the aperture array in absence of the plasmonic resonators. This problem can be solved using a variational approach where the currents on the aperture are assumed, and the impedance is calculated from their self reaction [164]. Unfortunately, the assumed current distribution is difficult to calculate for apertures. To calculate Z_a, we assumed the aperture impedance is due to currents travelling across the rectangular area extending

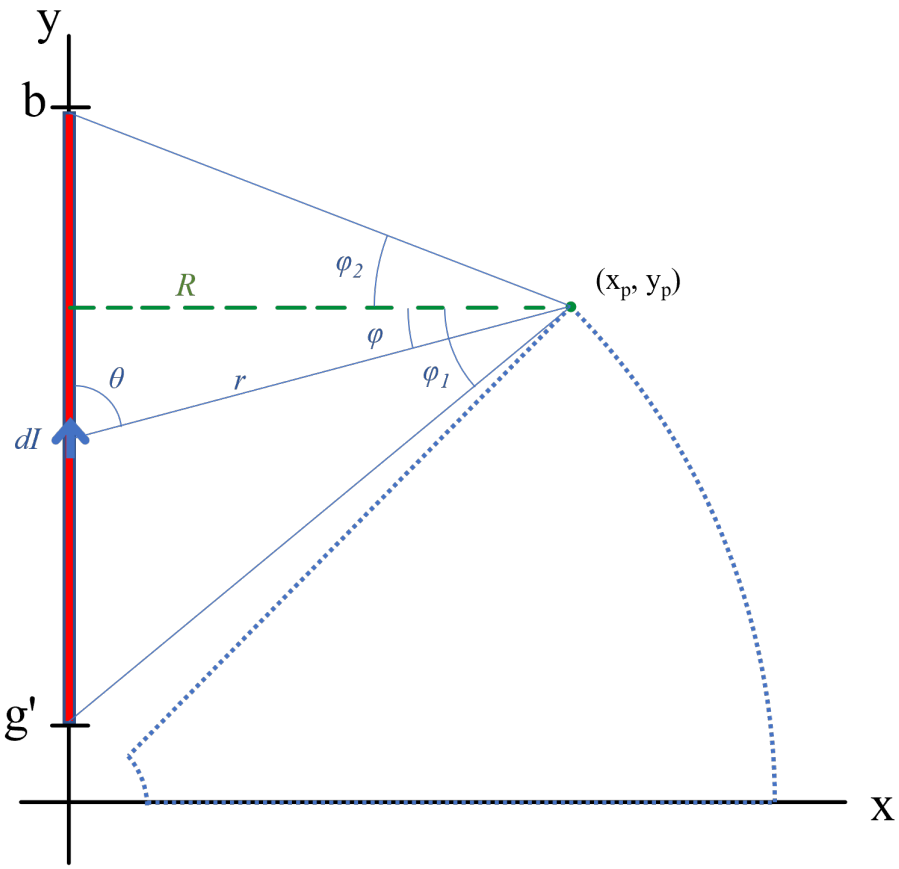

Figure B.6: Layout of quasi-static problem used to derive the inductive coupling parameter M_{12}.

over the full period vertically, and between the aperture edge and the symmetry boundary horizontally. This will overestimate the aperture impedance in general. The aperture impedance, calculated the same way as for Z_O, is thus:

$$Z_a = \frac{p/2}{p/2 - b}\sqrt{\frac{\mu_0}{\epsilon(\omega)}}. \tag{B.13}$$

B.2.4 M_{12}

The magnetic coupling coefficient is derived under quasi-static conditions using the Biot-Savart law [232]. The layout of the problem is shown in Fig. B.6, where the current on the vertical nanowire is assumed to be triangular. This attempts to model the resonant current distribution, which is sinusoidal, but simplifies the calculation. As a result, M_{12} is likely to be underestimated.

The magnetic coupling coefficient is the total magnetic flux through the area of the loop resonator (represented by the dotted blue lines) due to the current on the nanowire (represented by the red square). Assuming a triangular field distribution, the current on the nanowire is:

$$I = \frac{y - g'}{b - g'} I_0. \tag{B.14}$$

By the Biot-Savart law, the magnetic field at a point (x_p, y_p) in terms of y and θ is:

$$\bar{B} = \frac{\mu_0}{4\pi} \int_{g'}^{b} \frac{I \sin\theta dy}{|r|^2} \bar{a}_z. \tag{B.15}$$

It is most convenient to evaluate $\bar{B}$ in cylindrical coordinates centered at (x_p, y_p):

$$B = \frac{\mu_0 I_0}{4\pi} \int_{\phi_1}^{\phi_2} \left[\frac{\cos\phi}{x_p} \left(\frac{y - g'}{b - g'} \right) + \frac{\sin\phi}{b - g'} \right] d\phi. \tag{B.16}$$

This integral was solved analytically, then the resulting equation was parameterized to a polar coordinate system centred around the origin. Finally, the total magnetic flux was numerically integrated over the parameterized surface delineated by the blue dotted lines. This gives a magnetic coupling coefficient approximately two orders of magnitude smaller than L_w.

B.2.5 C_N

C_N describes the capacitance between nearest-neighbour wires. Treating the blue-dotted area in Fig. B.6 as a radial capacitor, we look to find $C = Q/V$. Assume a voltage V_0 across the capacitor plates, then by Laplace's equation in polar coordinates:

$$V = \frac{NV_0}{2\pi}\phi = \frac{4V_0}{\pi}\phi, \tag{B.17}$$

where ϕ is the polar angle extending from one of the plates. The electric field is then $E = -1/r dV/d\phi = -4V_0/\pi r \bar{a}_\phi$. Then, by Gauss' law using a cylindrical Gaussian surface:

$$Q/\epsilon_0 = \int_r \int_t \frac{-4V_0}{\pi r} dz dr = t\frac{-4V_0}{\pi} \ln(\frac{r_2}{r_1}). \tag{B.18}$$

Finally, we define the outer radius r_2 by translating the capacitor plates by $w/2$ to the surface of the nanowires, and the inner radius r_1 by the point where the nanogap ends:

$$C = \frac{N}{2\pi} t\epsilon_0 \ln\left(\frac{b - w/[2\sin(\pi/N)]}{g/[2\tan(\pi/N)]}\right). \tag{B.19}$$

We also add the nanogap at the tips of the nanowires, which has parallel plates:

$$C_N = \frac{\epsilon_0 t w}{2g\sin(\pi/N)} + \frac{N}{2\pi} t\epsilon_0 \ln\left(\frac{b - w/[2\sin(\pi/N)]}{g/[2\tan(\pi/N)]}\right). \tag{B.20}$$

Having neglected fringing fields, this capacitance is surely underestimated.

B.2.6 Z_B

Z_B represents the portion of the gold film that the currents that feed the 45° nanowire travel through. This impedance cannot be directly separated from the other film impedances, so we resort to an approximation based on the following assumed important parameters: (i) Z_B should grow with p as the length of the feeding region becomes longer, (ii) Z_B should scale inversely with b since the width of the feeding region decreases with b, and (iii) the frequency dispersion should follow the form of Z_a. This implies:

$$Z_B = \frac{p/2 - b/\sqrt{2}}{(b/2)} \sqrt{\frac{\mu_0}{\epsilon(\omega)}} \tag{B.21}$$

is a reasonable approximation.

B.2.7 C_G, C_{GN}, and M_{22}

C_G represents the capacitance due to all other wires in the aperture other than nearest neighbours. Since the geometry of the centre of the aperture is quite complicated, we assume that it is equal to C_N. C_{GN} is simply the parallel combination of C_G and C_N and is hence their sum. Finally, M_{22} is calculated

from a COMSOL simulation of a single loop resonator, fed with a 1 A current source over the capacitive gap. The induced magnetic flux is then integrated over the area where the loop's mirror image would exist and is assumed not to change with frequency.

B.3 The Drude Model

The Drude model for conductivity (and by extension, permittivity) describes a metal as a sea of non-interacting electrons in a lattice of heavy ions. It can be derived from the Lorentz force, Ohm's law, and a few classical assumptions [233]:

1. Electrons in the material only interact with other electrons or ions in the material through collisions. The neglect of interactions between electrons is known as the *independent electron approximation*, and the neglect of the interactions between electrons and ions is known as the *free electron approximation*.

2. Collisions in the Drude model are instantaneous.

3. An electron will travel for an average of τ s before experiencing a collision/scattering event, where τ is the relaxation time inside the material.

4. Electrons will emerge from collisions in a random direction and with an average momentum $\langle p \rangle = 0$.

In general, the derivation of the Drude model begins with the DC electrical conductivity of a metal, and later extends the model to time-varying driving fields, so I will do the same. First consider Ohm's law:

$$\bar{J} = \sigma \bar{E}, \tag{B.22}$$

where $\bar{J}$ is the vector free current density (made up of conduction electrons), σ is the electrical conductivity, and $\bar{E}$ is the vector electric field. $\bar{J}$ arises from the collective motion of free electrons through the metal driven by

the electric field. If there are n electrons per unit volume moving at an average velocity $\bar{v}$, each carrying a charge $-e$, the net current density is:

$$\bar{J} = -ne\bar{v}. \tag{B.23}$$

Next, we consider the effect of the electric field on an individual electron. After a collision, the electron will have a random velocity $\bar{v}_0$, and it will be accelerated according to the Lorentz law $\bar{v} = \bar{v}_0 - e\bar{E}t/m$. If we average the velocity over all electrons, the contribution of $\bar{v}_0$ disappears. Additionally, the average time an electron is accelerated for is the relaxation time, so the average electron velocity becomes:

$$\bar{v} = -\frac{e\bar{E}\tau}{m}. \tag{B.24}$$

Combining eqs. (B.22)–(B.24), we arrive at an expression for the DC conductivity of a metal:

$$\sigma_0 = \frac{ne^2\tau}{m}. \tag{B.25}$$

To allow the electric field to vary with time, we develop the time-varying equation of motion for electrons in the metal. To do this, we introduce the momentum at any time t, $p(t) = vm$. Then, if p is the momentum per electron, the current density is:

$$\bar{J} = -\frac{nep(t)}{m}. \tag{B.26}$$

Let us now advance time by an infinitesimal amount dt. An electron has a probability of scattering in this time of dt/τ, hence an electron has a probability of surviving of $1 - dt/\tau$. The electron that experienced a collision, on average, loses all momentum, whereas the surviving electron acquires momentum from some uniform driving field, $f(t)$. If we neglect the momentum gained by scattering electrons during the time dt after they scatter, we have:

$$p(t + dt) = (1 - \frac{dt}{\tau})[p(t) + f(t)dt], \tag{B.27}$$

which is simple to recast as a differential equation:

$$\frac{dp(t)}{dt} = -\frac{p(t)}{\tau} + f(t). \tag{B.28}$$

Let us now apply a time-harmonic electric field $E(t) = \Re(E_0 e^{j\omega t})$. From the Lorentz force, the momentum equation becomes:

$$\frac{dp(t)}{dt} = -\frac{p(t)}{\tau} - eE, \tag{B.29}$$

which has steady-state solutions of the form $p = \Re(pe^{j\omega t})$. Then, inserting the trial solution:

$$j\omega p = -\frac{p}{\tau} - eE. \tag{B.30}$$

We can now write the expression for the AC conductivity:

$$\sigma(\omega) = \frac{\sigma_0}{1 + j\omega\tau}, \tag{B.31}$$

and the Drude model for permittivity is:

$$\epsilon(\omega) = \epsilon_0 - \frac{j\sigma(\omega)}{\omega}. \tag{B.32}$$

The Drude model is often augmented by a high-frequency permittivity limit, ϵ_∞, which models the contribution of higher-frequency absorption bands to the lower-frequency permittivity. Moreover, the parameters for the Drude model are often given as ϵ_∞, the plasma frequency ω_p, and the damping frequency, Γ. In this case, the following equation is equivalent:

$$\epsilon(\omega) = \epsilon_\infty - \frac{\omega_p^2}{\omega(\omega - j\Gamma)}, \tag{B.33}$$

where ω, ω_p, and Γ are all in radial frequency.

Appendix C

Isolated NIR Plasmonic Nanowire

In this section, a model is developed to predict the localized surface plasmon resonance frequency of the nanowires used in the NIR MTM-lined aperture in isolation. Novotny *et al*. showed that the effective wavelength scaling of a localized surface plasmon on a rod is linear, and governed by the excitation of the fundamental TM11 mode on the rod [167]. Our goal is to model the nanoantennas that form the liner of the wagon-wheel model in Fig. 3.1b, with outer radius $b = 120$ nm, gap and wire widths $g = w = 10$ nm, and the number of nanowires $N = 8$. The nanoantenna model has a quarter-wave, monopolar resonant current distribution along the wire and length $b - g/(2\sin(\pi/N)) = 107$ nm. Extrapolating to a full wavelength of 428 nm, Novotny's Fig. 2 predicts a resonance at 255 THz for a rod with a 10-nm radius, which we predict is a good representation of our 50:10 nm aspect ratio rectangular nanorod.

To validate this result for our resonant nanowire acting as a monopole, we created a periodic scattering simulation consisting of a gold nanowire attached to a large "ground" slab, as shown in Fig. C.1. For periodicity, horizontal boundaries are perfect magnetic conductor (PMC)s, while vertical boundaries are PECs. Ports terminate the z-boundaries, and the scattering parameters are measured to find the reflection peak of the resonating nanowire. The scattering parameters are plotted in Fig. C.2 near the predicted nanowire resonance frequency, and we observe a scattering resonance at 260 THz. Inspecting the electric-field profile in Fig. C.3, it is clear that this resonance corresponds to

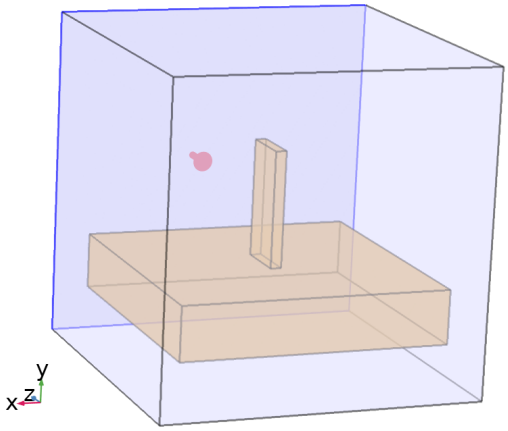

Figure C.1: Simulation layout of the representative resonant nanowire simulation. For periodicity, horizontal boundaries are PMCs, while vertical boundaries are PECs. Ports that excite a normal incidence, y-polarized plane wave terminate the z-boundaries (port 1 is highlighted in blue), and the scattering parameters are measured to find the reflection peak of the resonating nanowire.

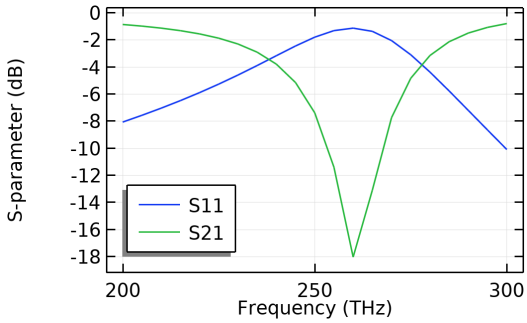

Figure C.2: Scattering spectrum of the grounded nanowire near the predicted resonance frequency of 255 THz. The maximum reflection is observed at 260 THz, very close to our prediction.

the quarter-wavelength monopolar resonance of the nanowire.

Changes to the periodic unit cell size or the ground size have a marginal effect on the resonance frequency, which is consistent with the observation that the nanowire controls the resonant frequency.

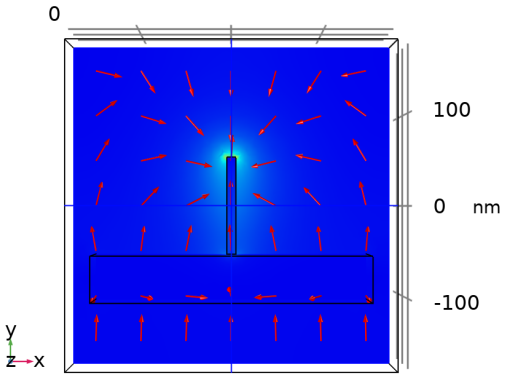

Figure C.3: Electric-field profile of the grounded nanowire at 260 THz, which demonstrates a quarter-wave monopolar resonance.

Appendix D

Comparable MIR Dipole Array

D.1 Field Intensity Enhancement Metric

In Ch. 3, we introduced a new performance metric, F_I, to quantify the expected absorption enhancement from the MIR MTM-lined discs. The majority of the literature to date focuses on creating individual hot spots, for which a reasonable metric is the maximum local electric field intensity enhancement. In COMSOL, an accurate measurement of this value in simulation can be difficult especially at sharp corners, requiring extremely fine meshes for convergence due to the sharp changes in fields [234]. Since the finite element method minimizes global error, integrated quantities converge must faster and accurate results can be achieved even for fairly coarse meshes. As a result, an average, integrated metric is likely to be more accurate than one derived from maximum fields.

A second consideration in creating a new metric for the performance of our MTS is the intended sample. While a single nanoantenna (or pair of nanoantennas) can probe a sample as small as a single molecule (in the case of SERS), a larger sample such as a continuous thin film, is more suitable for a nanoparticle array. In this case, any parts of the film accessible by the illumination may be used to enhance the absorption of the sample, and hence the field intensity enhancement over the full unit cell should be considered, rather than just the field intensity enhancement near a hotspot.

Thus we suggest F_I, which is the integral of the field intensity enhancement over the volume bounded by unit cell area and the film thickness, as

a readily quantifiable and comparable performance metric. F_I measures the total average field intensity enhancement, which is directly proportional to the absorption enhancement by the MTS.

D.2 MIR Coupled-Dipole Array

Unfortunately, F_I cannot be readily calculated from data available in the literature for comparison. To judge the performance of the MTM-lined disc array, a conventional end-coupled dipole array was generated to resonate at a wavelength of 15-µm. In order to make F_I comparable, the same constraints placed on the design of the MTM-lined disc should be applied. In particular, the unit cell area, the film thickness, and the minimum feature size must be identical. The minimum feature size sets the separation of the nanodipole tips at the periodic boundary and the nanodipole width, and the film thickness sets the nanodipole thickness. Creating a comparable area proves more difficult, as the last remaining degree of freedom for tuning the nanodipole resonance is the length and the weak contribution of the plasmon effect makes the dipoles unable to be miniaturized as significantly as the MTM-lined disc. As a result, the array period was made rectangular to allow the nanoantenna to be lengthened while maintaining a constant unit cell area.

The geometric layout of the coupled-dipole array is shown in Fig. D.1a, where the nanoantenna length is 4.2 µm, the parallel pitch is 4.3 µm, and the orthogonal pitch is $9/4.3 =\sim 2.1$ µm. The nanoantenna is gold (modelled with the same Drude model as before), the top half-space is air, and the bottom half-space is lossless ZnSe ($n = 2.29$). The reflectance, transmittance, and absorbance when excited with a normal-incidence plane wave polarized parallel to the antenna axis are shown in Fig. D.1c. The nanoantenna array shows a maximum reflectance at 20 THz, and the electric-field profile (shown in Fig. D.1b at the antenna surface) at resonance shows the clear half-wavelength fundamental dipole resonant field distribution. Over this spectrum, the coupled-dipole array has a maximum field enhancement ratio of 44 and an F_I of 5.2, less than one quarter that of the MTM-lined disc. Additionally, despite the lower loss,

the resonance is significantly less selective than the MTM-lined disc due to the larger characteristic length scale.

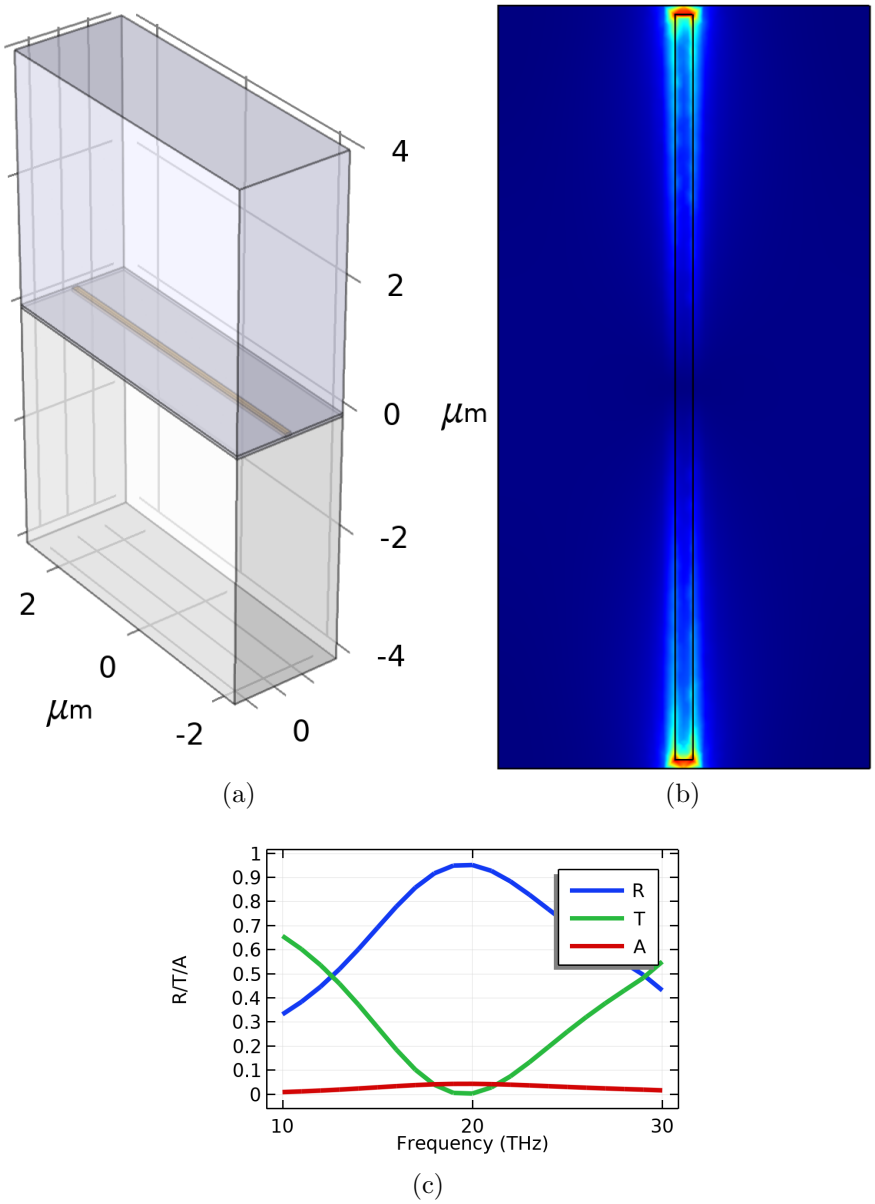

Figure D.1: (a) Layout of dipole array simulation, (b) electric-field profile at resonance, showing strong field enhancement at the coupled nanogaps, and (c) plane-wave scattering spectrum for an incident plane wave polarized parallel to the dipoles.

Appendix E

Detailed Experimental Parameters

E.1 Wagon-Wheel Fabrication

The gold film specimens were prepared on 1.1 mm-thick Borofloat 33 glass. The glass was first cleaned in a piranha solution, then dried and transferred to a Kurt J Lesker CMS-18 sputtering system, where first a Cr adhesion layer (5–10 nm) was deposited, followed by 50–90 nm of gold. The process parameters were as follows: the substrate temperature was 25 °C, deposition pressure was 7 mTorr, Ar flow rate was 55 sccm, and the substrate rotation was 20 RPM. For the Cr layer, the source power was set to 300 W and given a 30-s burn-in time to remove any contaminants from the source surface, and then 13–26 s to deposit. The Au film was sputtered with a source power of 80 W, a 30-s burn-in and a 169–305-s deposition time. The wafers were coated in HPR 504 photoresist, and diced into 10 mm×10 mm squares. The photoresist was removed with a combination of acetone and isopropyl alcohol (IPA). The samples were mounted onto aluminum microscope stubs with carbon tape, ensuring the sample sat flush with the stub surface to reduce sample tilt. Carbon tape was applied to one edge of each sample to ensure electrical conductivity to the stub. The samples were cleaned in a JEOL JAMP-9500F Auger Microprobe for 30 s in an Ar plasma, after which they were immediately loaded into the Zeiss Orion Nanofab to be imaged and milled. The patterns were designed and milled using the NPVE software to control the HIM.

E.2 Two-Wire Fabrication

E.2.1 Epitaxial Growth of Gold on LiF

The epitaxial films were grown in the AJA Orion 8 planar magnetron sputter system, "Moe". The deposition rate of gold was tested first at room temperature (25°C) since the crystal thickness monitor cannot be used at high temperatures. A deposition rate of 1.1 Å/s was measured with a 7% source power (40 W), a gas pressure of 4 mTorr, and a 20 sccm Ar gas flow rate.

As described in Ch. 4, 1 cm^3 LiF crystals were sourced from United Crystals [207]. The crystals were cleaved using a razor blade immediately before loading into the load lock. The substrate temperature was set to 460°, with a 10-minute soaking time before beginning the deposition at a base pressure of 3.75e-6 Torr. The source power was ramped up over 60 s, and a 60-s burn-in was performed before the shutter was opened. For the 65-nm film, the deposition lasted 681 s for a deposition rate of ∼0.95 Å/s.

E.2.2 Removal of LiF Substrate

To remove the LiF substrate, the sample was dissolved in HF. A solution of 40% HF was prepared, and the sample was immersed for 5 minutes. After the first minute, the film began to look rough as it began to loosen from the substrate surface. The sample was carefully removed from the HF and slowly lowered into a beaker of DI water, where the gold film detached and was left floating on the water surface. The gold flakes on the water surface were then retrieved with TEM grids.

Without any further processing, these samples were affixed to stubs and loaded into the HIM for patterning.

E.3 Two-wire Characterization

The microscope used in the characterization of the polarization-sensitive MTM-lined aperture MTS was designed and assembled by Kyle Scheuer in the DeCorby lab at the University of Alberta. The microscope component lay-

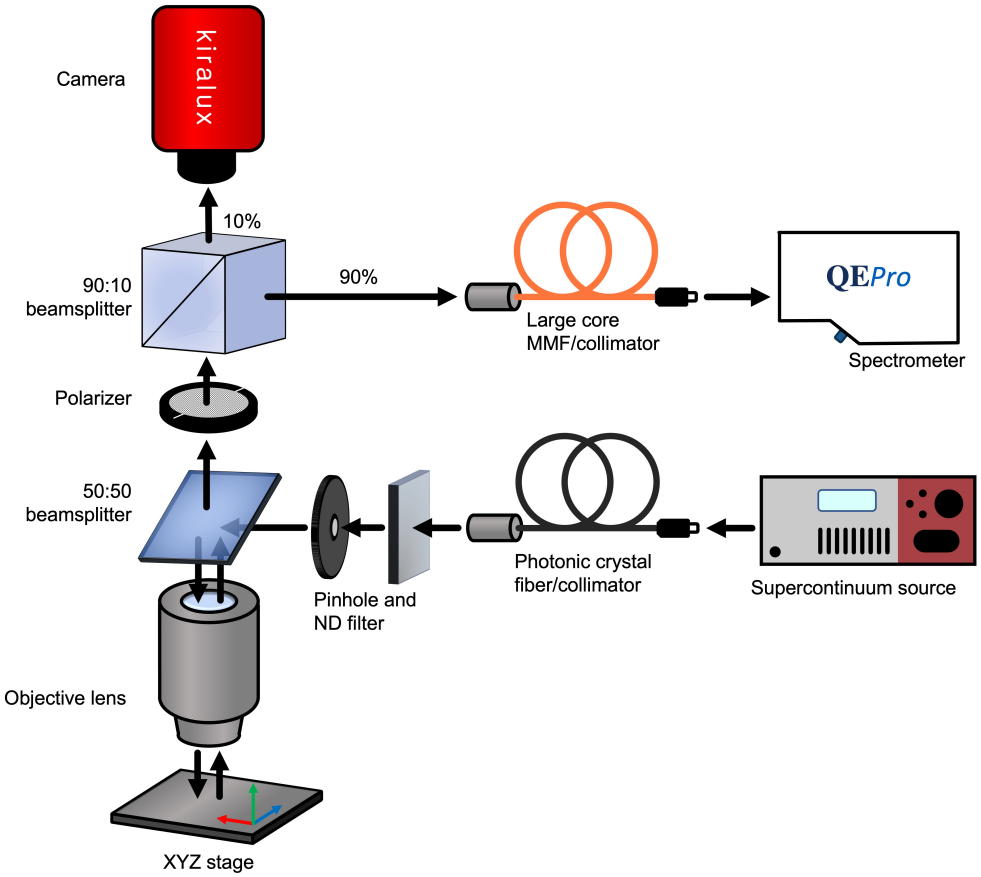

Figure E.1: Reflection-mode supercontinuum microspectrophotometer component layout used to measure the reflectance of the polarization-sensitive MTM-lined aperture MTS. Image courtesy of Kyle Scheuer.

out, shown in Fig. E.1, is important to understanding a number of challenges that arose in reliably measuring the MTS spectrum.

The microscope system consists of an NKT SuperK Compact supercontinuum laser with source wavelength of 450–2400 nm [235], coupled to a collimator [236]. The collimated beam travels through a 20 dB neutral-density filter [237] and an adjustable iris, then is reflected towards the sample using a non-polarizing 50/50 beamsplitter [238]. The beam is then focused onto the sample using a 100× objective [239], achieving a spot size of approximately 3.5 µm. After reflecting off the sample, the beam returns to the 50/50 beamsplitter, transmitting the reflected spectrum through a linear polarizer [240], then a final 90/10 beamsplitter [241], where 10% of the power is directed to a camera [242], and 90% of the power is focused using a collimator [243] to a

large-core fibre [244] coupled to an OceanOptics spectrometer [245].

E.4 MIR Fabrication

ZnSe substrates (ZnSe windows, Edmund Optics [214]) were coated in Electra-92 and a PMMA bilayer at the University of Alberta nanoFAB Centre, then exposed in the JBX-6300FS Electron Beam Lithography System at the University of Waterloo Quantum Nanofab. The samples were then returned to the University of Alberta and the patterns were developed (30 s in 7:3 IPA:H_2O + 30 s in H_2O), a 50-nm gold layer was deposited by electron-beam evaporation, and finally lifted off by sonication in acetone.

E.5 MIR Characterization

E.5.1 Helium Ion Microscopy

Due to the MTS having features on the order of 100 nm, conventional optical microscopy could not be used to accurately measure the features of the cell. Additionally, the MTS has no continuous conductive path, so scanning electron microscopy cannot be used. Helium ion microscopy is a minimally destructive imaging method with sub-nanometer resolution and the ability to image insulating samples.

The ZnSe chips were affixed to aluminum SEM stubs using carbon tape, then loaded into the Zeiss Orion HIM microscope with Helium and Gallium ion guns. The HIM is also equipped with an electron flood gun to mitigate the positive charge induced by the scattering ions. The images were taken using a current of 1.2 pA with the electron flood gun active and with 64 line-averages.

E.5.2 FTIR Spectroscopy

The reflected spectrum of the array was measured on a Nicolet 8700 Spectrophotometer with a Contiuμm microscope attachment. This microscope uses a cryogenically cooled HgCdTe (MCT) detector, a reflective 15$\times$ objective, and KBr refractive optics, which limit the acquisition of signals beyond

500 cm^{-1}. The microscope is purged with N_2. The reflection spectrum of each fabricated array was measured over a square 69 µm×69 µm aperture, and normalized to the reflection spectrum of a bare ZnSe surface.

The Reflachromat lenses used in the Contiuμm microscope are symmetric catoptric lenses, and hence none of the components of the focused beam arrive at normal incidence [246]. Furthermore, the Contiuμm microscope makes use of a patented aperture system that masks both the input and output beams, rejecting any diffracted power or off-specular reflections [247]. Without exact specifications on the beam path, it is impossible to predict the fractions of the spurious reflected waves (*i.e.*, the top-surface reflection and the higher-order bottom-surface reflections) that reach the detector, and hence we assume in our model that all power is captured, which gives good agreement with the observed experimental data. Due to the normalization, this assumption is accurate as long as the fraction of lost power is similar in both the top reflection and the bottom reflection. Given the wide bandwidth of the source, the coherence is weak and the intensities of the encoded interferograms reflected by all surfaces can be added directly.

E.5.3 Gas Cell

The experimental setup consisted of the custom glass gas cell loaded onto the Nicolet Continμum microscope stage, connected to gas cylinders and a venting valve via 1/4" plastic tubing. A schematic of the gas cell with illumination is shown in Fig. 5.6, and the inset shows a cartoon of the MTS exciting nearby CO_2 molecules (not to scale). The ZnSe window was epoxied to the glass cell. The microscope was focused onto the bottom surface of the yellow ZnSe substrate, where the MTS is patterned. 100% CO_2 or 100% N_2 gas was fed in from one side, and the pressure was measured with the regulator attached to the gas cell inlet. The output was vented outside the lab through a 1/4" plastic tube. The measurement was prepared by opening the N_2 valve and the venting valve for 2 minutes to purge the gas cell of air. The valves were then closed, the cell was left for 2 minutes to stabilize, and a measurement was taken. The same procedure was used to take measurements with CO_2.

The 10-PSI CO_2 measurement was taken with both the CO_2 and the venting valves open. Without mass flow controllers, this setup did not allow precise control over gas mixing nor gas pressure and was chosen as a simple, cheap, but effective means to load the MTS with a known quantity of CO_2.

Appendix F

MIR experiment noise analysis

In the following, the noise was calculated on the standard 2100–2200 cm^{-1} region of the spectrum as this region has the strongest signal and only very weak to no interfering absorption bands, depending on the lab environment [248]. Assuming the noise was the same over the measured spectrum, the amplitude of the noise was then extrapolated to the active spectral region near 667 cm^{-1}.

The 2100–2200 cm^{-1} window was first flattened by taking the difference between the raw spectra for N_2 and CO_2. The variance was then calculated on the difference [249]:

$$\sigma_a^2 = \sum_{i=1}^{n} \frac{(y_i - \hat{y})^2}{n-1}, \tag{F.1}$$

where $\hat{y}$ denotes the average of all samples.

Next, the variance of the original spectra was calculated. We assumed that the variance calculated above was evenly distributed between the two input spectra and that covariance of the noise was 0, and were hence able to solve for the original absolute variance, σ_b^2, as:

$$\sigma_a^2 = \sigma_b^2 + \sigma_b^2, \tag{F.2}$$

$$\sigma_b^2 = \frac{\sigma_a^2}{2}. \tag{F.3}$$

This absolute variance was assumed to be present throughout the entire spectrum. To get the variance on the final presented data, σ_t^2, the relative variance of each spectrum was added in the active region near 667 cm^{-1}:

$$\sigma_t^2 = \left(\frac{A}{B}\right)^2 \left(\frac{\sigma_a^2}{A^2} + \frac{\sigma_a^2}{B^2}\right), \tag{F.4}$$

where A represents the raw CO_2 data and B represents the raw N_2 data. The final data, plotted with error bars equal to $\pm\sigma_f$, is shown in Fig. F.1. The experimental and simulation data agree best for the MTS case, and the ZnSe case would agree better with a constant offset of ∼0.5%. Despite the error margins, the dip in reflection seen for the MTS case is clear and lies well outside of the predicted error.

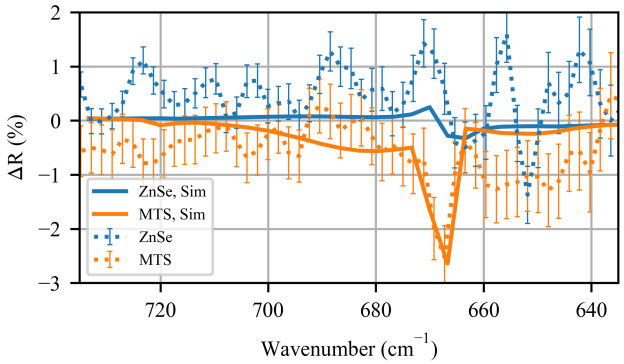

Figure F.1: Experimental data with calculated standard error bars (dotted) and simulation data (solid) for comparison. Reproduced from [180], CC BY 4.0.